國立臺灣大學理學院地質科學研究所

博士論文

Department of Geosciences

College of Science

National Taiwan University

Doctoral Dissertation

台灣西南海域增積岩體成岩作用與深部流體遷移

Diagenesis and migrations of deep fluids in accretionary prism offshore southwestern Taiwan

陳乃禎

Nai-Chen Chen

指導教授: 林立虹博士 (Li-Hung Lin, Ph.D.)

楊燦堯博士* (Tsang-Yao Yang, Ph.D.*)

*於民國 104 年 3 月辭世

*Deceased in March 2015

中華民國 109 年 01 月

January, 2020

doi:10.6342/NTU202000506

誌謝

在經過八年多的奮戰後終於畢業，感謝這段時間的際遇，我不敢忘了每個經過，也不敢忘了每個教誨。還清晰地記著每個環節，如何建構研究、如何解決問題、如何設計實驗、如何撰寫文章以及如何調適心態。

論文的產出基於許多人的貢獻與指導，首先特別感謝楊燦堯老師及過去一同出海採樣的同伴們，或稱他們為楊家將—佩涓、德芳、小州、小芬、瑋立、博文、心怡、筱琪、鈞元、宣文、艾荻、峻銘、惠文、小雄、靜宜、愉珺、小乖、小龜、大綸、又真、雅緻、汭芬、鎧文、國維、世榮、佳菱、悅婷、Lulu、Walia 及 Monika。楊老師總是極盡所能提供學生們在研究上的需要，包含採樣與出國研習。過去一同在天然氣水合物合作的瑋立、佩涓、筱琪、宣文、靜宜、愉珺、小龜以及 Lulu，他們不餘遺力地採樣以及分析，背後多次資料及書報討論，都讓我獲益良多。

在楊老師逝世後，受到諸位老師的關心，感謝博士班委員們以及大陳老師，給予我日常生活、採樣及論文上的指導。感謝能在立虹老師及珮玲老師的實驗室下，兩位老師對於學術的嚴謹及追求深植我心，畢竟在研究日新月異的時代下，即便時間成了我們最大的敵人，研究依然無法草率進行。立虹老師常分享他怎麼思考以及架構研究，在寫作上面也給予許多意見。兩位老師常招待實驗室的每個人，把我們當做自己的小孩看待。適應新環境期間，感謝其他學生、助理以及博後的激勵與陪伴。子慧、庭逢、俐陵、韻淳、岱怡、光庭、子灝、小靜、希瓠及後來讀博的悅婷在工作上互相幫助，工作之餘一同玩桌遊；筱君、柏宇在實驗上的指導及搞笑演出；子萱、妮娜、蘆育、汭芬、玲雯、貞年、雅方、婉綾、易峰、奕傑、資蓉、乙嘉在各方面的協助；每人的幫忙不計其數，無論是實質上或是情感上，實在難用三言兩語總結。

最後，感謝教會的弟兄姊妹們，在我經濟並不是那麼足夠時給我許多幫助，他們經常盛情款待，我好似變了個食客。我並非有信心的人，因著他們諸多的禱告，我心中感到平安。立虹老師常說博班只是一個過程，未來會有更多意想不到的關卡及困難。未來難以猜測，經過博班的訓練，我只知道面對每個挑戰，都要踏實完成。

doi:10.6342/NTU202000506

Abstract

The fluid migration and early diagenesis impose an important control on the geochemical cycling in accretionary prisms. The interaction between compounds supplied from land, seawater, and deeply-rooted fluids facilitate many microbial processes and degrade considerable organic matter, leaving refractory organic matter buried into great depths. The final product, methane, can be formed through thermogenic and microbial processes in subsurface sedimentary environments and then discharge into seawater and even the atmosphere, exerting profound impacts on biogeochemical cycles and greenhouse effects. Mineral-bound water would be also released as temperature and pressure increase with depths, bearing deeply-rooted signals as fluids migrating upward. However, the methane and fluids budgets along with microbial processes remain rarely explored, qualified and quantified in subduction systems. This study combined fluid gechemical analysis and numerical modeling to explore fluid processes and microbial activities, aiming at better systematically understanding of organic-carbon related microbial activities as well as cycling of methane and water in accretionary prisms.

In the first part, sediment cores distributed across a submarine mud volcano (SMV), TY1 (one of the Tsangyao Mud Volcano Group), were investigated to determine the

doi:10.6342/NTU202000506

characteristics of fluids generated through the convergence between the Eurasian and Phillippine Sea Plates. The fluid geochemistry indicated that fresh water derived from smectite dehydration at an equilibrium temperature of 100 to 150 ºC. The upward fluid velocities affected the rate and efficiency of anaerobic methanotrophy. About 1.1–28.6% of the smectite-bound water originally stored in the incoming sediments was exploded from SMVs, suggesting that SMVs could act as a conduit to channel the fluids produced from great depth/temperature into seafloor environments in a subduction system.

In the second part, the production, consumption, and migration of methane were systematically quantified along a continental margin in offshore southwestern Taiwan. Combined with published data, the results showed that high methane fluxes and the methane carbon isotopic values tend to be associated with structural features, suggesting a strong structural control on the methane transport. Anaerobic oxidation of methane played an effective biological filtration as a significant portion of ascending methane was consumed. The flux imbalance arose primarily due to the larger production of methane through deep microbial and thermogenic processes and could be likely accounted for by the sequestration of methane into hydrate forms, and clay absorption.

In the third part, TY1 was chosen to denote a model system that could witness how

doi:10.6342/NTU202000506

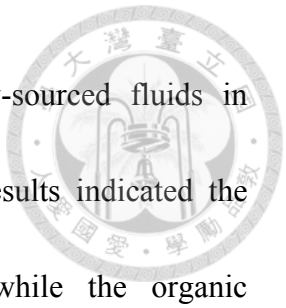

microbial activities react under mixing of seawater and deeply-sourced fluids in subsurface environment. Inorganic geochemical and simulation results indicated the porewater profiles were obviously affected by deep fluids while the organic geochemistry showed that the *in situ* microbial activities controlled the distribution of dissolved organic carbon and short-chain compounds.

In conclusion, tectonic-controlled fluids migration in accretionary prisms strongly influenced microbial activities in subsurface environment. Systematically investigation into methane and water could better understand the predominant mechanism in their cycling.

Keywords: submarine mud volcano, DOC, acetate, anaerobic oxidation of methane, methane, smectite, water, accretionary prism, subduction

doi:10.6342/NTU202000506

摘要

流體遷移和早期成岩作用控制著增生楔地球化學的訊號與循環。來自陸地、海水及深部流體的化合物之間的交互作用促進許多微生物反應，並使大量的有機物降解；不易分解的有機物則進而被掩埋於沉積物深處。有機物分解的最終產物—甲烷，其透過有機物的熱分解和微生物分解作用而形成，經由遷移而排放到海水甚至大氣中，對生物地球化學循環和溫室效應產生深遠影響。隱沒的含水礦物隨著溫度和壓力的增加從而被釋放，在被擠壓的構造環境中，隨著流體向上遷移，將深部流體帶入淺層沉積物中，亦使得淺層沉積物帶有深部流體的訊號。然而，對於隱沒帶甲烷、流體通量以及微生物作用尚未有系統性探討。因此，為了探索流體過程和微生物活動，這項研究結合了流體地球化學分析和數值模擬，旨在系統性了解有機碳相關的微生物活動以及增生楔中甲烷和水的循環。

本研究總共分成三個部分。本研究的第一部分在台灣西南海域的燦堯泥火山群（Tsanyao Mud Volcano Group）中的一座泥火山—TY1 採了一系列的岩心，用以探討歐亞大陸與菲律賓海板塊之間的匯聚所產生的流體的特徵。流體地球化學表明，蒙脫石在平衡溫度為 100 至 150 ℃ 時因脫水而產生了礦物解離水。此向上遷移的流體速度影響厭氧甲烷氧化的速率和效率。利用 TY1 的水排放量外推至西南海域其他 12 座泥火山，約有 1.1－28.6%的蒙脫石結合水在隱沒後，從西南海域的海底泥火山排出，這表明海底泥火山可以作為將深層/高溫下產生的流體引導

doi:10.6342/NTU202000506

到隱沒系統中的海底環境的管道。

在第二部分的研究進行台灣西南沿海近海大陸邊緣的甲烷源與匯系統性量化與探討。結合前人研究的發表數據，結果指出高甲烷通量和甲烷碳同位素值與地質構造相關，也就是說甲烷的遷移主要受到構造的控制。大部分的站位皆顯示厭氧氧化作用消耗了大量上升遷移的甲烷，顯示其為有效甲烷生物濾網。甲烷源與匯的通量整合計算顯示多餘的深層微生物和熱成熟產生的甲烷可能被儲存於天然氣水合物中抑或是以吸附於粘土上的形式存在。

在第三部分中，著重於深部流體與淺層沉積物的相互作用，以探討有機碳相關的微生物活動與環境之間的相互作用。 燦堯泥火山群中的一座海底泥火山（TY1）被選為此研究的模型系統，由於海底泥火山流體為海水與深部流體的混合，因此該系統可以反應出海水和深層流體混合中的微生物活動。無機地球化學和模擬結果顯示深層流體對孔隙水有明顯影響，而有機地球化學卻指出溶解有機碳和短鏈化合物主要被微生物活動控制。

綜合三個部分的研究成果，在增生楔中，構造控制的流體強烈影響了地下環境中的微生物活動。對甲烷和水的源與匯進行系統調查可以更深入了解影響循環系統下通量大小的主要機制。

關鍵詞：海底泥火山，溶解有機碳，乙酸鹽，甲烷，厭氧甲烷氧化，水，蒙托石，增生楔，隱沒系統

doi:10.6342/NTU202000506

Table of Contents

doi:10.6342/NTU202000506

doi:10.6342/NTU202000506

doi:10.6342/NTU202000506

doi:10.6342/NTU202000506

doi:10.6342/NTU202000506

List of Figures

doi:10.6342/NTU202000506

Figures in Appendix

doi:10.6342/NTU202000506

doi:10.6342/NTU202000506

List of Tables

Tables in Appendix

doi:10.6342/NTU202000506

doi:10.6342/NTU202000506

Chapter 1 Introduction

1.1 Overview

An accretionary prism forms from sediments scraped off and accreted on a non-subducting tectonic plate at a convergent plate boundary [e.g. *Cawood et al.*, 2009]. Faults, fractures, and mud diapirs incorporated in accretionary prism serve as good fluid conduits accelerating gas-charged materials migrating upward [e.g., *Tobin and Saffer*, 2009]. Mud volcanos (MVs), one of the distinct degassing structures, are often distributed along convergent plate margins where fluid-rich sediments are rapidly accumulated in accretionary prisms or trenches [*Hedberg*, 1974; *von Huene and Lee*, 1983; *Brown and Westbrook*, 1988; *Dimitrov*, 2002; *Kopf*, 2002]. They are thought to be a "window" to probing the origins and characteristics of deep fluids and muds because their formation is attributed to the migration of overpressurized muddy fluid connected to mud diapirs formed at or fractures extended to great depths [e.g. *Kopf*, 2002]. As the deposited sediments are not fully dewatered and consolidated during the burial processes, the fluidized sediments could escape from their source region with deeply seated volatiles. Such material channeling enables the voluminous addition of sediments, fluids, and gases into shallow subsurface, land surface or seafloor, forming topographically or bathymetrically distinct features like volcanic

doi:10.6342/NTU202000506

structure. Since deeply-sourced nutrients and microorganisms are also mobilized with fluids to shallow environments, land surface or seafloor, MVs offer great opportunities to observe microbial communities indigenous to deep subsurface and the impact of material recycling on near surface redox gradient and microbial processes [e.g. *Cheng et al.*, 2012; *Nuzzo et al.*, 2008; *Hoshino et al.*, 2017].

A portion of fluids in sediments from submarine mud volcanoes (SMVs) are thought to be generated by mineral dehydration processes at high temperatures and pressures. The release of fluid from the subducting plate into the overlying wedge decreases the liquidus temperature of lithospheric materials, thereby increasing the degrees of partial melting and facilitating melt extraction for arc magmatism [*Peacock*, 1990]. The presence of fluids also increases the pore pressure and reduces the effective stress of rocks, altering the rheology and deformation states for deep crustal environments. In addition to mineral dehydration, sediment compaction is essential for fluid circulation in an accretionary prism [*Moore and Vrolijk*, 1992]. These pore fluids volumetrically outcompete over mineral-bound fluids by a factor of at least 2 [e.g. *Chen et al.*, 2020; *Menapace et al.*, 2017]. Therefore, fluid circulation at shallow depths would be inevitably related to the compaction driven dewatering [e.g. *Moore and Vrolijk*, 1992]. Deconvolution of the contribution of mineral-bound fluids from

doi:10.6342/NTU202000506

pore fluids to the overall fluid budget is challenging since their intrinsic characteristics could be easily modified during transport and the access to the retrieval of pristine signatures is often limited. SMVs provide a route to access well-constructed channels and sampling of fluids formed at great depths. Of numerous marine systems, SMVs located at Nankai Trough and Mariana convergence systems have been extensively studied to illustrate the typical fluid circulation patterns for accretionary versus non-accretionary convergent systems, respectively [e.g. *Eickenbush et al.*, 2019; *Fryer et al.*, 1999; *Ijiri et al.*, 2018a, 2018b; *Saffer et al.*, 2009; *Toki et al.*, 2014]. Considering that accretionary systems represent at least 70% of the plate convergence, the role of mud volcanism and deep-seated dewatering processes are often constrained from geophysical approaches only (e.g., Costa Rica, Peru systems) [e.g. *Freundt, et al.*, 2014; *Jarrard*, 2003; *Menapace et al.*, 2017; *Völker et al.*, 2014]. The exact characteristics and quantities of fluids discharged from SMVs and the geochemical framework for the fluid budget in subduction systems are poorly understood in the western Pacific Ocean region.

Methane production and consumption processes are another important issue for volatile cycling in accretionary prisms. Methane is one of the final products for the decomposition of subducted organic matters. During the sediment burial at shallow

doi:10.6342/NTU202000506

depths, organic matters are converted to dissolved organic carbon (DOC) and carbon dioxide by microbial hydrolysis and fermentation, leaving refractory organic matters further buried to greater depths [e.g. *Komoda et al.*, 2013]. Methanogenesis would dominate over other diagenetic processes in sulfate depleted environments [e.g. *Reeburgh*, 2007] by harnessing different precursors, such as CO_2, acetate, and other kinds of methyl-type molecules produced from stepwise degradation processes. In addition to microbial methane, the increasing pressure and temperature associated with burial and subduction processes would lead to the cracking of refractory organic carbon and ultimately to the production of gaseous hydrocarbons (including methane; at more than 80 ^{o}C) [*Jørgensen*, 1982; *Martin et al.*, 1993; *Dimitrov*, 2002]. Since their formation occurs at great depths, thermogenic hydrocarbons are often confined within geological structures, forming economically feasible gas reservoirs. Regardless of the origins of methane, gas hydrates, a cage structure composed of H_2O and methane molecules, can be formed and sequester methane carbon in deep sediments under a favorable condition. Previous study has estimated that around 500–2,000 × 10^{12} g C are preserved in the form of methane hydrate [*Wallmann et al.*, 2012]. Such an enormous amount of gas hydrate stored in marine sediments could, however, become unstable and be transformed into mobile phase caused by environmental

doi:10.6342/NTU202000506

fluctuations (such as temperature, sea level, and slope stability). As methane migrates toward shallow depths, its concentration is susceptible to be altered by various microbial consumption processes, depending on the redox state and availability of specific electron acceptor (e.g., oxygen, nitrate, and sulfate). Such microbial removal mechanisms control the ultimate release of methane into the seawater column or the atmosphere, determining the contribution of sediment systems to the greenhouse effect [*Linke et al.*, 2005; *Judd and Hovland*, 2007; *Wallmann et al.*, 2006b]. Although intensive methane cycling occurs along continental margins, very few studies have provided a quantitative framework to simultaneously constrain the production, migration, and consumption of methane in a regional scale.

Sediments in the subsurface of SMVs are composed of not only deeply-sourced sediments but newly deposited terrestrial and marine materials. Over a degradative chain of reactions through microbial hydrolysis and fermentation, organic complexes inherited with the sediments are transformed into low-molecular-weight dissolved organic carbon (DOC) and short-chain organic acids, such as amino acids and volatiles fatty acids (VFAs) [*Henrichs and Farrington*, 1992; *Heuer et al.*, 2010; *Zhang et al.*, 2019]. Similar to methane, short-chain organic acids can be also produced by thermal cracking of refractory organic matters [*Wellsbury et al.*, 1997;

doi:10.6342/NTU202000506

Egeberg and Barth, 1998]. Field and laboratory experiments have shown that the concentration of acetate could range up to 120 ppm in the petroleum system experiencing intensive thermal maturation [e.g., *Cooles et al.*, 1987; *Lundegard and Kharaka*, 1990; *Shebl and Surdam,* 1996]. Regardless of their origins, VFAs contributed from combined microbial and thermogenic processes are energetic and can serve as an electron donor for various downstream electron accepting processes [*Amend and Shock*, 2001; *Whiticar*, 1999], such as metal reduction, sulfate reduction, denitrification, and methanogenesis [*Burdige*, 1993; *Glombitza et al.*, 2015; *Heuer et al.*, 2009; *Yoon et al.*, 2013]. Therefore, the rapid turnover renders their concentrations low in most marine sediments. Their distribution pattern in mud volcano environments remains rarely explored.

1.2 Geological background

Offshore southwestern Taiwan is a west-advancing accretionary prism lie in the transition region from subduction to collision, where the Luzon volcanic arc initially collides with the rifted China continental margin starting about 16 Myr [*Lin et al.*, 2009; *Shao et al.*, 2015; *Yang et al.*, 1995]. The passive China continental margin (passive margin) and the submarine Taiwan accretionary prism (active margin) are delineated by a deformation front and the Malina trench (DF and MT in Fig. 1.1) [e.g.

doi:10.6342/NTU202000506

Lin et al., 2009 and *Lin et al.*, 2014]. The active margin is further divided into two structural domains by out-of-sequence thrusts (OOST in Fig. 1.1), from west to east, the lower slope domain and the upper slope domain [*Reed et al.*, 1992; *Lin et al.*, 2009]. The right boundary of the upper slope was defined by *Lin et al.* [2009] (Fig. 1.1). The lower slope domain features NNW-striking fold-and-thrust structures [e.g. *Lin et al.*, 2008; *Lin et al.*, 2014] while mud diapirs and SMVs characterizes the upper slope domain [*Chen et al.*, 2014a; *Chuang et al.*, 2010]. The surface geothermal gradient calculated from heat-probe measurement (3 to 6 meter-long) ranges from 8 to 390 ^{o}C/km, and 62 °C/km in average [*Chiao*, 2015; *Shyu and Chang*, 2005]. The highest heat flow (530 mW/m^2; 390 ^{o}C/km) was detected at Tsanyao Mud Volcano Group (TYMV) while the heat flow at the margin of TYMV decreased to 30 mW/m^2 (25 ^{o}C/km) [*Wu*, 2016]. Based on BSR-controlled heat-flow estimations, geothermal gradient varies from 17 to 150 ^{o}C/km while it mostly ranges 20 to 30 ^{o}C/km in the upper slope [*Chi and Reeds*, 2008].

doi:10.6342/NTU202000506

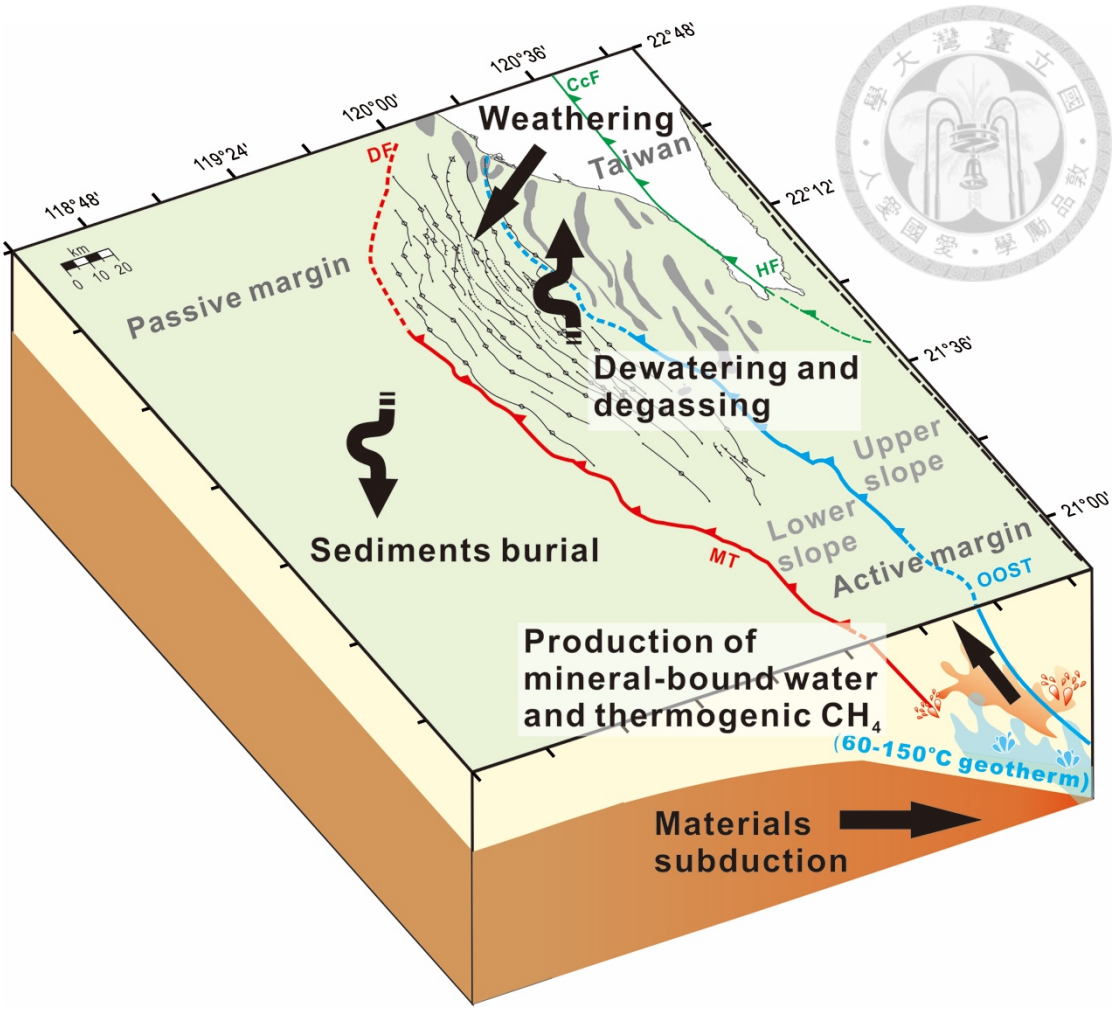

Figure 1.1. The conceptual sketch of subduction and fluid migration in offshore southwestern Taiwan. Map overlaid with the distribution of mud diapirs, geological structures [*Lin et al.*, 2009; *Lin et al.*, 2014]. Black arrows represent geological processes. Red and light blue area symbolizes the production of thermogenic methane and mineral-bounded freshwater, respectively. The medium-dashed line denotes the right boundary of the upper slope defined by *Lin et al.* [2009]. DF: deformation front; MT: Manila Trench; OOST: out od sequences thrusts; CcF: Chaochou fault; HF: Hengchun fault.

doi:10.6342/NTU202000506

1.3 Objectives

The overall objective of the study is to systematically deconvolute the volatile production, transport, and cycling in various compartments of the accretionary wedge off southwestern Taiwan using mud volcanoes as the target materials and sample access. The study is divided into three major parts, aiming at addressing (1) the origin of deeply-sourced fluids and water cycling, (2) the assessment on the production and consumption fluxes, and migration pathways of methane, and (3) the distribution of DOC and the factors controlling their transformation across the redox gradient. In the first and second parts, the deep sources of water and methane would be compared with the water discharging from SMVs and methane effluxes, respectively. As a result, the length of trench used for deep sources production calculation would be adjusted based on the SMVs distributed region and the methane effluxes investigation area. In the third part, the impact of deep sources on subsurface environment is discussed. Below describes the detailed design and justification of individual parts.

According to previous studies, fluids cycling impose importance on subduction systems. Although the quantitative approaches have been developed to constrain the fluid budget and transport in subduction zones using parameters inferred or obtained from various geophysical approaches [e.g. *Jarrard*, 2003; *Freundt et al.*, 2014;

doi:10.6342/NTU202000506

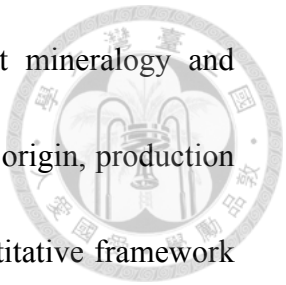

Menapace et al., 2017], the lack of knowledge about sediment mineralogy and physical properties renders the quantitative constraints on the fluid origin, production and discharge subject to high uncertainty. The lack of robust quantitative framework also impedes the possibility to address the impact of deeply fluids on cycling of methane and other elements susceptible to the modification of various processes. Therefore, in the first part of this study, an SMV, TY1, in the accretionary prism offshore southwestern Taiwan was chosen for investigation because TY1 is the biggest SMV in southwestern Taiwan [*Chen et al.*, 2014a]. Cored sediments across a transect of TY1 were collected for comprehensive gas and fluid geochemical analyses. These data were used to define the fluid characteristics and origin, to assess the formation temperature, and to deduce the fluid-rock ratio for the reaction in the source region. Reactive transport modeling was further applied to quantify the fluxes of fluids and methane and to address the effects of fluid and methane fluxes on the activities of microbial methane consumption and sulfate reduction. Finally, the fluid budget and transport were further discussed and inferred.

In the second part, the source and sink fluxes of methane across sediments impacted with/without seepage or mud volcanism off southwestern Taiwan were assessed using box model approaches (including mass balance of solute concentration

doi:10.6342/NTU202000506

and carbon isotopes). These terms include the production by microbial processes and thermal maturation at different depth intervals, and the consumption by microbial processes in either the geochemical transition or seawater-sediment interface. The model fluxes were further compared with the distribution of structural features and address the control of fractures on methane discharge. By integrating the results obtained from this and previous studies [*Chuang et al.*, 2006, 2010, 2013; *Ye et al.*, 2016], the fate and sequestration of methane in Taiwanese subduction system were also discussed.

In the third part, the distribution pattern of DOC and small organic acids for sediments in TY1 were uncovered to address microbial processes cycling DOC and organic acids. Bulk DOC and various organic acids (acetate, formate, propionate, butyrate, and lactate) are specifically targeted for analyses to complement to the other aqueous and gas geochemistry obtained in the previous study [*Chen et al.*, 2020]. These results were further integrated into a reactive transport modeling framework to constrain specific microbial activities and the effects of individual dissimilative and assimilative metabolisms on the pattern of bulk DOC.

doi:10.6342/NTU202000506

Chapter 2 Discharge of deeply rooted fluids from submarine mud volcanism in the Taiwan accretionary prism

2.1 Introduction

Fluid cycling is of great importance to magma and seismicity generation in subduction systems. The release of fluid from the subducting plate into the overlying wedge decreases the liquidus temperature of lithospheric materials, thereby increasing the degrees of partial melting and facilitating melt extraction for arc magmatism [*Peacock*, 1990]. Such fluid circulation in the deep crustal region also leads to increasing the pore pressure and reactivity of minerals, modifying the rheological property and weakening the rock strength [*Karato and Wu*, 1993; *Mei and Kohlstedt*, 2000; *Peacock*, 1990]. The discharge of deeply generated fluids into the bottom ocean further influences the distribution of biological communities and seawater chemistry [*Saffer and Tobin*, 2011; *Zellmer and Straub*, 2014]. Therefore, a systematic assessment of fluid origins and its intrinsic characteristics in subduction systems would facilitate the implementation of a quantitative framework for fluid cycling and budget.

Sediment compaction and mineral dehydration are the most important

doi:10.6342/NTU202000506

mechanisms for fluid generation and circulation in an accretionary prism [*Menapace et al.*, 2017; *Moore and Vrolijk*, 1992]. In essence, both mechanisms are driven by the increasing pressure and temperature associated with sediment burial and deformation. However, the geochemical signatures inherited from individual mechanisms are drastically different. Porewater excluded by sediment compaction through burial and deformation bears a composition essentially identical to seawater (e.g., ~560 mM chloride, and $\delta^{18}O$ and $\delta^{2}H$ values around 0‰). In contrast, lattice-bound water released by mineral dehydration is salt-free and carries $\delta^{18}O$ and $\delta^{2}H$ values deviating from its sourced fluid (e.g., seawater) [*Dählmann and De Lange*, 2003; *Hensen et al.*, 2007; *Ijiri et al.*, 2018]. Volatile elements (e.g., B, and Li) desorbed from clay minerals are also commonly accompanied with mineral dehydration [*Scholz et al.*, 2010; *Vanneste et al.*, 2011]. Fluids generated from different mechanisms are, however, susceptible to the mixing during migration, thereby obscuring the pristine signatures that could be used to constrain the source depth, physico-chemical parameters of reactions, and fluid budget. Elucidating the observed characteristics remains challenging and often requires a sampling strategy targeting specific geological features or structures.

As one of the prominent seafloor features, submarine mud volcanoes (SMVs) are

doi:10.6342/NTU202000506

commonly distributed in accretionary prisms where rapid sedimentation and tectonic interaction lead to the gravitational instability of unconsolidated shale/mudstone, fluid overpressurization, and formation of dense fracture array [*Brown*, 1990; *Brown and Westbrook*, 1988; *Hensen et al.*, 2007; *Vanneste et al.*, 2011]. Because the fracture network associated with the plate convergence could be extended to as deep as the lower crust, SMVs are able to efficiently export deeply sourced fluids, sediments, and reducing volatiles to the seafloor, generating morphological domes and depressions, mudflows, and even biological hotspots with colonies depending on leaked gaseous hydrocarbons [*Dählmann and De Lange*, 2003; *Hensen et al.*, 2007; *Ijiri et al.*, 2018]. While SMVs provide a window to witness the deep subsurface characteristics, upward migrating hydrocarbon gases produced by thermal maturation or methanogenesis also drive the sulfate-dependent anaerobic oxidation of methane (AOM) at shallow depths [*Hensen et al.*, 2007; *Ijiri et al.*, 2018]. Such a biological removal mechanism has been considered to be effective in maintaining a low level of methane in seawater [*Knittel and Boetius*, 2009]. Overall, the exact characteristics and quantities of deep fluids discharged from SMVs, and their impacts on biogeochemical activities remain poorly constrained in the subduction system of the western Pacific Ocean.

In this study, we present a comprehensive geochemical dataset of fluids extracted

doi:10.6342/NTU202000506

from sediment cores recovered from sites distributed across an SMV, TY1, in the accretionary prism offshore southwestern Taiwan (Fig. 2.1). These data were used to assess the fluid source, formation temperature, and fluid-rock ratio for the reaction in the source region. Reactive transport modeling was further applied to quantify the fluxes of fluid and methane exported from various sediment compartments to seawater. Finally, the possible fluid transport pathways in the Taiwan accretionary prism were discussed.

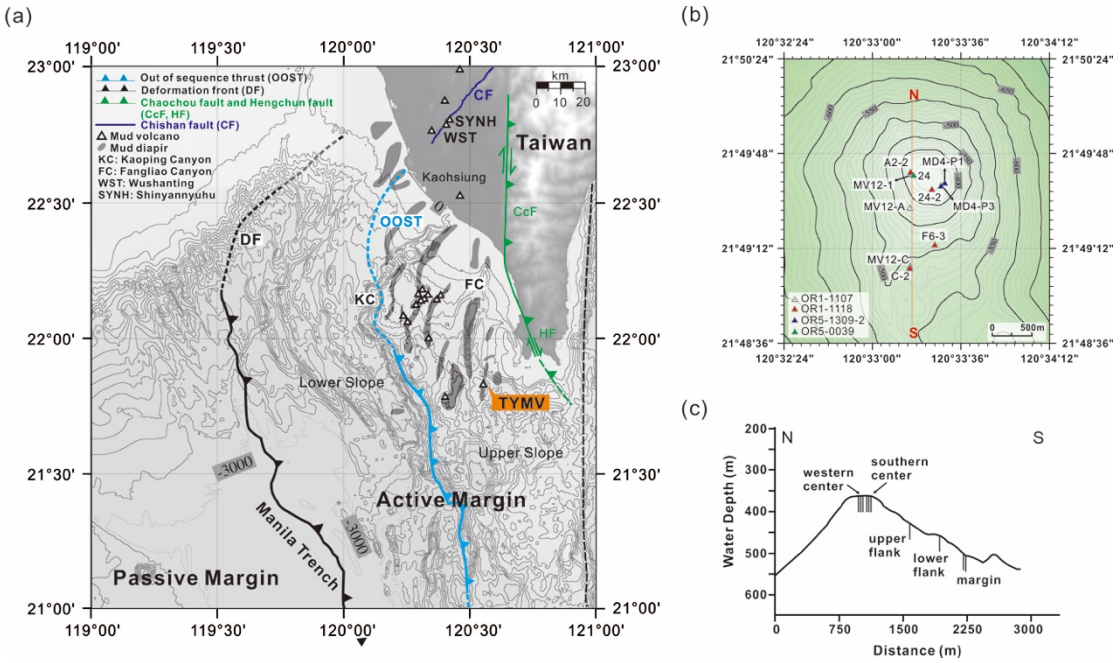

Figure 2.1. (a) Bathymetric map overlaid with the distribution of mud volcanoes, mud diapirs, geological structures, and study site TY1 offshore southwestern Taiwan [*Chen et al.*, 2014a; *Lin et al.*, 2014; *Yang et al.*, 2004] (the map was created by the open source GMT software [*Wessel and Smith*, 1998] using the NOAA public database [*Amante and Eakins*, 2009]). The right boundary of the upper slope is defined by *Lin et al.* [2009]. (b) Enlargement of the map for coring sites on TY1. (c) A topographic profile for TY1 (N to S in b) with the core sites projected.

doi:10.6342/NTU202000506

2.2 Materials and methods

2.2.1 Study area and geological setting

Offshore southwestern Taiwan is a westward extending accretionary prism related to the subduction of the Eurasian Plate underneath the Philippine Sea Plate since 18 Ma [*Lin et al.*, 2008; *Liu et al.*, 2006; *Teng*, 1990]. The deformation front and its southward extension, the Manila trench, defines the boundary between passive and active margins (Fig. 2.1a). The active margin is further divided into two structural domains separated by the out-of-sequence thrust: the lower slope and the upper slope domains [*Reed et al.*, 1992; *Lin et al.*, 2009] (Fig. 2.1a). The lower slope domain is featured with the fold-and-thrust ridges; in contrast, the upper slope domain is characterized by mud diapiric structures with mud volcanoes [*Lin et al.*, 2014]. To date, 13 submarine mud volcanoes have been identified [*Chen et al.*, 2014a]. The largest one, TYMV (re-named after MV12 [*Chen et al.*, 2017]), is composed of two mud volcanoes (TY1 and TY2; Appendix, Fig. A2.1) fed by one mud diapir, as evidenced by seismic reflection profiles [*Chen et al.*, 2014a; *Wu*, 2016]. The TY1 has a conical structure and a wide flat top with a diameter of ~500 m at a water depth of ~370 m [*Chen et al.*, 2014a] (Figs. 2.1b and 2.1c). Fluid/mud discharges occur at a frequency of every 3 to 10 seconds [*Chen et al.*, 2014b]. Two major gas plumes were

doi:10.6342/NTU202000506

detected on the crest by a multibeam echo sounder. These gas plumes could reach to a height of up to 367 m above the seafloor [*Chen et al.*, 2014b]. Other gas venting signals were also observed at the flank of the TY1 (Appendix, Fig. A2.2).

2.2.2 Sampling sites

Four expeditions were conducted in the offshore southwestern Taiwan by R/V Ocean Researcher 5 (legs 1309-2 and 0039) and R/V Ocean Researcher I (legs 1107 and 1118). Piston and gravity cores with lengths ranging from 102 to 720 cm were recovered along a transect from the center to the margin of the TY1 cone structure (Fig. 2.1c). Sampling sites are listed in Table 2.1 and shown in Figs. 2.1b and 2.1c.

Table 2.1. Information of coring sites.

cruise	site	longitude	latitude	location
OR5-1309-2	MD4-P3	120° 33.46'	21° 49.59'	southern center
OR5-1309-2	MD4-P1	120° 33.49'	21° 49.62'	southern center
OR5-0039	24	120° 33.28'	21° 49.66'	western center
OR1-1107	MV12-1	120° 33.28'	21° 49.67'	western center
OR1-1107	MV12-A	120° 33.27'	21° 49.47'	upper flank
OR1-1107	MV12-C	120° 33.26'	21° 49.08'	margin
OR1-1118	A2-2	120° 33.48'	21° 49.63'	western center
OR1-1118	24-2	120° 33.28'	21° 49.66'	southern center
OR1-1118	F6-3	120° 33.34'	21° 49.24'	lower flank
OR1-1118	C-2	120° 33.27'	21° 49.07'	margin

doi:10.6342/NTU202000506

2.2.3 Sampling and analytical methods

Sediments and core top seawater for gas analyses were collected and transferred into serum bottles. These bottles were later filled with saturated NaCl [*Chuang et al.*, 2013] (in cruises OR5-1309-2 and OR5-0039) or 1 N NaOH [*Cheng et al.*, 2012] (in cruises OR1-1107 and OR1-1118) as preservatives, sealed with butyl rubber stoppers, crimped with aluminum caps, and stored upside down at room temperature or 4 ^{o}C. Pore fluid samples for aqueous geochemistry were obtained through centrifugation and subsequently filtered through 0.2-μm Supor membrane syringe filters. The filtrates were further split into five fractions for the analyses of anion, cation, total alkalinity (TA), carbon isotopic compositions of DIC, and oxygen and hydrogen isotopic composition, and stored at 4 ^{o}C. For the cation samples, concentrated nitric acid (70%) was added at a volume ratio of 1:45 to preserve the valence state for elements sensitive to the redox change.

The concentrations of headspace hydrocarbon gases were determined by a gas chromatography (GC; SRI 8610C and Agilent 6890N) with the precision typically better than 5% [*Chen et al.*, 2017; *Cheng et al.*, 2012]. Ion concentrations were determined by an ion chromatography (IC, 882 Compact IC Plus) equipped with a Metrosep A Supp 5 column for anions and a Metrosep C 4 column for cations and

doi:10.6342/NTU202000506

with the detection limit around 0.1 ppm in weight [*Hu et al.*, 2017]. Lithium and boron were analyzed by a sector field inductively coupled plasma mass spectrometry (SF–ICP–MS) for ^{7}Li and ^{11}B at low resolution (M:ΔM ~300). Six standards were prepared from reference material NASS–5 (all from National Research Council Canada) with the uncertainty better than 3%. TA was determined by titrating the sample with 0.02 N HCl while bubbling with nitrogen [*Wallmann et al.*, 2006a]. Carbon isotopic compositions of methane and DIC were measured by an isotope ratio mass spectrometry (IRMS) in line with a gas chromatography and a combustion oven. Hydrogen and oxygen isotope compositions of porewater were measured by a LGR Liquid-Water Isotope Analyzer (LWIA; for cruises OR5-1309-2 and OR5-0039) and a Picarro L2140-i Analyzer (for cruises OR1-1107 and OR1-1118). The obtained isotopic compositions were expressed as the δ notation referenced to standards [$\delta = (R_{sample}/R_{std} - 1) \times 1000$ ‰, where R is the ratio of heavy over light isotopes]. Standards are the Vienna Pee Dee Belemnite (VPDB) for carbon isotope, and the Vienna Standard Modern Ocean Water (VSMOW) for hydrogen and oxygen isotopes. The precisions are ±0.3 ‰ for $\delta^{13}C$ values by the IRMS measurements, ±0.2 ‰ for $\delta^{18}O$ values and ±2.0 ‰ for $\delta^{2}H$ values by the LWIA measurements, and ±0.03 ‰ for $\delta^{18}O$ values and ±0.22 ‰ for $\delta^{2}H$ values by the Picarro spectroscopic measurements.

doi:10.6342/NTU202000506

The water content of the cored sediments was calculated based on the weight loss of the sediments after freeze-drying. The porosity was converted from the water content assuming a dry sediment density of 2.7 g cm^{-3} [*Chen*, 1981].

2.2.4 Reactive transport modeling

To deduce the velocity of upward fluid in such a dynamic environment [*Hiruta et al.*, 2017], a simplified one-dimensional reactive transport modeling was applied for porewater geochemistry profiles with a revised code [*Hong et al.*, 2017]. The concentration-depth profiles of five dissolved species, including chloride, sodium, potassium, sulfate, and methane, were calculated. This model is formulated by a partial differential equation for solute transport and reactions [*Boudread*, 1997; *Hong et al.*, 2017]. The modeling was first performed on conservative solutes (chloride and sodium) exempted from microbial processes and most abiotic reactions in shallow sediment environments to determine the range of upward advection rates. The sodium and chloride concentrations in the shallow sediments (the top 120 to 280 cm of sediments; Fig. 2.2) did not vary much and cannot be attributed to bioirrigation [*Schlüter et al.*, 2000]. Therefore, irrigation induced by bubble transport was incorporated to explain such constant concentrations [*Chuang et al.*, 2013; *Haeckel et al.*, 2007]. Microbial reactions involving sulfate and methane were considered [*Hong*

doi:10.6342/NTU202000506

et al., 2017; *Vanneste et al.*, 2011].

The model is formulated by a partial differential equation for solute transport and reactions [*Boudread*, 1997]:

$$\varphi \frac{\partial C_i}{\partial t} = D_i \frac{\partial}{\partial x}\left(\frac{\varphi}{\theta^2} \cdot \frac{\partial C_i}{\partial x}\right) - \frac{\partial \varphi u C_i}{\partial x} + \varphi \cdot R_{irr} + \varphi \cdot \Sigma R_i \quad (2.1)$$

where C_i is the concentration of dissolved species (i) in porewater, φ is porosity, u (m yr^{-1}) is upward fluid velocity, t (yr) is time, x (m) is depth, D_i (m^2 yr^{-1}) is the diffusion coefficient at *in situ* temperatures (10.5 ^{o}C) [*Boudread*, 1997; *Wallmann et al.*, 2006a], $\theta^2 (= 1 - \ln(\varphi^2))$ is the tortuosity used to correct the diffusion coefficients in porous media [*Boudread*, 1997], R_{irr} is the term for bubble irrigation [*Chuang et al.*, 2013], and ΣR_i defines the sum of reactions occurring in the simulated sediment column. The equations were solved numerically until the model results fit the observed profiles.

To conserve the mass transport through pore, the porosity variation along depth is adopted to determine the advection rate at each depth interval [*Boudread*, 1996]:

$$\varphi(x) = \varphi_f + (\varphi_0 - \varphi_f) \cdot e^{-rx} \quad (2.2)$$

doi:10.6342/NTU202000506

upward fluid velocity u is calculated as [*Berner*, 1980; *Vanneste et al.*, 2011]:

$$u(x) = \frac{u_0 \cdot \varphi_0}{\varphi(x)} \tag{2.3}$$

where φ_0 and φ_f are the measured porosity at the sediment-seawater interface and at the depth where porosity approaches a constant value, respectively. r is the porosity attenuation coefficient, which is an empirical constant obtained from data-fitting for the depth interval that covers the modeled depths. u_0 is the upward fluid velocity at the sediment-seawater interface. It is noted that the sedimentation rate (1.5×10^{-3} cm yr^{-1}) [*Su et al.*, 2018] is much smaller than the upward advection term. Therefore, sediment compaction alone is not enough to explain the freshening trend observed from our porewater profiles.

Bubble irrigation was incorporated into the modeling, assuming a penetration depth of at least one meter [*Chuang et al.*, 2013; *Haeckel et al.*, 2007]:

$$R_{irr} = \alpha_0 \cdot \frac{exp\left(\frac{L_{irr}-x}{\alpha_1}\right)}{1+exp\left(\frac{L_{irr}-x}{\alpha_1}\right)} \cdot (C_0 - C_i) \tag{2.4}$$

doi:10.6342/NTU202000506

where C_0 (mM) is the concentration of target solutes in the bottom water, L_{irr} (m) is the depth of the bubble irrigation layer, α_0 (yr^{-1}) is the intensity of bubble irrigation, and α_1 (m) is the parameter controlling how expeditiously this irrigation is weakened near the bottom of the irrigation zone. All these parameters were obtained by fitting our measured porewater profiles.

The compositions of porewater from the sediment surface and bottom of core were used as the upper and lower boundaries, respectively. Dirichlet boundary conditions (with fixed concentration) were applied, assuming that the input of deep fluid was always constant from the greatest depth of the model frame. The Neumann boundary condition (with no flux) was used in the lower boundary of sulfate. The depth and time grids (dx= 0.01 m and dt= 0.01 year for all sites) were determined by running the model with progressively smaller discretization until the results were numerically stable and accurate. The results of different discretization settings are shown in Appendix (Fig. A2.6). The model was executed to reach a steady state (within 1000 years simulation time) with initial conditions set as seawater composition.

In cold seep environments, sulfate is primarily consumed by organic matter

doi:10.6342/NTU202000506

(organoclastic sulfate reduction, OSR) and anaerobic oxidation of methane (AOM). Methanogenesis (ME) occurs below the sulfate-methane transition zone (SMTZ). Therefore, microbial reactions involving sulfate and methane were considered [*Vanneste et al.*, 2011]:

$$\Sigma R_{CH4} = K_G \cdot \frac{\Im \cdot C_{org}}{2} \cdot \frac{K_i SO4}{K_i SO4 + [SO_4^{2-}]} - R_{AOM} \quad (2.5)$$

$$\Sigma R_{SO4} = -K_G \cdot \frac{\Im \cdot C_{org}}{2} \cdot \frac{[SO_4^{2-}]}{K_{half-SO4} + [SO_4^{2-}]} - R_{AOM} \quad (2.6)$$

Where K_G represents the kinetic constant of organic matter degradation, $\Im$ is a parameter that converts carbon concentrations in units of wt.% C to mM and described as [*Burdige et al.*, 2016]:

$$\Im = \frac{ds}{12} \times 10^4 \times \frac{1-\varphi}{\varphi} \quad (2.7)$$

$K_{half\text{-}SO4}$ is the half-saturation constant for sulfate (0.5 mM) [*Wegener and Boetius*, 2009]; K_iSO4, the inhibition constant for the initiation of methanogenesis, is poorly constrained in natural environments and assumed to be the same as $K_{half\text{-}SO4}$ (0.5 mM); R_{AOM} is the reaction rate of AOM; C_{org} is the total organic carbon (TOC) content and

doi:10.6342/NTU202000506

assumed to be 0.45 wt.%, considering that TOC varied between 0.3 and 0.5 wt.% (Appendix, Fig. A2.4); K_G is assumed to be 10^{-6} yr^{-1}, which denotes the slow degradation of organic carbon in deep sea environment [*Middelburg*, 1989; *Vanneste et al.*, 2011]. The R_{AOM} term in Eq. (1.8) and (1.9) is described as [*Hong et al.*, 2017]:

$$R_{AOM} = R_{AOM}^{MAX} \cdot \frac{[SO_4^{2-}]}{K_{half-SO4}+[SO_4^{2-}]} \cdot \frac{[CH_4]}{K_{half-CH4}+[CH_4]} \quad (2.8)$$

where $K_{half-SO4}$ and $K_{half-CH4}$ are the half-saturation constants for sulfate and methane and assumed to be 0.5 and 5 mM, respectively [Nauhaus et al., 2002; *Vavilin*, 2013;*Wegener and Boetius*, 2009], $[CH_4]$ and $[SO_4^{2-}]$ are the concentrations of dissolved methane and sulfate in the porewater, and R_{AOM}^{MAX} is the theoretical maximum AOM rate obtained by fitting the sulfate profile (set as 2 mM yr^{-1}).

Details of the parameters used in the modeling are shown in Appendix (Table A2.4). The parameters for best fittings are shown in Appendix (Table A2.5). Chloride profiles from the previous study were also modeled for comparisons (sites MV12-1 and MV12-A) [*Chen et al.*, 2017]. Due to the short core recovery from site MV12-1, it is difficult to constrain the upward fluid velocity with the available observations. Therefore, physical conditions between sites MV12-1 and A2-2 were assumed to be

doi:10.6342/NTU202000506

the same to estimate the reaction rates at MV12-1. The variation of chloride concentration at site F6-3 is too small to derive the advection rate. Because of degassing during core retrieval, concentrations of methane measured in the pore fluids do not represent *in situ* concentrations. The saturation concentration of methane (CH4L) was calculated on the basis of the in situ temperature and pressure at the center sites (96.4 mM; calculated from *Tishchenko et al.* [2005]). At the upper flank (site MV12-A) and lower flank (site F6-3) sites, our model was able to fit the observed sulfate profile by assigning CH4L as 7 and 30 mM, respectively, mostly due to the short recovery of the core (Appendix, Table S2.5). A detailed description of additional sensitivity tests is given in the Appendix C.

2.2.5 Water discharge from SMVs

To estimate the total discharge of brackish water from SMVs, the upward fluid velocities across the TY1 were compiled first with those obtained in the previous study [*Chen et al.*, 2017]. The upward fluid velocities generally decreased with increasing distance from the edge of crater. Such a trend is also found in other SMVs in offshore Norway and the Gulf of Cadiz [*Vanneste et al.*, 2011; *de Beer*, 2006] (such as the Håkon Mosby and Carlos Ribeiro SMVs). To generalize the fluid velocities across the entire cone structure, the variations in velocity with distance from the edge

doi:10.6342/NTU202000506

of the crater were fitted with the exponential equation. The calculation was based on the assumption that the fluid flow was confined through porespace and driven by a single, pressurized fluid source.

The velocity distribution was further integrated with the ring area coverage (Appendix, Fig. A2.9b) to derive the total brackish water discharge using the following equation [*Vanneste et al.*, 2011]:

Brackish water discharge (kg yr^{-1})

$$= \text{porosity} \times \text{area } (m^2) \times \text{upward fluid velocity } (m\ yr^{-1}) \times \text{density } (kg\ m^{-3}) \quad (2.9)$$

In this calculation, the crater radius of 250 m, the cone diameter of 3600 m [*Chen et al.*, 2014a], and the porosity of 36% (an average value of the porosity of TY1; Appendix, Fig. A2.5) were used. The density of water was assumed to be 1000 kg m^{-3}. The same approach was applied to other 12 SMVs assuming that the upward velocity at the crater of individual SMVs was the same as that at TY1. Since each SMV has different diameters of its crater and cone structure, the relationship between

doi:10.6342/NTU202000506

the velocity and the distance ratio was constructed (normalized to the distance from the edge of crater). Such a relationship was then applied to calculate the discharge fluxes of other individual SMVs (Appendix, Table A2.6). Terrestrial mud volcanoes were not considered because their sizes are too small when compared to SMVs [*Hong et al.*, 2013a].

doi:10.6342/NTU202000506

2.3 Results

2.3.1 Fluid geochemistry

2.3.1.1 Variation of solute profiles across TY1 submarine mud volcano

Profiles of solute and gas concentrations are shown in Figs. 2.2 and 2.3. Most porewater in the upper 120 to 280 cm of sediment had a seawater-like composition. Below this interval at the center sites, concentrations of most ions decreased with depth (potassium, sodium, magnesium, calcium, chloride, and sulfate). In contrast, concentrations of total alkalinity (TA), boron, and lithium increased with depth. Between 120 and 280 cm below seafloor (cmbsf), sulfate was undetectable and accompanied by an increase in methane concentration (1–2 mM), forming a sulfate to methane transition zone (SMTZ). Changes in concentration gradient of other solutes were also observed across the SMTZ. For example, calcium and magnesium concentrations decreased to ca. 1 mM and lower than 5 mM below the SMTZ, respectively. The decrease was coincident with the increase in TA concentration (to around 35 mM).

At the upper flank (site MV12-A) and lower flank (site F6-3) sites, significant decreases in sulfate, calcium, and magnesium concentrations coincided with the increase in methane and TA concentrations (Figs. 2.2 and 2.3). Both lithium and boron concentrations remained at constant values throughout the core at the upper flank site. In contrast, boron and lithium concentrations increased with depth at the lower flank site, where SMTZ was observed at the bottom of the core.

At margin sites (sites MV12-C and C-2), concentrations of most ions were close to seawater values. In addition, methane concentrations only increased to at most 50

doi:10.6342/NTU202000506

μM. Both boron and lithium concentrations at site MV12-C decreased with depth (Fig. 2.3b).

2.3.1.2 Porewater isotope data

Profiles of $\delta^{18}O$ and $\delta^{2}H$ values of porewater are shown in Fig. 2.4. At center sites, $\delta^{18}O$ and $\delta^{2}H$ values of porewater were close to 0 ‰ at either above 120 or 280 cmbsf, and increased and decreased, respectively, further down core. The data for the deepest sample deviated from the global meteoric water line (GMWL) in a way that $\delta^{18}O$ values increased to +6 to +7 ‰ while $\delta^{2}H$ values decreased to –20 to –12 ‰ (Fig. 2.4d and 2.4e). At the upper flank (site MV12-A) and lower flank (site F6-3) sites, only slight variations in $\delta^{18}O$ and $\delta^{2}H$ values were observed at the bottom of the core ($\delta^{18}O$ value increased to +0.7 ‰ and $\delta^{2}H$ value decreased to –1.1 ‰). At the margin sites (sites MV12-C and C-2), $\delta^{18}O$ values were close to 0 ‰ throughout the core, while $\delta^{2}H$ values decreased slightly to –1.4 ‰ at the bottom of the core.

doi:10.6342/NTU202000506

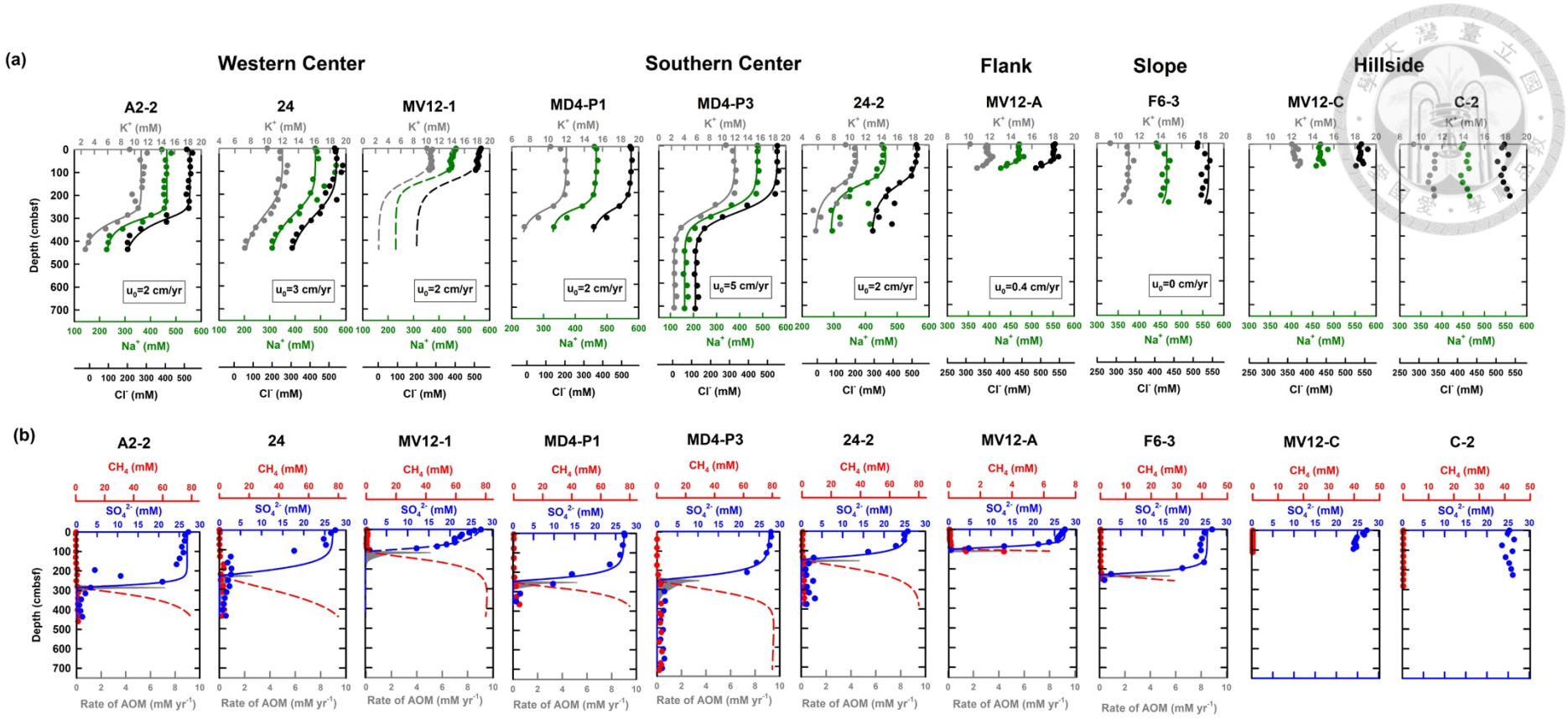

Figure 2.2. Concentration depth profiles and results of reactive transport modeling. (a) Chloride (in black), sodium (in green), and potassium (in gray) concentration depth profiles at ten sites investigated in this and previous studies (for sites MV12-A) [*Chen et al.*, 2017]. The solid lines represent the best fit of the modeled results. The lower boundary conditions at site MV12-1 (in dashed line) were assumed to be the same as those at site A2-2. The modeled upward velocity was also provided. (b) Modeled results for sulfate (blue solid line) and methane (red dashed line) depth profiles and AOM rates (R_{AOM}; gray area) at eight sites.

doi:10.6342/NTU202000506

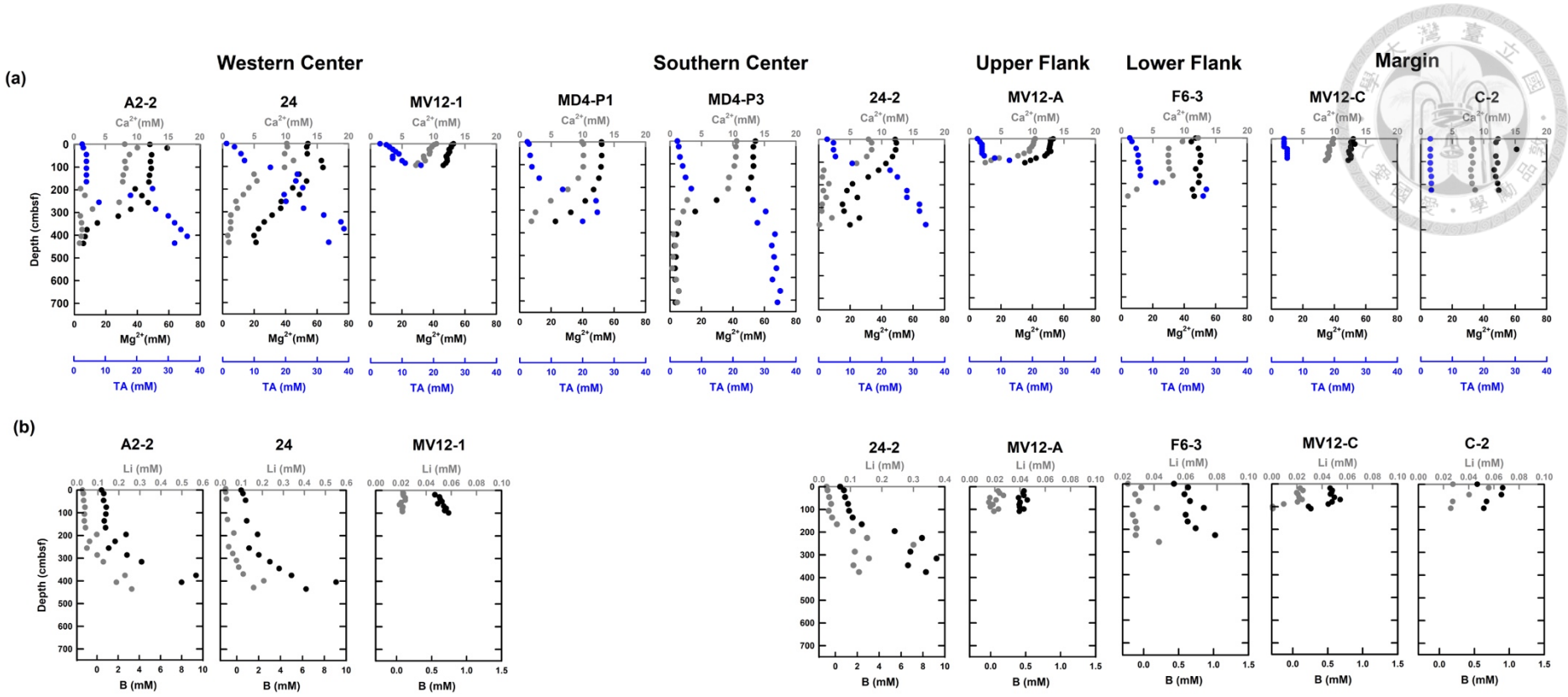

Figure 2.3. Cation abundance and total alkalinity profiles. (a) Calcium (in gray), magnesium (in black), and TA (in blue) concentration profiles at ten sites investigated in this and previous studies (for sites MV12-A) [*Chen et al.*, 2017]. (b) Lithium (gray dot) and boron (black dot) concentration profiles at eight sites.

doi:10.6342/NTU202000506

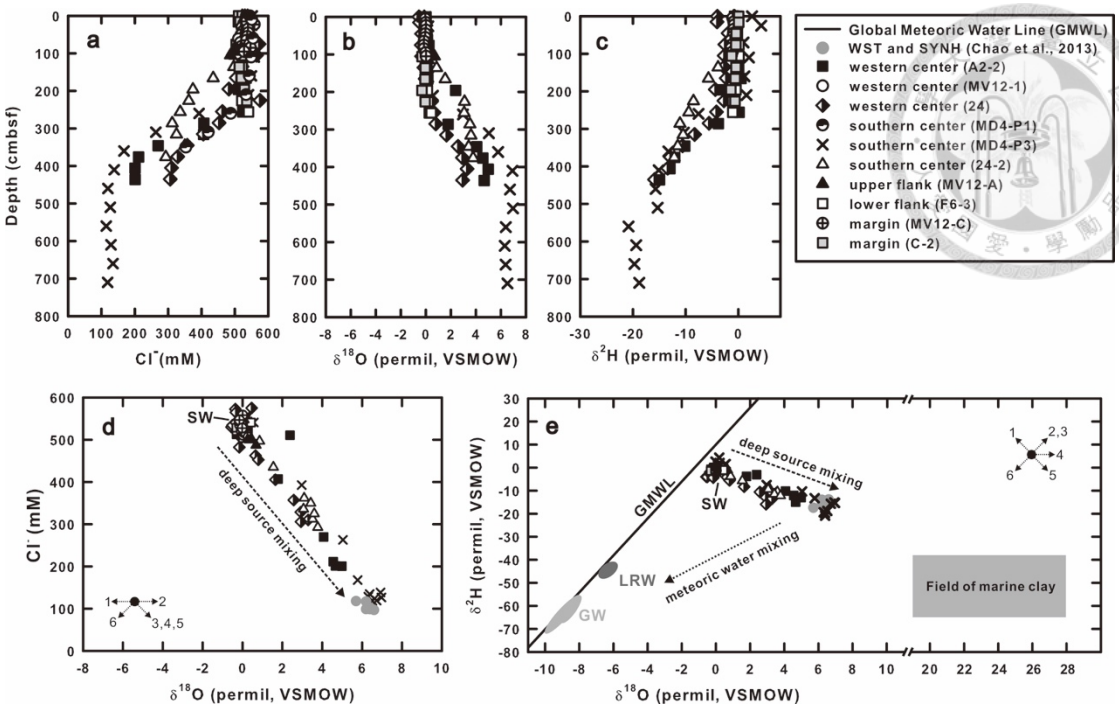

Figure 2.4. (a) to (c): Profiles of chloride concentrations and $\delta^{18}O$ and $\delta^{2}H$ values. (d) and (e): Plots of $\delta^{18}O$ value versus chloride concentration and $\delta^{18}O$ versus $\delta^{2}H$ values. Gray dots are data from terrestrial mud volcanoes for comparison [*Chao et al.*, 2013]. The black line in (e) indicates the Global Meteoric Water Line (GMWL; $\delta^{2}H = 8 \times \delta^{18}O + 10$). Areas denote with "LRW" and "GW" in (e) marked the ranges of isotopic compositions for local meteoric water and groundwater from adjacent onshore areas, respectively [*Wang et al.*, 1999]; gray square area represents the $\delta^{18}O$ and $\delta^{2}H$ values of marine clay [*Lecuyer et al.*, 1998; *Savin and Esptein*, 1970a; *Savin and Esptein*, 1970b; *Yeh and Esptein*, 1978]. Arrows marked with numbers in (d) and (e) represent processes potentially occurring at the source depth, and their directions denote the trends associated with the processes [*Dählmann and De Lange*, 2003]: 1: volcanic ash alteration at temperatures lower than 300 ^{o}C; 2: volcanic ash alteration at temperatures higher than 300 ^{o}C; 3: gas hydrate dissociation; 4: biogenic opal recrystallization; 5: clay mineral dehydration; 6: meteoric water input.

doi:10.6342/NTU202000506

2.3.2 Hydrocarbon gases and carbon isotopic compositions

At the western and southern center sites, $\delta^{13}C\text{-}CH_4$ values increased from –40 ‰ on the seafloor to –20 ‰ above the SMTZ. The $\delta^{13}C\text{-}CH_4$ value was the smallest at the SMTZ (–50 to –45 ‰) and remained at a constant value below the sulfate reduction zone (Fig. 2.5). At the upper flank (site MV12-A) and lower flank (site F6-3) sites, the $\delta^{13}C\text{-}CH_4$ value was the smallest at the SMTZ (–70 ‰ at site MV12-A and –48 ‰ at site F6-3). The $\delta^{13}C$-DIC (dissolved inorganic carbon) patterns for center and flank sites were similar in a way that the values were the smallest at the SMTZ (–30 ‰ at site 24; –20 ‰ at sites MD4-P3 and MD4-P1) and increased towards the seafloor (~0 ‰) and the bottom of the cores.

The C_1/C_{2+} ratios and the $\delta^{13}C\text{-}CH_4$ values for sites A2-2 and MD4-P3 were between 25 and 90, and between –35.9 and –44.5 ‰, respectively, falling in the region of thermogenic methane in the plot of C_1/C_{2+} ratio versus $\delta^{13}C\text{-}CH_4$ value (Fig. 2.6). For sites 24 and 24-2, the $\delta^{13}C\text{-}CH_4$ values were between –48 and –37 ‰, whereas the C_1/C_{2+} ratios increased to more than 120. These data points fell in a region between microbial and thermogenic methane.

doi:10.6342/NTU202000506

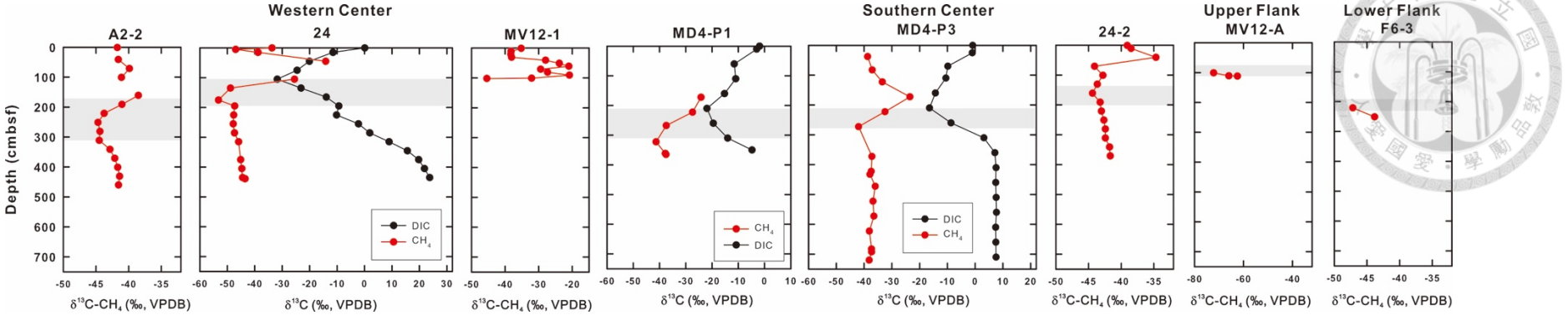

Figure 2.5. Profiles of δ^{13}C-CH_4 (in red) and δ^{13}C-DIC values (in black). Gray shadows represent the SMTZ at each site.

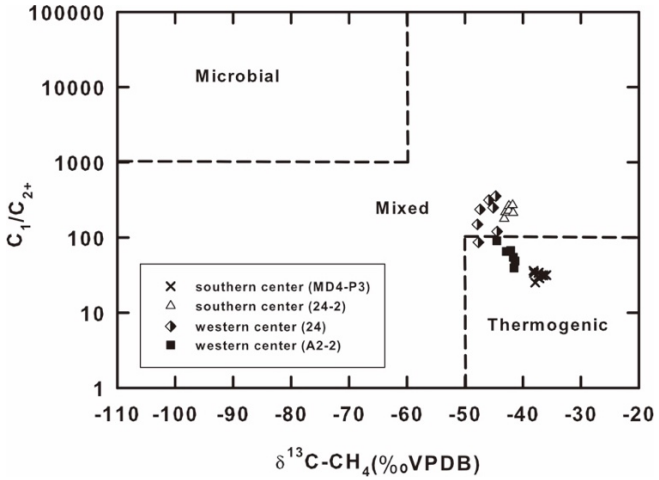

Figure 2.6. Plot of δ^{13}C-CH_4 value versus C_1/C_{2+} ratio for samples collected at center sites. The assignment of gas origin is based on Bernard et *al.* [1976].

doi:10.6342/NTU202000506

2.3.3 Reactive transport modeling and fluid flux from SMVs

The reactive transport modeling yielded that upward fluid velocities at western and southern center sites were in the range of 2 to 3 and 2 to 5 cm yr^{-1}, respectively (Fig. 2.2). Upward fluid migration is likely absent at the margin site as the solute concentration do not change significantly with depth. The total fluid discharges from the craters and the rest of the cone structures of 13 SMVs were calculated to be 2.9 to 7.3 $\times 10^6$ kg yr^{-1} and 1.0 to 1.7 $\times 10^7$ kg yr^{-1}, respectively (Appendix, Table A2.6).

The modeled methane fluxes beneath the depth of SMTZ at the western and southern centers were in the range of 1020–1530 and 972–2990 mmol m^{-2} yr^{-1}, respectively (Table 2.2). The methane fluxes above the SMTZ at these center sites were 162–1380 mmol m^{-2} yr^{-1}. The methane flux beneath and above the depth of SMTZ was much lower (347–456 and 9–47 mmol m^{-2} yr^{-1}, respectively) at the flank sites (sites MV12-A and F6-3) than at the center sites. While the methane fluxes above and beneath the SMTZ decreased with the distance from the center, the ratios (flux beneath SMTZ/flux above SMTZ) were relatively higher at the flank sites than at the center sites. Such a variation was translated into an increase in AOM efficiency from 54% at the center sites to 98% at the lower flank sites (Table 2.2).

doi:10.6342/NTU202000506

Table 2.2. Microbial activity derived from reactive transport modeling.

		Western center			Southern center			Upper flank	Lower flank
	unit	A2-2	24	MV12-1*	MD4-P1	MD4-P3	24-2	MV12-A	F6-3
Rate of anaerobic methanotrophy	mmol m^{-2} yr^{-1}	858	861	872	943	1610	740	300	447
Rate of organic sulfate reduction	mmol m^{-2} yr^{-1}	40.5	31.8	14.2	33.6	4.80	19.9	14.5	34.4
Rate of methaogenesis	mmol m^{-2} yr^{-1}	24.2	32.9	52.2	20.0	68.0	36.6	1.78	5.57
Methane flux from depth	mmol m^{-2} yr^{-1}	1020	1530	1150	1280	2990	972	347	456
AOM-filteration efficiency	%	84	56	76	74	54	76	86	98

*: Parameters (core length and lower boundary conditions) are assumed to be the same as those for site A2-2 (Supplementary Information, Table S4).

doi:10.6342/NTU202000506

2.4 Discussion

2.4.1 The characteristics and formation temperature of fluid from TY1

The decreasing chloride concentration with depth (Fig. 2.4a) and carbon isotopic composition and abundance patterns of methane (Figs. 2.5 and 2.6) suggest an input of freshwater and thermogenic methane from great depth. Crossplots among $\delta^{18}O$ values, $\delta^{2}H$ values, and chloride concentrations (Fig. 2.4e) indicate the deviation of the fluid compositions for the center sites from the GMWL and seawater. The geochemical variation could be best accounted for by the impact of seawater and a deep fluid characterized by low chlorinity, high $\delta^{18}O$ values, and low $\delta^{2}H$ values. Such variations in $\delta^{18}O$ and $\delta^{2}H$ values cannot be explained by gas hydrate dissociation, ash alteration at high or low temperature, or biogenic opal recrystallization, as these reactions enrich fluids with ^{2}H or cause no fractionation on hydrogen isotopes [*Dählmann and De Lange*, 2003; Ijiri et al., 2018]. Dehydration of other sedimentary minerals, zeolites, and hydrous alteration phases are also excluded because all these processes would produce water enriched in ^{18}O, ^{2}H, potassium, and sodium [*Mottl et al.*, 2003] which are significantly different from fluids of TY1 (Fig. 2.2 and 2.4). Clay dehydration appears to be the most plausible mechanism to account for the observed geochemical signature.

To approximate the temperature of fluid formation, specific cation-ratios were used to derive the fluid temperature [*Fouillac and Michard*, 1981; *Kharaka and Mariner*, 1989; *Michard*, 1990]. The validity of geothermometers lies in the requirement of the presence of reactant mineral. Since sediments or mineralogy in the

doi:10.6342/NTU202000506

source region are not available, the constituent mineral for the formation currently outcropping in southwestern Taiwan was first adopted to evaluate the applicability of the specific geothermometer. The inference is based on the fact that the subduction of the Eurasian Plate underneath the Philippine Sea Plate generated a series of westward propagating thrusts that sequentially exhumed the sediments once deposited offshore Taiwan [*Teng*, 1990]. Therefore, the strata on land could mirror the characteristics and constituents of sediments in the potential source region that is accessible only with the deep drilling. The Plio-Pleistocene *Gutingkeng Formation* formed in shelf break environments was chosen as the analogy for the source material. The formation is primarily composed of mudstone with lens of siltstone and sandstone [*Castelltort et al.*, 2011]. Feldspars at abundances of up to 5% in this formation have been observed [*Chen*, 2014]. In addition to the constraint from the formation in terrestrial environments, feldspars in cores retrieved from the ODP 1144 site in the abyssal region of the South China Sea amounted up to 1.33 wt.% of the total sediments [*Tamburin et al.*, 2003]. Therefore, both observations support the possibility that feldspars are available in the source region and serve the source of sodium and potassium in fluids. The geothermometer based on the Na/Li and Na/K ratio were used for the temperature estimation [*Fouillac and Michard*, 1981; *Michard*, 1990; *Reitz et al.*, 2011]:

$$T(℃) = \frac{1195}{log\left(\frac{Na}{Li}\right)-0.13} - 273 \tag{2.10}$$

$$T(℃) = \frac{1170}{log\left(\frac{Na}{K}\right)+1.42} - 27 \tag{2.11}$$

doi:10.6342/NTU202000506

where the concentration is in molality in Eq. (2.10) and mg/kg in Eq. (2.11). The Ca-Mg-K and Mg/Li geothermometers were not considered because the porewater chemistry for all depths at the TY1 is oversaturated with respect to a number of carbonate minerals, such as dolomite and Mg-calcite (Appendix A and Table A2.1). Furthermore, the concentration of magnesium is lower than what is expected by the dilution of seawater by freshwater alone, again suggesting the potential removal of magnesium by carbonate precipitation (Appendix, Fig. A2.3). The SiO_2 geothermometers were not applied due to the potential underestimate caused by rapid cooling through the intrusion of the overlying seawater [*Kharaka and Mariner*, 1989].

The fluid temperature was calculated to range between 100 and 150 ^{o}C. Our estimated temperature is supported by the high concentrations of lithium and boron (Fig. 2.3b), a pattern consistent with the results from laboratory experiments by which lithium and boron are preferentially released from silicate minerals in marine sediments starting at ca. 50 ^{o}C [*Chan*, 1994; *James et al.*, 2003; *You et al.*, 1996]. The estimated temperature is also consistent with the predominance of thermogenic methane over microbial methane as being inferred on the basis of isotopic compositions and abundance ratios (Fig. 2.6). Furthermore, the geothermal gradients measured at TY1 vary from 25 ^{o}C/km at the margin sites to 390 ^{o}C/km at the center sites [*Wu*, 2016]. Since the crater is directly connected with the conduit channeling hot fluids from great depth, the measured geothermal gradient would be distorted toward a higher value by the advective fluid flow [*Chi and Reed*, 2008; *Liao et al.*, 2014; *Wu*, 2016]. Instead, the averaged value (25 ^{o}C/km) measured at the margin sites and in surface sediments in the region was chosen to represent the regional geothermal gradient [*Chi and Reed.*, 2008]. Using this value, the depth producing the

doi:10.6342/NTU202000506

observed geochemical signatures was calculated to range between 3.6 and 5.7 kmbsf (kilometer below seafloor).

2.4.2 The source and production of freshwater

These lines of evidence indicate that a significant fraction of pore fluid is contributed from clay dehydration at high temperatures. Illite and chlorite, which are considerably abundant in sediments offshore southwestern Taiwan [*Liu et al.*, 2008], are excluded because illite and chlorite are dehydrated at a much higher temperature range (>237 ^{o}C for illite and >650 ^{o}C for chlorite) [*Drits and McCarty*, 2007; *Padrón-Navarta et al.*, 2015]. Kaolinite is also excluded as a result of being less abundant in the northern South China Sea [*Liu et al.*, 2010] and stable over the temperature range estimated in this study (decomposed at >800 °C and 19 GPa) [*Hwang et al.*, 2017]. Since the transformation of smectite to illite proceeds at a temperature higher than 60 ^{o}C and produces fluids enriched in ^{18}O and depleted in ^{2}H, smectite is considered to be the most plausible mineral candidate to account for the observed geochemical signature [*Dählmann and De Lange*, 2003; *You et al.*, 1996]. As abundant smectite and mixed layer (1.1–24.8 wt.% in bulk sediments) have been found in the active margin [*Blattmann et al.*, 2019] and passive margin off southwestern Taiwan [*Chen*, 1978; *Liu et al.*, 2010] and sediments off the Luzon Arc (ODP, sites 1144 and 1146) [*Hu et al.*, 2012; *Liu et al.*, 2003; *Wan et al.*, 2007; *Wang et al.*, 2000], smectite sourced from Taiwan orogeny and Luzon Arc volcanism and later being subducted/accreted as part of the Taiwan accretionary prism is the most likely source.

To further assess the smectite dehydration, we adopted an isotopic mass balance

doi:10.6342/NTU202000506

to calculate the ratio of water to rock (W/R) for reactions considering the exchange of oxygen and hydrogen between minerals and pore fluid under a closed-system condition [*Ray et al.*, 2013]. The fluid-to-mineral ratio for the reaction was calculated based on the mass balance for hydrogen and oxygen isotope compositions [*Ray et al.*, 2013]:

$$W_o\delta^{18}O_{pw}^{i} + R_o\delta^{18}O_r^{i} = W_o\delta^{18}O_{pw}^{f} + R_o\delta^{18}O_r^{f} \quad (2.12)$$

$$W_H\delta^{2}H_{pw}^{i} + R_H\delta^{2}H_r^{i} = W_H\delta^{2}H_{pw}^{f} + R_H\delta^{2}H_r^{f} \quad (2.13)$$

where W_O and W_H are moles of oxygen and hydrogen, respectively, in porewater; and R_O and R_H are moles of oxygen and hydrogen, respectively, in target minerals. The superscripts *i* and *f* represent the initial and final isotopic compositions, respectively. The subscripts *r* and *pw* denote isotopic compositions of rock and porewater, respectively. By rearranging Eqs. (2.12) and (2.13), $\delta^{18}O_{pw}^{f}$ and $\delta^{2}H_{pw}^{f}$ values were calculated using Eqs. (2.14) and (2.15):

$$\delta^{18}O_{pw}^{f} = \frac{\frac{W_O}{R_O}\delta^{18}O_{pw}^{i} - \Delta_{r-w}^{O} + \delta^{18}O_r^{i}}{1+\frac{W_O}{R_O}} \quad (2.14)$$

$$\delta^{2}H_{pw}^{f} = \frac{\frac{W_H}{R_H}\delta^{2}H_{pw}^{i} - \Delta_{r-w}^{H} + \delta^{2}H_r^{i}}{1+\frac{W_H}{R_H}} \quad (2.15)$$

where Δ_{r-w}^{O} and Δ_{r-w}^{H} are isotopic fractionations of oxygen and hydrogen isotopes, respectively, during the exchange of isotopes between rock and porewater ($\Delta = 10^3 \ln \alpha$; α is the fractionation factor). The W/R ratios for oxygen and hydrogen are assumed

doi:10.6342/NTU202000506

to be identical ($W_O/R_O = W_H/R_H$). A value of 0 ‰ was assigned for both the $\delta^2 H_{pw}^i$ and $\delta^{18} O_{pw}^i$ values based on the bottom water measurements. The $\delta^{18} O_r^i$ and $\delta^2 H_r^i$ values for marine clays range between +15.0 and +28.5 ‰ and between –80 and –4.1 ‰, respectively [*Lecuyer and Robert*,1998; *Savin and Epstein*, 1970a; *Savin and Epstein*, 1970b; *Yeh and Epstein*, 1978]. The $\delta^{18} O_r^i$ and $\delta^2 H_r^i$ values were assumed to range from +19 to +28‰ and from −80 to −36‰, respectively. The temperature dependence for the fractionation factors for oxygen and hydrogen isotopes was calculated according to previous studies for a temperature range between 100 and 150 ^oC [*Capuano*, 1992; *Sheppard and Gilg*, 1996]. The calculations yielded the $\delta^{18}O$ and δ^2H values varying as a function of equilibrium temperature and W/R ratio (Fig. 2.7). Using the measured isotopic compositions of the porewater collected from the center sites (site MD4-P3, Fig. 2.1b), the W/R ratios were estimated to be <0.5, 0.3–0.9, and 1.1–1.9 if the $\delta^{18} O_r^i$ values were set as +19 ‰, +20 to +22 ‰, and +23 to +28 ‰, respectively.

doi:10.6342/NTU202000506

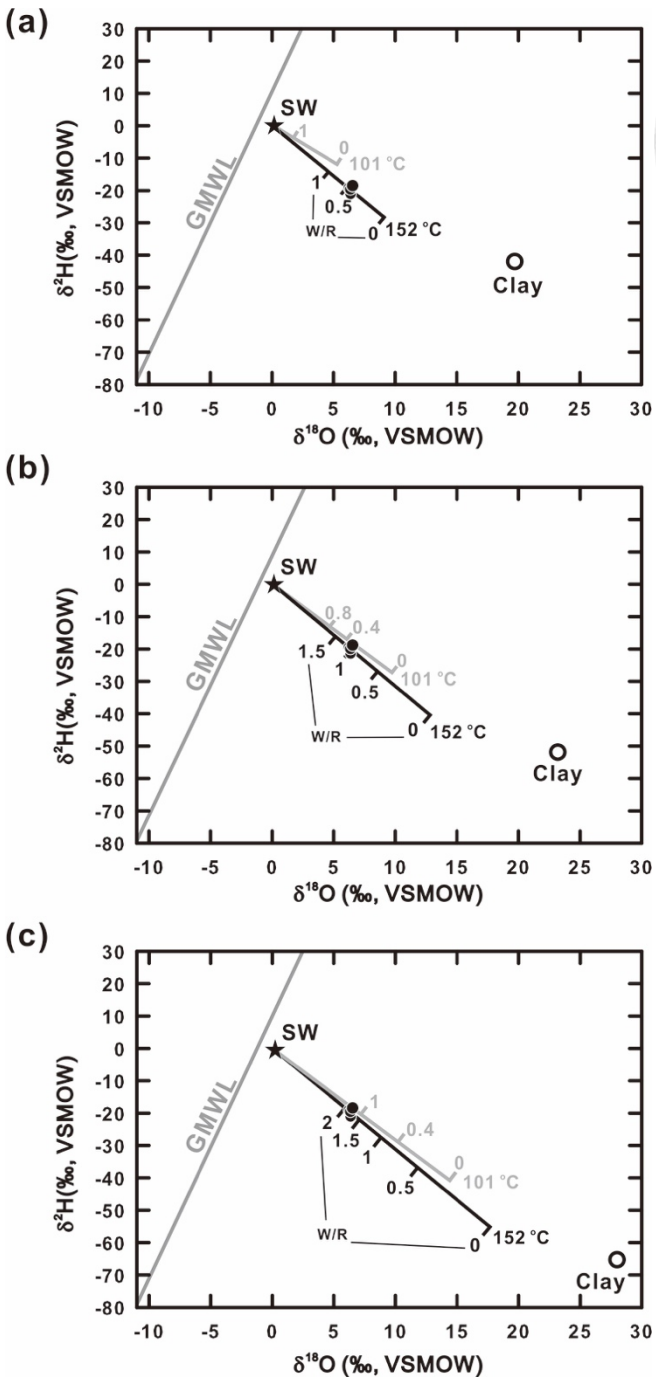

Figure 2.7. Isotopic compositions of fluids under different fluid-rock ratios (W/R) at different temperatures. The star symbol represents the seawater value ($\delta^{18}O$= 0‰; $\delta^{2}H$ = 0‰). The gray line is the global meteoric water line (GMWL). Data obtained from the bottom part of site MD4-P3 are plotted as black dots. The open circles denote $\delta^{18}O^{i}$ and $\delta^{2}H^{i}$ values of smectite used in each case: (a) $\delta^{18}O^{i}$-rock = +19 ‰; $\delta^{2}H^{i}$ of rock = –39‰. (b) $\delta^{18}O^{i}$-rock = +23 ‰; $\delta^{2}H^{i}$ of rock = –51‰. (c) $\delta^{18}O^{i}$-rock = +28 ‰; $\delta^{2}H^{i}$ of rock = –66‰.

doi:10.6342/NTU202000506

The amount of needed smectite could be further deduced from these W/R ratios considering the possible volume of porewater and assuming the complete reactivity of all available porewater and smectite. To constrain the possible porosity at the depth estimated for smectite dehydration, the porosity variation for cores collected from the Nankai Trough (IODP 358, site C0002, 3.2-km long) [*Tobin et al.*, 2019] was used for the extrapolation. The measurement from IODP 358 yielded a porosity of 17 % at the depth of 3.2 kmbsf [*Tobin et al.*, 2019]. By applying the exponential reduction function, the porosity at 5.7 kmbsf was calculated to be 5.6% (Appendix, Table A2.2). Assuming that the porespace is saturated with porewater and that the porosity is 6 %, the quantity of porewater would be lower than 3 wt.% of the bulk sediment. To fulfill the estimated W/R ratios (0.3–1.9) for smectite dehydration, 1.6–10 wt.% of smectite is needed. Such a mineral abundance is consistent with the measured amount of smectite in the current active and passive margin (1.1 to 6.2 wt.% in sediments collected by a sediment trap deployed southwestern Taiwan; 4.5 to 24.8 wt.% in sediments from the ODP 1144 and 1146) [*Blattmann et al.* 2019; *Liu et al.*, 2003; *Wan et al.*, 2007; *Wang et al.*, 2000].

As subducted-smectite could be the source of freshwater, fluid fluxes in the SMV region of the accretionary wedge were further assessed. The total amount of smectite-bound fluid within the incoming plate was estimated considering the weight of the incoming plate and the content of smectite and porosity in the sediments [*Freundt et al.*, 2014; *Jarrard*, 2003; *von Huene and Scholl*, 1991]:

$$F_a = C_a \cdot H \cdot (1 - \varphi_a) \cdot \rho \cdot V_a \cdot L_a \tag{2.16}$$

doi:10.6342/NTU202000506

where F_a is the flux, C_a is the weight percentage of mineral-bound water in smectite, H is the pre-subducted sediment thickness, ρ is the density of dry sediments, φ_a is the porosity of sediments from the incoming plate, L_a is the length of trench, and V_a is the subduction rate. The details for calculations were stated in Appendix B. The total smectite-bound fluid from the incoming plate was calculated to be 0.7 – 8.8 $\times 10^8$ kg yr^{-1}.

As sediments are subducted, the buried seawater-like pore fluid and produced smectite-bound fluid would be squeezed and lost gradually with the increasing temperature and pressure. As a result, the actual amount of water released into SMVs region would be substantially lower than that from the incoming plate. Of the overall flux of brackish fluid expelled from SMVs offshore Taiwan (1.3 – 2.5$\times 10^7$ kg yr^{-1}), approximately 80% of this flux could be attributed to the smectite-bound fluid (1–2 $\times 10^7$ kg yr^{-1}) considering the mixing of seawater and freshwater end components (based on the chloride concentration, 110 mM, at the bottom of site MD4-P3). This quantity of smectite-bound fluid released from the SMVs in the region constituted about 1.1–28.6% of the smectite-bound fluid originally subducted into the trench (0.7–8.8$\times 10^8$ kg yr^{-1}).

Previous modeling study using the data integrated from geophysical and mineralogical observations for the Nankai Trough demonstrated that the majority of the smectite-bound fluids (4.17$\times 10^8$ kg yr^{-1}; 88% of total smectite-bound fluids in the incoming plate) would be lost to the frontal prism, leaving a total of 0.56$\times 10^8$ kg yr^{-1} smectite-bound fluids further released into the overlying wedge as the descending sediments reach the region beneath the Kumano basin where mud volcanoes are abundant [*Menapace et al.*, 2017]. If such a fluid budget for the Nankai system is

doi:10.6342/NTU202000506

directly applied to the Taiwan subduction system, a total of 0.8–10.4×10^7 kg yr^{-1} (=0.7 – 8.8 ×10^8 / (4.17×10^8/ 88%/ 0.56×10^8)) smectite-bound fluids would be released from the descending sediments into the wedge in the Upper Slope. This estimated flux is comparable with the flux of freshwater expelled into seawater through SMVs offshore Taiwan obtained in this study (1–2 ×10^7 kg yr^{-1}). Whether such an analogy of the fluid budget could be drawn directly remains to be explored even though the plate geometry, heat flux, mineral type and content, convergence rate, and the distance between trench to mud volcanoes are comparable between the Nankai and Taiwan subduction systems (Appendix, Table A2.3).

Additional production or consumption of freshwater includes saponite dehydration [*Menapace et al.*, 2017], dehydration of illite or other mafic minerals (e.g. serpentine) [*Doo et al.*, 2015] and serpentinization. Ra ratio ranges from 0.78 to 6.2 at Chung-lun mud pool and area closed to Tulungwan-Chaochou-Hengchun fault system in south central Taiwan, suggesting mantle fluids escaped [*Chen et al.*, 2019; *Yang et al.*, 2003]. Since the thickness and mineralogy of the subducted relic of oceanic crust are not available, the precise quantification of water production and hydration at greater depths warrants further investigation.

2.4.3 The influence of upward fluid

The impact of the deep fluid on shallow subsurface microbial processes is reflected in geochemical profiles. The decreasing rate of upward fluid flow from the center towards the margin sites (Fig. 2.2) varied concomitantly in a similar and an opposite trend with the modeled AOM rates and efficiency, respectively (Table 2.2 and Table A2.5). For example, at site MD4-P3 where the upward velocity was the

doi:10.6342/NTU202000506

greatest, the AOM rate was the highest among eight sites (1610 mmol m^{-2} yr^{-1}), and the AOM efficiency was the lowest (54%) (Table 2.2). In contrast, the upward fluid flow was absent at the lower flank site, whereas the AOM efficiency reached 98% (Table 2.2). Such an observation suggests that the upward velocity of the fluid is the primary control of AOM rates. As the capacity of AOM is limited, the efficiency of methane removal could not accommodate the extremely high supply of methane at center sites. This pattern is consistent with those obtained in onshore mud volcanoes in Taiwan [*Chen et al.*, 2017; *Cheng et al.*, 2012] and SMVs elsewhere (e.g., the Hakon Mosby SMV) [*Felden et al.*, 2010].

doi:10.6342/NTU202000506

2.5 Conclusions

Porewater and gases for cores distributed along a transect of TY1 were systematically analyzed to assess the spatial variation of fluid velocities and biogeochemical activities and further constrain the fluid budget. The co-variation of the isotopic composition and chloride concentration demonstrate that the majority of fluid retrieved from the crater is derived from smectite dehydration at a temperature of 100 to 150 °C or a depth of 3.6 to 5.7 kmbsf. Assuming that the isotopic equilibrium is reached, the water-rock interaction proceeds at a water-rock ratio of more than 0.3. Reactive transport modeling for compounds inert to microbial processes yielded that the velocity of upward migrating fluid varied from 2 to 5 cm yr^{-1} at the center sites to a negligible level at the margin sites. By extrapolating such a variation pattern for other SMVs offshore Taiwan, the overall flux discharged from SMVs ranged from 1.3 to 2.5×10^{7} kg yr^{-1}. This fluid quantity accounts for 1.1–28.6% of the smectite-bound water originally stored in the incoming sediments, implying that SMVs could act as a conduit to channel the fluid produced from great depth/temperature into seafloor environments. The flux variations across the transect of a mud volcano strongly impact the magnitude and efficiency of the biological filtration of methane through methanotrophy.

doi:10.6342/NTU202000506

Chapter 3 Production, consumption, and migration of methane in accretionary prism of southwestern Taiwan

3.1 Introduction

Atmospheric methane is ~23 times more effective in heat absorption than carbon dioxide on the basis of 100-year residence time [*Forster et al.*, 2007]. Even with ~200 times less concentration than carbon dioxide in the atmosphere, methane contributes 20–25% of the overall greenhouse effect [*Lelieveld et al.*, 1998]. Scenario modeling and geological records both have shown that its impact on climatic fluctuations over various timescales could have been substantial [*Dickens et al.*, 1995; *Kennett et al.*, 2000].

Marine sediments along continental margins have been estimated to store a total of 4.55×10^5 Tg of methane carbon, representing the largest methane reservoir on the Earth [*Wallmann et al.*, 2012]. Over the past few decades, great efforts have been dedicated to understanding the processes of methane cycling and to deconvolving the quantities of methane released from seafloor or seawater worldwide [*Milkov*, 2004; *Wallmann et al.*, 2012]. Of various tectonic settings, sediments eroded from high-relief mountainous

doi:10.6342/NTU202000506

area in tectonically active margins are rapidly deposited and accumulated at km thickness, providing organic matter that is readily exploited for methane formation through thermal maturation and/or microbial degradation. Methane produced from either mechanism could be trapped as gas hydrate or in gas form within sediments in the subsurface [*Katz et al.*, 2002; *Milkov et al.*, 2005]. The substantial amount of carbon sequestered in active margins could become unstable and be transformed into the mobile phase caused by environmental fluctuations, such as temperature, sea level, and slope stability, prior to ascending into the overlying seawater or even being discharged into the atmosphere [*Judd and Hovland*, 2007].

The ultimate release of methane from marine sediments is, however, controlled by multiple mechanisms and processes, such as thermal maturation of organic matter, microbial methanogenesis at depth, fluid channeling and sealing, hydrate sequestration, and biological filtration near the seafloor [*Reeburgh*, 2007; *Hong et al.*, 2017]. Although intensive methane cycling occurs along continental margins [*Pohlman et al.*, 2009; *Archer and Buffett*, 2012], very few studies have provided a quantitative framework to constrain the production, consumption and migration of methane simultaneously at a regional scale in tectonically active environments. In particular, the overall methane inventory and leakage from different tectonic regimes could be greatly

doi:10.6342/NTU202000506

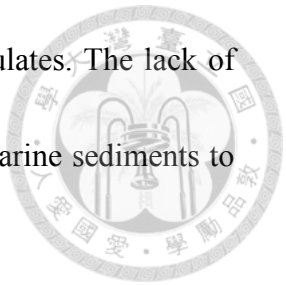

influenced by the supply, burial and degradation of organic particulates. The lack of such knowledge limits a better assessment of the contribution of marine sediments to global methane emission.

In this paper, a systematic and comprehensive approach was adopted to quantify the rates for the methane sources and sinks from different compartments and to address the methane origin within the Taiwan accretionary prism. First, the diffusive fluxes of methane across the sulfate-methane-transition zone (SMTZ) and sediment-water interface were estimated by using 384 porewater profiles, 210 of which were newly reported here. The correlation between the fluxes and distribution of geological structure was discussed. Combined with the methane fluxes previously reported for terrestrial mud volcanoes [*Yang et al.*, 2004; *Chao et al.*, 2010; *Hong et al.*, 2013a], an estimate of the regional flux entering the seawater column and atmosphere was provided. The diffusion-based rates of anaerobic oxidation of methane (AOM) were also evaluated with the results independently obtained from the box model which considers the mass balance of solute concentrations and carbon isotopic compositions [*Hong et al.*, 2013b]. Secondly, the percentages of microbial to thermogenic methane production at great depth (>1 km) were constrained using published isotopic compositions of hydrocarbons from field samples and incubation

doi:10.6342/NTU202000506

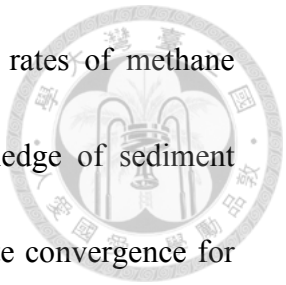

experiments [*Sun et al.*, 2009; *Ling et al.*, 2012]. The potential rates of methane production by thermal maturation were assessed with the knowledge of sediment volume and properties, together with the rate and geometry of plate convergence for the accretionary prism. Finally, the hydrocarbon abundance ratios combined with their isotopic compositions from the cored bottom sediments were used to constrain the origins of hydrocarbon gases. Overall, we present a quantitative framework to assess the methane inventory within the Taiwan accretionary prism, and the possible source and sink mechanisms that control the methane leakages into surface environments. This study represents part of the outcomes for the decadal efforts in systematically exploring the distribution of methane seeps and hydrates as well as their environmental impacts off southwestern Taiwan.

doi:10.6342/NTU202000506

3.2 Materials and methods

3.2.1 Study area and geological setting

Offshore southwestern Taiwan is a west-advancing accretionary prism formed during the subduction of the Eurasian plate beneath the Philippine Sea plate starting about 16 Myr [*Shao et al.*, 2015; *Yang et al.*, 1995]. The accretionary prism has obliquely impinged on the northern South China Sea margin through the collision between the Luzon Arc and Eurasian plate since 5 Myr [*Teng*, 1996; *Lin et al.*, 2008]. The uplift associated with the plate convergence generates extremely high rates of weathering and erosion onshore and drives rapid accumulation of organic matter in the abyssal plain of the northern South China Sea through numerous river systems [*Dadson et al.*, 2003; *Hsu et al.*, 2014]. With such a plate geometry, a transect from onshore to offshore southwestern Taiwan could be translated into a transition from active to passive continental margins. At the active margin, tectonic compression of the accreted terranes from the east generates a series of folds and thrusts propagating westward [*Lin et al.*, 2008]. The active margin has been considered to consist two structural domains divided by the out-of-sequence thrust (OOST; Fig. 3.1); namely, the lower slope and upper slope [*Reed et al.*, 1992]. At the upper slope, offshore mud diapiric structures and mud volcanoes are commonly observed [*Chiang et al.*, 2004].

doi:10.6342/NTU202000506

These geological features could be further traced into their terrestrial counterparts that are aligned with the identified fault systems [*Lin et al.*, 2008]. In contrast, the lower slope consists of a series of anticlinal ridges related to active thrusting and folding [*Lin et al.*, 2008].

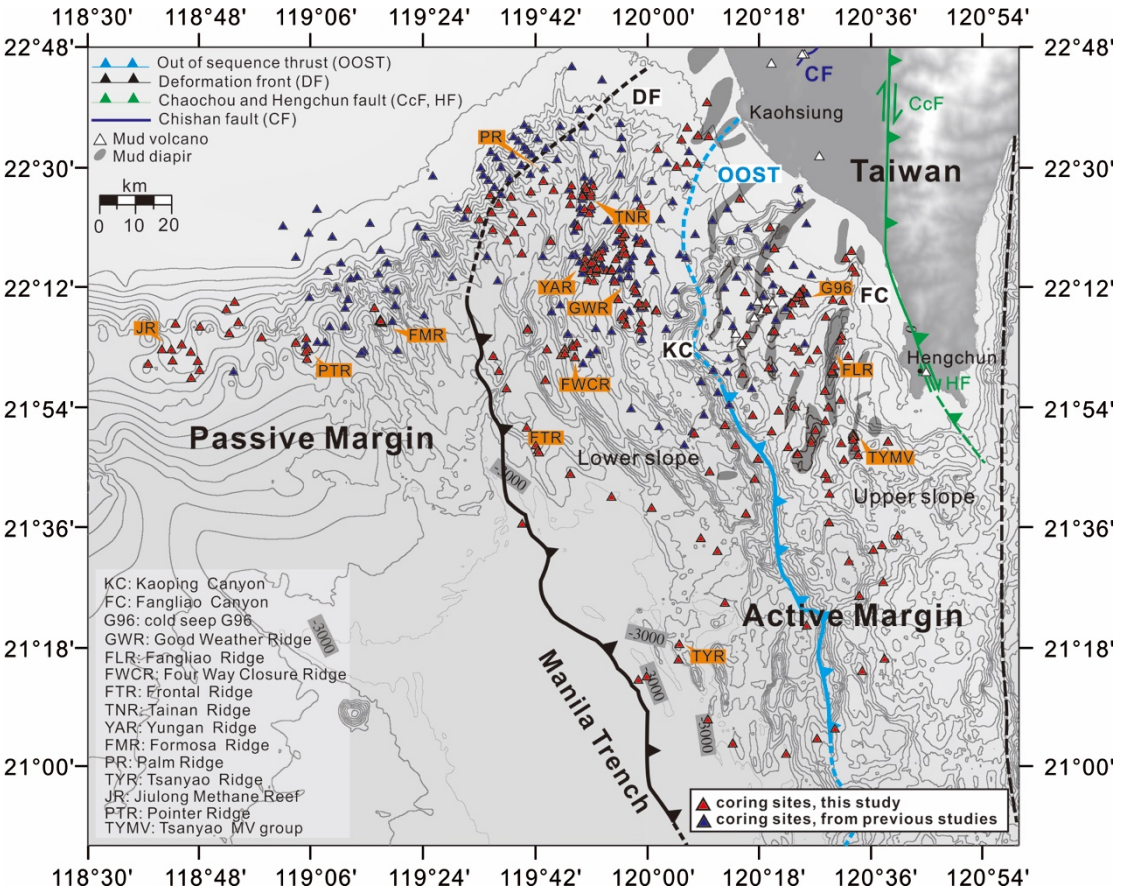

Figure 3.1. Map of coring sites offshore southwestern Taiwan (red triangles; n = 210). The locations of totally 384 sites were shown with 174 of them being previously reported (blue triangles) [*Chuang et al.*, 2006, 2010, 2013; *Ye et al.*, 2016]. The black line shows the deformation front (DF) and the blue line near the shelf edge denotes out of sequence thrust (OOST). The black medium-dashed line represents the right boundary of upper slope defined by *Lin et al.* [2009]. The tectonic structures are modified from *Lin et al.* [2009] and *Lin et al.* [2014]. The map was created by the open source GMT software [*Wessel and Smith*, 1998] using the NOAA public database [*Amante and Eakins*, 2009].

doi:10.6342/NTU202000506

3.2.2 Sediment and core top seawater samples

Sediment and core top seawater samples at 210 sites were retrieved during cruises of the R/V Ocean Researcher I (OR1; legs 804, 828, 834, 835, 860, 902, 934, 961, 978, 1029, 1044, 1070, 1107 and 1118), R/V Ocean Researcher III (OR3; legs 1323, 1368, 1384, and 1405), and R/V Ocean Researcher V (OR5; legs 1309-2 and 1311) using piston and gravity corers, and during R/V Marion Dufresne leg MD147 and MD178-10 using the Giant Piston Corer (GPC) and Calypso Square Corer (CASQ). Most sampling sites are located at (1) cold seep G96, Fangliao ridge (FLR), and Tsanyao mud volcano groups (TYMV) above mud diapirs; (2) Frontal ridge (FTR), Four way closure ridge (FWCR), Palm ridge (PR), Tainan ridge (TNR), and Tsanyao ridge (TYR) identified as anticlinal ridges; (3) Good weather ridge (GWR) and Yungan ridge (YAR) identified as monoclinal ridges; and (4) Formosa ridge (FMR) in the passive margin [*Lin et al.*, 2013]. Detailed sampling sites and core lengths are shown in Fig. 3.1 and Appendix (Table A3.1), respectively.

doi:10.6342/NTU202000506

3.2.3 Sampling and analytical methods

Sediments (10 mL; 15 mL was used during MD178-10 cruise) and core top seawater for gas analyses were collected, and transferred into serum bottles with saturated NaCl as a preservative. The serum bottles were sealed with butyl rubber stoppers, crimped with aluminum rings, and stored upside down at room temperature or 4 ^{o}C. Pore water for aqueous geochemistry was obtained through centrifugation and subsequent filtration through a 0.22 μm pore-sized nylon membrane syringe filter. The filtrates were split into three fractions for anion, cation and dissolved inorganic carbon (DIC) analyses. For cation analysis, concentrated nitric acid (70%) was added at a volume ratio of 1:45 for the preservation of redox sensitive metals. The DIC samples were collected in a 5 mL polypropylene vial without gas bubbles and stored at 4 ^{o}C.

The concentrations of hydrocarbon gases were determined using gas chromatography (GC). Two approaches were used: (1) Samples obtained from MD147, OR1- 804, 828, 834, and 835 were analyzed using a GC equipped with a MS-13X (molecular sieve) column and a Hayesep D column in line with two thermal conductivity and one flame ionization detectors with H_2 and Ar as carrier gases (injection temperature 30 ^{o}C, held isothermal for 2 mins, ramped to 250 ^{o}C at 120 ^{o}C

doi:10.6342/NTU202000506

min^{-1}); (2) samples from other cruises were introduced into a GC equipped with a 4 m-long Hayesep D column in line with a helium ionization detector. The temperature scheme for gas separation proceeded as the initial injection at 50 ^{o}C, being held for 9 minutes, and ramped to 200 ^{o}C at a rate of 90 ^{o}C min^{-1}. Analytical precision is typically better than 5%.

Major ion concentrations (sulfate, calcium, and magnesium) were determined using an ion chromatography (882 Compact IC Plus) with a detection limit of 0.1 ppm in weight. Total alkalinity was determined by titrating the sample with 0.02 N HCl while bubbling nitrogen through the sample [*Wallmann et al.*, 2006a]. The concentrations and carbon isotopic compositions of DIC were measured using an OI Analytical total organic carbon (TOC) analyzer combined with a Picarro G1101–*i* cavity ring down spectrometer (CRDS) isotopic analyzer. A total of 10–15 mL of water sample was treated with 5% H_3PO_4 in a glass vial at 25 °C on line. The CO_2 produced was stripped with N_2 and introduced into the detectors. The carbon isotopic compositions of methane were measured using a Methane Carbon Isotope Analyzer (MCIA) equipped with a tunable diode laser absorption spectrometry or an isotope ratio mass spectrometry (IRMS) in line with a GC and a combustion oven. The hydrogen isotopic compositions of methane were determined using an IRMS in line

doi:10.6342/NTU202000506

with a GC and a pyrolysis oven. The obtained isotopic compositions were expressed as the δ notation referenced to standards [$\delta = (R_{sample}/R_{std} - 1) \times 1000$ ‰, where R is the ratio of heavy to light isotopes]. The standards for carbon and hydrogen isotopes are the Pee Dee Belemnite (PDB) and Vienna Standard Modern Ocean Water (VSMOW), respectively. The precisions are ±0.5–1 ‰ for CRDS measurements, ±0.5–1 ‰ for MCIA measurements; and ±0.5 ‰ for δ^{13}C-methane and ±3 ‰ for δ^{2}H of methane by the IRMS.

3.2.4 Calculations of fluxes across different interfaces

The diffusive fluxes of methane across the SMTZ were calculated using the Fick's First Law [*Berner*, 1980]:

$$F = -\varphi \cdot D_s \cdot \frac{\partial C}{\partial x} \quad (3.1)$$

where F is the flux, φ is the porosity converted from water content assuming a sediment density of 2.7 g cm^{-3} [*Chen*, 1981; *Chen*, 2004–2011; *Yang*, 2013–2014], D_s is the bulk sediment diffusion coefficient corrected for tortuosity, C is the methane concentration, and x is the depth. D_s was calculated using Equation (3.2):

doi:10.6342/NTU202000506

$$D_s = D_w/(1 - \ln(\varphi^2)) \quad (3.2)$$

where D_w is the diffusion coefficient in seawater at *in situ* temperatures [*Jähne et al.*, 1987; *Boudreau*, 1997]. Because the measured methane quantity represents the residual fraction post-degassing during core recovery, the calculated diffusive flux is a conservative estimate. Raw data of methane and sulfate concentration are listed in Appendix (Table A3.2.1) [*Chen*, 2009; *Chen*, 2010; *Chen*, 2011; *Chuang et al.*, 2006; *Chuang et al.*, 2010; *Chuang et al.*, 2013; *Hu et al.*, 2017; *Yang*, 2007–2014; *Su*, 2015].

Fluid advection is assumed negligible. The assessment was based on the consideration that chloride is inert to biological and most abiotic reactions, thereby serving the best tracer for fluid migration. In addition, deeply-sourced fluids are commonly characterized with low salinity derived from either hydrate dissociation or clay dehydration [*Kastner et al.*, 1991]. The contrast chloride concentrations between deeply-sourced fluid and seawater render chloride a sensitive tracer to investigate whether advection is significant and affects the shallow-ranging geochemical characteristics. Of 101 sites (including sites described in previous studies [*Chuang et al.*, 2013; *Lin et al., 2014*; *Ye et al.*, 2016]) with chloride data available (Appendix,

doi:10.6342/NTU202000506

Table A3.2.1), most sites (94 sites) were characterized with no or insignificant in chloride concentration, suggesting small contribution of advection in these shallow sediments. Only seven sites proximal to mud volcanoes, mud diapirism or structural features are characterized by downward decreasing chloride concentrations. The chloride profiles from six of them (OR1-1070-C11, OR1-1070-C9, MD178-3292, MD178-3280, OR1-902A-9 and OR1-1107-MV12-1) showed a linear decreasing trend, whereas the other one (OR1-1107-MV12-A) exhibited a concave downward shape. The linear decreasing of chloride content indicating the dominancy of diffusion, whereas the concave-downward profile suggests the combinative effect of diffusion and advection only on this site. To constrain the advection rate, the fluid transport equation (combining diffusion and advection) was used to fit the observed chloride variation. Our calculation yielded an advection rate of ~0.4 cm yr^{-1}. Such an advection rate could be translated into an advective methane flux of 1.55×10^{-1} mol m^{-2} yr^{-1} at the SMTZ (using a porosity of 0.35 and a methane concentration of 0.11 mM). The diffusive flux across the SMTZ was calculated to be 3.80×10^{1} mol m^{-2} yr^{-1}, a magnitude approximately 240 times greater than the advective flux. Therefore, the advective flux could be considered negligible even in the region with relatively high fluid flow. The modeling calculation also demonstrates that unless the sampling was

doi:10.6342/NTU202000506

conducted right at the structural features, the majority of sampling area is governed by diffusive transport of methane.

Methane concentration gradients were calculated from the depth intervals where the concentrations linearly increased. Linear regression was then applied to the target depth of interest. For methane fluxes across the SMTZ, at least three data points across the sulfate minimum to methane minimum were used for the analyses. Methane concentration data from 64 sites (with 20 sites reported by from *Chuang et al.* [2006, 2010, and 2013], *Lin* et al. [2014], and *Ye et al.* [2016]) were calculated. The fluxes at 11 sites obtained from *Chuang et al.* [2010] were included for comparison. The obtained diffusive fluxes across the SMTZ were further categorized into two groups using a probability plot from which the flux corresponding to the drastic change of flux to frequency ratio was selected as the threshold value for categorization [*Sinclair*, 1974]: hot sites with fluxes more than 10^{-1} mmol m^{-2} d^{-1} and normal sites with fluxes lower than 10^{-1} mmol m^{-2} d^{-1}. The ranges of flux were multiplied with the areas to obtain the total area-based methane consumption rates, considering that this geochemical transition resulted from the AOM process alone. Using the distribution of sites, the areas of the passive margin and active margin for normal sites were calculated to be 3,400 and 11,777 km^2, respectively (Appendix, Fig.

doi:10.6342/NTU202000506

A3.1). The areas of all hot sites were estimated to range from 0.11 to 40.7 km^2. To simplify the calculation and avoid the contributions from extreme values, a minimum area of 0.11 km^2 was used to represent all hot sites. We estimated the area occupied by hot sites from the distribution of methane flux across the sediment-water interface as the coverage of this sampling is large enough for representative estimation. The resulting area of hot sites on the passive and active margins are 0.33 (n=2) and 2.86 (n=26) km^2, respectively.

The diffusive boundary layer (DBL) is defined as the interface between seawater and sediment. Methane effluxes across the DBL were calculated using the following equation [*Jørgensen et al.*, 1990]:

$$F_{DBL} = D_w \cdot \frac{C_0 - C_w}{Z_{diff}} \quad (3.3)$$

where F_{DBL} is the flux across the sediment-seawater interface (i.e. efflux), C_0 is the methane concentration immediately below the DBL in the surficial sediments, C_w is the concentration in the bottom water, and Z_{diff} is the thickness of DBL and is assumed to be 1.0 mm [*Boudreau and Guinasso*, 1982]. Because C_0 is an unknown value, the mass balance relationship between the methane efflux across the DBL and

doi:10.6342/NTU202000506

methane flux at the top sediments was adopted to derive C_0 and hence the efflux using the following equation [*Dale et al.*, 2008b]:

$$D_w \cdot \frac{C_0 - C_w}{z_{diff}} = \varphi_0 \cdot \left(D_s \cdot \frac{C_1 - C_0}{\Delta x} - v \cdot C_0 \right) \quad (3.4)$$

where φ_0 is the sediment porosity at the seabed, C_1 is the methane concentration at the grid node immediately below C_0, Δx is the distance between depths of C_0 and C_1, and v is the advective flow rate. The methane concentration at the shallowest depth of the core was used as C_1, whereas v was assumed to be negligible. For sites without methane concentrations of bottom water, C_w for sites nearby was used. Methane concentration data from 370 sites (with 171 sites collected from *Chuang et al.* [2006, 2010, and 2013]) were calculated.

The calculated effluxes at specific sites were further extrapolated to derive the area-based discharge of methane into seawater. Following a similar approach described above, the obtained diffusive effluxes were further categorized into normal and hot sites using an arbitrary threshold value of 10^{-2} mmole m^{-2} d^{-1}. The ranges of flux were multiplied by the areas to obtain the total quantity of methane discharged per unit time. The area sizes for individual categories were the same as those

doi:10.6342/NTU202000506

described previously. These marine effluxes were compared with the published methane emission from terrestrial mud volcanoes [*Yang et al.*, 2004; *Chao et al.*, 2010; *Hong et al.*, 2013a] and from submarine environments elsewhere.

3.2.5 Methane production and consumption constrained by the box model

The methane production and consumption rates (or fluxes) at the SMTZ were calculated to evaluate the diffusion-based AOM rates independently using the solute and isotopic data available at these depth ranges. The box model [*Hong et al.*, 2013b] which considers the mass balance between five reactions: organotrophic sulfate reduction (OSR), AOM, carbonate precipitation (CP), methanogenesis (ME), and CO_2 reduction (CR), were employed. CR represents the reversible pathway that is accompanied internally with AOM [*Yoshinaga et al.*, 2014], whereas methanogenesis (ME) produces methane from the degradation of organic matter. Although the product is the same, these two reactions are intrinsically different and involve different populations. Fluxes from deep sources are used to satisfy the mass balance at the SMTZ (Appendix, Table A3.3). Methane flux was derived by subtracting the total sulfate reduction rate from the sulfate consumption with organic matter, assuming that methane-fueled AOM is responsible for the rest of the sulfate reduction. The gradients

doi:10.6342/NTU202000506

of SO_4^{2-}, Ca^{2+}, Mg^{2+} and DIC were used to derive the fluxes or rates for individual reactions. Carbon isotopes were used as an additional constraint. The carbon isotopic fractionation factors related to AOM and CR were assumed to be 1.004 and 1.06, respectively [*Whiticar*, 1999]. While most organic matter can be degraded in shallow sediments through OSR, the rest is buried into the methanogenic zone for methane production. The partition factor of organic degradation via OSR was assumed to be 0.8 based on the modeling results from *Chuang et al.* [2013]. Because of the data availability, 11 sites (Appendix, Fig. A3.2 and Table A3.3) were chosen for model calculations, and all the geochemical characteristics were assumed to reach a steady state. Since the site numbers were small, no categorization for hot versus normal sites was performed. The calculated AOM rates were compared to those obtained from the concentration gradients to validate the diffusive fluxes. The calculated methane production and AOM rates were also used to assess the methane balance at shallow depth.

3.2.6 Fractions of microbial methane production at great depth

The absolute quantity of deep microbial methane production (>1 km) was obtained by combining the fraction of pure microbial to thermogenic methane with the rates of thermogenic methane production deduced from subduction geometry and

doi:10.6342/NTU202000506

parameters (see section 3.2.7). The fraction of deep microbial methane production was first estimated using published isotopic compositions of hydrocarbons collected from the bubbling pools of terrestrial mud volcanoes [*Sun et al.*, 2008 and 2010]. The generalization of terrestrial for marine environments stems from the fact that sediments in both compartments share genetic relationships. As plate convergence has been driven by the accretion of the Luzon arc for at least 9.7 Myr [*Huang et al.*, 2006], all sediments previously deposited offshore southwestern Taiwan would be subject to a similar path of burial and tectonic displacement or deformation, regardless of deposition time. Therefore, sediments currently located at great depth in both terrestrial and marine compartments were assumed to retain similar reactivity for microbial methane formation. While sediment retrieval directly from great depth in marine environments is not yet available, fluids and sediments from the bubbling pools of terrestrial mud volcanoes are perhaps the best alternative materials to characterize the source of deep fluid, considering that rapid fluid transport along fractures prevents the geochemical characteristics of pool fluids and sediments from being altered or modified [*Ling et al.*, 2012 and *Wang et al.*, 2014]. The following equation was used to obtain the fractions of microbial and thermoganic methane from great depths:

doi:10.6342/NTU202000506

$$\delta^{13}C_{measured} = \delta^{13}C_m \times f_{mgd} + \delta^{13}C_t \times (1 - f_{mgd}) \quad (3.5)$$

where $\delta^{13}C_{measured}$ is the measured $\delta^{13}C$ value of methane, $\delta^{13}C_m$ is the $\delta^{13}C$ value of microbial end-component, $\delta^{13}C_t$ is the $\delta^{13}C$ value of thermogenic methane, and f_{mgd} represents the fraction of microbial methanogenesis at great depth.

To obtain the isotopic composition of pure thermogenic methane ($\delta^{13}C_t$ in Eq. 3.5), the natural gas plot was adopted [*Chung et al.*, 1988; *Milkov et al.*, 2007]. This approach lies in the rationale that the $\delta^{13}C$ value and the reciprocal of carbon number of hydrocarbon (*1/n*) would obey a linear relationship for hydrocarbons produced purely by thermogenesis. The slope and intercept at *1/n* of 0 could be translated to the maturity and initial composition of a hydrocarbon source, respectively. Published $\delta^{13}C$ values of hydrocarbons (C_1-nC_5) retrieved from gas seeps and mud volcanoes in southwestern Taiwan [*Sun et al.*, 2008 and 2010] were applied to the natural gas plot. A threshold of R^2 value at 0.9 obtained from linear regression was arbitrarily chosen in order to determine whether the $\delta^{13}C$ values of C_1-nC_5 were linearly distributed (Appendix, Fig. A3.3a). For the covariance between $\delta^{13}C$ value and *1/n* (R^2 values greater than 0.9), the equation generated from regression was used to calculate the

doi:10.6342/NTU202000506

$\delta^{13}C$ values of pure thermogenic methane and hydrocarbon source. For regression with R^2 values less than 0.9, the $\delta^{13}C$ values of C_{2+} generally clustered within ±1‰, and were, therefore, averaged and extrapolated to *1/n* of 1 and 0 for the determination of $\delta^{13}C$ values of pure thermogenic methane and hydrocarbon source, respectively (Appendix, Fig. A3.3b). Since microbial oxidation and synthesis would leave the residual hydrocarbons (mostly C_1, C_3, and C_4) enriched with ^{13}C and produce ^{13}C-depleted methane, respectively [*James and Burns*, 1984], such an analysis allows for the identification of potential microbial processes that deviate $\delta^{13}C$ values of hydrocarbons from the predictive thermogenic trend. The projected $\delta^{13}C$ values of pure thermogenic methane ($\delta^{13}C_t$, Table 3.1) combined with the $\delta^{13}C$ values of pure microbial methane produced from the decomposition of organic matter (see next paragraph) were further used to estimate the microbial contribution to the overall methane inventory through Eq. 3.5.

doi:10.6342/NTU202000506

Table 3.1. Summary of $\delta^{13}C$ values of hydrocarbons from onshore mud volcanoes and seeps, projected $\delta^{13}C$ values of pure thermogenic methane, and potential contribution of microbial methanogenesis.

Sample name	Measured $\delta^{13}C$ (‰)[a]					Projected $\delta^{13}C$ (‰) from natural gas plot		Δ ($\delta^{13}C_m$-$\delta^{13}C_p$)[b]	f_{mgd}		
	C_1	C_2	C_3	nC_4	nC_5	Thermo C_1 ($\delta^{13}C_t$)	Hydro - carbon source		Aceto-clastic fraction[c]	CO_2 reduction fraction[d]	CO_2 reduction fraction[e]
KTL-06	-32.9	-23.5	-23.9	-24.0	-23.7	-23.8	-23.8	-9.1	0.49	0.24	0.16
CLB-B12	-26.5	-25.3	-24.5	-24.0		-26.6	-23.4	0.1	0.00	0.08	0.05
CLB-SW06	-33.0	-24.1	-24.8	-24.8		-24.6	-24.6	-8.4	0.47	0.22	0.15
YNH-12	-31.3	-27.7	-24.3	-24.7	-24.7	-31.4	-22.5	0.1	0.00	0.22	0.15
SYNH-10	-31.6	-25.9	-25.2	-25.2	-25.6	-31.1	-23.0	-0.5	0.04	0.22	0.14
WSD-04	-30.3	-26.3	-22.3	-23.5		-30.4	-20.3	0.1	0.00	0.24	0.16
LYS-02a	-29.9	-24.3	-26.7	-25.6		-25.5	-25.5	-4.4	0.26	0.12	0.08
KSP-12	-51.0	-36.0	-30.2	-27.6		-51.1	-20.0	0.1	0.01	0.73	0.50
95G908	-33.2	-25.3	-23.5	-23.6	-23.5	-32.7	-20.0	-0.5	0.05	0.31	0.21
95G925	-33.4	-19.2	-15.6	-18.3		-32.5	-9.7	-0.9	0.09	0.45	0.33
95G926	-32.7	-24.8	-26.3	-26.2	-25.9	-25.8	-25.8	-6.9	0.41	0.19	0.12
95G907	-27.9	-24.2	-23.9	-24.3	-24.1	-24.1	-24.1	-3.8	0.21	0.10	0.07
95G924	-29.6	-23.2	-22.7	-24.5		-23.5	-23.5	-6.1	0.32	0.16	0.10
95G913	-31.3	-26.6	-24.6	-24.7	-24.4	-31.2	-22.2	-0.1	0.01	0.23	0.15
95G927	-39.0	-26.8	-24.6	-24.1	-23.6	-38.3	-19.7	-0.7	0.17	0.45	0.31

[a] Terrestrial mud volcano data source from *Sun et al.* [2008] and [2010].

[b] $\Delta(\delta^{13}C_m$-$\delta^{13}C_p)$ represents the difference of $\delta^{13}C$ values between measured methane and projected pure thermogenic methane.

[c] Potential contribution of acetoclastic methanogenesis to the total methane was calculated on the basis of Equation (2.5) and a fractionation factor of 1.020 obtained from incubation experiments [*Ling et al.*, 2012].

[d] Potential contribution of CO_2 reduction fraction to the total methane was calculated on the basis of Equation (2.5) and a fractionation factor of 1.040 [*Ling et al.*, 2012; *Whiticar*, 1999].

[e] Potential contribution of CO_2 reduction fraction to the total methane was calculated on the basis of Equation (2.5) and a fractionation factor of 1.060 [*Whiticar*, 1999].

doi:10.6342/NTU202000506

Three scenarios were employed to constrain the $\delta^{13}C_m$ values in Eq. 3.5. In any scenarios, the isotopic fractionation between particulate organic matter and methanogenic precursor was assumed to be negligible. Therefore, the scenario $\delta^{13}C$ value of pure microbial methane could be deduced by subtracting the $\delta^{13}C$ value of particulate organic matter with the isotopic fractionation associated with methanogenesis. The $\delta^{13}C$ values of the projected source composition or of organic matter in offshore sediments [*Hsu et al.*, 2014; *Yang*, 2012] (Table A3.2.2) clustered mostly between −25 and −20‰. Therefore, a median value of −22.5‰ was chosen to represent the isotopic composition of organic matter subject to microbial degradation. The first scenario considered that the predominant methanogenic pathway was through acetate fermentation with a carbon isotope fractionation of 20‰. This assumption is based on the incubation results using mud volcano sediments in the region as inoculum and acetate as substrate [*Ling et al.*, 2012]. The $\delta^{13}C_m$ value was calculated to be –42.5‰ (–22.5‰ – 20‰ = –42.5‰). The second and third scenarios focused on methanogenesis through CO_2 reduction with carbon isotopic fractionations of 40‰ and 60‰ [*Ling et al.*, 2012; *Whiticar*, 1999], respectively. For these two scenarios, the $\delta^{13}C_m$ values were calculated to be −62.5‰ and −82.5‰, respectively. The obtained f_{mgd} (Table 3.1) was further transformed into the

doi:10.6342/NTU202000506

microbial-to-thermogenic ratio, and multiplied by the total thermogenic methane production (see the section 3.2.7) to derive the quantity of regional microbial contribution.

3.2.7 Thermogenic methane produced by subduction and accretion

The production rate of thermogenic methane within the accretionary prism was estimated based on the following equation proposed by *Schmoker* [1994]:

$$R_{thermo} = R_{acc\text{-}M} \cdot m \cdot PP \tag{3.6}$$

where R_{thermo} is production rate of thermogenic methane, $R_{acc\text{-}M}$ is the sediment mass accumulated within the accretionary prism, m is the maturity of the sediments, and PP is the hydrocarbon potential of the sediments (i.e. the weight of hydrocarbon per unit weight of sediments). To determine the m value, the following two assumptions were made:

1) 70% of sediments were assumed to subduct along with the plate, with the remaining 30% of sediments being accreted [*von Huene and Scholl*, 1991]. All the sediments being subducted were assumed to be totally matured once they reached the depth of the gas window. This assumption ignores the possibility that subducted

doi:10.6342/NTU202000506

organic matter could be completely oxidized to CO_2 or graphitized. The remaining 30% accreted sediments could be matured for hydrocarbon formation if the sediments are buried to a depth greater than 1.29 kmbsf considering an average geothermal gradient of 70 ^{o}C km^{-1} [*Chi and Reed*, 2008] and 90 ^{o}C for the gas window. Based on the seismic reflection signals near the current trench and deformation front, the thickness of pre-subducted sediments was calculated to be 1.24–4.49 km [*Yeh and Hsu*, 2004; *Liao et al.*, 2016]. The contribution of thermogenic methane from such accreted sediments is small and insignificant. For example, the greatest thickness of pre-subducted sediments is 4.49 km. The thickness of accreted sediments would be less than 1.35 km (4.49 km × 30%). The proportion of accreted sediments immediately subject to thermal maturation at subduction would be only 1.3% ((1.35–1.29) km /4.49 km × 100%). The fraction will be even smaller for the pre-subducted sediments that is thinner than 4.49 km. Moreover, the thickness of pre-subducted sediments more than 4 km is only representing 11% of the trench in length. As the potential accreted sediments for thermal maturation is small and the exact accretion rate has not been constrained well, the thermogenic methane contributed from the accreted sediments was assumed to be negligible.

2) Given that 40% of the total hydrocarbons are in cyclic structures and resistant to

doi:10.6342/NTU202000506

thermal decomposition, all the other hydrocarbons were assumed to be eventually converted to methane under high temperatures and pressures [*Hunt*, 1995]. Therefore, *m* was calculated to be 42% (70% × 0.6 = 42%). Based on the results from the four ODP sites (ODP leg184, Site 1144, 1145, 1146, and 1148; at the northern slope of the South China Sea [*Wang et al.*, 2000]), the values of hydrocarbon potential (*PP* in Eq. 3.6) were assumed to be 0.15– 0.5 mg of hydrocarbon per kg sediments.

$R_{acc\text{-}M}$ in Eq. 3.6 was calculated by assuming a simplified geometry of the accretionary prism (Fig. 3.2) and the density of bulk sediments (ρ_{bulk}) using the following equation:

$$R_{acc\text{-}M} = R_{acc\text{-}V} \cdot \rho_{bulk} \tag{3.7}$$

where $R_{acc\text{-}V}$ is the rate of sediment volume accumulated, calculated by the following equation [*von Huene and Scholl*, 1991]:

$$R_{acc\text{-}V} = H_{tr} \cdot L_{tr} \cdot R_{sd} \tag{3.8}$$

where H_{tr} is the thickness of the sediments in the trench, L_{tr} is the length of the trench,

doi:10.6342/NTU202000506

and R_{sd} is the subduction rate. Specifically, the thickness of sediments in the trench (H_{tr}) was assumed to be 1.24–4.49 km (described above). Based on the investigated area (from 21°N to 23.5°N), the trench length (L_{tr}) used in the model calculation was assumed to be 284 km (Fig. 3.2). The subduction rate (R_{sd}) was assumed to be 66 – 76 km Myr^{-1} [*Suppe*, 1981; *Lundberg et al.*, 1997]. In order to convert the volume of sediments to its mass ($R_{acc\text{-}M}$), porosity and ρ_{bulk} values from ODP sites mentioned above were used [*Wang et al.*, 2000]. The obtained quantity represents the volume of methane potentially formed through the subduction and accretion for the investigated trench length. All parameters used in the calculation are summarized in Table A3.4.

doi:10.6342/NTU202000506

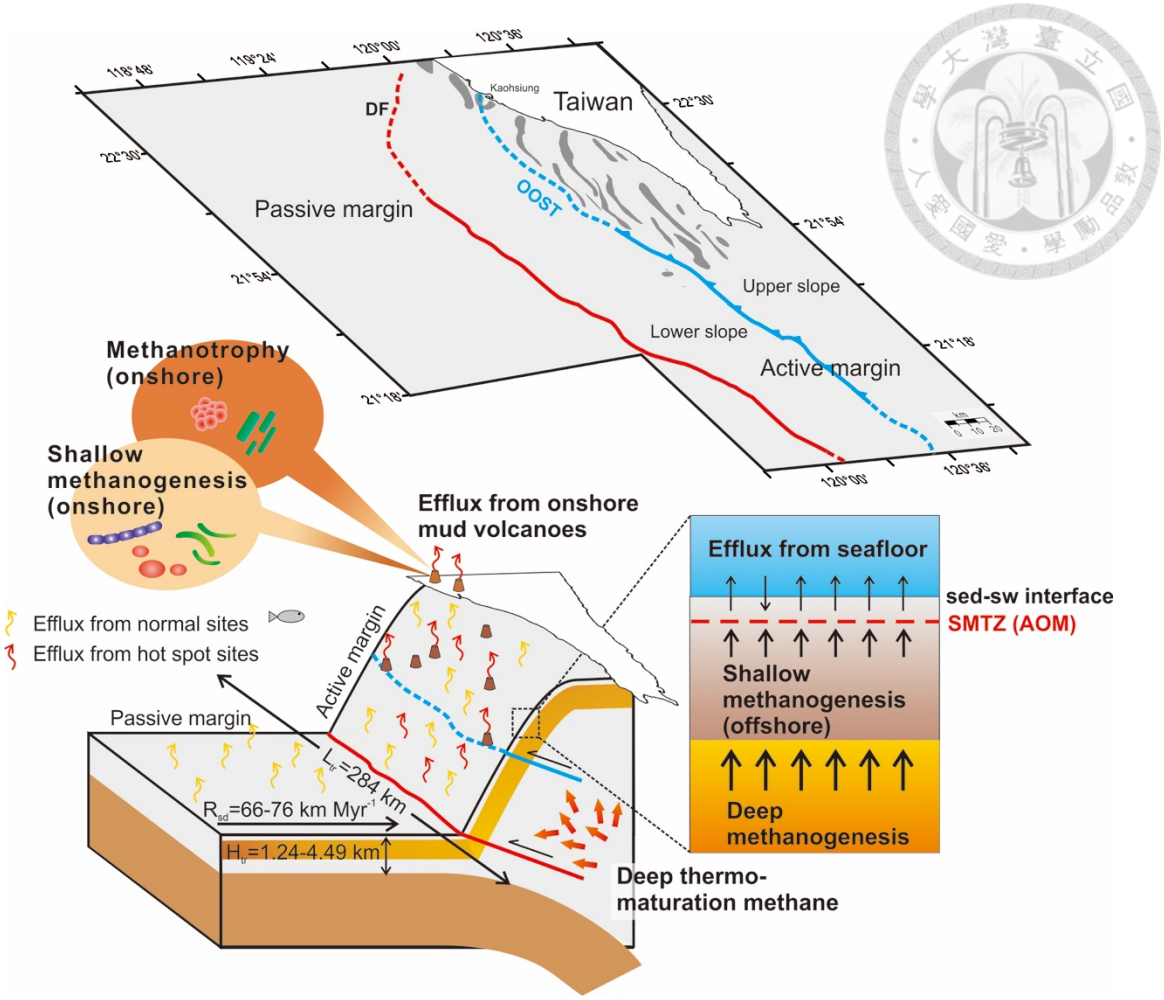

Figure 3.2. Conceptual framework of methane cycling and transport and from various tectonic compartments of the Taiwan accretionary prism. All processes considered for methane effluxes, sinks, and sources are shown. The red line shows the deformation front (DF) and the blue line near the shelf edge denotes out of sequence thrust (OOST) [*Lin et al.*, 2014].

doi:10.6342/NTU202000506

3.3 Results

3.3.1 Methane fluxes across geochemical transitions at shallow depth

The calculations yielded diffusive methane fluxes ranging from 2.71×10^{-3} to 2.78×10^{-1} mmol m^{-2} d^{-1} (n=64, Fig. 3.3) across the SMTZ, and from -1.88×10^{-1} to 3.97×10^{0} mmol m^{-2} d^{-1} at the sediment-seawater interface (n=370; Fig. 3.4; 29 sites had negative values; Appendix Table A3.1). For the SMTZ, fluxes at most sites were in the range between 10^{-2} and 10^{-1} mmol m^{-2} d^{-1}. Fluxes with higher values (more than 10^{-1} mmol m^{-2} d^{-1}) were observed predominantly at ridges and seep area, including sites at TNR (0.32 mmol m^{-2} d^{-1}), FTR (0.25 mmol m^{-2} d^{-1}), area between YAR and GWR (0.23 mmol m^{-2} d^{-1}), and cold seep G96 (0.11 mmol m^{-2} d^{-1}; Fig. 3.3 and Appendix Fig. A3.4). Combined 11 sites with previous results [*Chuang et al.*, 2010] and area coverage, the area-based methane consumptions mediated by AOM were from 188 to 5976 (mean = 2054) Mg yr^{-1} in the active margins. Since only one site of flux across SMTZ was obtained in the passive margin, no area-based flux was calculated. For the sediment-seawater interface, the effluxes at most sites were between 10^{-5} and 10^{-3} mmol m^{-2} d^{-1}. Most effluxes in active margin were around 10^{-4} mmol m^{-2} d^{-1} and around 10^{-5} mmol m^{-2} d^{-1} in the passive margin (Fig. 3.4). Sites at cold seeps G96, TYMV, and FMR exhibited particular higher fluxes (more than 10^{-1}

doi:10.6342/NTU202000506

mmol m^{-2} d^{-1}). The few negative fluxes were excluded from further calculation of area-based effluxes, because the high methane concentrations of bottom seawater might result from the disturbance caused by the coring penetration. With the area coverage described above, the area-based methane effluxes were 0.04–47.0 (mean = 4.21) Mg yr^{-1} and 0.3–683 (mean = 52.0) Mg yr^{-1} in the passive and active margins, respectively.

doi:10.6342/NTU202000506

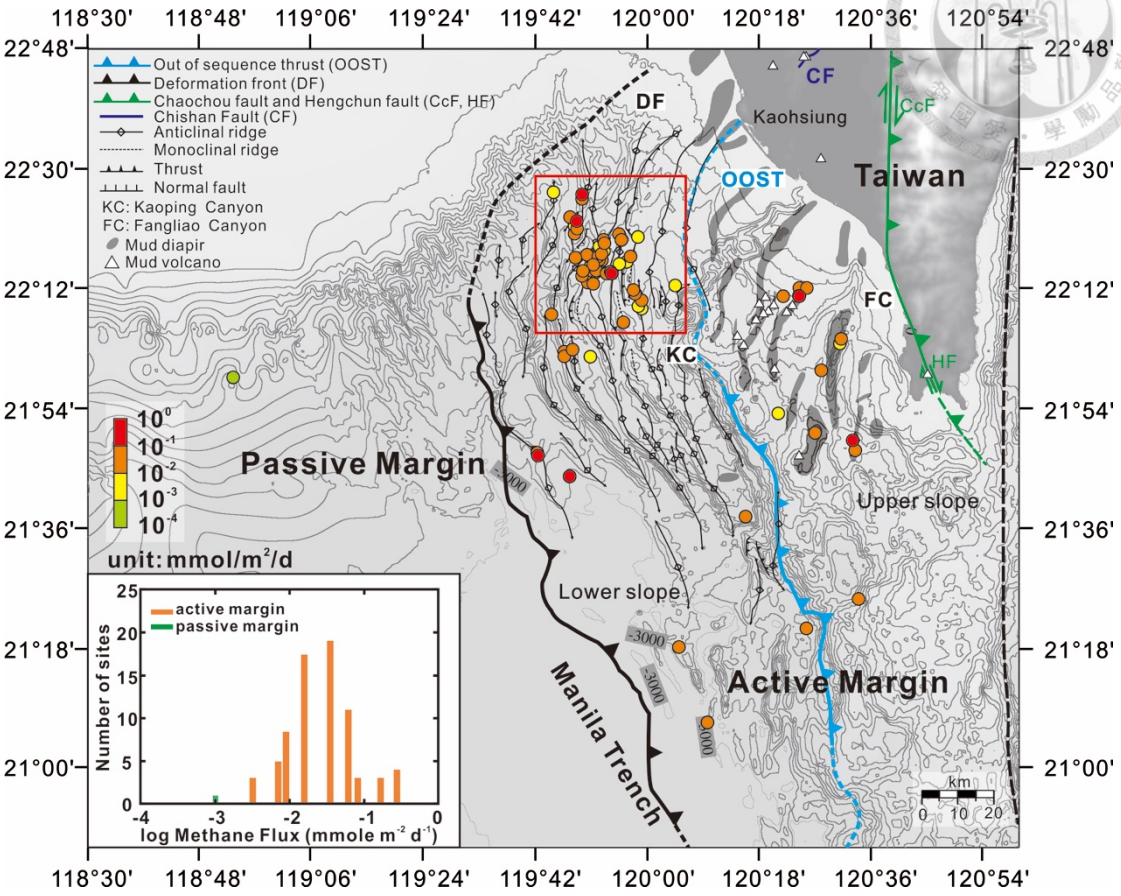

Figure 3.3. Methane fluxes across the SMTZ of the investigated area (n = 75). The red rectangle defines the region with intensive sampling, and enlarged as shown in Appendix, Fig. A3.4. The tectonic structures are cited from *Lin et al.* [2014]. Part of data used for calculation was adopted from *Chuang et al.* [2013] and *Ye et al.* [2016]. The fluxes obtained from *Chuang et al.* [2010] are included for comparison (n = 11). The black medium-dashed line represents the right boundary of upper slope defined by *Lin et al.* [2009].

doi:10.6342/NTU202000506

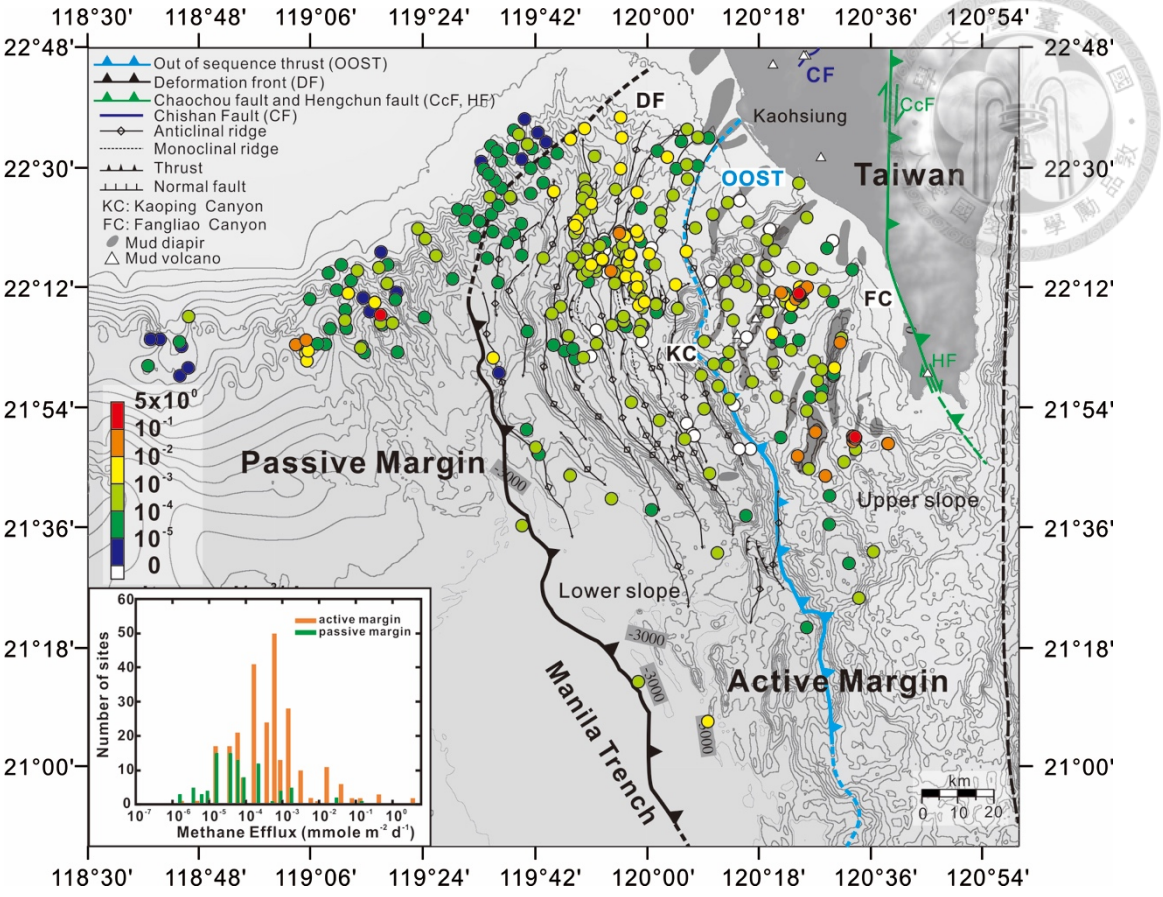

Figure 3.4. Methane effluxes (fluxes across the sediment-seawater interface) of the investigated area (n = 370). Open circles indicate negative values of fluxes. Part of data used for calculation was adopted from *Chuang et al.* [2006, 2010, 2013]. The black medium-dashed line represents the right boundary of upper slope defined by *Lin et al.* [2009].

doi:10.6342/NTU202000506

3.3.2 Methane production and consumption at shallow depth

AOM, OSR, CP, CR, and ME rates derived from the box model for the SMTZ zone at 11 sites ranged from 0.08 – 2.42, 0.07 – 1.15, 0.15 – 1.92, 0.17 – 0.84, and 0.04 – 0.57 × 10^{-1} mmol m^{-2} d^{-1}, respectively (Appendix, Table A3.3). AOM accounted for the majority of sulfate consumption at seven sites (AOM/OSR ratios exceeded 1.7; Table A2.3), whereas rates of AOM and OSR were nearly equivalent (the proportion of sulfate consumed by AOM ranged between 43–53%) at the other three sites. The AOM rates derived from the box model were comparable with diffusive fluxes for sites C17, EN1, C5, 3289 and 3280 (Appendix, Table A3.3), but were greater than diffusive fluxes by a factor of 3.2–5.6 for the remaining sites. The overall methane production (ME+CR) was 0.3–1.7 times the consumption (AOM) rates.

3.3.3 Microbial and thermogenic methane production at great depth

The natural gas plot (Appendix, Figs. A3.3 and A3.5) was applied to project the isotopic composition of the pure thermogenic methane. Of the 15 datasets, six sets (terrestrial mud volcanoes: CLB-SW06, KTL-06, LYS-02A, 95G926, 95G907 and 95G024) that did not meet the R^2 threshold (R^2 value < 0.9) obtained from the

doi:10.6342/NTU202000506

regression analysis exhibited almost invariant $\delta^{13}C$ values of C_{2+} compounds (Table 3.1). The extension of averaged $\delta^{13}C$ values of C_{2+} to *1/n* of 1 predicted the $\delta^{13}C$ values ranging between –25.8‰ and –23.8‰ for methane produced purely by thermal maturation. The offsets between the predicted and measured $\delta^{13}C$ values of methane ranged from 3.8‰ to 9.1‰ (Table 3.1 and Appendix, Fig. A3.5). Eight out of the remaining nine samples possessed $\delta^{13}C$ values of C_1-nC_5 compounds varying in a linear fashion (R^2 value > 0.9). The regression analyses yielded $\delta^{13}C$ values of hydrocarbon source from –23.4‰ to –19.7‰ and of pure thermogenic methane from –51.1‰ to –26.6‰. The predicted $\delta^{13}C$ values of methane differed from the measured ones by < 1‰. The analytical scheme described above was not directly applied to sample 95G925. Regression for 95G925 yielded an improbable $\delta^{13}C$ value of hydrocarbon source (–9.7‰) with an R^2 value of 0.92. Therefore, the data was excluded from further interpretation and discussion.

The offsets between the measured and projected $\delta^{13}C$-CH_4 values for six sets of data represent thermogenic hydrocarbons impacted by methanogenesis at various degrees. For a scenario with acetatocalstic methanogenesis as microbial end-component, the contribution of microbial methane to the overall methane inventory at great depth ranged from 21 – 49% with a mean of 39%. For a scenario

doi:10.6342/NTU202000506

with hydrogenotrophic methanogenesis, the microbial contribution ranged from 10% to 24% with a mean of 17% and from 7% to 16% with a mean of 11% using isotopic fractionation factors of 40‰ and 60‰, respectively.

Using the rock properties and geometry of the subduction wedge, thermogenic methane production rates for the investigated area (60% of onshore and offshore area) were calculated to range between 1,406 and 21,979 Tg Myr^{-1}. Depending on the microbial scenarios described above, microbial processes could contribute 106–21,117 Tg Myr^{-1} methane at great depth, considering offshore and onshore areas combined.

3.3.4 Methane origins

By using the Bernard plot [*Bernard et al.*, 1976], the abundance ratios of hydrocarbons against isotopic data identified the possible origin of methane (Fig. 3.5). These data points were obtained from the deepest sample of the cores, where sulfate was depleted and methane was abundant (except for site MV12-1, a submarine mud volcano, where sulfate concentration was 10 mM and methane concentration was more than 2 mM; Appendix, Table A3.2.1). The only C_1/C_{2+} ratio and the $\delta^{13}C\text{-}CH_4$ value from the passive margin (site 3264) were 935 and –90.5‰, respectively, falling in the region of mixed microbial and thermogenic methane (Fig. 3.5 and Table A3.5).

doi:10.6342/NTU202000506

Ratios of C_1 to C_{2+} for sites located at the lower slope were between 78 – 38,115, whereas the corresponding $\delta^{13}C\text{-}CH_4$ values ranged from –103.0‰ to –68.1‰. Equal numbers of sites were classified into the field of purely microbial methane and a mixture of microbial and themogenic methane. At the upper slope, C_1/C_{2+} ratios were between 9.2 and 3,893 while $\delta^{13}C\text{-}CH_4$ values were in the range between –81.0‰ and –35.6‰. Most $\delta^{13}C\text{-}CH_4$ values obtained from the upper slope were greater than –50‰. However, their, C_1/C_{2+} ratios varied considerably. While only data from two sites (site MV12-3 and MD4-P3) fell into the field of thermogenic methane, all the other sites were in the field with mixed sources. The $\delta^{2}H\text{-}CH_4$ values ranged between –225‰ and –170‰. These values, combined with their corresponding $\delta^{13}C\text{-}CH_4$ values, were plotted in the field of methanogenesis through CO_2 reduction for most of the samples analyzed. Only data for site GT39B fell in the field of thermogenic methane.

doi:10.6342/NTU202000506

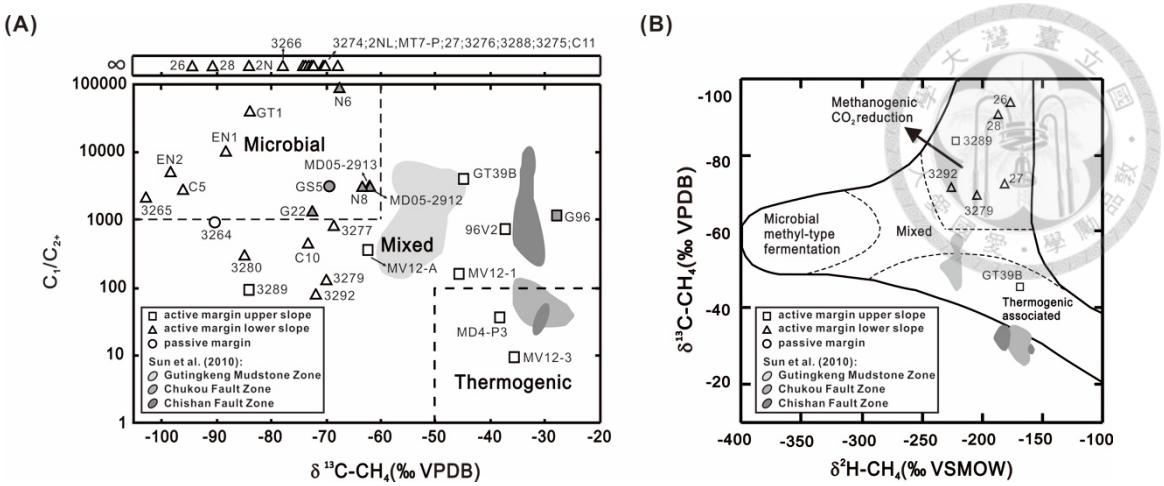

Figure 3.5. Plots of (a) hydrocarbon abundance ratios versus δ^{13}C-CH_4 and of (b) δ^{13}C-CH_4 versus δ^{2}H-CH_4. The assignment of the region for specific gas origin is based on *Bernard et al.* [1976] and *Whiticar* [1999]. Data previously reported in *Chuang et al.* [2010, 2013] and terrestrial mud volcanoes in southwestern Taiwan from *Sun et al.* [2010] are shown by the gray symbols and regions, respectively. Square symbols denote data from the upper slope; triangle symbols are data from the lower slope.

doi:10.6342/NTU202000506

3.4 Discussion

3.4.1 Fluxes across different interfaces and correlations with structural features

The results obtained in this and previous studies [*Chuang et al.*, 2006, 2010, 2013; *Ye et al.*, 2016] indicate that, except for the cold-seep sites at the Formosa Ridge, methane fluxes across the SMTZ and sediment-seawater interface (i.e. effluxes) are low in passive margins (Figs. 3.3 and 3.4). In contrast, methane fluxes are elevated at the bathymetric high of the active margin, including sites from TNR, FTR, YAR, and GWR, G96 seep, and Tsanyao mud volcano (Figs. 3.3, 3.4 and A3.4). The fluxes derived from the concentration gradient were generally comparable with those obtained by the box model calculation (i.e. within the same order of magnitude), validating the utility of diffusive fluxes to a broader area coverage.

All the ridges described above are distributed at the lower slope of the active margin, where a series of anticlines was formed by displacement of blind thrusts [*Lin et al.*, 2008; *Lin et al.*, 2009; *Lin et al.*, 2013]. Seismic data show that emergent thrusts exist near YAR and GWR, titling the strata perpendicular to seafloor [*Lin et al.*, 2009]. By comparison, mud diapirism is prevalent at the upper slope. EK500 sonar-gram also reveals that a number of mud volcanoes are distributed at upper slope

doi:10.6342/NTU202000506

[*Chen et al.*, 2010 and 2014; *Yang et al.*, 2014]. The intimate association between methane fluxes and structural features suggests the structurally controlled transport of methane. Migration of deeply sourced methane is facilitated by the potential fluid channels along faults and/or stratigraphic interlayers as well as by the buoyant migration associated with mud diapirism. The similar structural correlation could be also observed from the terrestrial setting where mud volcanoes in southwestern Taiwan are well aligned along NNE-SSW trending faults [*Chao et al.*, 2013]. These faults provide a fluid channel through which unconsolidated sediments with gases and fluids generated from water-rock interactions could ascend to surface environments. Although methane flux and structural feature are qualitatively correlated to a certain degree, most profiles of chloride did not indicate substantial influence of fluid advection in shallow sediments. It is likely that rapid fluid migration only proceeded at restricted spots where structural features are directly exposed on seabed or extended to very shallow depth intervals. For the majority of investigated area, methane transport in shallow sediments in still dominated by diffusion.

3.4.2 Methane origins

Our results, compiled with previous studies [*Chuang et al.*, 2010; *Sun et al.*, 2010], revealed that most methane from the passive margin and the lower slope of the

doi:10.6342/NTU202000506

active margin was microbial in origin (Fig. 3.5). The $\delta^{13}C\text{-}CH_4$ values became greater with increasing landward distance from the passive margin, suggesting greater inputs of thermogenic gas at the active margin and onshore mud volcanoes.

Seeps and mud volcanoes at the upper slope and onshore are associated with mud diapirism and faults, respectively [*Lin et al.*, 2009 and 2013]. The increasing contribution of thermogenic methane to the observed geochemical signatures suggests that the permeability of fluid channels at the upper slope and onshore is great. Therefore, thermogenic hydrocarbons formed through sediment burial at depth could transport transiently within the fluid channel with relatively limited incorporation of microbial methane formed at shallow depth. In contrast, microbial contribution to the overall methane inventory increases dramatically at the lower slope and passive margin. The transport of deeply sourced thermogenic methane could be impeded with either the overlying thick, fine-grained sediments, or low connectivity and permeability of fluid channels. As such, thermogenic methane could be trapped within the strata, thereby allowing the detection of the predominance of microbial methane formed at shallow depth. The abundance ratios and isotopic compositions, however, did not enable us to infer the possible depth range for the generation of microbial methane, even though the available deepest sample was considered. This is because

doi:10.6342/NTU202000506

any microbial methane produced could have ascended either with deeply sourced fluids over a long distance, or through diffusion within the local depth range.

The δ^2H and $\delta^{13}C$ values of methane from site GT39B located at FLR (submarine diapir), Gutingkeng Mudstone zone (terrestrial area), and Chishan Fault (terrestrial area) suggest that methane was predominantly produced by thermal maturation (Fig. 3.5b). However, the C_1/C_{2+} ratios were higher than 1,000 (Fig. 3.5a), a characteristic typical of microbial methane. Such contradictory inferences for a gas origin have also been observed in some seeps and mud volcanoes in Azerbaijan, Japan, and Italy where an inverse correlation between C_1/C_{2+} ratio and gas flux has been identified [*Etiope et al.*, 2007 and 2009]. For these examples, the abundance ratios were higher than 1,000 before mud eruption (with low flux), and decreased gradually thereafter (with high flux). The temporal variations in abundance ratio or isotopic composition suggest that both fluid residence time and magnitude of isotopic fractionation might play a role in controlling the observed geochemical signatures. With a longer gas-water-mud interaction time and a smaller isotopic fractionation associated with methanogenesis, *in situ* microbial processes could produce methane and significantly enhance the C_1/C_{2+} ratio while maintaining low $\delta^{13}C$ values. A small isotopic fractionation has been observed for acetoclastic methanogenesis in sediments

doi:10.6342/NTU202000506

collected from the Gutingkeng Mudstone zone [*Ling et al.*, 2012], partially supporting the assertion described above.

3.4.3 Biofiltration efficiency of AOM

To investigate the efficiency of microbial filtration of methane, sites with flux estimates from two interfaces (the SMTZ and sediment-seawater interface; 61 sites) were chosen (Appendix, Table A3.1). The biofiltration efficiency (BE) of AOM was calculated as the following equation:

$$BE = \frac{\text{fluxes across SMTZ}}{\text{fluxes across SMTZ + effluxes}} \times 100\% \quad (3.9)$$

Since the penetration depth of dissolved oxygen is commonly less than 1 cm [*Sommer* et al., 2010; *Boetius and Wenzhöfer*, 2013], the oxygen availability for aerobic oxidation of methane (AeOM) would be greatly limited. Therefore, the methane sink catalyzed by AeOM was assumed to be negligible. Of all investigated sites (included previous studies), 51 had positive effluxes, indicating that methane escaped from sediments to overlying seawater. Although the negative fluxes could also originate from the net benthic consumption through AeOM, additional measurements of benthic fluxes for methane and oxygen would be needed to prove this assertion. These

doi:10.6342/NTU202000506

negative fluxes were excluded from further discussion. The BE values for the majority of sites were greater than 50% (Appendix, Table A3.1), suggesting that AOM plays an important role in regulating the quantity of methane exported to seawater. The effectiveness of AOM is also supported by the elevated DIC concentrations (Appendix, Fig. A3.2), the percentage of sulfate consumed by AOM (Appendix, Table A3.3), and abundant anaerobic methanotrophs at the SMTZ [*Lin et al.*, 2014]. The exceptions (less effective AOM) were sites located proximal to cold seeps or with shallower SMTZ (<50 cmbsf; including cold seep G96, YAR, GWR, and area between YAR and GWR).

The BE values for offshore sediments appear to be comparable with the terrestrial counterpart. Reactive transport modeling for geochemical profiles obtained from the Shing-yang-nyu-hu MV in southwestern Taiwan indicated that sulfate-dependent AOM processes in the mud platform surrounding the bubbling pool could account for the removal of 60% of deeply sourced methane [*Cheng et al.*, 2012]. Such efficiency could have decreased to an even lower level for the mud pool, considering that fluid advection is substantial and sulfate is less abundant (14 – 249 μM in the pool versus ~4 mM in the top sediments) [*Cheng et al.*, 2012]. Overall, biological filtration of methane mediated by anaerobic methanotrophy is generally

doi:10.6342/NTU202000506

effective in sediments offshore and onshore southwestern Taiwan. However, their magnitudes in terrestrial settings might vary by a considerable magnitude, particularly at sites where fluid advection is significant.

The variation in BE value for sediments offshore southwestern Taiwan (21–100%) has also been observed in other marine methane-rich sediments (Appendix, Table A3.1 and A3.6) [*Boetius and Wenzhöfer*, 2013]. Sites right above cold seeps and submarine mud volcanoes are generally interpreted to be controlled by the velocity of fluid flow. Previous field observations and modeling results indicate that rapid advection would enable the advancement of oxidant-deprived fluids to very shallow depths, thereby greatly restraining the penetration of seawater sulfate and the activity of sulfate dependent anaerobic methanotrophy [*Niemann et al.*, 2006; *Wallmann et al.*, 2006b; *Felden et al.*, 2010]. As a consequence, the net flux of methane released into the seawater column would be enhanced at seeps with high advection rates [*Treude et al.*, 2003; *Haese et al.*, 2003; *Wallmann et al.*, 2006b]. Alternatively, mud volcanism and associated temperature fluctuations have been considered to inhibit benthic methane consumption [*Feseker et al.*, 2014]. In this study, the BE values for six sites proximal to cold seeps and mud diapirs were less than 50%. Although the corresponding chloride profiles do not indicate rapid fluid

doi:10.6342/NTU202000506

advection (Appendix, Fig. A3.6), the relationships between the lower BE values and seepage/mud diapirism might still suggest partial control of fluid regime on the efficiency of microbially mediated methane removal.

3.4.4 Fate of methane in Taiwan accretionary prism: from source to sink

Three categories, including efflux, sink and source of methane, were provided in Table 3.2 with each composed of the contributions from individual compartments or processes. Such an assessment allows us to examine the overall methane budget in a region where methane cycling and transport are highly tectonically controlled.

Considering the area sizes, the mean area-based methane effluxes were calculated to be ~52 Mg yr^{-1} with the majority contributed by normal sites (46 Mg yr^{-1}; Table 3.2). The area-based methane effluxes from all onshore mud volcanoes in southwestern Taiwan were summed to be 130 Mg yr^{-1} [*Hong et al.,* 2013a]. Considering the small area coverage, onshore mud volcanoes contribute disproportionately greater to methane discharge than their marine counterparts.

The primary sink considered was the methane consumptions mediated by AOM processes. To calculate the total AOM consumption, AOM rates for the hot sites and normal sites were multiplied by the area coverage to yield the area-based methane

doi:10.6342/NTU202000506

sink rates, ranging from 1.82 –5.57 Mg yr^{-1} and from 186 – 5970 Mg yr^{-1} for the hot and normal sites, respectively. Although most coring operations targeted sites with high methane ebullition and higher AOM rates, the overall area-based methane sink is apparently skewed by the area size. The normal sites outcompeted the hot sites in methane removal by orders of magnitude. Methane consumptions of AOM and AeOM from terrestrial mud volcanoes were 9.48×10^{-3} and 6.17×10^{-3} Mg yr^{-1}, respectively [*Cheng et al.*, 2012]. The summed area-based methane consumption for onshore mud volcanoes were two orders of magnitude further lower than the offshore hot sites. Their impacts to the overall methane cycling and budget could be marginally ignored.

Major methane sources include microbial methane production in the near seafloor and deep sediments, and thermal decomposition of organic matter during subduction. For near-seafloor marine sediments, the methane production rates (CR (CO_2 reduction) + ME (methanogenesis)) estimated by the results of box model and a previous study ranged from $0.56 – 14.1 \times 10^{-2}$ mmol m^{-2} d^{-1} [*Chuang et al.*, 2013]. The area-based rates were calculated to be 385 – 9,700 Mg yr^{-1} (Table 3.2). The methane production rate from onshore near surface sediments (0.36 mmol m^{-2} d^{-1}) was larger than that in marine counterparts [*Cheng et al.*, 2012]. However, the small

doi:10.6342/NTU202000506

area renders the contribution of near surface methanogenesis negligible (0.01 Mg yr^{-1}).

doi:10.6342/NTU202000506

Table 3.2. Assessment of sources, sinks, and effluxes in offshore and onshore southwestern Taiwan.

	Flux/rate (mmol m^{-2} d^{-1})	Area (km^2)	Area-based fluxes (Mg yr^{-1})	Area-based fluxes (Tg Myr^{-1})	# of sites/ features	References
Effluxes						
Efflux from onshore mud volcanoes	1×10^{-1} to 1×10^{4}	0.0089	130	130		*Yang et al.* [2004]; *Hong et al.* [2013a]
Efflux from sediment to seawater (normal sites)	1.78×10^{-6} to 8.92×10^{-3}	11777	0.12 – 613 (46*)	0.12 – 613 (46*)	225	This study; *Chuang et al.* [2013]
Efflux from sediment to seawater (hot sites)	1.05×10^{-2} to 3.97	2.86	0.18 – 69.6 (6.23*)	0.18 – 69.6 (6.23*)	26	This study
Total			130 – 813	130 – 813		
Sinks						
Methanotrophy (onshore mud volcanoes)	0.03	0.0089	0.016	0.016	1	*Cheng et al.* [2012]
AOM (offshore normal sites)	0.27 to 8.68×10^{-2}	11777	186 – 5,970 (2,050*)	186 – 5,970 (2,050*)	67	This study; *Chuang et al.* [2010]; *Lin et al.* [2014]
AOM (offshore hot sites)	1.04 to 3.18×10^{-1}	2.86	1.82 – 5.57 (4.01*)	1.82 – 5.57 (4.01*)	7	This study; *Chuang et al.* [2010]
Total			188 – 5,976 (2,054*)	188 – 5,976 (2,054*)		
Sources						
Shallow methanogenesis (onshore)	36×10^{-2}	0.0089	0.01	0.01	1	*Cheng et al.* [2012]
Shallow methanogenesis (offshore)	0.56 to 14.1×10^{-2}	11,780	385 – 9,700	385 – 9,700	18	This study; *Chuang et al.* [2013]
Deep methanogenesis (through acetoclatic methanogenesis)	0.12 to 23.8×10^{-2}	20,260	374 – 21,117	374 – 21,117		This study; *Ling et al.* [2012]; *Sun et al.* [2008, 2010]
Deep methanogenesis (through CO_2 reduction)		20,260	106 – 6,941	106 – 6,941		This study; *Sun et al.*, [2008, 2010]
Deep thermogenic methane	1.58 to 24.8×10^{-2}	20,260	1,406 – 21,979	1,406 – 21,979		This study
Total			1,512 – 43,096	1,512 – 43,096		

*mean values.

doi:10.6342/NTU202000506

Our model calculation (Eq. 3.5) suggests that deep microbial methanogenesis could contribute 7–49% of the overall methane production. With the estimates of 1,406–21,979 Tg Myr^{-1} of thermogenic methane produced during the sediment subduction, deep microbial methanogenesis was calculated to produce methane at an area-based rate of 106–21,117 Tg Myr^{-1}, depending on the fractionation factors used for individual pathways (Table 3.2).

The overall methane fluxes estimated for individual categories revealed an imbalanced budget with the deep methane production rates potentially exceeding the sum of methane consumption rates and effluxes by orders of magnitude. Since such estimates were based on specific assumptions or data coverage, several considerations are provided below to assess the accuracy and validity of individual fluxes, and to provide additional consideration that remains to be addressed in future investigation.

Of all individual fluxes, those related to offshore shallow methanogenesis and methane consumption were calculated on the basis of the box model involving reactions related to methane, organic and inorganic carbon, and sulfate transformation. For most sites investigated, the calculated AOM rates were comparable with those derived from the concentration gradient, suggesting that the reactions considered for the box model were sufficient, and that the rate estimates were constrained properly. The results from

doi:10.6342/NTU202000506

the box model also suggest that shallow microbial methanogenesis was mostly offset by AOM within the SMTZ zone (within an order of magnitude; see Table 3.2 for the exact quantity). The calculation based on the box model described above was primarily applied to the hot sites near seeps or mud volcanoes. For the normal sites, the rates between methane production and consumption could be offset to an even greater degree, leading to a smaller methane leakage. In this way, extrapolation to the whole investigated offshore area is considered valid, even though the lack of complete datasets renders the estimate of shallow microbial methane production for all sites impossible.

The nearly equal rates between methane production and consumption for shallow offshore sediments leave the potentially imbalanced methane budget controlled by deep microbial methanogenesis and thermal maturation. The major uncertainties associated with the estimates for deep microbial methaonogenesis stemmed from the pathways and fractionation factors chosen for deep subsurface environments. A previous study has demonstrated that methanogens utilizing H_2/CO_2, acetate, and methyl compounds are all viable in hot muddy sediments emanating from a terrestrial mud volcano [*Ling et al.*, 2012]. Molecular analyses yielded the predominance of *Methanosaeta thermophilia* over the others in the archaeal community. The fractionation factors for *M. thermophilia* have been experimentally determined to be less than 10‰ [*Valentine et al.*, 2004].

doi:10.6342/NTU202000506

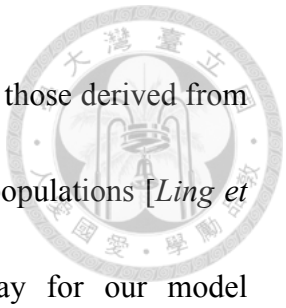

These fractionation factors based on pure strain are comparable with those derived from incubations amended with acetate at high temperatures for natural populations [*Ling et al.*, 2012]. The designation of a specific methanogenic pathway for our model calculation could be complicated by the small fractionation factor (<10‰) associated with hydrogenotrophic methanogens (strain 121) under extremely high pressure (>40 MPa) and temperature (>110^{o}C) [*Takai et al.,* 2008]. With decreasing pressures and temperatures imposed, the fractionation factors would resemble those commonly observed for hydrogenotrophic methanogens. *Head et al.* [2003] and *Jones et al.* [2008] argued that methanogesis in petroleum system proceeds with syntrophic partnerships between the fermentation of complex organic matters and hydrogenotrohpic/acetoclastic methane production at ≤80^{o}C (equivalent to ~3 km depth or 30 MPa hydrostatic pressure, assuming a geothermal gradient of 25 ^{o}C/km and a surface temperature of 25 ^{o}C). Therefore, it is likely that methanogens residing at great depths catalyze methane production with the isotopic fractionation at a magnitude across a wide range, which has been observed in a 2.5 km deep borehole offshore Japan [*Inagaki et al.*, 2015]. The current data did not allow us to attribute a specific fractionation factor or pathway to obtain a more precise estimate.

The uncertainties for estimates of thermogenic methane production through

doi:10.6342/NTU202000506

sediment subduction stem from two main factors: the sediment thickness above the subducted plate, and hydrocarbon potential (*PP* value). Because the South China Sea is a small marginal sea, sediment accumulation would be strongly affected by sediment discharge from the nearby Eurasian plate and islands, thereby resulting in variable sediment thicknesses in the leading Eurasian plate during the pre-subduction phase [*Lin et al.*, 2008]. In addition, the hydrocarbon potential could be dependent on sediment reactivity, which is intrinsically related to its source properties and transport pathways. Low TOC contents have been commonly observed for sediments offshore southwestern Taiwan (<0.7% in wt) [*Hsu et al.*, 2014; *Su*, 2015]. This range of TOC is much lower than that for sediments in other marginal basins where hydrocarbons or hydrates are abundant (e.g. >2% in the Black Sea and Ulleung Basin), and might reflect the possibility that rapid uplift, short-term soil development, strong chemical weathering and physical erosion, and multiple cycling events associated with Taiwan's tectonic configuration could have led to the reduced contents and enhanced recalcitrance of organic matter. Whether the exact hydrocarbon potential is the same as that cited in the literature remains to be determined.

The summed area-based rates of deep methane production by microbial methanogenesis and thermal maturation ranged between 1,512 and 43,096 Tg Myr^{-1}. If

doi:10.6342/NTU202000506

the rates for shallow methanogenesis are assumed to offset those for AOM completely, the deep methane production rates exceed the summed effluxes of 130–813 Tg Myr^{-1} by various degrees, regardless of which microbial scenarios are considered. The imbalance between deep methane production and efflux might be best accounted for by the presence of huge volume of gas hydrates stored in the current sediments. Using the depth and distribution of the bottom reflection simulator and temperature-pressure stability condition of methane hydrate, the potential amount of gas hydrate was estimated to be 1,269 km^3 or between 537 and 631 Tg in the active margin [*Chung et al.*, 2016]. Similarly, hydrocarbon gases absorbed on surface of clay minerals have been quantified to exceed the volume of free or dissolved gases in marine sediments [*Ertefai et al.*, 2010]. The capacity of clay minerals for absorbing methane is dependent on pressure imposed and *in situ* methanogenesis. Assuming an absorption capacity of 0.01 mmole of methane per kg of sediments [*Ertefai et al.*, 2010] and 1 km thickness of sediments, the overall quantity of methane absorbed in offshore and onshore subsurface could reach 8 Tg. An order of magnitude greater in absorption capacity and several kilometers of sediments would make the absorbed methane a significant untapped source. Nevertheless, gas hydrates and absorbed methane stored within the sediments could at least partially account for the budget imbalance described above.

doi:10.6342/NTU202000506

Finally, the timescale represented by the measured datasets or the model calculation was unavoidably small when compared to the long-term tectonic activity. The geological background and associated organic characteristics and microbial activities were assumed to be invariant over a million-year timescale. The incorporation of field measurements into a long-term budget estimate could be biased due to the undersampling limitation.

doi:10.6342/NTU202000506

3.5 Conclusions

We have presented a systematic and comprehensive approach to quantify methane fluxes in individual compartments of the Taiwan accretionary prism. Based on the data obtained in this and previous studies, the calculated diffusive fluxes across the SMTZ and effluxes spanned over four and six orders of magnitude, respectively. Such a wide range of fluxes was controlled by the distribution of structural features, with high values generally proximal to mud diaprism, thrusts, ridges and formation intersection. Abundance ratios combined with isotopic compositions further indicated the increasing contribution of thermogenic methane along a transect from the lower slope, to the upper slope and onshore mud volcanoes. It is likely that the permeability of fluid channeling determines the quantity of microbial methane incorporated from shallow depth. The flux calculation also indicated that biological filtration, catalyzed by AOM processes, is effective in removing >50% of methane reaching the shallow depth at most offshore and onshore investigated sites, leaving a small fraction of methane leaked into the seawater or atmosphere. The exceptions are sites located near mud diapirs or cold seeps, where high fluid flow and/or temperature fluctuation associated with mud volcanism could have inhibited microbial methane consumptions to a great degree. The calculation based on the box model not only independently validated the diffusive fluxes derived from the

doi:10.6342/NTU202000506

concentration gradient, but also indicated that the rates of methanogenesis and AOM at shallow depths were nearly balanced, a phenomenon comparable with that observed in other marginal seas. The methane fluxes at shallow depth are, however, imbalanced from those at great depth. The mass balance based on the observed isotopic compositions for field samples and incubation experiments, and the scenario configuration, projected that microbial methane could contribute 7–49% of the total methane inventory at great depth. With the wedge geometry of subduction and sediment property inferred from pre-existing data, the rates of methane production through combined microbial methanogenesis and thermal maturation was estimated to be 1,512–43,096 Tg Myr^{-1}. As the effluxes were much less than the fluxes of the deep source, the methane generated at depth has to be sequestered into hydrate forms or clay minerals. The exact quantities of these two untapped components remain to be validated through other independent methods. The quantitative framework constrained by multiple methodologies highlights the possible decoupling of a deep production source from shallow methane cycles and the factors that would enable better assessments on the regional methane budget in the future.

doi:10.6342/NTU202000506

Chapter 4 Pattern of dissolved organic carbon in a marine mud volcano offshore southwestern Taiwan

4.1 Introduction

Organic matter stored in marine sediments has been estimated to amount up to 7.8×10^7 Gt C [*Mackenzie et al.*, 2004], constituting the most important organic reservoir involved in global carbon cycle [*Hedges and Keil*, 1995]. Despite its sources from terrestrial detritus and marine primary producers, the burial of organic matter beneath seafloor proceeds with a series of remineralization pathways accompanied with the production and consumption of dissolved organic carbon (DOC). While DOC is generally more degradable than recalcitrant particulate organic carbon, the benthic export of DOC into deep ocean would exert profound effects on marine DOC budget, nutrient cycling and even structure of food web [*Haas et al.*, 2011; *Pohlman et al.*, 2010; *Eickenbusch et al.*, 2019].

The proximity to terrestrial and nutrient sources renders continental margin the locus of organic remineralization. Previous estimates suggest that about 60 to 80% of total organic carbon (TOC) pool is converted to dissolved inorganic carbon (DIC) and high molecular-weight organic complex through microbial respiration and fermentation

doi:10.6342/NTU202000506

[*Kandasamy and Nagender Nath*, 2016]. Such degradation processes cascade to the stepwise production of low-molecular-weight DOC (such as amino acids and monosaccharides) and further downstream short-chain organic acids and alcohols (such as volatiles fatty acids (VFAs) and methanol) [*Burdige et al.*, 2016; *Heuer et al.*, 2010; *Komoda et al.*, 2013; *Zhang et al.*, 2019]. These intermediate products are energetic, thereby serving the ideal electron donors for different terminal electron accepting processes. Based on the concentration profiles and incubation experiments, acetate has been identified to serve as an important substrate for manganese or iron reduction [*Burdige*, 1993], sulfate reduction [*Glombitza et al.*, 2015], methanogenesis [*Parkes et al.*, 2007; *Heuer et al.*, 2009], or denitrification [*Amend and Shock*, 2001; *Thauer et al.*, 1989; *Yoon et al.*, 2013] in shallow marine sediments. Furthermore, a fraction of VFAs (particularly acetate) could be also directly assimilated into biomass [*Heuer et al.*, 2009; *Morono et al.*, 2011; *Na et al.*, 2015], contributing to the pool of particulate organic carbon. The nature of rapid turnover enables the limited accumulation of these intermediate, energetic substrates in most marine sediments. For example, pore water acetate in marine sediments typically occurs in the micromolar range [*Sørensen et al.*, 1981; *Finke et al.*, 2007; *Valdemarsen and Kristensen*, 2010]. Therefore, although these molecules bear great implication for subseafloor microbial processes, their distribution

doi:10.6342/NTU202000506

pattern remains rarely explored.

Submarine mud volcanoes (SMVs) and seeps represent the seafloor expression of conduits tapping deep fluid reservoirs where thermally or microbially activated cracking of organic matters at high temperatures often lead to the production of high quantity of DOC. Few studies have demonstrated that the concentrations of specific DOC compounds could range up to the millimolar range [e.g. *Egeberg and Barth*, 1998; *Nuzzo et al.*, 2008]. Although such high concentrations are confined in a narrow depth range, the strong contrast from background seawater concentrations (few μM or less) could have sustained a high flux exported to the deep seawater. Recent studies indicated that the DOC benthic fluxes from cold seeps and mud volcanoes in offshore southwestern Taiwan (28 to 1264 μmol m^{-2} d^{-1}) is several times higher than most DOC fluxes in coastal and continental margin sediments, and its integrated benthic flux is approximately 24% of the annual DOC flux (36×10^6 mol yr^{-1}) from the Pearl River [*Hung et al.*, 2016]. If the estimates based on observations of few mud volcanoes are valid across the basin, the contribution of DOC from mud volcanoes and seeps would constitute a significant proportion of marine DOC pool and shape the biogeochemical network and ecosystem in benthic environments. As the DOC pool represents a mixture of various individual compounds, it remains unclear regarding whether the fluxes of

doi:10.6342/NTU202000506

specific substrates are comparable with the bulk DOC pattern.

This study aims to uncover the distribution pattern of DOC and small organic acids for sediments in a submarine mud volcano, TY1, offshore southwestern Taiwan. The TY1 was chosen because fluids and gases exported to the seawater column originated from a source depth estimated to be 3 to 5 km below seafloor (kmbsf) [*Chen et al.*, 2020], providing ideal materials to address how microbial cycling of organic carbon at shallow depths interacts with the impact of deep fluids. Bulk DOC and various organic acids (acetate, formate, propionate, butyrate, and lactate) are specifically targeted for analyses to compliment the other aqueous and gas geochemistry obtained in the previous study. These results were further integrated into a reactive transport modeling framework to constrain specific microbial activities and the effects of individual dissimilative and assimilative metabolisms on the pattern of bulk DOC. This study represents the first study to quantify the distribution of small organic acids in mud volcanoes in the region.

doi:10.6342/NTU202000506

4.2 Materials and methods

4.2.1 Geological settings and sampling sites

Offshore southwestern Taiwan is at the frontal area of the accretionary wedge generated during the subduction–collision between the Luzon Arc and the Eurasian passive continental margin [e.g. *Teng*, 1990]. The boundary between the passive and active margins is defined by the deformation front, which is a northward extension of the Manila trench. The active margin is further divided by the out-of-sequence thrust into the Upper Slope and Lower Slope domains [e.g. *Lin et al.*, 2009; *Lin et al.*, 2014]. Through the seismic reflection profiles and remote operated vehicle (ROV) survey, a total of 13 submarine mud volcanoes (SMVs) have been identified at the Upper Slope domain of offshore southwestern Taiwan (Fig. 4.1a) [*Chen et al.*, 2014a]. Two mud volcanoes fed by one mud diapir constitute the Tsangyao Mud Volcano Group (TYMV; re-named after MV12) [*Chen et al.*, 2017], which has been found the largest SMV offshore southwestern Taiwan. One of the mud volcanoes, TY1, has a conical structure and a wide flat top with a diameter of ~500 m at a water depth of ~370 m (Figs. 1b and 1c) [*Chen et al.*, 2014a]. Two major gas plumes, one at the west and the other at the south, were detected on the crest by a multibeam echo sounder. These gas plumes reached to a height of up to 367 m above the seafloor [*Chen et al.*, 2014b]. The

doi:10.6342/NTU202000506

expedition was conducted in the offshore southwestern Taiwan by R/V Ocean Researcher I (leg 1118). Piston cores with lengths ranging from 260 to 450 cm were recovered along a transect from the center to the margin of the TY1 cone structure (Fig. 4.1c). Sampling sites are listed in Table 4.1 and shown in Figs. 4.1b and 4.1c.

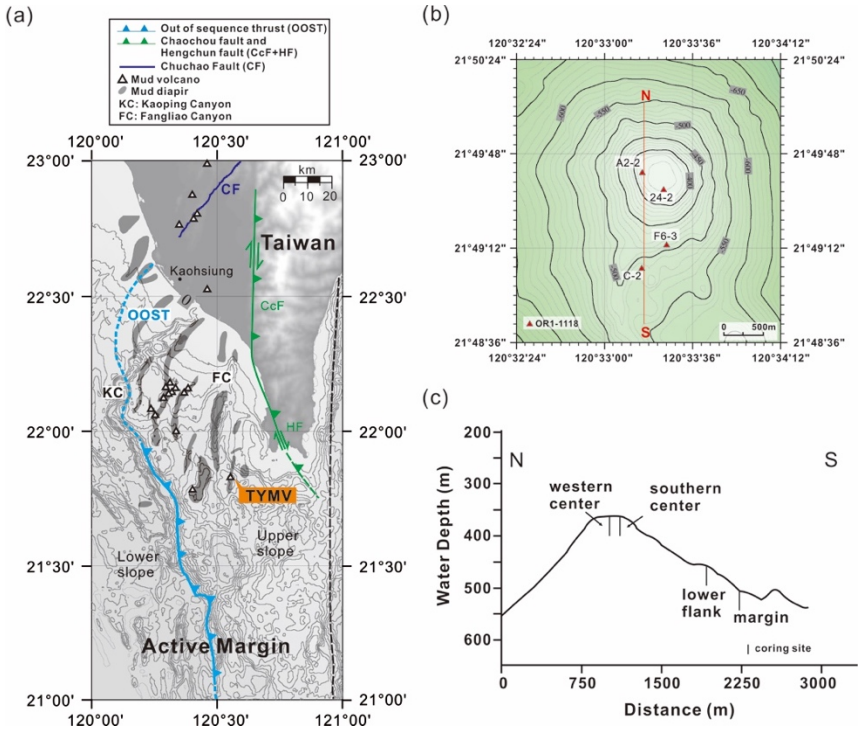

Figure 4.1. Coring sites in this study. The map was created by the open source GMT software [*Wessel and Smith*, 1998] using the NOAA public database [*Amante and Eakins*, 2009]. The right boundary of the upper slope is defined by *Lin et al.* [2009].

Table 4.1. Information of coring sites.

cruise	site	longitude	latitude	location
OR1-1118	A2-2	120° 33.48'	21° 49.63'	western center
	24-2	120° 33.28'	21° 49.66'	southern center
	F6-3	120° 33.34'	21° 49.24'	lower flank
	C-2	120° 33.27'	21° 49.07'	margin

doi:10.6342/NTU202000506

4.2.2 Sampling and analytical methods

Pore fluid samples for aqueous geochemistry were obtained through centrifugation and subsequently collected through the filtration using polypropylene rubber-free syringes and disposable 0.2-μm Supor membranes. The filtrate was split into six fractions for the analyses of anion, cation, total alkalinity (TA), carbon isotopic compositions of dissolved inorganic carbon (DIC), and oxygen and hydrogen isotopic composition of water, and DOC. The filtrates for DOC and VFAs analyses were collected in pre-combusted 2-ml glass vials with Teflon-coated screw caps and kept frozen at –20 ^{o}C until analyses. Prior to sample collection, all glass vials were soaked in 10% HNO_3 for 3 days, rinsed with Milli-Q water, and then combusted at 550 ^{o}C for 4 hrs. For cation samples, concentrated nitric acid (70%) was added at a volume ratio of 1:45 to preserve the valence state for elements sensitive to the redox change.

Dissolved manganese was analyzed by an inductively coupled plasma optical emission spectrometry (ICP-OES). Bromide and ammonium were measured by an ion chromatography (IC, 882 Compact IC Plus) [*Chen et al.*, 2020; *Hu et al.*, 2017]. The concentrations of DOC were determined by the Shimadzu-TOC-L carbon analyzer (Shimadzu Corp., Kyoto, Japan) equipped with a non-dispersive infrared detector and auto-sampler. Samples were manually diluted by 10 to 30 fold, acidified with HCl, and

doi:10.6342/NTU202000506

purged using helium stream prior to the injection into the analyzer. Five standards were prepared from the Consensus Reference Material material, CRM (purchased from Hansell Lab, Miami, USA) with an uncertainty smaller than 5%. The analyses of VFAs were determined by an Agilent HPLC system, model 1260 Infinity LC (Agilent Technologies, Santa Clara, CA, USA) equipped with a quaternary solvent pump, degasser, thermostatted column compartment, auto-sampler, and a diode array detector (DAD). An ion exchange column (Agilent Hi-Plex H, 8 μm, 300 × 7.7 mm) coupled to a guard column (PL Hi-Plex H, 50 × 7.7 mm) was used to separate VFAs (targets including lactate, formate, acetate, propionate, and butyrate) at a flow rate of 0.6 mL min^{-1} of eluent 4.0 mM H_2SO_4 with a column temperature maintained at 65 °C. Five standards were prepared from 10 mM stocks of individual target compounds at a purity of ≥98%. Standard solutions (5 and 10 μM) were injected after every 5 analyses in order to monitor the drift of the retention time and signal intensity. The instrument detection limit was 1.5 μM based on the multiple injection (n=7) of 5 μM standard solution (n=7) and using *Student's* t value.

doi:10.6342/NTU202000506

4.2.3 Reactive transport modelling

4.2.3.1 Reactions for modeling

Previous study has established a framework to model the rates of fluid advection and various metabolisms, and the impact of deep fluid on shaping the concentration profiles for chloride, sulfate, and methane [*Chen et al.*, 2020]. In brief, the concentration profiles of chloride (which is inert to biological and most abiotic reactions) constrain that the deep fluid (from 5 km below seafloor) migrates upward at a rate of 2 cm yr^{-1}, reducing the extent of downward migration of solutes contributed from overlying seawater. Such an impact of deep fluids on shallow porewater chemistry decreases with the increasing distance from the center or crater of the TY1, enabling higher *in-situ* rates of organoclastic sulfate reduction (OSR), anaerobic oxidation of methane (AOM), and methanogenesis (ME), and a higher biological filtration efficiency of methane at the rim of the TY1. Therefore, the modeling carried out in this study was amended to these previous works with the additional consideration of DOC metabolisms. The reaction framework firstly incorporated the degradation of particulate organic matter (POC degradation) for the production of DOC. As POC was degraded, denitrification and the release of bromide occur concurrently [*Burdige et al.*, 2016; *Wallmann et al.*, 2006a; *Wei et al.*, 2008]. Seven species in porewater — bromide, ammonium, total alkalinity

doi:10.6342/NTU202000506

(TA), DOC, magnesium, and calcium—were used in the modeling.

4.2.3.2 The construction of reactive transport modeling

Site A2-2 was chosen for numerical modeling because the upward fluid flow was significant so that the impact of deep sourced DOC could be observed and quantified. A simplified one-dimensional reactive transport modeling was applied to porewater geochemistry profiles with a revised code [*Chen et al.*, 2020; *Hong et al.*, 2017]. The basic construction of the modeling has been described in Chapter 2, Eq. (2.1) to (2.4).

Except for DOC, the compositions of porewater from the surface and bottom of core were used as the upper and lower boundaries, respectively. Because labile DOC was degraded easily, the measured DOC could represent the residual one. The ammonium concentrations from the surface and bottom of core were multiplied with the C/N_s ratio (TOC/TN in sediment; Su, 2015) to set the upper and lower boundaries of DOC. The depth and time grids (dx= 0.01 m and dt= 0.01 year for all sites) were determined by running the model with progressively smaller discretization until the results were numerically stable and accurate. The model was executed to reach a steady state (within 1000 years simulation time) with initial conditions set as seawater composition.

doi:10.6342/NTU202000506

The mineralization reactions proceed with the degradation of POC for the production of DOC. Such a process coexists with the release of bromide and ammonium and fuels downstream OSR and ME. The reactions involved in the POC degradation and other biogeochemical processes were listed below:

OSR:

$$(CH_2O)(NH_3)_{\frac{N_S}{C}}(Br)_{r_{Br}} + \frac{1}{2}\cdot SO_4^{2-} + \frac{1}{C/N_S}H^+ \rightarrow \frac{1}{2}H_2S + HCO_3^- + \frac{1}{C/N_S}\cdot NH_4^+ + r_{Br}\cdot Br^- \quad (4.1)$$

DOC-ME:

$$(CH_2O)(NH_3)_{\frac{N_S}{C}}(Br)_{r_{Br}} + \left(\frac{13}{5} - \frac{N_S}{2C}\right)H_2O \rightarrow \left(\frac{N_S}{2C} - \frac{3}{5}\right)CO_2 + \left(\frac{6}{5} - \frac{N_S}{2C}\right)CH_4 + \frac{2}{5}HCO_3^- + \frac{1}{C/N_S}\cdot NH_4^+ + r_{Br}\cdot Br^- \quad (4.2)$$

AOM:

$$CH_4 + SO_4^{2-} \rightarrow HCO_3^- + HS^- + H_2O \quad (4.3)$$

doi:10.6342/NTU202000506

Carbonate precipitation (CP):

$$Mg^{2+} + Ca^{2+} + 2HCO_3^- \rightarrow CaMg(CO_3)_2 + 2H^+ \quad (4.4)$$

Reaction laws for individual compounds were described in accordance with the Monod kinetics and stoichiometric relationships, and were shown below [Burdige et al., 2016; Vanneste et al., 2011; Wallmann et al., 2006]:

Production of DOC:

$$R_{DOC} = K_G \cdot C_{org} \cdot \Im \cdot \frac{K_C}{[DIC]+[CH_4]+K_C} \quad (4.5)$$

DIC pool:

$$\Sigma R_{DIC} = R_{OSR} + R_{AOM} - \left(\frac{N_s}{2C} - \frac{1}{5}\right) R_{ME} - R_{CP} \quad (4.6)$$

Bulk rate of methanogenesis:

$$R_{ME} = K_G \cdot C_{org} \cdot \Im \cdot \frac{K_C}{[DIC]+[CH_4]+K_C} \cdot \frac{K_iSO4}{K_iSO4+[SO_4^{2-}]} \quad (4.7)$$

doi:10.6342/NTU202000506

Bulk rate of sulfate reduction:

$$R_{OSR} = K_G \cdot C_{org} \cdot \Im \cdot \frac{K_C}{[DIC]+[CH_4]+K_C} \cdot \frac{[SO_4^{2-}]}{K_{half-SO4}+[SO_4^{2-}]} \quad (4.8)$$

Rate of anaerobic oxidation of methane:

$$R_{AOM} = R_{AOM}^{MAX} \cdot \frac{[SO_4^{2-}]}{K_{half-SO4}+[SO_4^{2-}]} \cdot \frac{[CH_4]}{K_{half-CH4}+[CH_4]} \quad (4.9)$$

Rate of carbonate precipitation:

$$R_{CP} = R_{CP}^{MAX} \cdot exp\left(-0.5 \cdot \frac{x_{cp}-x}{s_{cp}}\right) \quad (4.10)$$

Production of ammonium:

$$R_{NH4} = \frac{1}{C/N_s} \cdot R_{DOC} \quad (4.11)$$

Production of bromide:

$$R_{Br} = r_{Br} \cdot R_{DOC} \quad (4.12)$$

Where K_G represents the kinetic constant of organic matter degradation (assumed to be

doi:10.6342/NTU202000506

10^{-6} yr^{-1}) [*Hong et al.*, 2017; *Middleburg*, 1989; *Vanneste et al.*, 2011]; K_C denotes a Monod kinetic constant; $\Im$ is a parameter that converts carbon concentrations in unit of wt.% C to mM [*Burdige et al.*, 2016]; $K_{half\text{-}SO4}$ is the half-saturation constant for sulfate (0.5 mM) [*Middelburg*, 1989]; K_iSO_4 is the inhibition constant for the initiation of methanogenesis, and assumed to be the same as $K_{half\text{-}SO4}$ (0.5 mM); C_{org} is the total organic carbon (TOC) content and assumed to be 0.45 wt.%, considering that TOC varied between 0.3 and 0.5 wt.% (Chen et al., submitted); $K_{half\text{-}CH4}$ is the half-saturation constant for methane and assumed to be 5 mM [*Nauhaus et al.*, 2002; *Vavilin*, 2013; *Wegener and Boetius*, 2009]; $[CH_4]$ and $[SO_4^{2-}]$ are the concentrations of methane and sulfate in the porewater; R_{AOM}^{MAX} is the theoretical maximum AOM rate obtained by fitting the sulfate profile (set as 2 mM yr^{-1}); R_{CP} is a function of depth (x) and assumed to be a Gaussian function [*Burdige et al.*, 2016]; x_{cp} is the sediment depth of maximum R_{CP} and was assumed to be close to the depth of the SMTZ; s_{cp} is the parameter defining the width of the Gaussian function for the depth distribution of R_{CP}; R_{CP} was determined by fitting the Ca^{2+} and Mg^{2+} porewater data through varying R_{CP}^{MAX}, x_{cp} and s_{cp}; C/N_s is the TOC/TN ratio in TY1 sediment (average=5.68; Su, 2015); r_{Br} represents the Br/POC ratio in sediment offshore southwestern Taiwan (7.6 mg-Br/g-TOC) [*Kandasamy et al.*, 2018]. Details of the parameters used in the

doi:10.6342/NTU202000506

modeling and the parameters for best fittings are shown in Table 4.2. Modeling would be conducted in three cases. In case 1, only transportations (diffusion and advection) were considered. In case 2, all reactions were involved in modeling, but only diffusion were considered. In case 3, all reactions and transportations were considered.

doi:10.6342/NTU202000506

Table 4.2. Parameters and boundary conditions applied in numerical modeling.

parameter	symbol	unit	A2-2	reference
temperature		^{o}C	10.5	*Chen et al.* [2020]
diffusion coefficient of total alkalinity	DiTA	$m^2\ yr^{-1}$	0.0251	*Wallmann et al.* [2006]
diffusion coefficient of calsium	DiCa	$m^2\ yr^{-1}$	0.0173	*Boudreau* [1997]
diffusion coefficient of magnesium	DiMg	$m^2\ yr^{-1}$	0.0157	*Boudreau* [1997]
diffusion coefficient of DOC	DiDOC	$m^2\ yr^{-1}$	0.0051	*Komada et al.* [2013]
diffusion coefficient of bromide	DiBr	$m^2\ yr^{-1}$	0.0463	*Boudreau* [1997]
diffusion coefficient of ammonium	DiNH4	$m^2\ yr^{-1}$	0.0441	*Boudreau* [1997]
Length of model column		m	4.4	*Chen et al.* [2020]
porosity at sediment surface			0.50	*Chen et al.* [2020]
porosity at end of coulmn			0.41	*Chen et al.* [2020]
empirical coefficient for porosity fitting	γ	m^{-1}	2	*Chen et al.* [2020]
total organic carbon (TOC)	C-org	wt %	0.45	*Chen et al.* [2020]
rate constant of degradation of organic carbon	KG	yr^{-1}	10^{-6}	*Vanneste et al.* [2011]
velocity of upward fluid	u_0	$m\ yr^{-1}$	0.02	*Chen et al.* [2020]
depth of bubble irrigation	L_{irr}	m	2.8	*Chen et al.* [2020]
Irrigation coefficient (alpha0, yr -1)	α_0	yr^{-1}	0.55	*Chen et al.* [2020]
Irrigation coefficient (alpha1, cm)	α_1	m	0.1	*Chen et al.* [2020]
rate constant of AOM	K_{AOM}	$mM^{-1}\ yr^{-1}$	2	*Chen et al.* [2020]
half saturation constant of sulfate	K_{half}-SR		0.5	*Nauhaus et al.* [2002]; *Vavilin* [2013]; *Wegener and Boetius* [2009]
half saturation constant of methane	K_{half}-AOM		5	
Ca concentration at upper boundary	CaU	mM	9	
Ca concentration at lower boundary	CaL	mM	1	
Mg concentration at upper boundary	MgU	mM	49	
Mg concentration at lower boundary	MgL	mM	8	
TA concentration at upper boundary	TAU	mM	2.7	
TA concentration at lower boundary	TAL	mM	36	
DOC concentration at upper boundary	DOCU	mM	0.17*	
DOC concentration at lower boundary	DOCL	mM	2.23*	
Bromide concentration at upper boundary	BrU	mM	0.7	
Bromide concentration at lower boundary	BrL	mM	0.27	
Ammonium concentration at upper boundary	NH4U	mM	0.03	
Ammonium concentration at lower boundary	NH4L	mM	0.4	
ratio of TOC to TN in sediment	C/Ns		5.58	*Su* [2015]

Note: *: DOCU and DOCL were set by NH4U and NH4L times C/Ns ratio, respectively.

doi:10.6342/NTU202000506

4.2.4 Gibbs energy calculations

Gibbs energy of hydrogentrophic and acetoclastic methanogenesis (Eq. (4.13) and (4.14)), sulfate reduction (Eq. (4.15) and (4.16)), and acetogenic CO_2 reduction (Eq. (4.17) were calculated according to Eq. (4.18).

Hydrogentrophic methanogenesis (H_2-ME):

$$2H_2 + HCO_3^- + H^+ \rightarrow CH_4 + 3H_2O \quad (4.13)$$

Acetoclastic methanogenesis (AcME):

$$CH_3COO^- + H_2O + H^+ \rightarrow CH_4 + HCO_3^- \quad (4.14)$$

Acetoclastic sulfate reduction (AcSR):

$$CH_3COO^- + SO_4^{2-} + H^+ \rightarrow HS^- + 2HCO_3^- \quad (4.15)$$

formate-sulfate reduction (formate-SR):

$$4HCOO^- + SO_4^{2-} + H^+ \rightarrow HS^- + 4HCO_3^- \quad (4.16)$$

Acetogenic CO_2 reduction (AcCR):

$$2HCO_3^- + 4H_2 + H^+ \rightarrow CH_3COO^- + 4H_2O \quad (4.17)$$

doi:10.6342/NTU202000506

$$\Delta G_r = \Delta G_r^0 + RTln\frac{\Pi_i a_{(product)}{}^{v_i}}{\Pi_i a_{(reactant)}{}^{v_i}} \quad (4.18)$$

In Eq. (4.18), R (0.008314 kJ mol^{-1} K^{-1}) is the universal gas constant, T (in K) is the temperature, a denotes the activities of the reaction participants (reactants and products), and v is the stoichiometric coefficient of the i-th reactant or product. The activities were approximated by multiplying measured concentrations of the species by their activity coefficients. Activity coefficients were calculated from an extended version of the Debye-Hückel Extended equation [*Helgeson*, 1969]. Temperatures in sediments were calculated based on *in situ* bottom water temperature (10.5 ^{o}C) and a temperature gradient of 0.39 ^{o}C/m at TY1 [*Wu*, 2016]. pH values were close to 8. Density of porewater and the concentration of hydrogen were assumed to be 1.03 g/cm^3 and 2 nM, respectively. The numerical modeling results of concentrations of methane and hydrogen sulfide were used for calculation of Gibbs free energy [*Chen et al.*, 2020].

doi:10.6342/NTU202000506

4.3 Results

4.3.1 Variation of solutes profiles across TY1 submarine mud volcano

Profiles of solutes concentrations are shown in Fig. 4.2. The bromide concentrations ranged from 0.2 to 0.8 mM and generally followed the trend of chloride concentrations. Bromide decreased with depth below SMTZ at sites A2-2 and 24-2 while it stayed in constant at sites F6-3 and C-2. Ammonium concentrations varied in the range between 30 and 600 μM. Unlike the trend of bromide, ammonium increased with depths at sites A2-2 and 24-2. At sites F6-3 and C-2, ammonium concentrations were typically lower than 100 μM throughout the whole core except for values at depth 72 and 256 cmbsf. The concentration of dissolved manganese was lower than 9 μM and decreased with depth at all sites.

The concentration of DOC ranged from 100 to 1200 μM. At the western and southern center sites (sites A2-2 and 24-2), the DOC concentration varied in a zick-zack trend with a mean value of around 400 μM and slightly increased with depth. At the lower flank site (site F6-3), the DOC was enriched at above 130 cmbsf (up to 1000 μM) and decreased to around 250 μM at core bottom; at site C-2, DOC concentrations were almost at constant (around 200 μM). Of all analyzed VFAs, formate and acetate

doi:10.6342/NTU202000506

appear to be the most abundant (Fig. 4.2) with the ratios of acetate to DOC ranging from 2 to 8, from 4 to 8, from 2 to 4, and from 4 to 17% at sites A2-2, 24-2, F6-3, and C-2, respectively (Fig. 4.2). At sites A2-2 and 24-2, formate concentrations ranged from 3 to 30 μM and were higher than 13 μM at above 100 cmbsf and lower than 10 μM below that depth. At site F6-3 and C-2, the formate concentrations were nearly at constant (below 6 μM). Acetate concentrations were generally higher than formate and lactate and ranged from 3 to 55 μM. At site A2-2, acetate concentrations increased with depth. For comparison, no obvious trend with the exception of two peaks at 100 and 250 cmbsf was observed at site 24-2. At site F6-3, acetate concentrations varied between 10 and 20 μM. A peak at 42 uM was observed for the porewater at 220 cmbsf. At site C-2, acetate concentrations were around 20 μM and increased to 30 μM at 130 to 200 cmbsf. Propionate and butyrate were below the detection limit for all samples, whereas lactate up to 9 uM was sporadically detected for few samples (Fig. 4.2).

The ratios of DOC to ammonium were generally greater at shallower depths or above SMTZ and decreased to a lower level at great depth or below SMTZ (Fig. 4.2). However, the degrees of relative enrichment or depletion of DOC varied from site to site. At sites A2-2 and F6-3, the ratios for shallow enrichment ranged to be greater than 10. In contrast, the ratios were generally less than 3 throughout the depth at site

doi:10.6342/NTU202000506

24-2, and such ratios were between 3 to 6 at site C-2.

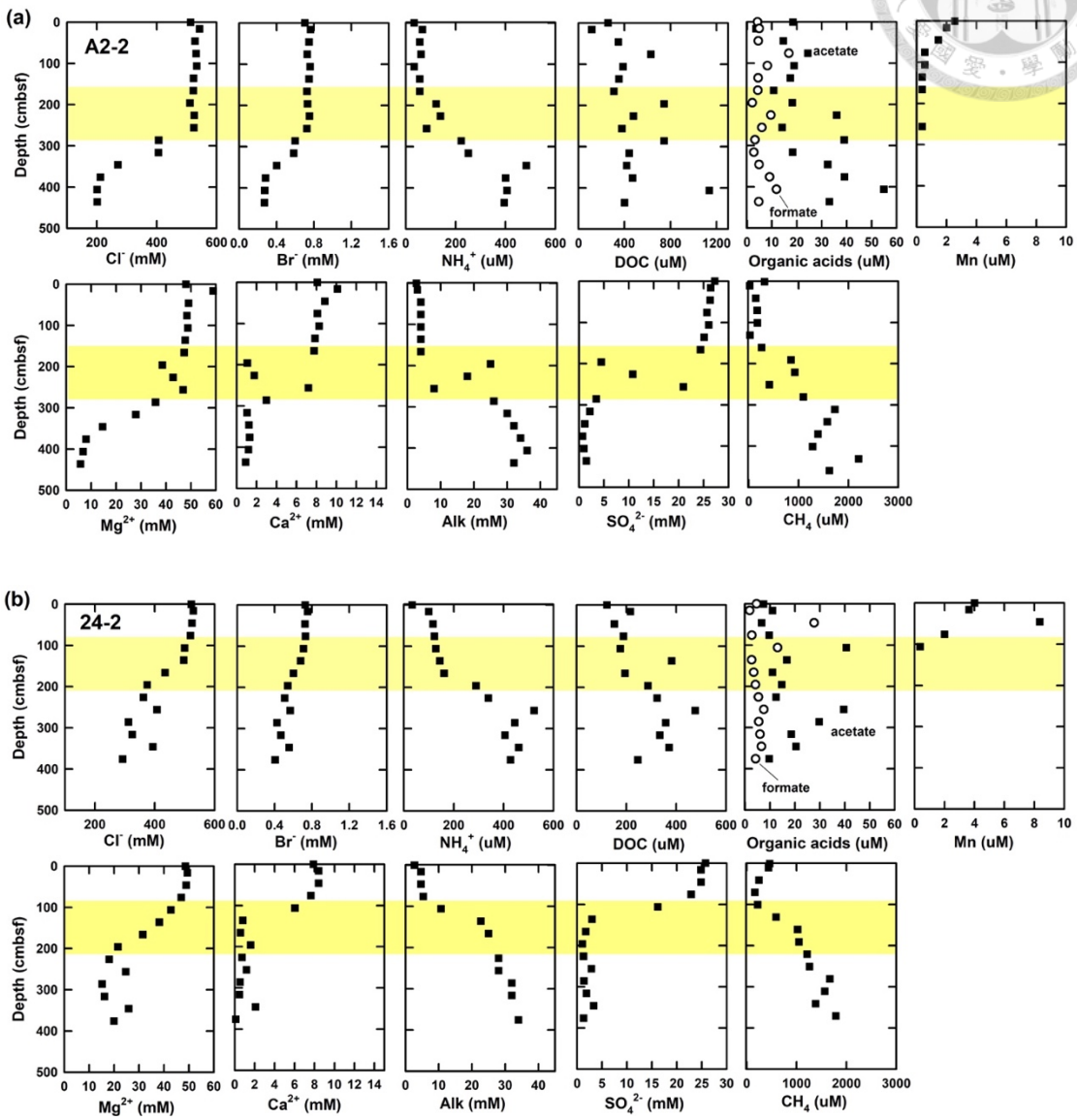

Figure 4.2. Geochemical profiles of sites A2-2, 24-2, F6-3, and C-2 at TY1. Shadow areas denote SMTZ.

doi:10.6342/NTU202000506

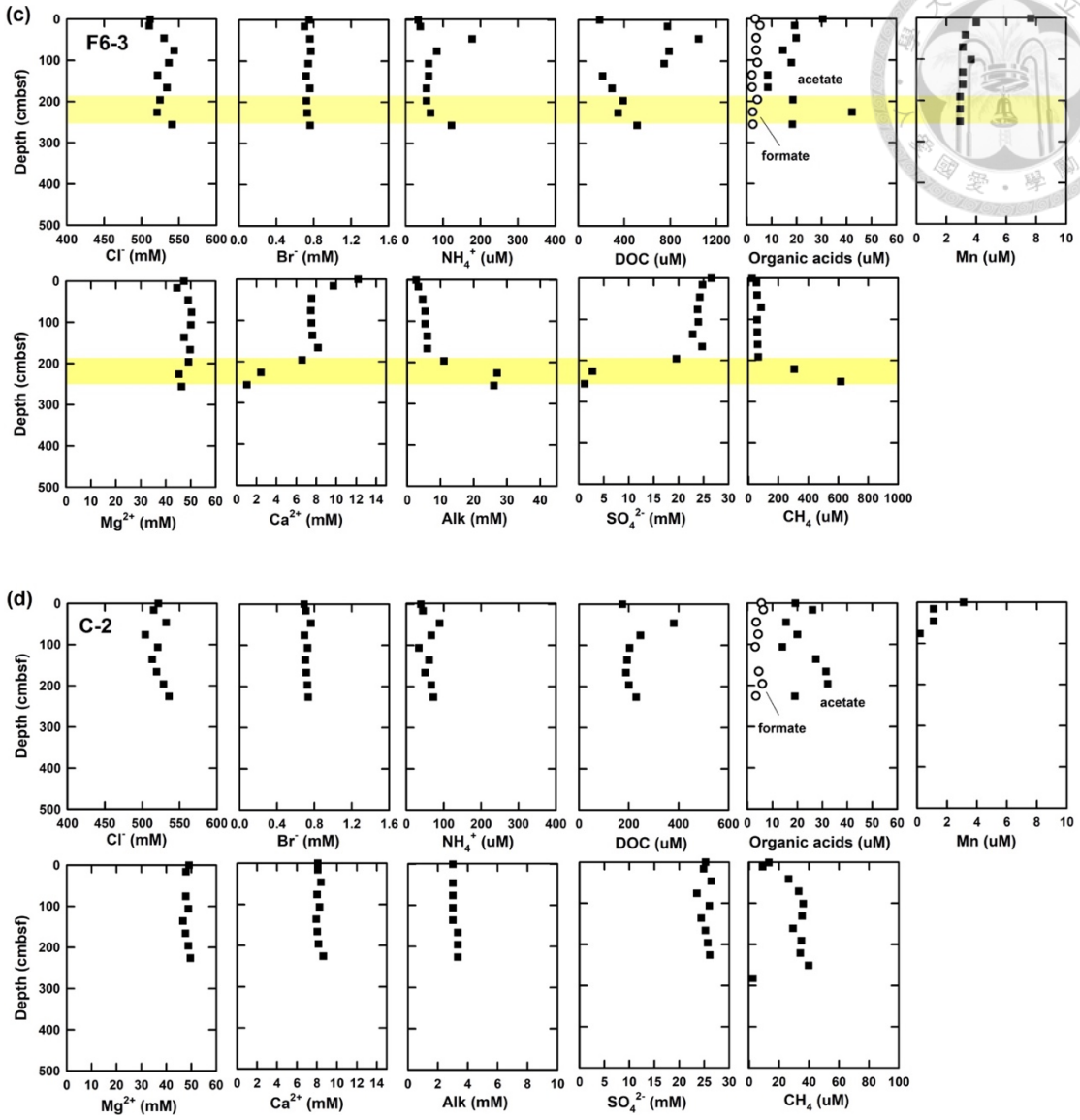

Figure 4.2. (continued)

doi:10.6342/NTU202000506

4.3.2 Numerical modeling scenarios

Numerical modeling results were shown in Fig. 4.3. By considering all reactions and transportations (case 3), the modeling results matched the observations for most ions. For DOC, modeling results in all cases were higher than real data below 2.86 mbsf. For bromide, case 2 could not fit well with real data while case 1 and case 3 could match. For ammonium, modeling results in all cases followed the trend of real data while results of case 3 approached them the most. For calcium, neither case 1 nor case 2 could fit real data. Although case 3 was the best fitting for calcium, part of data above 2.86 mbsf could not be fitted well. For magnesium, only case 2 could not match real data. Similar to calcium, only case 3 could fit TA profile. The depth integration in case 3 yielded that the POC degradation (or DOC production) rate was 90.2 mmol m^{-2} yr^{-1} with approximate 42.3% of the flux attributed to the consumption mediated by OSR and ME.

doi:10.6342/NTU202000506

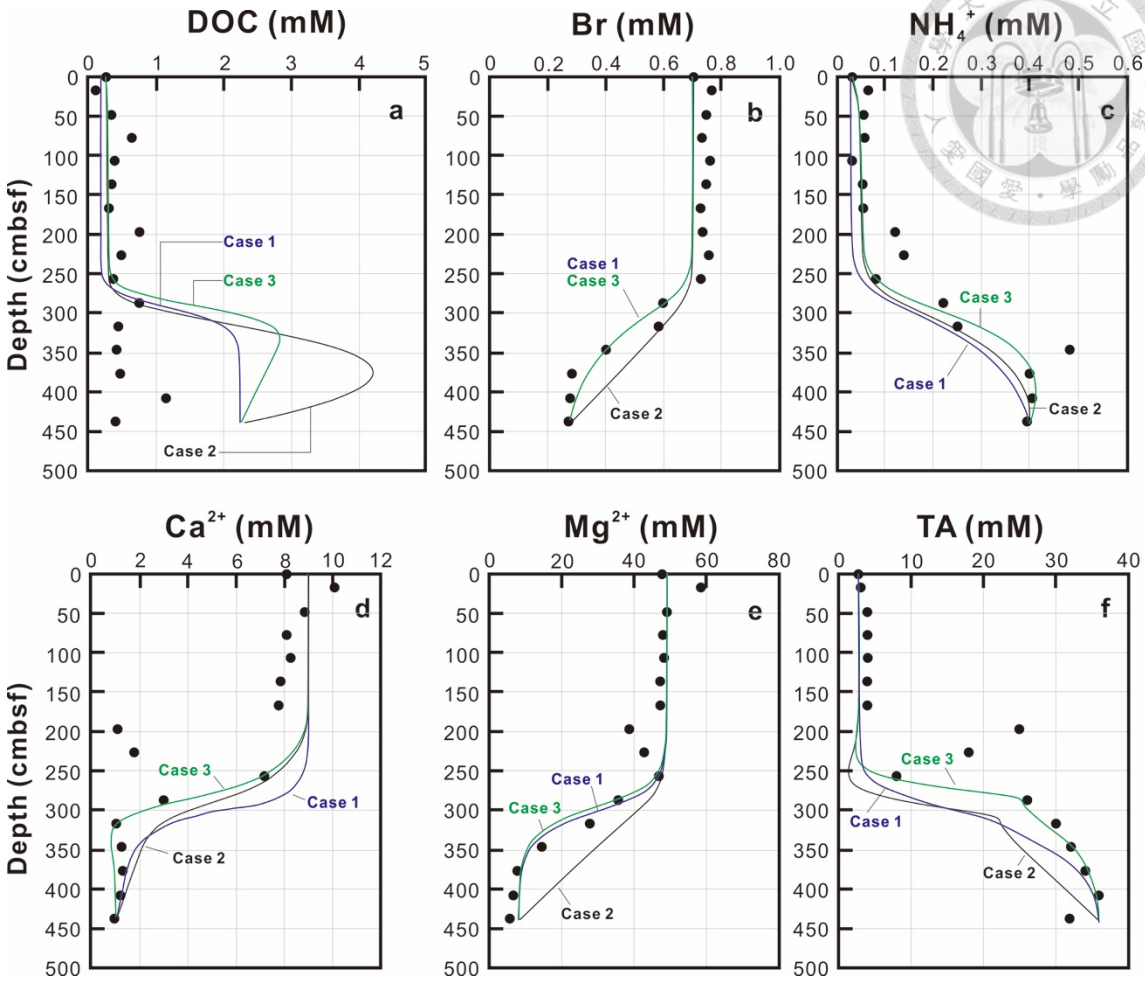

Figure 4.3. The modeling results of site A2-2 in cases 1 to 3 of DOC, bromide, ammonium, calcium, magnesium, and TA. Dots were real data, and lines denoted the modeling results.

doi:10.6342/NTU202000506

4.3.3 Gibbs energies of formate and acetate in sulfate reduction, methanogenesis, and acetogenesis

The highest energy yields (most negative Gibbs energies) of acetoclastic sulfate reduction (AcSR, Table 4.4) were calculated for samples above SMTZ (1.66 to 2.86 mbsf) showing ΔG values between –60 and –70 kJ (mol acetate)$^{-1}$. The energy yield of this metabolic process stays in constant above SMTZ but slightly decreases throughout SMTZ accompanied with the decrease of sulfate concentrations (Fig. 4.2a) and increase in DIC. The lowest energy yields (highest ΔG values) at the bottom of the SMTZ were –38 kJ (mol acetate)$^{-1}$. Similar to acetate, the ΔG values of formate-sulfate reduction (formate-SR) were lowest above SMTZ and slightly increased in and below SMTZ.

ΔG values of acetoclastic methanogenesis (AcME, Fig. 4.4) was around –40 to –35 kJ (mol CH_4)$^{-1}$ above the bottom SMTZ (2.86 mbsf) and suddenly increased to even positive values (around +3 (mol CH4)$^{-1}$). Similar to AcME, the ΔG values of hydrogentrophic methanogenesis (H_2ME, Table 4.4) was around –10 to –12 kJ (mol CH_4)$^{-1}$ above the bottom SMTZ (2.86 mbsf) and suddenly increased to up to –1.0 kJ (mol CH_4)$^{-1}$. Energy yields decreased with increasing depth as a result of increasing DIC and methane concentrations. By contrast, ΔG values of Acetogenic CO_2 reduction (AcCR, Table 4.3) was constantly low, and the energy yield was slightly less than –10kJ

doi:10.6342/NTU202000506

(mol acetate)$^{-1}$.

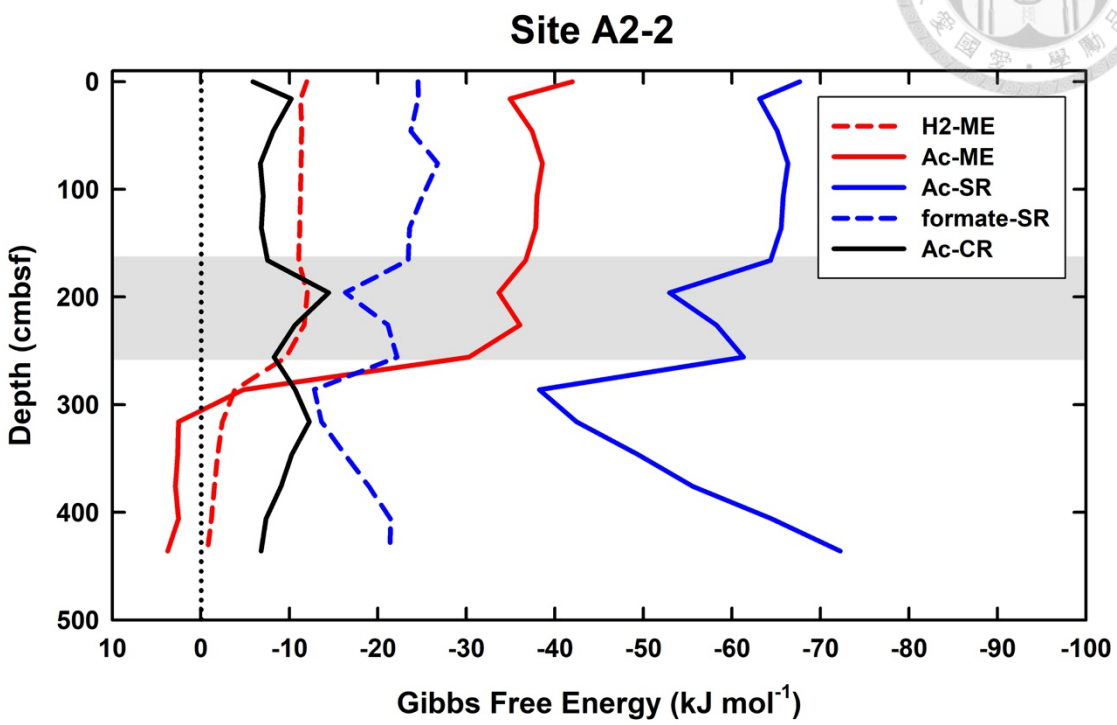

Figure 4.4. Gibbs energies calculated for five microbial activities—hydrogentrophic methanogenesis (H2-ME), acetoclastic methanogenesis (Ac-ME), acetoclastic sulfate reduction (Ac-SR), formate oxidized and sulfate reduction (formate-SR), and acetogenic CO_2 reduction (Ac-CR).

doi:10.6342/NTU202000506

4.4. Discussion

4.4.1 The impact of deep fluid on DOC distribution

Based on the inert nature of chloride to most biological and abiotic processes, previous study has identified that the freshened (chloride depleted), deep fluid originating from a depth of 3 to 5 kmbsf migrated upward at a rate of 2 cm yr^{-1} at the crater center of the TY1 mud volcano. These fluids mix with seawater percolating downward from the seabed, generating great salinity and other geochemical gradients in shallow sediments. Accompanied with advection transport, a large quantity of thermogenic methane was released into the shallow sediments, fueling sulfate driven AOM as well as irrigating shallow porespace with seawater composition. The effect of fluid advection was swapped with the diffusive transport as the distance from the crater increased, lowering OSR and AOM rates but enhancing AOM efficiency [*Chen et al.*, 2020]. In this study, chloride was used again to assess the modulation of fluid versus heterotrophic processes on the organic mineralization and the downstream products of DOC and VFAs (Table 4.5). Similar to chloride, bromide concentrations at depths shallower than SMTZ at site A2-2 were invariant. At and below SMTZ (2.3 mbsf), bromide was positively correlated with chloride (r = +1.0). Although bromide has been considered to be released with the degradation of organic matter, the highly positive

doi:10.6342/NTU202000506

correlation with chloride suggests that bromide also represents a mixture of seawater and bromide-depleted deep fluid. Contribution of bromide from organic degradation is negligible. Similar positive correlation between chloride and bromide was also observed for porewater at or below SMTZ at site 24-2 where the fluid activity was prominent ($r > +0.99$). For sites F6-3 and C-2 distributed on the flank and margin of the TY1, respectively, bromide concentrations were invariant through depth, suggesting limited impact of deep fluid and *in situ* organic degradation.

In contrast to bromide, concentrations of ammonium and TA generally increased with depth and were negatively correlated with chloride at different degrees. While ammonium and bicarbonate are both derived from the degradation of particulate organic matter, the concentration profiles suggest the *in situ* organic degradation and the net accumulation of the reaction products, a pattern typically observed for marine sediments. For comparison, the patterns of DOC and VFAs varied considerably from site to site. At crater sites (A2-2 and 24-2), the DOC concentrations generally increased with depth with some spiked values deviating from the increasing trend. In contrast, the flank sites (F6-3 and C-2) were generally characterized by high concentrations at shallow depths and low concentrations at depth. Regardless of the pattern, the DOC concentrations were positively correlated with the ammonium concentrations at most depth intervals

doi:10.6342/NTU202000506

and sites ($r > 0.5$; except for below SMTZ at site A2-2). Ratios of DOC to ammonium were also higher at shallow depths than at great depths. While either terrestrial or marine detritus possess the C/N_s ratios greater than 5 [*Hsu et al.*, 2014; *Su*, 2015], the degradative products exempted from further exploitation postdating formation would share DOC/NH_4^+ ratios similar to the source characteristics considering nitrate or other soluble nitrogen compounds are generally negligible when compared with the ammonium pool. Therefore, low DOC/NH_4^+ ratios (particularly lower than 5) suggest a more pronounced degree of organic degradation. Under these contexts, organic degradation in the deeper sediments is speculated to be more extensive and complete than in shallow sediments. We noted that the variations in source composition could alter the produced and residue DOC/NH_4^+ ratios.

Of all investigated VFAs, acetate and formate appear to be more abundant and prevalent. Although their concentrations ranged up to 57 uM, they either fluctuated greatly or remained at a low level along depth. Acetate concentrations were positively correlated with ammonium and DOC at crater sites. No significant correlation between acetate and ammonium or DOC was observed for the flank sites. Except for depth below SMTZ at site 24-2, formate concentrations were almost neither correlated with acetate, nor DOC and ammonium concentrations. All these lines of evidence suggest

doi:10.6342/NTU202000506

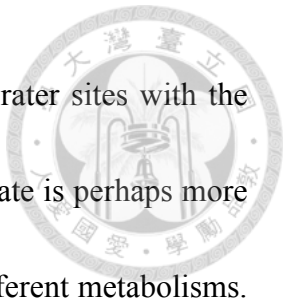

that acetate metabolisms were linked with organic degradation at crater sites with the exact cause remaining unknown. The pattern also suggests that formate is perhaps more labile than acetate or bulk DOC and rapidly turned over between different metabolisms. Acetate and formate are both competitive substrates for terminal electron accepting processes [e.g. *Hoehler et al.*, 1998]. Culture tests have shown that metal reduction, sulfate reduction and methanogenesis compete for these two potential substrates and hydrogen gas for metabolic energy [e.g. *Oremland and Polcin*, 1982]. Because they are primarily produced from the fermentation of complex organic matter, their abundances in natural environments are regulated at a certain low level to fulfill the efficient energy transfer between producing and consuming metabolisms [*Beulig et al.*, 2018; *Glombitza et al.*, 2015; *Orcutt et al.,* 2013]. Exceptions occur particularly for oil or natural gas reservoirs where acetate and formate produced by thermo-cracking and further biodegradation could amount up to a scale of mM [*Egeberg and Barth*, 1998]. The scenario is complicated by the fact that acetate could be also produced by acetogenesis from hydrogen and a fraction of these two VFAs could be assimilated into cell biomass through acetyl-CoA or formate dehydrogenase. The complex reaction network and the contribution of individual pathways or community members in SMV environments remains largely unraveled. Overall, the pattern indicates that VFAs and DOC were

doi:10.6342/NTU202000506

mostly related to the in situ organic degradation and cycling. Contributions from deep sources appear to be negligible.

doi:10.6342/NTU202000506

Table 4.3. Correlation with chloride, acetate, and DOC.

site	depth	chloride	bromide	ammonia	TA	DOC	acetate
correlation with chloride							
A2-2	below SMTZ (2.3 mbsf)		1.00	–0.92	–0.87	–0.30	–0.74
24-2	below SMTZ (1.7 mbsf)		0.99	0.13	–0.93	0.66	0.43
correlation with acetate							
A2-2	above SMTZ	–0.29	–0.09	0.51	0.47	0.57	
	below SMTZ	–0.74	–0.73	0.63	0.70	0.80	
24-2	above SMTZ	–0.15	–0.05	0.28	0.19	0.12	
	below SMTZ	0.43	0.34	0.72	–0.42	0.92	
F6-3	at all depth	–0.41	–0.12	–0.07	0.49	–0.12	
C-2	at all depth	–0.17	–0.30	–0.04	0.61	–0.47	
correlation with DOC							
A2-2	above SMTZ	–0.44	–0.19	0.55	0.71		0.57
	below SMTZ	–0.30	–0.29	0.17	0.37		0.80
24-2	above SMTZ	–0.18	–0.24	0.52	0.64		0.12
	below SMTZ	0.66	0.59	0.69	–0.69		0.92
F6-3	at all depth	0.35	0.19	0.61	–0.23		–0.12
C-2	at all depth	0.31	0.74	0.77	–0.26		–0.47

doi:10.6342/NTU202000506

4.4.2 Numerical modeling evaluation

In this study, POC degradation has been changed in order to simulate the DOC profile in detail. Although the POC degradation term is different from *Chen et al.* [2020], the rate of OSR and ME are still in the same order. In addition, the rate of AOM is still higher than that of OSR and almost in the same value as that reported in *Chen et al.* [2020].

The modeling scenarios elucidate the impact caused by different terms. The modeling results in case 3 (within advection term) can fit the real data much more than that in case 2 (without advection term; Fig. 4.3). Such observation could be obviously found when comparing with other chemicals modeling (sulfate and methane, Fig. 2.2) [*Chen et al.*, 2020], indicating the upward fluid flow predominantly controls this system. Although bromide could be related to POC degradation [*Burdige et al.*, 2016; *Wallmann et al.*, 2006a; *Wei et al.*, 2008], comparing cases 2 and 3, our modeling results suggest that bromide is also mainly controlled by advection (Fig. 4.3b). The atomic Br/C ratio used in our model (Br/TOC=7.6 $\times 10^{-3}$) is not only the highest value in offshore southwestern Taiwan but also higher than the organic-rich area (Br/TOC=2–7$\times 10^{-3}$; Sea of Okhotsk) [*Kandasamy et al.*, 2018; *Wallmann et al.*, 2006a], suggesting that the production of bromide could be apparent. However, the DOC production rate is only in

doi:10.6342/NTU202000506

the range of 0.7 to 2.8×10^{-2} mole m^{-3} yr^{-1}, which is much smaller than the shift caused by advection. Both impact of POC degradation and advection can reflect in ammonium modeling (Fig. 4.3c); the ammonium modeling results of case 3 can almost fit the real data. Modeling results of calcium and TA also indicate the existence of POC degradation and advection is essential, suggesting such deep fluids are TA-enriched and calcium-depleted. Case 3 (within carbonate precipitation) is only slightly different from case 1 in the results of magnesium modeling (Fig. 4.3f), suggesting that magnesium modeling could be only affected by transportation; namely, such deep fluids could be also magnesium-depleted.

As DOC and ammonium are the production of POC, DOC/NH_4^+ should follow C/Ns. However, because DOC are easily degradable, the concentration of DOC could be lower than what is expected. As a result, the boundary condition of DOC is often set based on concentrations of ammonium. Therefore, whatever the cases are, concentrations in modeling are higher than real data because the lower boundary condition of DOC (2.23 mM) is higher than the real data (0.4 mM). Based on modeling results of other ions, case 3 could be the best fitting (Fig. 4.3a). Comparing C/Ns and DOC/NH_4^+ throughout core at site A2-2 (Fig. 4.2), DOC/NH_4^+ are close or higher than C/Ns above SMTZ while they decrease agt and below SMTZ. DOC/NH_4^+ ratios in real data are lower than

doi:10.6342/NTU202000506

5 or even 1 below SMTZ (Table 4.2), which is much lower than C/Ns (5.58). Above SMTZ, samples with a DOC/NH_4^+ closer to or higher than the C/Ns ratio suggest that such DOC could come from *in situ* POC degradation. Some fluctuations could be also observed as DOC/NH_4^+ jumps to 1 at 0.16 mbsf but increases to 10 at 0.46 mbsf. At the subsurface of SMVs, its condition may be caused by change of redox environment or the input of fresh TOC. It has shown that the input of O_2 and elevated electron fluxes could stimulate degradation of refractory TOC [*Reimers et al.*, 2013]. Although the sedimentation rate near TY1 is 1.5×10^{-3} cm yr^{-1} [*Su et al.*, 2018], which is 1000 times lower than the upward fluid flow (2 cm yr^{-1}) [*Chen et al.*, 2020], fresh TOC still has potential to accumulate in the surface of TY1. In addition, dynamic SMV could entangle fresh TOC with explosion mud [*Hiruta et al.*, 2017]. In our model construction, the accumulation of TOC is simplified, and POC degradation constant (K_G) is set to be 10^{-6} yr^{-1} [*Middelberg*, 1989], making it difficult to fit the real data above SMTZ well. Below SMTZ, the low DOC/NH_4^+ could be caused by two reasons: 1) the consumption of *in situ* microbial processes because DOC is degradable; or (2) an input of low deep-sourced DOC fluid because intrusive deep fluid has been shown below SMTZ based on the evidence of δ^2H and $\delta^{18}O$ [*Chen et al.*, 2020].

doi:10.6342/NTU202000506

4.5 Conclusions

We aimed to study the control on DOC and VFA concentrations in a mud volcano subsurface sediments and their role in microbial processes. The concentration profiles of several VFAs (lactate, formate, acetate, propionate and butyrate) in pore water were measured, covering sulfate reduction and methanogenesis zones. In our preliminarily results, bulk DOC concentrations fluctuated with depths, which were probably primarily controlled by *in situ* microbial processes. Lactate could be detectable in some samples while propionate and butyrate were under detection limit. Acetate and formate concentrations were consistently and uniformly low throughout all chemical zones with a slight increasing trend with depth at center sites, suggesting active utilization and turnover by the terminal steps of organic matter mineralization. Numerical modeling for five materials (DOC, bromide, calcium, magnesium, ammonium, and TA) and the calculations of the Gibbs energy of metabolic redox reactions were further applied to the western center site (site A2-2). Our modeling results suggest that both impacts from POC degradation and advection are apparent. The Gibbs energy of metabolic redox reactions shows that acetoclastic sulfate reduction yields the highest energy, implying such reaction could exist below SMTZ. Acetoclastic methanogenesis yields the lowest energy may result in the increase trend of acetate.

doi:10.6342/NTU202000506

Chapter 5 Conclusions

We have presented comprehensive studies on water cycling, methane budgets, and the related microbial processes in accretionary prism southwestern Taiwan. Porefluid collected from TY1 suggest that freshwater was produced from smectite dehydration at a temperature of 100 to 150 ^{o}C and a depth of 3.6 to 5.7 kmbsf. Assuming that the isotopic equilibrium is reached, the water-rock interaction proceeds at a water-rock ratio of more than 0.3. Such fluids migrated upward in a velocity of 2 to 5 cm yr^{-1} at the crater of TY1. By extrapolating such a variation pattern for other 12 SMVs offshore Taiwan, the overall flux discharged from SMVs ranged from 1.3 to 2.5×10^{7} kg yr^{-1}. Such a fluid quantity accounts for 1.1–28.6% of the smectite-bound water originally stored in the incoming sediments, implying that SMVs could act as a conduit to channel the fluid produced from great depth/temperature into seafloor environments. The upward-migrating fluids facilitate the methane flux toward SMTZ at TY1 and lower down the efficiency of the biological filtration through methanotrophy.

Based on the data obtained in this and previous studies in offshore southwestern Taiwan, the calculated diffusive fluxes across the SMTZ and effluxes spanned over four and six orders of magnitude, respectively. Such a wide range of fluxes was controlled by the distribution of structural features, with high values generally proximal to mud diaprism, thrusts, ridges and formation intersection. C_1/C_{2+} ratios combined with isotopic compositions further indicated the increasing contribution of thermogenic methane along a transect from the lower slope, to the upper slope and onshore mud volcanoes. It is likely that the permeability of fluid channeling determines the quantity of microbial methane incorporated from shallow depth. The flux

doi:10.6342/NTU202000506

calculation also indicated that biological filtration, catalyzed by AOM processes, is effective in removing >50% of methane reaching the shallow depth at most offshore and onshore investigated sites, leaving a small fraction of methane leaked into the seawater or atmosphere. The exceptions are sites located near mud diapirs or cold seeps, where high fluid flow and/or temperature fluctuation associated with mud volcanism (including TY1) could have inhibited microbial methane consumptions to a great degree. Although methane could easily escape form such hot sites, based on the distribution and area, AOM process still removes most of methane in accretionary prism. The calculation based on the box model not only independently validated the diffusive fluxes derived from the concentration gradient, but also indicated that the rates of methanogenesis and AOM at shallow depths were nearly balanced, a phenomenon comparable with that observed in other marginal seas. The methane fluxes at shallow depth are, however, imbalanced from those at great depth. The mass balance based on the observed isotopic compositions for field samples and incubation experiments, and the scenario configuration, projected that microbial methane could contribute 7–49% of the total methane inventory at great depth. With the wedge geometry of subduction and sediment property inferred from pre-existing data, the rates of methane production through combined microbial methanogenesis and thermal maturation was estimated to be 1,512–43,096 Tg Myr^{-1}. As the effluxes were much less than the fluxes of the deep source, the methane generated at depth has to be sequestered into hydrate forms or clay minerals. The exact quantities of these two untapped components remain to be validated through other independent methods.

The DOC and VFA concentrations in a mud volcano, TY1, have been analyzed. Numerical modeling and the calculations of the Gibbs energy of metabolic redox reactions were further

doi:10.6342/NTU202000506

applied to these data. Our modeling results suggest that both impacts from POC degradation and advection are apparent. The Gibbs energy of metabolic redox reactions implied acetoclastic sulfate reduction could exist below SMTZ. Acetoclastic methanogenesis yields the lowest energy may result in the increase trend of acetate.

doi:10.6342/NTU202000506

Refernce

Amante, C. & Eakins, B.W. ETOPO1 1 Arc-Minute Global Relief Model: Procedures, Data Sources and Analysis. NOAA Technical Memorandum NESDIS NGDC-24. National Geophysical Data Center, NOAA; doi:10.7289/V5C8276M (2009).

Amend, J. P., & Shock, E. L. Energetics of overall metabolic reactions of thermophilic and hyperthermophilic Archaea and Bacteria. *FEMS Microbial. Rev.*, **25**(2), 175–243; 10.1111/j.1574-6976.2001.tb00576.x (2001).

Archer, D. E. & Buffett, B. A. A two-dimensional model of the methane cycle in a sedimentary accretionary wedge. *Biogeosciences*, **9**(8), 3323–3336; 10.5194/bg-9-3323-2012 (2012).

Bernard, B. B. *et al.* Natural gas seepage in the Gulf of Mexico. *Earth Planet. Sci. Lett.*, **31**(1), 48–54; 10.1016/0012-821X(76)90095-9 (1976).

Berner, R. A. *Early Diagenesis—A Theoretical Approach*, Princeton Univ. Press, Princeton, N. J. (1980).

Beulig F., Røy H., Glombitza C. & Jørgensen B. B. Control on rate and pathway of anaerobic organic carbondegradation in the seabed. *Proc. Natl. Acad. Sci.*, **115**, 367–372; 10.1073/pnas.1715789115 (2018).

Blattmann, T. M. *et al.*, Mineralogical control on the fate of continentally derived organic matter in the ocean. *Science*, **366**(6466), 742–745; 10.1126/science.aax5345 (2019).

Boetius, A. & Wenzhöfer, F. Seafloor oxygen consumption fuelled by methane from cold seeps. *Nat. Geosci.*, **6**(9), 725–734; 10.1038/ngeo1926 (2013).

Boudreau, B. P. *Diagenetic models and their implementation*, vol. 505, 132 pp., Springer, Berlin (1997).

Boudreau, B. P. The diffusive tortuosity of fine-grained unlithified sediments. *Geochim. Cosmochim. Acta*, **60**(16), 3139–3142; 10.1016/0016-7037(96)00158-5 (1996).

Boudreau & Guinasso. The influence of a modeling sublayer on accretion, dissolution, and diagenesis at the sea floor, in *The Dynamic Environment of the Ocean Floor*, edited by K. A. Fanning and F. T. Manheim, pp. 115–145, Lexington Books, Rowman & Littlefield International, Lexington, Mass (1982).

Brown, K. M. The nature and hydrogeologic significance of mud diapirs and diatremes for accretionary systems. *J. Geophys. Res. Solid Earth*, **95**(B6), 8969–8982; 10.1029/JB095iB06p08969 (1990).

Brown, K. & Westbrook, G. K. Mud diapirism and subcretion in the Barbados Ridge accretionary complex: the role of fluids in accretionary processes. *Tectonics*, **7**(3), 613–640; 10.1029/TC007i003p00613(1988).

Burdige, D. J. The biogeochemistry of manganese and iron reduction in marine sediments. *Earth-Sci. Rev.*, **35**(3), 249–284; 10.1016/0012-8252(93)90040-E (1993).

doi:10.6342/NTU202000506

Burdige, D. J., Komada, T., Magen, C., & Chanton, J. P. Carbon cycling in Santa Barbara Basin sediments: A modeling study. *J. Mar. Res.*, **74**(3), 133–159; 10.1357/002224016819594818 (2016).

Capuano, R. M. The temperature dependence of hydrogen isotope fractionation between clay minerals and water: Evidence from a geopressured system. Geochim. Cosmochim. Acta, 56(6), 2547–2554; 10.1016/0016-7037(92)90208-Z (1992).

Castelltort, S. *et al.* Sedimentology of early Pliocene sandstones in the south-western Taiwan foreland: Implications for basin physiography in the early stages of collision. *J. Asian Earth Sci.*, **40**(1), 52–71; 10.1016/j.jseaes.2010.09.005 (2011).

Cawood, P. A. *et al*. Accretionary orogens through Earth history. *Geol. Soc., London, Spec. Publ.*, **318**(1), 1–36; 10.1144/SP318.1 (2009).

Chan, L. H., Gieskes, J. M., You, C. F., & Edmond, J. M. Lithium isotope geochemistry of sediments and hydrothermal fluids of the Guaymas Basin, Gulf of California. *Geochim. Cosmochim. Acta*, **58**(20), 4443–4454; 10.1016/0016-7037(94)90346-8 (1994).

Chao, H. C., You, C. F., Liu, H. C., & Chung, C. H. The origin and migration of mud volcano fluids in Taiwan: Evidence from hydrogen, oxygen, and strontium isotopic compositions. *Geochim. Cosmochim. Acta*, 114, 29–51; 10.1016/j.gca.2013.03.035 (2013).

Chao, H. C. *et al.* Gases in Taiwan mud volcanoes: chemical composition, methane carbon isotopes, and gas fluxes. *Appl. Geochem.*, **25**(3), 428–436; 10.1016/j.apgeochem.2009.12.009 (2010).

Chen, A. T. et al. Mantle fluids associated with crustal-scale faulting in a continental subduction setting, Taiwan. *Sci. Rep.*, **9**(1), 1–7; 10.1038/s41598-019-47070-2 (2019).

Chen, H. C. Halogen Profiles of Pore Waters from Gas Hydrate Potential Area Offshore of SW Taiwan. Master thesis, Department of Geosciences, National Taiwan University (in Chinese with English abstract); 10.6342/NTU.2010.02645 (2010).

Chen, H. W. Geochemistry and Origin of Pore Water Compositions of Cored Sediments in Offshore Southwestern Taiwan. Master thesis, Department of Geosciences, National Taiwan University (in Chinese with English abstract); 10.6342/NTU.2011.00960 (2011).

Chen, J. C. Grain size, mineralogy and physical properties of cored sediments in gas hydrate potential area off SW Taiwan (1/4). *Report of Central Geological Survey* **2004**, 93-25-B, 86 pp. (in Chinese with English abstract) (2004).

Chen, J. C. Grain size, mineralogy and physical properties of cored sediments in gas hydrate potential area off SW Taiwan (2/4). *Report of Central Geological Survey* **2005**, 94-26-B, 118 pp. (in Chinese with English abstract) (2005).

Chen, J. C. Grain size, mineralogy and physical properties of cored sediments in gas hydrate potential area off SW Taiwan (3/4). *Report of Central Geological Survey* **2006**, 95-26-B, 140 pp. (in Chinese with English abstract) (2006).

doi:10.6342/NTU202000506

Chen, J. C. Grain size, mineralogy and physical properties of cored sediments in gas hydrate potential area off SW Taiwan (4/4). *Report of Central Geological Survey* **2007**, 96-27-B, 113 pp. (in Chinese with English abstract) (2007).

Chen, J. C. New energy resource offshore southwest Taiwan – natural gas hydrates resources survey and evaluation of geochemical research (2/4)－The relationship between sediment properties and the occurrence of gas hydrate offshore SW Taiwan. *Report of Central Geological Survey* **2008**, 97-29-G, 105 pp. (in Chinese with English abstract) (2008).

Chen, J. C. New energy resource offshore southwest Taiwan – natural gas hydrates resources survey and evaluation of geochemical research (2/4)－The relationship between sediment properties and the occurrence of gas hydrate offshore SW Taiwan. *Report of Central Geological Survey* **2009**, 98-27-F, 89 pp. (in Chinese with English abstract) (2009).

Chen, J. C. New energy resource offshore southwest Taiwan – natural gas hydrates resources survey and evaluation of geochemical research (3/4)－The relationship between sediment properties and the occurrence of gas hydrate offshore SW Taiwan. *Report of Central Geological Survey* **2010**, 99-26-F, 102 pp. (in Chinese with English abstract) (2010).

Chen, J. C. New energy resource offshore southwest Taiwan – natural gas hydrates resources survey and evaluation of geochemical research (4/4)－The relationship between sediment properties and the occurrence of gas hydrate offshore SW Taiwan. *Report of Central Geological Survey* **2011**, 100-25-F, 122 pp. (in Chinese with English abstract) (2011).

Chen, K. T. A study on the synthesis of ultramarine from mudstones of Kuting-Keng formation. Doctoral Dissertation, Department of Resources Engineering, National Cheng Kung University; 10.6844/NCKU.2015.00362 (2014).

Chen, M. P. Geotechnical properties of sediments off the coast of Hsinchu-northwest Taiwan related to sedimentary environment. *Acta Oceanogr. Taiwan.*, **12**, 28–53 (1981).

Chen, N. C. The carbon isotopes of DIC and methane gas from gas hydrate potential area offshore SW Taiwan. Master thesis, Department of Geosciences, National Taiwan University (in Chinese with English abstract); 10.6342/NTU.2009.02789 (2009).

Chen, N. C. *et al.* Discharge of deeply rooted fluids from submarine mud volcanism in the Taiwan accretionary prism. *Sci. Rep.*; 10.1038/s41598-019-57250-9 (2020).

Chen, N. C. *et al.* Production, consumption, and migration of methane in accretionary prism of southwestern Taiwan. *Geochem. Geophys. Geosyst.*, **18**(8), 2970–2989; 10.1002/2017GC006798 (2017).

Chen, P. Y. Minerals in bottom sediments of the South China Sea. *Geol. Soc. Am. Bull.*, **89**(2), 211–222; 10.1130/0016-7606(1978)89<211:MIBSOT>2.0.CO;2 (1978).

Chen, S. C. *et al.* Gas seepage, pockmarks and mud volcanoes in the near shore of SW Taiwan. *Mar. Geophys. Res.*, **31**(1–2), 133–147; 10.1007/s11001-010-9097-6 (2010).

Chen, S. C. *et al.* Distribution and characters of the mud diapirs and mud volcanoes off southwest Taiwan. *J. Asian Earth Sci.*, **92**, 201–214; 10.1016/j.jseaes.2013.10.009 (2014a).

doi:10.6342/NTU202000506

Chen, S. C. *et al.* Active mud volcanoes in the gas hydrate potential area of the upper Kaoping Slope, off southwest Taiwan. In *OCEANS 2014-TAIPEI* (pp. 1-6), IEEE; 10.1109/OCEANS-TAIPEI.2014.6964312 (2014b).

Cheng, T. W. *et al.* Metabolic stratification driven by surface and subsurface interactions in a terrestrial mud volcano. *ISME J.*, **6**(12), 2280–2290; 10.1038/ismej.2012.61 (2012).

Chi, W. C. & Reed, D. L. Evolution of shallow, crustal thermal structure from subduction to collision: An example from Taiwan. *Geol. Soc. Am. Bull.*, **120**(5–6), 679–690; 10.1130/B26210.1 (2008).

Chi, W. C. *et al.* Tectonic wedging along the rear of the offshore Taiwan accretionary prism. *Tectonophysics*, **374**(3), 199–217; 10.1016/j.tecto.2003.08.004 (2003).

Chiang, C. S. *et al.* Characteristics of the wedge-top depozone of the southern Taiwan foreland basin system. *Basin Res.*, **16**(1), 65–78; 10.1111/j.1365-2117.2004.00222.x (2004).

Chuang, P. C. *et al.* Extremely High Methane Concentration in Bottom Water and Cored Sediments from Offshore Southwestern Taiwan. *Terr. Atmos. Oceanic Sci.*, **17**(4), 903–920 (2006).

Chuang, P. C. *et al.* Estimation of Methane Flux Offshore SW Taiwan and the Influence of Tectonics on Gas Hydrate Accumulation. *Geofluids*, **10**, 497–510, doi:10.1111/j.1468-8123.2010.00313.x (2010).

Chuang, P. C. *et al.* Relating sulfate and methane dynamics to geology: the accretionary prism offshore SW Taiwan. *Geochem. Geophys. Geosyst.*, **14**(7), 2523–2545; 10.1002/ggge.20168 (2013).

Chung, H. M. *et al.* Origin of gaseous hydrocarbons in subsurface environments: Theoretical considerations of carbon isotope distribution. *Chem. Geol.*, **71**, 97–104; 10.1016/0009-2541(88)90108-8 (1988).

Chung, S. H. *et al.* Geological Investigation of Gas Hydrate Resource Potential in the Offshore Areas of South-Southwest Taiwan. *Central Geological Survey Special Publication*, **30**, 1–42 (2016). (in Chinese with English abstract)

Dadson, S.J. *et al.* Links between erosion, runoff variability and seismicity in the Taiwan orogen. *Nature*, **426**, 648–651, doi:10.1038/nature02150 (2003).

Dählmann, A., & De Lange, G. J. Fluid–sediment interactions at Eastern Mediterranean mud volcanoes: a stable isotope study from ODP Leg 160. *Earth Planet. Sci. Lett.*, **212**(3), 377–391; 10.1016/S0012-821X(03)00227-9 (2003).

Dale, A. W. *et al.* Anaerobic oxidation of methane (AOM) in marine sediments from the Skagerrak (Denmark): II. Reaction-transport modeling. *Geochim. Cosmochim. Acta*, **72**(12), 2880–2894; 10.1016/j.gca.2007.11.039 (2008a).

Dale, A. W. *et al.* Methane efflux from marine sediments in passive and active margins: Estimations from modeling bioenergetic reaction-transport simulations. *Earth Planet. Sci. Lett.*, **265**(3–4), 329–344; 10.1016/j.epsl.2007.09.026 (2008b).

doi:10.6342/NTU202000506

Dale, A. W. *et al.* Pathways and regulation of carbon, sulfur and energy transfer in marine sediments overlying methane gas hydrates on the Opouawe Bank (New Zealand). *Geochim. Cosmochim. Acta*, **74**(20), 5763–5784; 10.1016/j.gca.2010.06.038 (2010).

de Beer, D., Sauter, E., Niemann, H., Kaul, N., Foucher, J. P., Witte, U., Schlüter, M., & Boetius, A. In situ fluxes and zonation of microbial activity in surface sediments of the Håkon Mosby Mud Volcano. *Limnol. Oceanogr.*, **51**(3), 1315–1331; 10.4319/lo.2006.51.3.1315 (2006).

Dickens, G. R. *et al.* Dissociation of Oceanic Methane Hydrate as a Cause of the Carbon-Isotope Excursion at the End of the Paleocene. *Paleoceanography*, **10**(6), 965–971; 10.1029/95PA02087 (1995).

Doo, W.-B., Lo, C.-L., Kuo, C.-H., Brown, D., & Hsu, S.-K. Exhumation of serpentinized peridotite in the northern Manila subduction zone inferred from forward gravity modeling. *Geophys. Res. Lett.*, **42**(19), 7977–7982; 10.1002/2015GL065705 (2015).

Drits, V. A., & McCarty, D. K. The nature of structure-bonded H_2O in illite and leucophyllite from dehydration and dehydroxylation experiments. *Clays Clay Miner.*, **55**(1), 45–58; 10.1346/CCMN.2007.0550104 (2007).

Eickenbusch, P. *et al.* Origin of short-chain organic acids in serpentinite mud volcanoes of the Mariana Convergent Margin. *Front. Microbiol.*, **10**, 1729; 10.3389/fmicb.2019.01729 (2019).

Egeberg P. K. & Barth T. Contribution of dissolved organic species to the carbon and energy budgets of hydrate bearing deep sea sediments (Ocean Drilling Program Site 997 Blake Ridge). *Chem. Geol.*, **149**(1–2), 25–35; 10.1016/S0009-2541(98)00033-3 (1998).

Ertefai, T. F. *et al.* The biogeochemistry of sorbed methane in marine sediments. *Geochim. Cosmochim. Acta*, **74**(21), 6033–6048; 10.1016/j.gca.2010.08.006 (2010).

Etiope, G. *et al.* Methane seeps and mud volcanoes in Italy: gas origin, fractionation and emission to the atmosphere. *Geophys. Res. Lett.*, **34**(14); 10.1029/2007GL030341 (2007).

Etiope, G. *et al.* Terrestrial methane seeps and mud volcanoes: a global perspective of gas origin. *Mar. Pet. Geol.*, **26**(3), 333–344; 10.1016/j.marpetgeo.2008.03.001 (2009).

Felden, J. *et al.* Transport and consumption of oxygen and methane in different habitats of the Håkon Mosby Mud Volcano (HMMV). *Limnol. Oceanogr.*, **55**(6), 2366–2380; 10.4319/lo.2010.55.6.2366 (2010).

Feseker, T. *et al.* Eruption of a deep-sea mud volcano triggers rapid sediment movement. *Nat.* commun., **5**; 10.1038/ncomms6385 (2014).

Finke N., Vandieken, V. & Jørgensen, B. B. Acetate, lactate, propionate, and isobutyrate as electron donors for iron and sulfate reduction in Arctic marine sediments, Svalbard. *FEMS Microbiol. Ecol.*, **59**, 10–22; 10.1111/j.1574-6941.2006.00214.x (2007).

Forster, P. *et al.* Changes in atmospheric constituents and in radiative forcing in *Climate Change 2007. The Physical Science Basis* (2007).

doi:10.6342/NTU202000506

Fouillac, C., & Michard, G. Sodium/lithium ratio in water applied to geothermometry of geothermal reservoirs. *Geothermics*, **10(**1), 55–70; 10.1016/0375-6505(81)90025-0 (1981).

Freundt, A. *et al.* Volatile (H_2O, CO_2, Cl, S) budget of the Central American subduction zone. *International Journal of Earth Sciences*, **103**(7), 2101–2127; 10.1007/s00531-014-1001-1 (2014).

Glombitza, C., Jaussi, M., Røy, H., Seidenkrantz, M. S., Lomstein, B. A., & Jørgensen, B. B. Formate, acetate, and propionate as substrates for sulfate reduction in sub-arctic sediments of Southwest Greenland. *Front. Microbial.*, **6**, 846; 10.3389/fmicb.2015.00846 (2015).

Haas, A. F. *et al.* Effects of coral reef benthic primary producers on dissolved organic carbon and microbial activity. *PloS one*, **6**(11), e27973; 10.1371/journal.pone.0027973 (2011).

Haeckel, M., Boudreau, B. P., & Wallmann, K. Bubble-induced porewater mixing: A 3-D model for deep porewater irrigation. *Geochim. Cosmochim. Acta*, **71**(21), 5135–5154; 10.1016/j.gca.2007.08.011 (2007).

Haese, R. R. *et al.* Carbon geochemistry of cold seeps: Methane fluxes and transformation in sediments from Kazan mud volcano, eastern Mediterranean Sea. *Earth Planet. Sci. Lett.*, **212** (3–4), 361–375; 10.1016/S0012-821X(03)00226-7 (2003).

Head, I. M. *et al.* Biological activity in the deep subsurface and the origin of heavy oil. *Nature*, **426**(6964), 344–352; 10.1038/nature02134 (2003).

Hedges, J. I., & Keil, R. G. Sedimentary organic matter preservation: an assessment and speculative synthesis. *Mar. Chem.*, 49(2-3), 81–115; 10.1016/0304-4203(95)00008-F (1995).

Helgeson H. C. Thermodynamics of hydrothermal systems at elevated temperatures and pressures. *Am. J. Sci.*, **267**, 729– 804; 10.2475/ajs.267.7.729 (1969).

Hensen, C. *et al.* Sources of mud volcano fluids in the Gulf of Cadiz—indications for hydrothermal imprint. *Geochim. Cosmochim. Acta*, **71**(5), 1232–1248;10.1016/j.gca.2006.11.022 (2007).

Heuer, V. B., Krüger, M., Elvert, M., & Hinrichs, K. U. Experimental studies on the stable carbon isotope biogeochemistry of acetate in lake sediments. *Org. Geochem.*, **41**(1), 22–30; 10.1016/j.orggeochem.2009.07.004 (2010).

Heuer, V. B., Pohlman, J. W., Torres, M. E., Elvert, M., & Hinrichs, K. U. The stable carbon isotope biogeochemistry of acetate and other dissolved carbon species in deep subseafloor sediments at the northern Cascadia Margin. *Geochim. Cosmochim. Acta*, **73**(11), 3323–3336; 10.1016/j.gca.2009.03.001 (2009).

Hiruta, A. *et al.* Activation of gas bubble emissions indicated by the upward decreasing Lead-210 activity at a submarine mud volcano (TY1) offshore southwestern Taiwan. *J. Asian Earth Sci.*, **149**, 160–171; 10.1016/j.jseaes.2017.08.007 (2017).

doi:10.6342/NTU202000506

Hoehler T. M., Alperin M. J., Albert D. B. & Martens C. S. Thermodynamic control on hydrogen concentrations in anoxic sediments. *Geochim. Cosmochim. Acta*, **62**, 1745–1756; 10.1016/S0016-7037(98)00106-9 (1998).

Hong, W. L. *et al.* Methane flux from miniseepage in mud volcanoes of SW Taiwan: Comparison with the data from Italy, Romania, and Azerbaijan. *J. Asian Earth Sci.*, **65**, 3–12, doi:10.1016/j.jseaes.2012.02.005 (2013a).

Hong, W. L. *et al.* Carbon cycling within the sulfate-methane-transition-zone in marine sediments from the Ulleung Basin. *Biogeochemistry*, **115**(1–3), 129–148, doi:10.1007/s10533-012-9824-y (2013b).

Hong, W. L. *et al.* Removal of methane through hydrological, microbial, and geochemical processes in the shallow sediments of pockmarks along eastern Vestnesa Ridge (Svalbard). *Limnol. Oceanogr*, **61**, S324–S343; 10.1002/lno.10299 (2016).

Hong, W. L. *et al.* Seepage from an Arctic shallow marine gas hydrate reservoir is insensitive to momentary ocean warming. *Nat. commun*., **8**, 15745; 10.1038/ncomms15745 (2017).

Hu, C. Y. *et al.* Biogeochemical cycles at the sulfate-methane transition zone (SMTZ) and geochemical characteristics of the pore fluids offshore southwestern Taiwan. *J. of Asian Sci.*, **149**, 172–183; 10.1016/j.jseaes.2017.07.002 (2017).

Hu, D. *et al.* Deep sea records of the continental weathering and erosion response to East Asian monsoon intensification since 14 ka in the South China Sea. *Chem. Geol.*, **326**, 1–18 (2012).

Huang, C. Y. *et al.* Temporal and spatial records of active arc continent collision in Taiwan: A synthesis. *Bull. Geol. Soc. Am.*, **118**, 274–288, doi:10.1130/B25527.1 (2006).

Huene, R. & Scholl, D. W. Observations at convergent margins concerning sediment subduction, subduction erosion, and the growth of continental crust. *Rev. Geophys.*, **29**(3), 279–316; 10.1029/91RG00969 (1991).

Hung, C. W. *et al.* Benthic fluxes of dissolved organic carbon from gas hydrate sediments in the northern South China Sea. *Sci. Rep.*, **6**, 29597; 10.1038/srep29597 (2016).

Hunt, J. M. The origin of natural gas. *Petroleum geochemistry and geology*, pp. 186–232, W. H. Freeman, New York (1996).

Hsu, F. H. *et al.* Accumulation of terrestrial organic carbon on an active continental margin offshore southwestern Taiwan: Source-to-sink pathways of river-borne organic particles. *J. Asian Earth Sci.*, **91**, 163–173; 10.1016/j.jseaes.2014.05.006 (2014).

Hwang, H. *et al.* A role for subducted super-hydrated kaolinite in Earth's deep water cycle. *Nat. Geosci.*, **10**(12), 947; 10.1038/s41561-017-0008-1 (2017).

Ijiri, A. *et al.* Deep-biosphere methane production stimulated by geofluids in the Nankai accretionary complex. *Sci. Adv.*, **4**(6), eaao4631; 10.1126/sciadv.aao4631 (2018).

Inagaki, F. *et al.* Exploring deep microbial life in coal-bearing sediment down to ~2.5 km below the ocean floor. *Science*, **349**(6246), 420–424; 10.1126/science.aaa6882 (2015).

doi:10.6342/NTU202000506

Jähne, B., Heinz, G., and Dietrich, W. (1987). Measurement of the diffusion coefficients of sparingly soluble gases in water. *J. Geophys. Res. Oceans*, 92(C10), 10767–10776, doi: 10.1029/JC092iC10p10767.

James, A. T. & Burns, B. J. Microbial alteration of subsurface natural gas accumulations. *AAPG Bull.*, **68**(8), 957–960 (1984).

James R. H., Allen D. E., & Seyfried W. E. An experimental study of alteration of oceanic crust and terrigenous sediments at moderate temperatures (51 to 350 °C): insights as to chemical processes in near-shore ridge-flank hydrothermal systems. *Geochim. Cosmochim. Acta,* **67**, 681–691; 10.1016/S0016-7037(02)01113-4 (2003).

Jarrard, R. D. Subduction fluxes of water, carbon dioxide, chlorine, and potassium. *Geochem. Geophys. Geosyst.*, **4**(5); 10.1029/2002GC000392 (2003).

Jones, D. M. *et al.* Crude-oil biodegradation via methanogenesis in subsurface petroleum reservoirs. *Nature*, **451**(7175), 176–180; 10.1038/nature06484 (2008).

Jørgensen, B. B. & Des Marais, D. J. The diffusive boundary layer of sediments: Oxygen microgradients over a microbial mat. *Limnol. Oceanogr.*, **35**(6), 1343–1355; 10.4319/lo.1990.35.6.1343 (1990).

Judd, A. G. & M. Hovland. *Seabed Fluid Flow: The Impact of Geology, Biology and the Marine Environment*. Cambridge Univ. Press, Cambridge, U. K. (2007).

Kandasamy, S., Lin, B., Lou, J. Y., Kao, S. J., Chen, C. T. A., & Mayer, L. M. Estimation of Marine Versus Terrigenous Organic Carbon in Sediments Off Southwestern Taiwan Using the Bromine to Total Organic Carbon Ratio as a Proxy. *J. Geophys. Res-Biogeo.*, **123**(10), 3387-3402; 10.1029/2018JG004674 (2018).

Kandasamy, S., & Nagender Nath, B. Perspectives on the terrestrial organic matter transport and burial along the land-deep sea continuum: Caveats in our understanding of biogeochemical processes and future needs. *Front. Mar. Sci.*, **3**, 259; 10.3389/fmars.2016.00259 (2016).

Karato, S. & P. Wu. Rheology of the upper mantle: A synthesis. *Science*, **260**, 771–778; 10.1126/science.260.5109.771(1993).

Kastner, M. *et al.* Fluids in Convergent Margins: What do We Know about their Composition, Origin, Role in Diagenesis and Importance for Oceanic Chemical Fluxes? *Philos. Trans. A Math. Phys. Eng. Sci.*, **335**(1638), 243–259; 10.1098/rsta.1991.0045 (1991).

Katz, B. J. *et al.* Significance of microbial processes in gases of the South Caspian basin. *Mar. Pet. Geol.*, **19**(6), 783–796; 10.1016/S0264-8172(02)00086-7 (2002).

Kennett, J. P. & B. N. Fackler-Adams. Relationship of clathrate instability to sediment deformation in the upper Neogene of California. *Geology*, **28**(3), 215–218; 10.1130/0091-7613(2000)28<215:ROCITS>2.0.CO;2 (2000).

Kharaka, Y. K. & Mariner, R. H. Chemical geothermometers and their application to formation waters from sedimentary basins in *Thermal history of sedimentary basins* (eds Naeser N.D. and McCulloh T.H.) 99–117 (Springer, 1989).

doi:10.6342/NTU202000506

Kim, J. H. *et al.* Geochemical characterization of the organic matter, pore water constituents and shallow methane gas in the eastern part of the Ulleung Basin, East Sea (Japan Sea). *Isl. Arc*, **16**(1), 93–104; 10.1111/j.1440-1738.2007.00560.x. (2007).

Knittel, K. & Boetius, A. Anaerobic oxidation of methane: progress with an unknown process. *Annu. Rev. Microbiol.*, **63**,311–334, 10.1146/annurev.micro.61.080706.093130 (2009).

Komada, T., Burdige, D. J., Crispo, S. M., Druffel, E. R., Griffin, S., Johnson, L., & Le, D. Dissolved organic carbon dynamics in anaerobic sediments of the Santa Monica Basin. *Geochim. Cosmochim. Acta*, **110**, 253–273; 10.1016/j.gca.2013.02.017 (2013).

Laufer, K. *et al.* Anaerobic microbial Fe(II) oxidation and Fe(III) reduction in coastal marine sediments controlled by organic carbon content. *Environ. Microbiol.*, **18**, 3159–3174; 10.1111/1462-2920.13387 (2016).

Lecuyer, C., Gillet, P., & Robert, F. The hydrogen isotope composition of seawater and the global water cycle. *Chem. Geol.*, **145**(3–4), 249–261; 10.1016/S0009-2541(97)00146-0 (1998).

Lelieveld, J. O. S. *et al.* Changing concentration, lifetime and climate forcing of atmospheric methane. *Tellus B*, **50**(2), 128–150; 10.1034/j.1600-0889.1998.t01-1-00002.x (1998).

Liao, W. Z. *et al.* A study on tectonic and sedimentary development in the rifted northern continental margin of the South China Sea near Taiwan. *Interpretation*, 4(3), SP47–SP65, doi:10.1190/INT-2015-0209.1 (2016).

Liao, W. Z., Lin, A. T., Liu, C. S., Oung, J. N., & Wang, Y. Heat flow in the rifted continental margin of the South China Sea near Taiwan and its tectonic implications. *J. of Asian Sci.*, **92**, 233–244; 10.1016/j.jseaes.2014.01.003 (2014).

Lin, A. T. *et al.* Tectonic features associated with the overriding of an accretionary wedge on top of a rifted continental margin: An example from Taiwan. *Mar. Geol.*, **255**(3), 186–203; 10.1016/j.margeo.2008.10.002 (2008).

Lin, A. T., Yao, B., Hsu, S. K., Liu, C. S., & Huang, C. Y. Tectonic features of the incipient arc-continent collision zone of Taiwan: Implications for seismicity. *Tectonics.*, **479**(1-2), 28–42; 10.1016/j.tecto.2008.11.004 (2009).

Lin, C. C. *et al.* Geological controls on BSR occurrences in the incipient arc-continent collision zone off southwest Taiwan. *Mar. Pet. Geol.*, **26**(7), 1118–1131; 10.1016/j.marpetgeo.2008.11.002 (2009).

Lin, C. C. *et al.* Canyon-infilling and gas hydrate occurrences in the frontal fold of the offshore accretionary wedge off southern Taiwan. *Mar. Geophys. Res.*, **35**(1), 21–35; 10.1007/s11001-013-9203-7 (2014).

Liu, C. S. *et al.* Distribution and characters of gas hydrate offshore of southwestern Taiwan. *Terr. Atmos. Ocean Sci.*, **17**, 615–644 (2006).

Liu, Z. *et al.* Clay mineral assemblages in the northern South China Sea: implications for East Asian monsoon evolution over the past 2 million years. *Mar. Geol.*, **201**(1), 133–146; 10.1016/S0025-3227(03)00213-5 (2003).

doi:10.6342/NTU202000506

Liu, Z. *et al.* Clay mineral distribution in surface sediments of the northeastern South China Sea and surrounding fluvial drainage basins: source and transport. *Mar. Geol.*, **277**(1-4), 48–60; 10.1016/j.margeo.2010.08.010 (2010).

Liu, Z. *et al.* Detrital fine-grained sediment contribution from Taiwan to the northern South China Sea and its relation to regional ocean circulation. *Mar. Geol.*, **255**(3–4), 149–155; 10.1016/j.margeo.2008.08.003 (2008).

Lin, L. H. *et al.* Distributions and assemblages of microbial communities along a sediment core retrieved from a potential hydrate–bearing region offshore southwestern Taiwan. *J. Asian Earth Sci.*, **92**, 276–292; 10.1016/j.jseaes.2014.02.014 (2014).

Ling, Y. C. *et al.* Potential of microbial methane formation in a high-temperature hydrocarbon seep. *Appl. Geochem.*, **27**(8), 1666–1678; 10.1016/j.apgeochem.2012.04.002 (2012).

Linke, P. *et al.* In situ benthic fluxes from an intermittently active mud volcano at the Costa Rica convergent margin. *Earth Planet. Sci. Lett.*, **235**(1), 79–95; 10.1016/j.epsl.2005.03.009 (2005).

Luff, R. & Wallmann, K. Fluid flow, methane fluxes, carbonate precipitation and biogeochemical turnover in gas hydrate-bearing sediments at Hydrate Ridge, Cascadia Margin: Numerical modeling and mass balances. *Geochim. Cosmochim. Acta*, **67**(18), 3403–3421; 10.1016/S0016-7037(03)00127-3 (2003).

Lundberg, N. *et al.* Forearc-basin closure and arc accretion in the submarine suture zone south of Taiwan. *Tectonophysics*, **274**(1), 5–23; 10.1016/S0040-1951(96)00295-8 (1997).

Mackenzie, F. T., Lerman, A., & Andersson, A. J. Past and present of sediment and carbon biogeochemical cycling models. *Biogeosci. Discuss.*, **1**(1), 27–85; (2004).

Mei, S., & Kohlstedt, D. L. Influence of water on plastic deformation of olivine aggregates: 1. Diffusion creep regime. *J. Geophys. Res–Sol. Ea.*, **105**(B9), 21457–21469; 10.1029/2000JB900179 (2000).

Menapace, W., Völker, D., Kaul, N., Tryon, M. D., & Kopf, A. J. The role of mud volcanism and deep-seated dewatering processes in the Nankai Trough accretionary prism and Kumano Basin, Japan. *Geochem. Geophys. Geosyst.*, **18**(7), 2486–2509; 10.1002/2016GC006763 (2017).

Michard, G. Behaviour of major elements and some trace elements (Li, Rb, Cs, Sr, Fe, Mn, W, F) in deep hot waters from granitic areas. *Chem. Geol.*, **89** (1–2), 117–134; 10.1016/0009-2541(90)90062-C (1990).

Middelburg, J. J. A simple rate model for organic matter decomposition in marine sediments. *Geochim. Cosmochim. Acta*, **53**(7), 1577–1581; 10.1016/0016-7037(89)90239-1 (1989).

Milkov, A. V. Global estimates of hydrate-bound gas in marine sediments: how much is really out there? *Earth Sci. Rev.*, **66**(3), 183–197; 10.1016/j.earscirev.2003.11.002 (2004).

doi:10.6342/NTU202000506

Milkov, A. V. *et al.* Gas hydrate systems at Hydrate Ridge offshore Oregon inferred from molecular and isotopic properties of hydrate-bound and void gases. *Geochim. Cosmochim. Acta*, **69**(4), 1007–1026; 10.1016/j.gca.2004.08.021 (2005).

Milkov, A. V. & Dzou, L. Geochemical evidence of secondary microbial methane from very slight biodegradation of undersaturated oils in a deep hot reservoir. *Geology*, **35**, 455, doi:10.1130/G23557A.1 (2007).

Moore, J. C. & Vrolijk, P. Fluids in accretionary prisms. *Rev. Geophys.*, **30**(2), 113–135;10.1029/92RG00201(1992).

Morono, Y. *et al.* Carbon and nitrogen assimilation in deep subseafloor microbial cells. *Proc. Natl. Acad. Sci. U.S.A.*, **108**, 18295–18300; 10.1073/pnas.1107763108 (2011).

Mottl, M. J., Komor, S. C., Fryer, P., & Moyer, C. L. Deep-slab fluids fuel extremophilic Archaea on a Mariana forearc serpentinite mud volcano: Ocean Drilling Program Leg 195. *Geochem., Geophy., Geosy.*, **4**(11); 10.1029/2003GC000588 (2003).

Na, H., Lever, M. A., Kjeldsen, K. U., Schulz, F. & Jørgensen, B. B. Uncultured Desulfobacteraceae and Crenarchaeotal group C3 incorporate ^{13}C-acetate in coastal marine sediment. *Environ. Microbiol. Rep.*, **7**, 614–622; 10.1111/1758-2229.12296 (2015).

Nauhaus, K., Boetius, A., Krüger, M., & Widdel, F. In vitro demonstration of anaerobic oxidation of methane coupled to sulphate reduction in sediment from a marine gas hydrate area. *Environ. Microbial.*, **4**(5), 296–305, doi:10.1046/j.1462-2920.2002.00299.x (2002).

Niemann, H. *et al.* Novel microbial communities of the Haakon Mosby mud volcano and their role as a methane sink. *Nature*, **443**(7113), 854–858; 10.1038/nature05227 (2006).

Oremland R. S. & Polcin S. Methanogenesis and sulfate reduction: competitive and noncompetitive substrates in estuarine sediments. *Appl. Environ. Microbiol.*, **44**, 1270–1276 (1982).

Orcutt, B. N. *et al.* Microbial activity in the marine deep biosphere: progress and prospects. *Front. Microbiol.*, **4**, 189; 10.3389/fmicb.2013.00189 (2013).

Padrón-Navarta, J. A. *et al.* On topotaxy and compaction during antigorite and chlorite dehydration: an experimental and natural study. *Contrib. Mineral Petrol.*, **169**(4), 35; 10.1007/s00410-015-1129-4 (2015).

Parkes, R. J. *et al.* Biogeochemistry and biodiversity of methane cycling in subsurface marine sediments (Skagerrak, Denmark). *Environ. Microbiol.*, **9**(5), 1146-1161; 10.1111/j.1462-2920.2006.01237.x (2007).

Peacock, S. A. Fluid processes in subduction zones. *Science*, **248**, 329–337; 10.1126/science.248.4953.329 (1990).

Pohlman, J. W., Bauer, J. E., Waite, W. F., Osburn, C. L., & Chapman, N. R. Methane hydrate-bearing seeps as a source of aged dissolved organic carbon to the oceans. *Nat. Geosci.*, **4**(1), 37; 10.1038/ngeo1016 (2011).

doi:10.6342/NTU202000506

Pohlman, J. W. *et al.* Methane sources in gas hydrate-bearing cold seeps: Evidence from radiocarbon and stable isotopes. *Mar. Chem.*, **115**(3–4), 102–109; 10.1016/j.marchem.2009.07.001 (2009).

Ray, J. S. *et al.* Origin of gases and water in mud volcanoes of Andaman accretionary prism: implications for fluid migration in forearcs. *Chem. Geol.*, **347**, 102–113; 10.1016/j.chemgeo.2013.03.015 (2013).

Reeburgh, W. S. Oceanic methane biogeochemistry. *Chem. Rev.*, **107**(2), 486–513; 10.1021/cr050362v (2007).

Reed, D., Lundberg, N., Liu, C. S., & Kuo, B. Y. Structural relations along the margins of the offshore Taiwan accretionary wedge: Implications for accretion and crustal kinematics. *Acta Geologica Taiwanica*, 30, 105–122 (1992).

Reimers, C. E. *et al.* Redox effects on the microbial degradation of refractory organic matter in marine sediments. *Geochim. Cosmochim. Acta*, 121, 582–598; 10.1016/j.gca.2013.08.004 (2013).

Reitz, A. *et al.* Sources of fluids and gases expelled at cold seeps offshore Georgia, eastern Black Sea. *Geochim. Cosmochim. Acta*, **75**(11), 3250–3268; 10.1016/j.gca.2011.03.018 (2011).

Saffer, D. M. & Tobin, H. J. Hydrogeology and mechanics of subduction zone forearcs: Fluid flow and pore pressure. *Annu. Rev. Earth Pl. Sc.*, **39**, 157–186; 10.1146/annurev-earth-040610-133408 (2011).

Savin, S. M. & Epstein, S. The oxygen and hydrogen isotope geochemistry of clay minerals. *Geochim. Cosmochim. Acta*, **34**(1), 25–42; 10.1016/0016-7037(70)90149-3 (1970a).

Savin, S. M. & Epstein, S. The oxygen and hydrogen isotope geochemistry of ocean sediments and shales. *Geochim. Cosmochim. Acta*, 34(1), 43–63; 10.1016/0016-7037(70)90150-X (1970b).

Schmoker, J. W. Volumetric calculation of hydrocarbons generated. *The petroleum system– from source to trap, Memoirs-American Association of Petroleum Geologists*, pp. 323–323 (1994).

Scholz, F. *et al.* Lithium isotope geochemistry of marine pore waters–insights from cold seep fluids. *Geochim. Cosmochim. Acta*, **74**(12), 3459–3475; 10.1016/j.gca.2010.03.026 (2010).

Schlüter, M., Sauter, E., Hansen, H. P., & Suess, E. Seasonal variations of bioirrigation in coastal sediments: Modelling of field data. *Geochim. Cosmochim. Acta*, **64**(5), 821–834; 10.1016/S0016-7037(99)00375-0 (2000).

Shao, W. Y., Chung, S. L., Chen, W. S., Lee, H. Y., & Xie, L. W. Old continental zircons from a young oceanic arc, eastern Taiwan: Implications for Luzon subduction initiation and Asian accretionary orogeny. *Geology*, **43**(6), 479–482; 10.1130/G36499.1 (2015).

Sheppard, S. M. F. & Gilg, H. A. Stable isotope geochemistry of clay minerals. *Clay Minerals*, **31**(1), 1−24 (1996).

doi:10.6342/NTU202000506

Sinclair, A. J. Selection of threshold values in geochemical data using probability graphs. *J. Geochem. Explor.*, **3**, 129–149, doi:10.1016/0375-6742(74)90030-2 (1974).

Sommer, S. *et al.* Efficiency of the benthic filter: Biological control of the emission of dissolved methane from sediments containing shallow gas hydrates at Hydrate Ridge. *Global Biogeochem. Cy.*, **20**(2), GB2019; 10.1029/2004GB002389 (2006).

Sommer, S. *et al.* Benthic respiration in a seep habitat dominated by dense beds of ampharetid polychaetes at the Hikurangi Margin (New Zealand). *Mar. Geol.*, **272**(1), 223–232; 10.1016/j.margeo.2009.06.003 (2010).

Sørensen, J., Christensen, D. & Jørgensen, B. B. Volatile fatty acids and hydrogen as substrates for sulfate-reducing bacteria in anaerobic marine sediment. *Appl. Environ. Microbiol.*, **42**, 5–11 (1981).

Su, C. C. Investigation of Gas Hydrate Resource Potential: Seismic, Heat Flow and Geochemical Studies (4/4) – gas composition of bottom water and sediments offshore southwest Taiwan. *Report of Central Geological Survey* **2015**, 104-11-F, 106 pp (in Chinese with English abstract) (2015).

Su, C. C., Hsu, S. T., Hsu, H. H., Lin, J. Y., & Dong, J. J. Sedimentological characteristics and seafloor failure offshore SW Taiwan. *Terr. Atmos. Ocean. Sci.*, **29**(1); 10.3319/TAO.2017.06.21.01 (2018).

Sun, C. H. *et al.* Origins of Taiwan's mud volcanoes: Evidence from geochemistry. *J. Asian Earth Sci.*, **37**(2), 105–116; 10.1016/j.jseaes.2009.02.007 (2010).

Sun, C. H. *et al.* Hydrocarbon seepages of Kaohsiung foothills, southwestern Taiwan. *Petroleum Geology Taiwan*, **38**, 117–133 (2008).

Suppe, J. Mechanics of mountain building and metamorphism in Taiwan. *Mem. Geol. Soc. China*, **4**(6), 67–89 (1981).

Takai, K. *et al.* Cell proliferation at 122 °C and isotopically heavy CH_4 production by a hyperthermophilic methanogen under high-pressure cultivation. *Proc. Natl. Acad. Sci. USA*, **105**, 10949–11954; 10.1073/pnas.0712334105 (2008).

Tamburin, F. *et al.* Investigating the history of East Asian monsoon and climate during the last glacial–interglacial period (0–140 000 years): mineralogy and geochemistry of ODP Sites 1143 and 1144, South China Sea. *Mar. Geol.*, **201**(1), 147–168; 10.1016/S0025-3227(03)00214-7 (2003).

Teng, L. S. Geotectonic evolution of late Cenozoic arc continent collision in Taiwan. *Tectonophysics*, **24**(10), 949–952; 10.1016/0040-1951(90)90188-e (1990).

Teng, L. S. Extensional collapse of the northern Taiwan mountain belt. *Geology*, **24**(10), 949–952; 10.1130/0091-7613 (1996).

Thauer, R. K., Zinkhan, D. M., & Spormann, A. M. Biochemistry of acetate catabolism in anaerobic chemotrophic bacteria. *Annu. Rev. Microbiol.*, **43**(1), 43–67; (1989).

doi:10.6342/NTU202000506

Tishchenko, P., Hensen, C., Wallmann, K., & Wong, C. S. Calculation of the stability and solubility of methane hydrate in seawater. *Chem. Geol.*, **219**(1–4), 37–52; 10.1016/j.chemgeo.2005.02.008 (2005).

Tobin, H. *et al.* NanTroSEIZE Plate Boundary Deep Riser 4: Nankai Seismogenic/Slow Slip Megathrust. *International Ocean Discovery Program Expedition 358 Preliminary Report*; 10.14379/iodp.pr.358.2019 (2019).

Tobin, H. J., & Saffer, D. M. Elevated fluid pressure and extreme mechanical weakness of a plate boundary thrust, Nankai Trough subduction zone. *Geology*, **37**(8), 679–682; 10.1130/G25752A.1 (2009).

Treude, T. *et al.* Anaerobic oxidation of methane above gas hydrates at Hydrate Ridge, NE Pacific Ocean. *Mar. Ecol. Prog. Ser.*, 264, 1–14 (2003).

Ussler, W. & Paull, C. K. Rates of anaerobic oxidation of methane and authigenic carbonate mineralization in methane-rich deep-sea sediments inferred from models and geochemical profiles. *Earth Planet. Sci. Lett.*, **266**(3–4), 271–287; 10.1016/j.epsl.2007.10.056 (2008).

Valentine, D. L. *et al.* Carbon and hydrogen isotope fractionation by moderately thermophilic methanogens. *Geochim. Cosmochim. Acta*, **68**(7), 1571–1590; 10.1016/j.gca.2003.10.012 (2004).

Vandieken, V., Finke, N. & Thamdrup, B. Hydrogen, acetate, and lactate as electron donors for microbial manganese reduction in a manganese-rich coastal marine sediment. *FEMS Microbiol. Ecol.*, **87**, 733–745; 10.1111/1574-6941.12259 (2014).

Vanneste, H. *et al.* Spatial variation in fluid flow and geochemical fluxes across the sediment–seawater interface at the Carlos Ribeiro mud volcano (Gulf of Cadiz). *Geochim. Cosmochim. Acta*, **75**(4), 1124–1144; 10.1016/j.gca.2010.11.017 (2011).

Vavilin, V. A. Estimating changes of isotopic fractionation based on chemical kinetics and microbial dynamics during anaerobic methane oxidation: apparent zero-and first-order kinetics at high and low initial methane concentrations. *Antonie van Leeuwenhoek*, **103**(2), 375–383; 10.1007/s10482-012-9818 (2013).

von Huene, R. & D. W. Scholl Observations at convergent margins concerning sediment subduction, subduction erosion, and the growth of continental crust. *Rev. Geophys.*, **29**(3), 279–316; 10.1029/91RG00969 (1991).

Wallmann, K. *et al.* Kinetics of organic matter degradation, microbial methane generation, and gas hydrate formation in anoxic marine sediments. *Geochim. Cosmochim. Acta*, **70**(15), 3905–3927; 10.1016/j.gca.2006.06.003 (2006a).

Wallmann, K. *et al.* Methane discharge into the Black Sea and the global ocean via fluid flow through submarine mud volcanoes. *Earth Planet. Sci. Lett.*, **248**(1), 545–560; 10.1016/j.epsl.2006.06.026 (2006b).

Wallmann, K. *et al.* The global inventory of methane hydrate in marine sediments: A theoretical approach. *Energies*, **5**(7), 2449–2498; 10.3390/en5072449 (2012).

doi:10.6342/NTU202000506

Wan, S., Li, A., Clift, P. D., & Stuut, J. B. W. Development of the East Asian monsoon: mineralogical and sedimentologic records in the northern South China Sea since 20 Ma. *Palaeogeogr., Palaeoclimatol., Palaeoecol.*, **254**(3–4), 561–582; 10.1016/j.palaeo.2007.07.009 (2007).

Wang, C. H., Chiang, C. J., Peng, T. R., & Liu, W. C. Deterioration of groundwater quality in the coastal Pingtung Plain, southern Taiwan. In: Ellis, J.B. (Ed.), Impacts of Urban Growth on Surface Water and Groundwater Quality. *International Association of Hydrological Sciences Publication*, No. 259, Wallingford, pp. 39–45. (1999).

Wang, P. *et al.* Exploring the Asian monsoon through drilling in the South China Sea. In *Proceedings of the Ocean Drilling Program: Initial Report* (Vol. 184, pp. 1-77); 10.2973/odp.proc.ir.184.2000 (2000).

Wang, P. L. *et al.* Spatial variations of community structures and methane cycling across a transect of Lei-Gong-Hou mud volcanoes in eastern Taiwan. *Front. Microbiol.*, 5, doi:10.3389/fmicb.2014.00121 (2014).

Wang, P. *et al. Proc. ODP, Init. Repts.*, 184. Texas A&M University, College Station, USA; 10.2973/odp.proc.ir.184.2000 (2000).

Wegener, G. & Boetius, A. An experimental study on short-term changes in the anaerobic oxidation of methane in response to varying methane and sulfate fluxes. *Biogeosciences*, **6**, 867–876; 10.5194/bg-6-867-2009 (2009).

Wei, W., Kastner, M., & Spivack, A. Chlorine stable isotopes and halogen concentrations in convergent margins with implications for the Cl isotopes cycle in the ocean. *Earth Planet. Sci. Lett.*, **266**(1-2), 90–104; 10.1016/j.epsl.2007.11.009 (2008).

Wessel, P. & Smith, W. H. F. New, improved version of the Generic Mapping Tools released. EOS Transactions AGU, **79**, 579; doi.org/10.1029/98EO00426 (1998).

Whiticar, M. J. Carbon and hydrogen isotope systematics of bacterial formation and oxidation of methane. *Chem. Geol.*, **161**(1–3), 291–314; 10.1016/S0009-2541(99)00092-3 (1999).

Wu, J. X. New data processing algorithm for marine heat flow and thermal modeling for Tsan-Yao mud volcano offshore SW Taiwan. Master thesis, Institute of Oceanography College of Science, National Taiwan University (in Chinese with English abstract); 10.6342/NTU201602190 (2016).

Yang, T. F. Gas Hydrate Resource Potential Area: Geological Surveys and Geochemical Investigation (4/4) – gas composition of bottom water and sediments offshore southwest Taiwan. *Report of Central Geological Survey* **2007**, 96-27-F, 71 pp (in Chinese with English abstract) (2007).

Yang, T. F. Investigation and Assessment of Gas Hydrate Resource Potential: Geochemical Studies (1/4) – gas composition of bottom water and sediments offshore southwest Taiwan. *Report of Central Geological Survey* **2011**, 97-29-A, 64 pp (in Chinese with English abstract) (2008).

doi:10.6342/NTU202000506

Yang, T. F. Investigation and Assessment of Gas Hydrate Resource Potential: Geochemical Studies (2/4) – gas composition of bottom water and sediments offshore southwest Taiwan. *Report of Central Geological Survey* **2011**, 98-27-A, 62 pp (in Chinese with English abstract) (2009).

Yang, T. F. Investigation and Assessment of Gas Hydrate Resource Potential: Geochemical Studies (3/4) – gas composition of bottom water and sediments offshore southwest Taiwan. *Report of Central Geological Survey* **2011**, 99-26-A, 56 pp (in Chinese with English abstract) (2010).

Yang, T. F. Investigation and Assessment of Gas Hydrate Resource Potential: Geochemical Studies (4/4) – gas composition of bottom water and sediments offshore southwest Taiwan. *Report of Central Geological Survey* **2012**, 100-25-A, 99 pp (in Chinese with English abstract) (2011).

Yang, T. F. Investigation of Gas Hydrate Resource Potential: Seismic, Heat Flow and Geochemical Studies (1/4) – gas composition of bottom water and sediments offshore southwest Taiwan. *Report of Central Geological Survey* **2012**, 101-22-F, 108 pp (in Chinese with English abstract) (2012).

Yang, T. F. Investigation of Gas Hydrate Resource Potential: Seismic, Heat Flow and Geochemical Studies (2/4) – gas composition of bottom water and sediments offshore southwest Taiwan. *Report of Central Geological Survey* **2013**, 102-19-F, 113 pp (in Chinese with English abstract) (2013).

Yang, T. F. Investigation of Gas Hydrate Resource Potential: Seismic, Heat Flow and Geochemical Studies (3/4) – gas composition of bottom water and sediments offshore southwest Taiwan. *Report of Central Geological Survey* **2014**, 103-16-F, 105 pp (in Chinese with English abstract) (2014).

Yang, T. F., Chou, C. Y., Chen, C. H., Chyi, L. L. & Jiang, J. H. Exhalation of radon and its carrier gases in SW Taiwan. *Radiat. Meas.*, **36**, 425–429 (2003).

Yang, T. F., Tien, J. L., Chen, C. H., Lee, T., & Punongbayan, R.S. Fission-track dating of volcanics in the northern part of the Taiwan-Luzon Arc: Eruption ages and evidence for crustal contamination. *J. Southeast Asian Earth Sci.*, **11**, 81–93; 10.1016/0743-9547(94)00041-C (1995).

Yang, T. F. *et al.* Composition and exhalation flux of gases from mud volcanoes in Taiwan. *Environ. Geol.*, **46**(8), 1003–1011; 10.1007/s00254-004-1086-0 (2004).

Yang, T. H. *et al.* Temporal Variations of Methane Flux from Submarine Mud Volcanoes off Southwest Taiwan. Abstract in the 12th International Conference of Gas in Marine Sediments, Ministry of Science and Technology, Taipei, Taiwan (2014).

Ye, H. *et al.* Pore water geochemistry in shallow sediments from the northeastern continental slope of the South China sea. *Mar. Pet. Geol.*, **75**, 68–82; 10.1016/j.marpetgeo.2016.03.010 (2016).

doi:10.6342/NTU202000506

Yeh, H. W. & Epstein, S. Hydrogen isotope exchange between clay minerals and sea water. *Geochim. Cosmochim. Acta*, **42**(1), 140–143; 10.1016/0016-7037(78)90224-7 (1978).

Yeh, Y. C. & Hsu, S. K. Crustal structures of the northernmost South China Sea: Seismic reflection and gravity modeling. *Mar. Geophys. Res.*, **25**(1–2), 45–61; 10.1007/s11001-005-0732-6 (2004).

Yoon, S., Sanford, R. A., & Löffler, F. E. *Shewanella spp.* use acetate as an electron donor for denitrification but not ferric iron or fumarate reduction. *Appl. Environ. Microbiol.*, **79**(8), 2818–2822; 10.1128/AEM.03872-12 (2013).

Yoshinaga, M. Y. *et al.* Carbon isotope equilibration during sulphate-limited anaerobic oxidation of methane. *Nat. Geosci.*, **7**(3), 190–194; 10.1038/ngeo2069 (2014).

You C. F., Castillo P. R., Gieskes J. M., Chan L. H., & Spivack A. J. Trace element behavior in hydrothermal experiments: Implications for fluid processes at shallow depths insubduction zones. *Earth Planet. Sci. Lett.*, **140**, 41–52;10.1016/0012-821X(96)00049-0 (1996).

Zhang, Y., Luo, M., Hu, Y., Wang, H., & Chen, D. An Areal Assessment of Subseafloor Carbon Cycling in Cold Seeps and Hydrate-Bearing Areas in the Northern South China Sea. *Geofluids*, **2019**; 10.1155/2019/2573937 (2019).

Zellmer, G. F., Edmonds, M., & Straub, S. M. Volatiles in subduction zone magmatism. *Geol. Soc. London Spec. Publ.*, **410**(1), 1–17;10.1144/SP410.13 (2014).

doi:10.6342/NTU202000506

Appendix

A. Thermodynamic calculations for the saturation state of authigenic carbonate

Ionic strength (I) was first calculated based on the concentrations of major and some minor ions. The calculation yielded I decreasing from around 0.6 to 0.7 for the top sediments (0 to 280 cmbsf) to 0.28 at core bottom. The Debye-Hückel Extended Law was further used to calculate activity coefficients (γ_i):

$$log\gamma_i = \frac{-Az_i^2\sqrt{I}}{1+Ba_i\sqrt{I}} \quad \text{(A2.1)}$$

where A and B are constants based on in situ temperature, z_i is ion charge, a_i is effective ionic radius, and i represents each ion. The values of A, B, and a_i were cited from *Manov et al.* [1943]. Temperatures in sediments were calculated based on in situ bottom water temperature (10.5 ^{o}C) and a temperature gradient of 0.39 ^{o}C/m at TY1[2]. Density of porewater was assumed to be 1.03 g/cm^3.

The activity quotients (Q) for the carbonate precipitation (reactions below) at site A2-2 were calculated using pH 8 and shown in Table S1. The solubility product constant (K_{sp}) values were calculated using Eq. (S2):

Dolomite: $Mg^{2+} + Ca^{2+} + 2HCO_3^- \rightarrow CaMg(CO_3)_2 + 2H^+$ $\Delta G^o = 20.24$

Mg-calcite: $Mg^{2+} + HCO_3^- \rightarrow MgCO_3 + H^+$ $\Delta G^o = 29.5$

Calcite: $Ca^{2+} + HCO_3^- \rightarrow CaCO_3 + H^+$ $\Delta G^o = 11.54$

$$logK_{sp} = \frac{-\Delta G^\circ}{2.303RT} \quad \text{(A2.2)}$$

where R is the ideal gas constant, and T is the in situ temperature.

doi:10.6342/NTU202000506

Estimation of initial water budgets

The total amount of smectite-bound fluid within the incoming plate is estimated considering the weight of the incoming plate and the content of smectite and porosity in the sediments [*Freundt et al.*, 2014; *Jarrard*, 2003; *von Huene and Scholl*, 1991]:

$$F_a = C_a \cdot H \cdot (1 - \varphi_a) \cdot \rho \cdot V_a \cdot L_a \quad \text{(A2.3)}$$

where F_a is the flux, C_a is the weight percentage of mineral-bound water in smectite, H is the pre-subducted sediment thickness (1 km; 30% and 70% of sediments assumed to be accreted and subducted along with the plate, respectively[9]), ρ is the density of dry sediments (2.7 g cm^{-3}) [*Chen*, 1981], φ_a is the porosity of the sediments from the incoming plate (50%) [*Wang et al.*, 2000], L_a is the length of trench (172 km; the trench length covering the region with SMVs) [*Chen et al.*, 2014a], and V_a is the subduction rate (66–76 mm yr^{-1}) [*Lundberg et al.*, 1997; *Suppe*, 1981]. For seawater-like pore fluid, φ_a instead of $(1 - \varphi_a)$ in Eq. (A2.3) was used. For smectite-bound fluid, smectite abundances at 4.5–24.8 wt.% for the passive margin and abundances of mineral-bound fluid in smectite at 10 to 20% were adopted for calculation [*Bird* ,1984; *Hu et al.*, 2012; *Liu et al.*, 2003; *Wan et al.*, 2007; *Wang et al.*, 2000]. With these parameters, C_a was calculated to be 0.5 – 5.0 wt.%. For seawater-like pore fluid, the parameters include ρ (1.03 g/cm^3) and C_a (100 wt.%). The total smectite-bound fluid and seawater-like pore fluid from the incoming plate were calculated to be 0.7 – 8.8 ×10^8 kg yr^{-1} and 5.9 – 6.7 ×10^9 kg yr^{-1}, respectively.

doi:10.6342/NTU202000506

B. Modeling sensitivity test

We modeled profiles for site A2-2 (at western center) as an example of sensitivity tests. The details of tests are described below:

(1) Discretization of depth and time (dx and dt):

The depth and time (dx= 0.01 m and dt= 0.01 year for all sites) grids were determined by running the model with progressively smaller discretization until the results were numerically stable and accurate. Our results showed that the modeled profiles display almost the same trend regardless of whether dx was equal to 0.01 or 0.005 (Fig. A2.6a). When dt was decreased from 0.01 to 0.001, profiles of methane concentrations slightly changed, resulting in only an increase of 15 % in AOM rates (R_{AOM}; Fig. A2.6b).

(2) Considerations of reaction terms (rates of AOM and organic matter degradation) and bubble irrigation:

To better illustrate the significance of each terms, we tested our model in three cases: (a) with bubble irrigation, organic matter degradation (including OSR and ME), and AOM; (b) without bubble irrigation and organic matter degradation; (c) without bubble irrigation. Our results showed that profiles were not fitted in case (b) (Fig. A2.7b) or in case (c) (Fig. A2.7c), suggesting that bubble irrigation was vital to explain no significant variation of chloride concentration at the top intervals (0 to 280 cmbsf) (Fig. A2.7a).

(3) Upward fluid velocity (u_0), depth of bubble irrigation (L_{irr}), two irrigation coefficients (α_1 and α_0), and lower boundary of methane (CH4L):

Our model-derived advection rates (u_0) were most sensitive to the changes in irrigation depth (L_{irr}) with 2–2.5 folds differences in u_0 for only a 10% variation in L_{irr} (Fig. A2.8a). The variations (±10%) of L_{irr} changed the AOM rate by 2 to 3% (Fig. A2.8b). If L_{irr} was half of the best fitting value (the best value of L_{irr} is 2.8 m), the rate of AOM was shifted by 3%. When L_{irr} was increased by 50%, the AOM rate became almost twice the best fitting one; however, such condition would not occur because the theoretical limitation of L_{irr} is up to 3 m [*Haeckel et al.*, 2007]. The change (±50%) of α_1 and α_0 resulted in 5–6% and 2–4% variations in rates of AOM, respectively (Figs. A2.8c and A2.8d). Modelled values for benthic methane fluxes were insensitive to variations (±50%) in u_0 and CH4L probably because of impact of bubble irrigation (Fig. A2.8e). In addition, methane benthic fluxes did not vary significantly with L_{irr} (±50%).

doi:10.6342/NTU202000506

C. Estimation of brackish water expelled from 13 SMVs in Taiwan

We first fitted the calculated velocities versus distance from the edge of crater ((x–L') in Fig. A2.9b) with exponential equations (Fig. A2.9a). Based on different (x–L'), velocity distribution could be further integrated with different ring areas (Fig. S9b, dashed-line) using Eq. 2.9. Since each SMV has different diameters of its crater and cone structure, the exponential relationships derived from (x–L') were replaced with "Ratio" ((x–L')/ (L–L') in Fig. A2.9b) and shown as follow:

$$velocity_{max} = 5\ (cm\ yr^{-1}) \times EXP(-13 \times Ratio) \quad \text{(A2.4)}$$

$$velocity_{min} = 2\ (cm\ yr^{-1}) \times EXP(-10 \times Ratio) \quad \text{(A2.5)}$$

The corresponding velocity variation along the transect at each SMV was calculated. Diameters of each crater and SMV are cited from previous observations [*Chen et al.*, 2014a]. Fluxes of brackish water discharged from each SMV are shown in Table A2.6.

doi:10.6342/NTU202000506

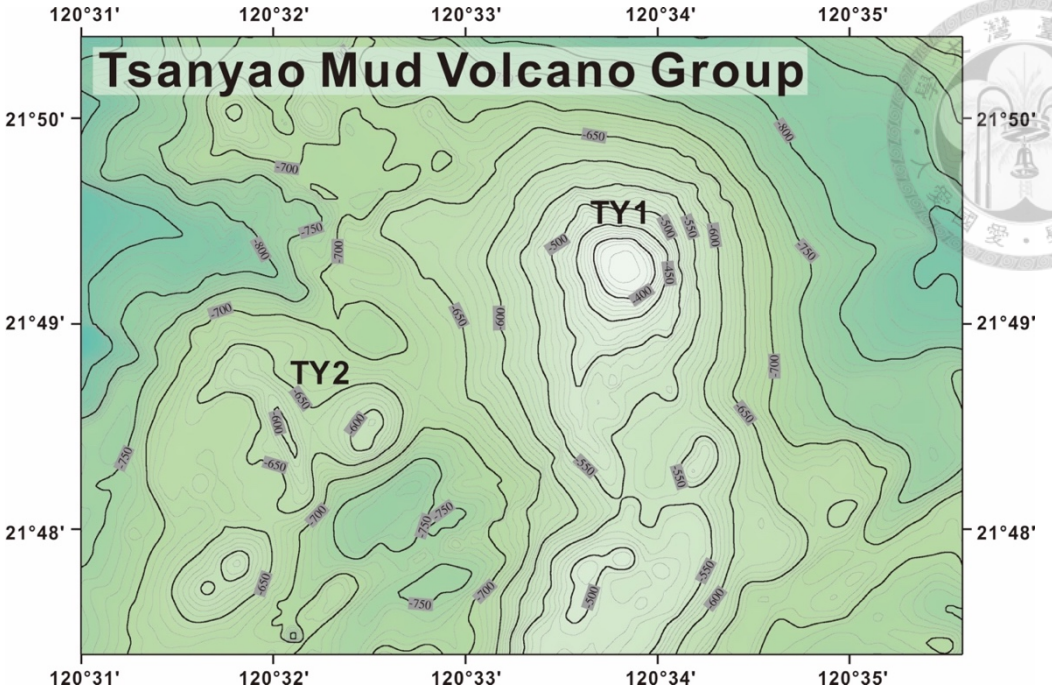

Figure A2.1. Bathymetric map of Tsanyao Mud Volcano Group.

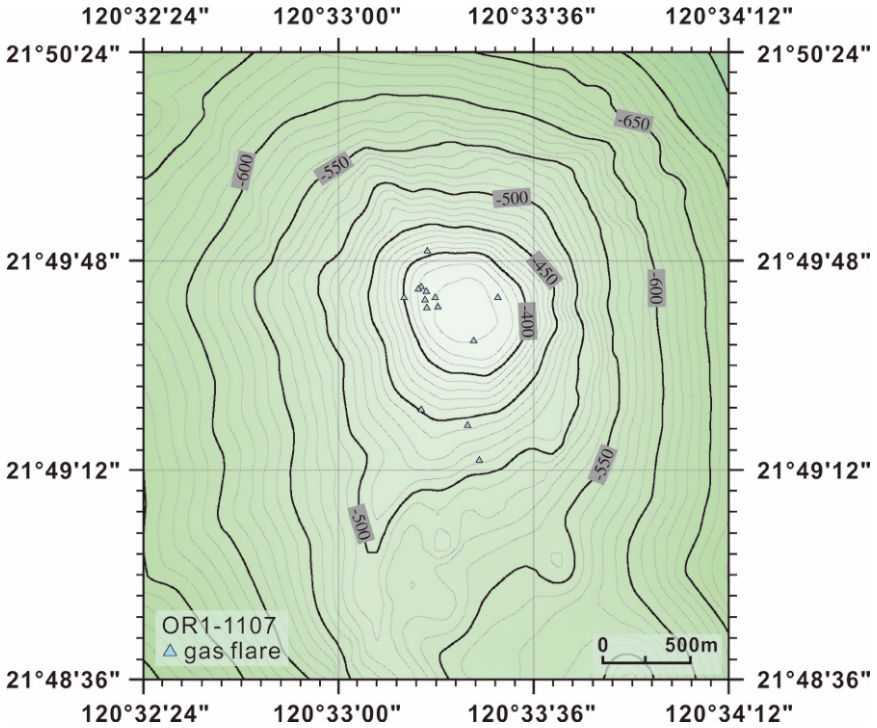

Figure A2.2. Distribution of gas flares (triangles) found on TY1 during the cruise OR1-1107.

doi:10.6342/NTU202000506

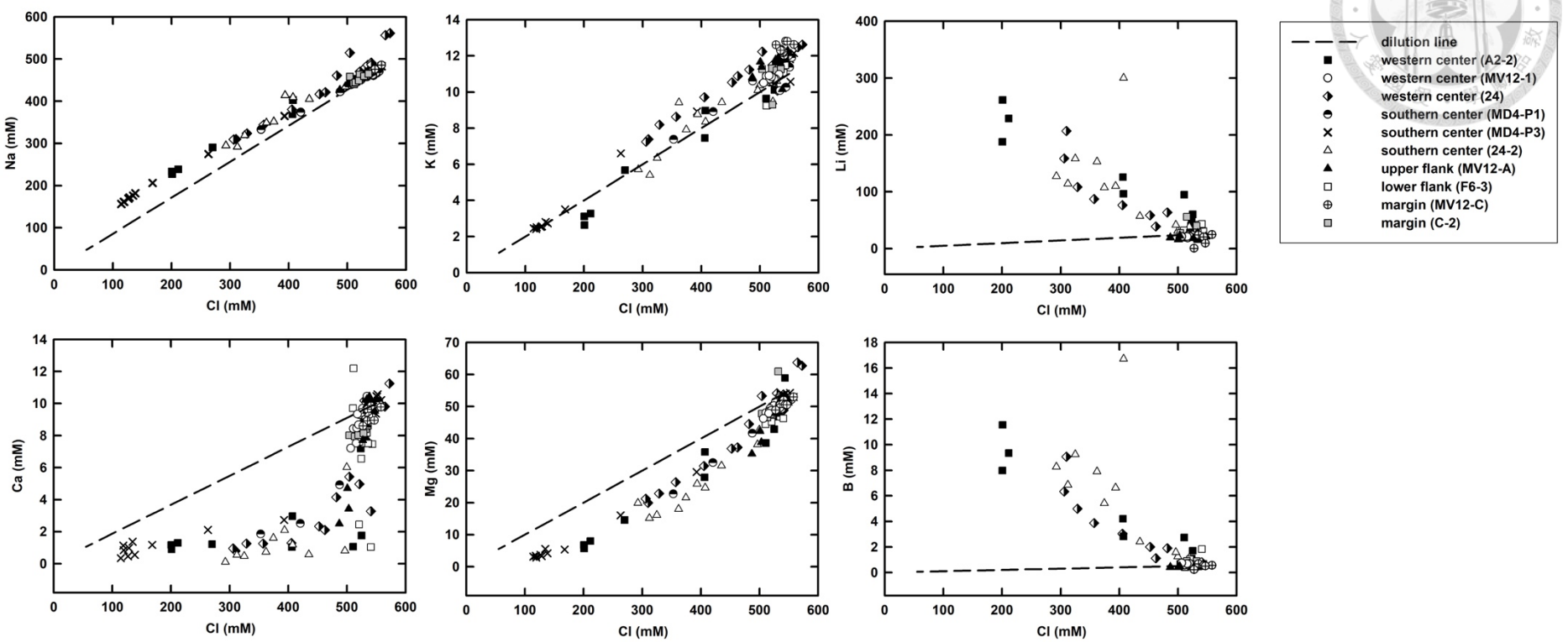

Figure A2.3. Concentrations of sodium, potassium, calcium, magnesium, lithium, and boron versus chloride. The dashed-line denotes the equal dilution trend between specific ion and chloride.

doi:10.6342/NTU202000506

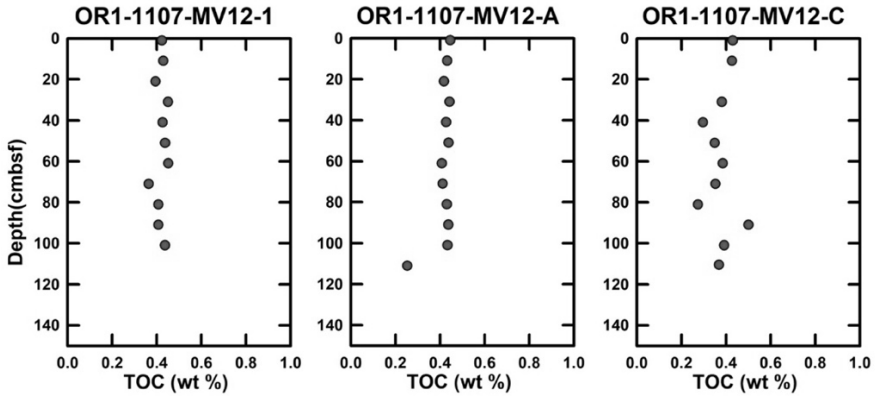

Figure A2.4. TOC concentration (wt%) depth profiles at TY1.

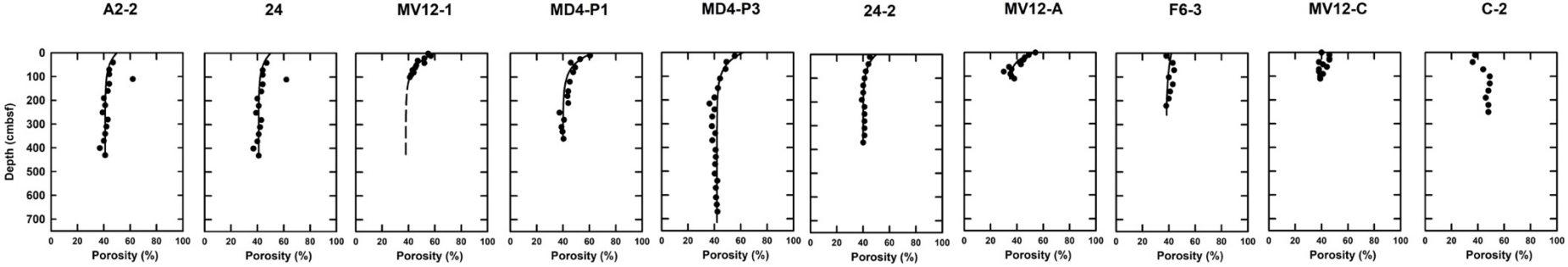

Figure A2.5. Observed and modeled (black line) porosity variation with depth. Without real data, the porosity of site 24 was assumed to be the same as that of site A2-2.

doi:10.6342/NTU202000506

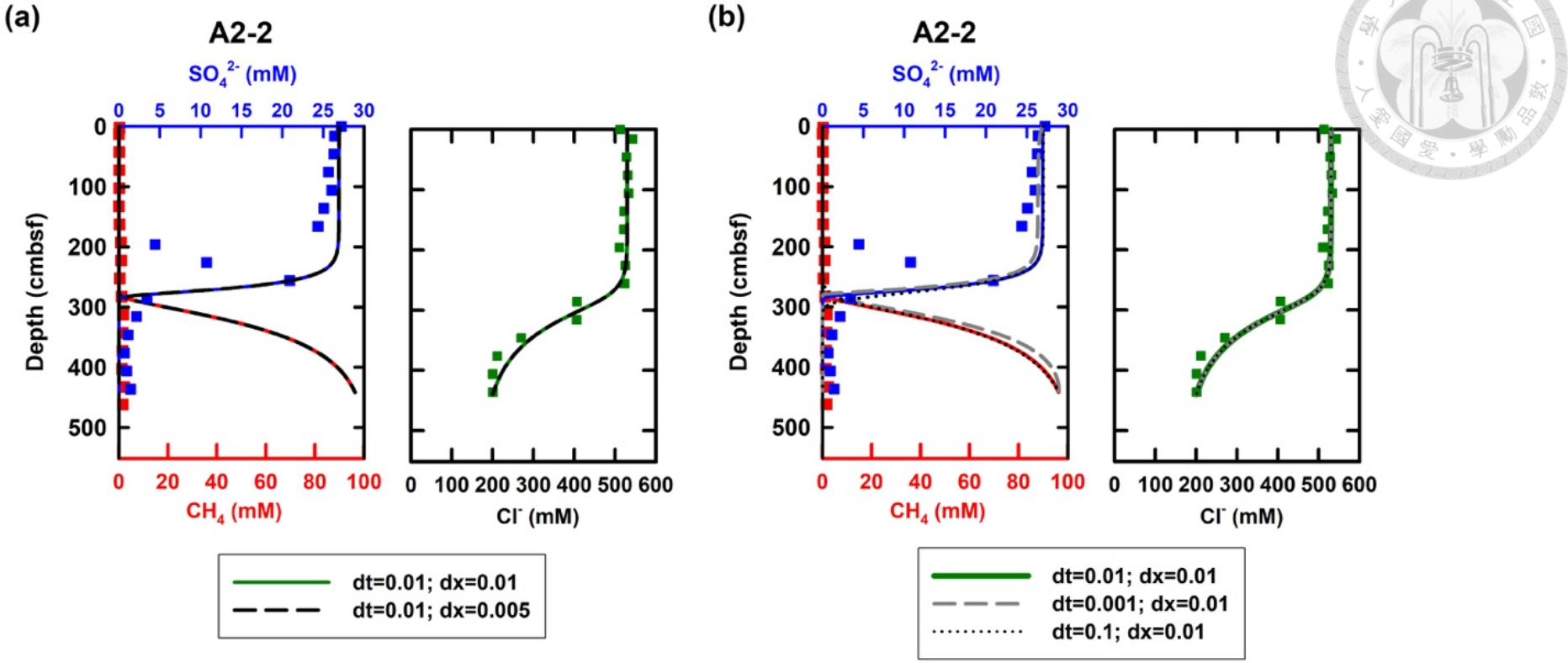

Figure A2.6. Results of reactive-transport model based on different combinations of time and depth discretization.

doi:10.6342/NTU202000506

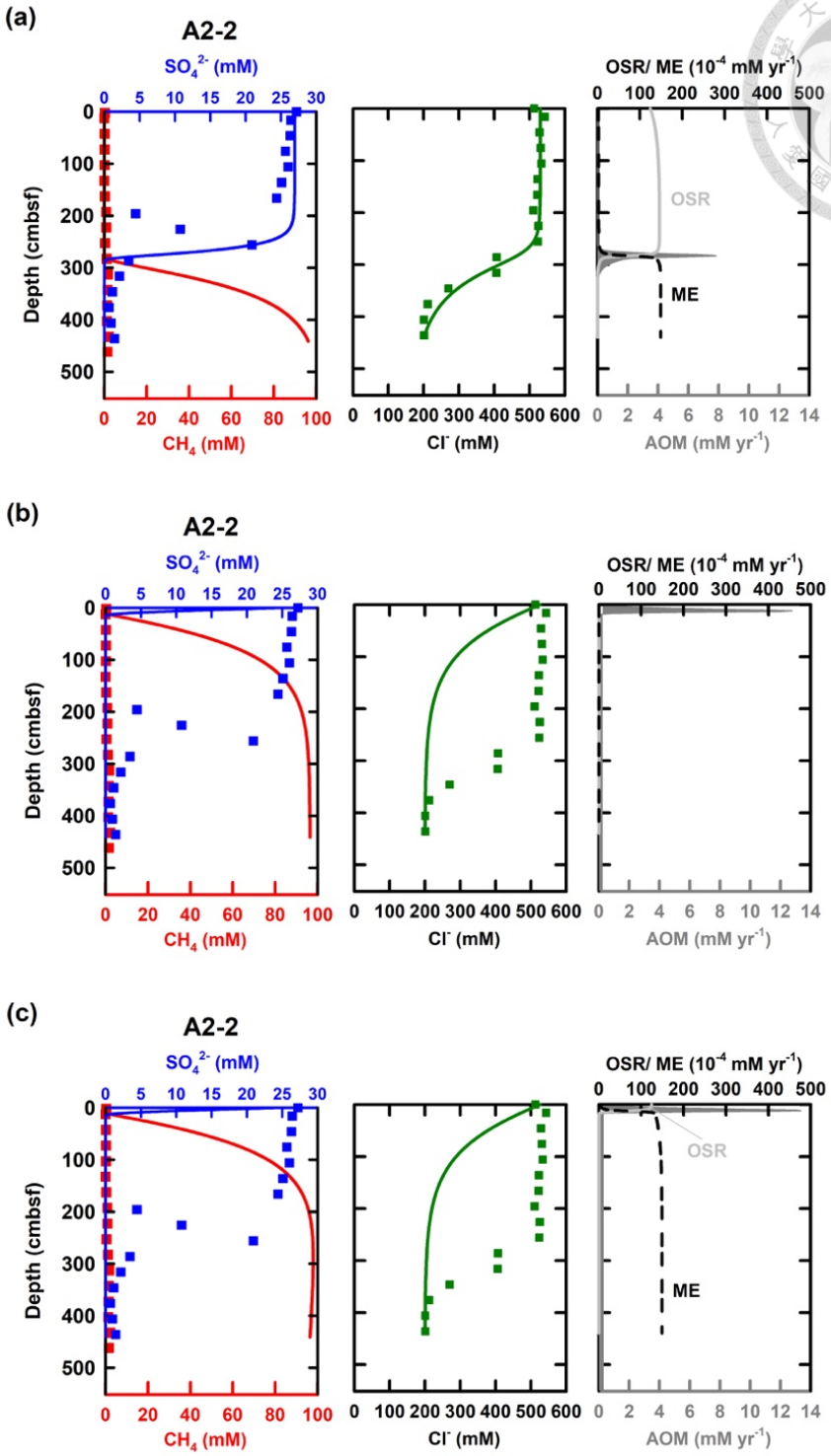

Figure A2.7. Three scenarios for model test: (a) with bubble irrigation, organic matter degradation (OSR+ME), and AOM; (b) without bubble irrigation and organic matter degradation; (c) without bubble irrigation.

doi:10.6342/NTU202000506

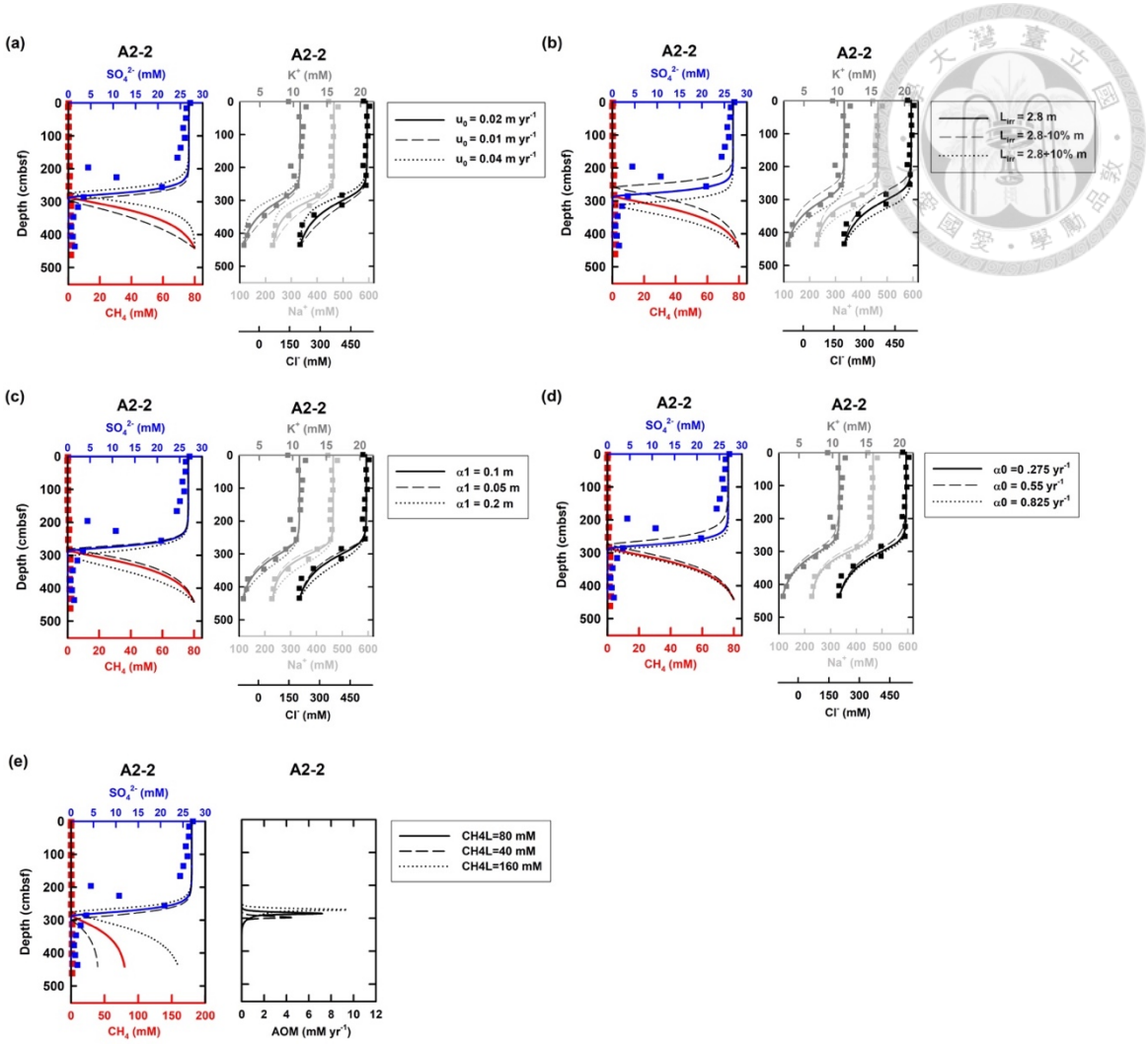

Figure A2.8. Results for sensitivity tests of: (a) upward fluid velocity (u_0); (b) depth of bubble irrigation (L_{irr}); (c) two irrigation coefficients (α_1 and α_0); (d) lower boundary of methane (CH4L). The best fit between modeling and analyzed data is denoted by solid line.

doi:10.6342/NTU202000506

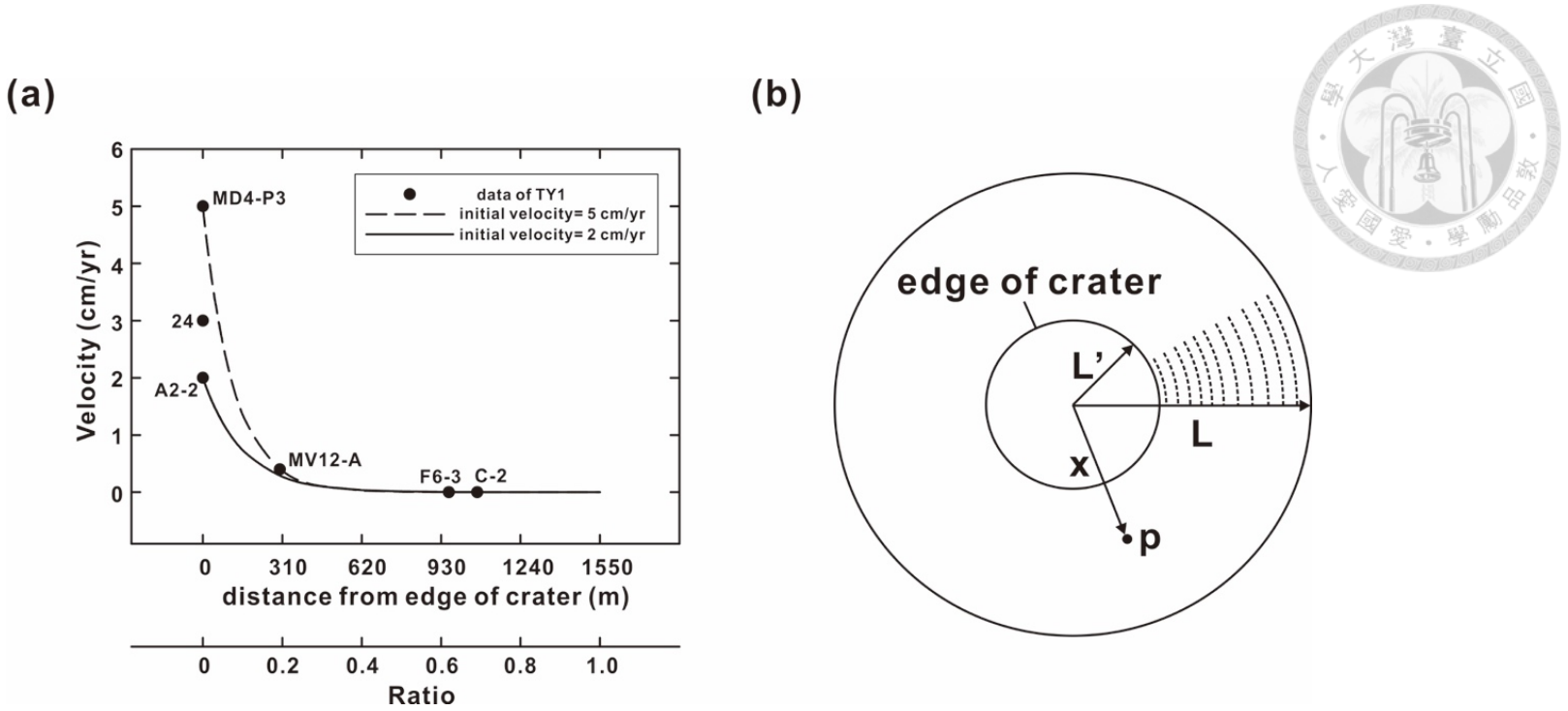

Figure A2.9. (a) Exponential relationship between velocity and distance from edge of crater (x in Fig. A2.8b) at TY1. (b) A conceptual sketch of plane view of TY1. L is the radius of the mud volcano; L' is the radius of crater; x is the distance between center and point p, which denotes any location between edge of crater and periphery. "Ratio" in Fig. S9a is derived from (x–L')/ (L–L').

doi:10.6342/NTU202000506

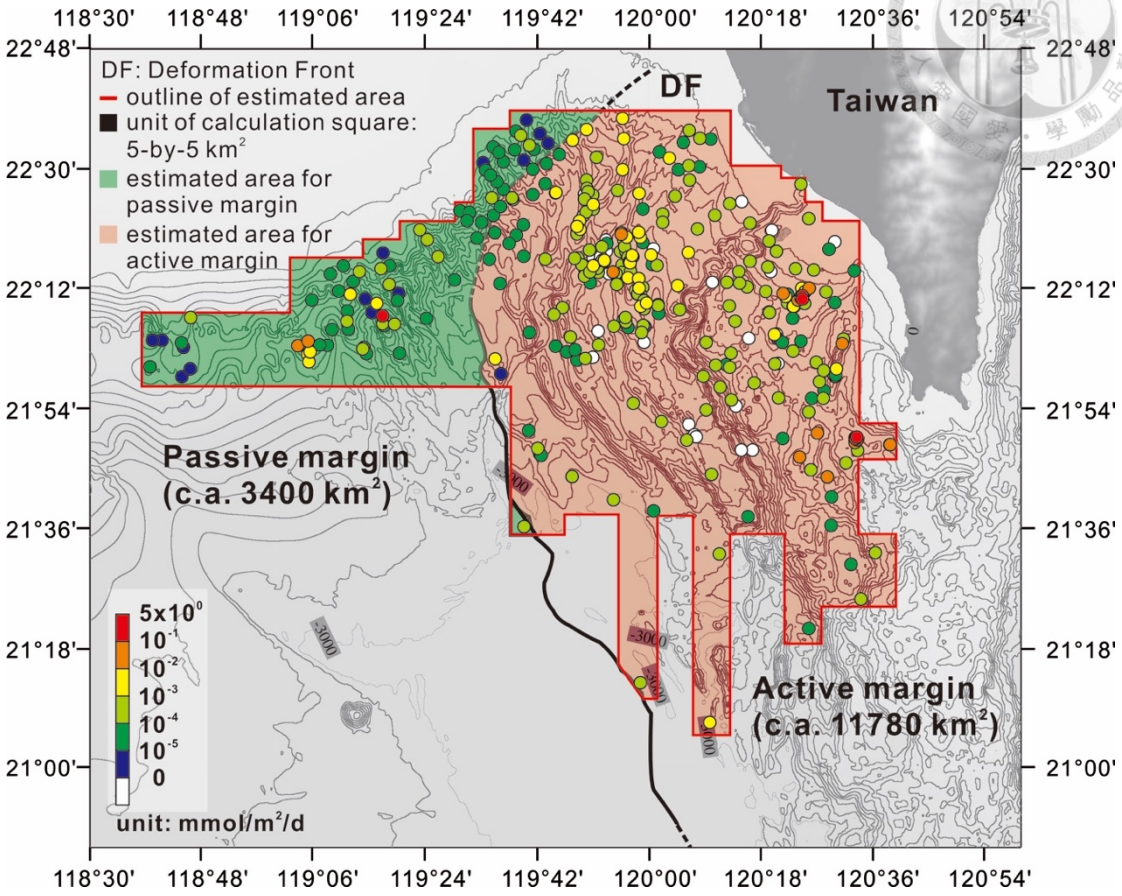

Figure A3.1. Area coverage for the sampling in active and passive margin used for the area-based rate calculation. The underlay was based on the results of effluxes.

doi:10.6342/NTU202000506

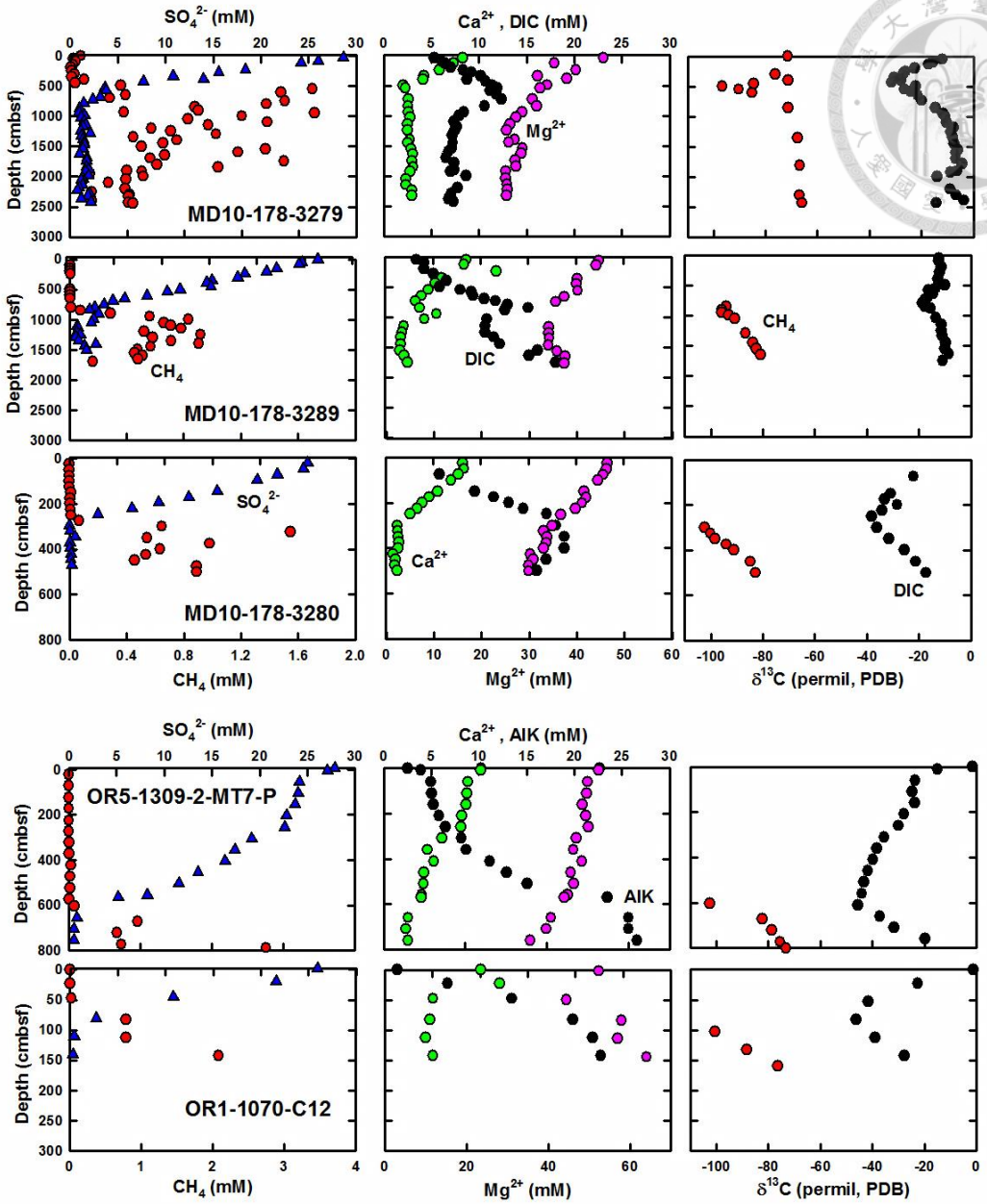

Figure A3.2. Pore water profiles of data available for carbon mass balance. Data for site 3280 except for Ca^{2+} and Mg^{2+} are adopted from *Lin et al.* [2014].

doi:10.6342/NTU202000506

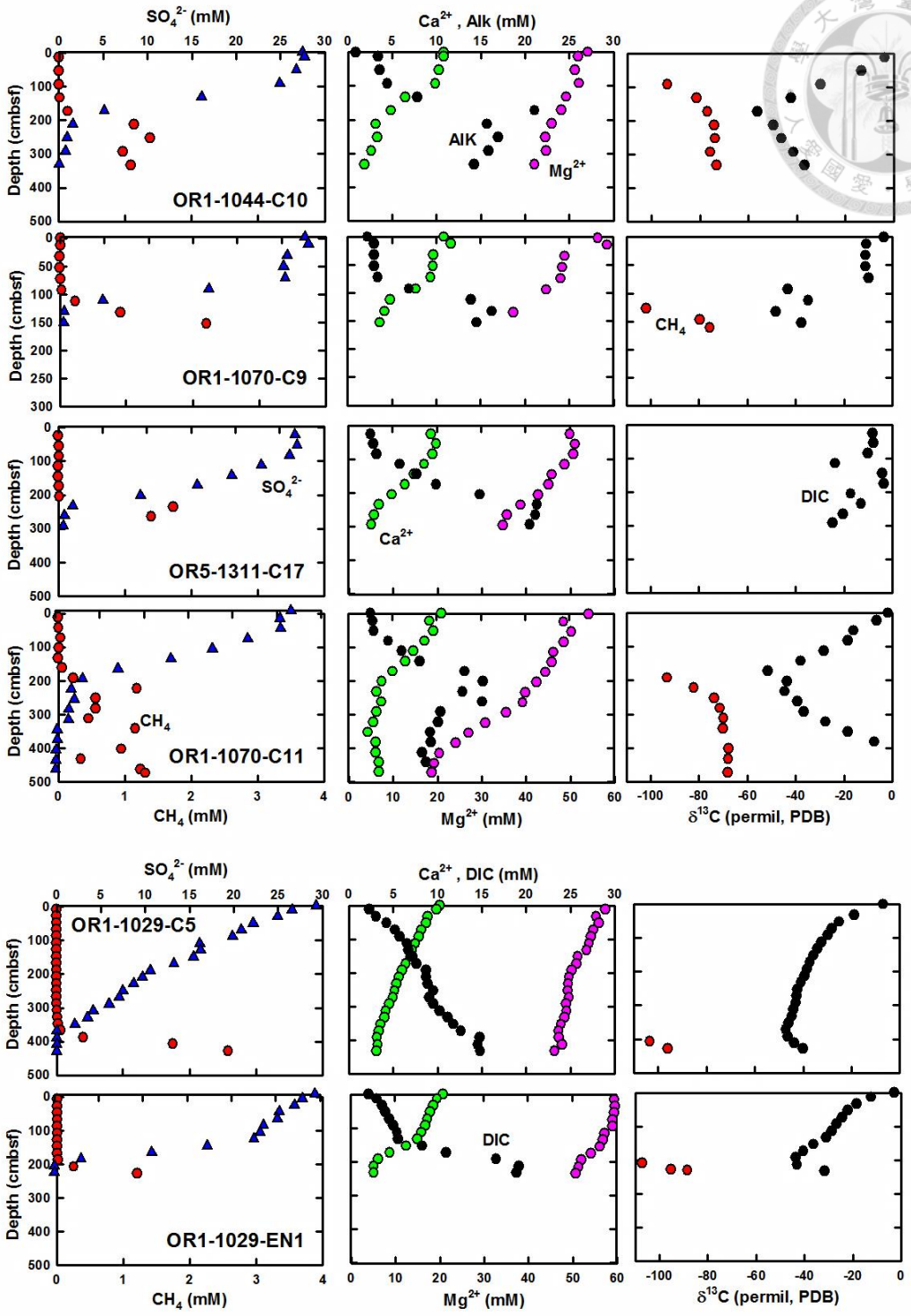

Figure A2.2. Continued.

doi:10.6342/NTU202000506

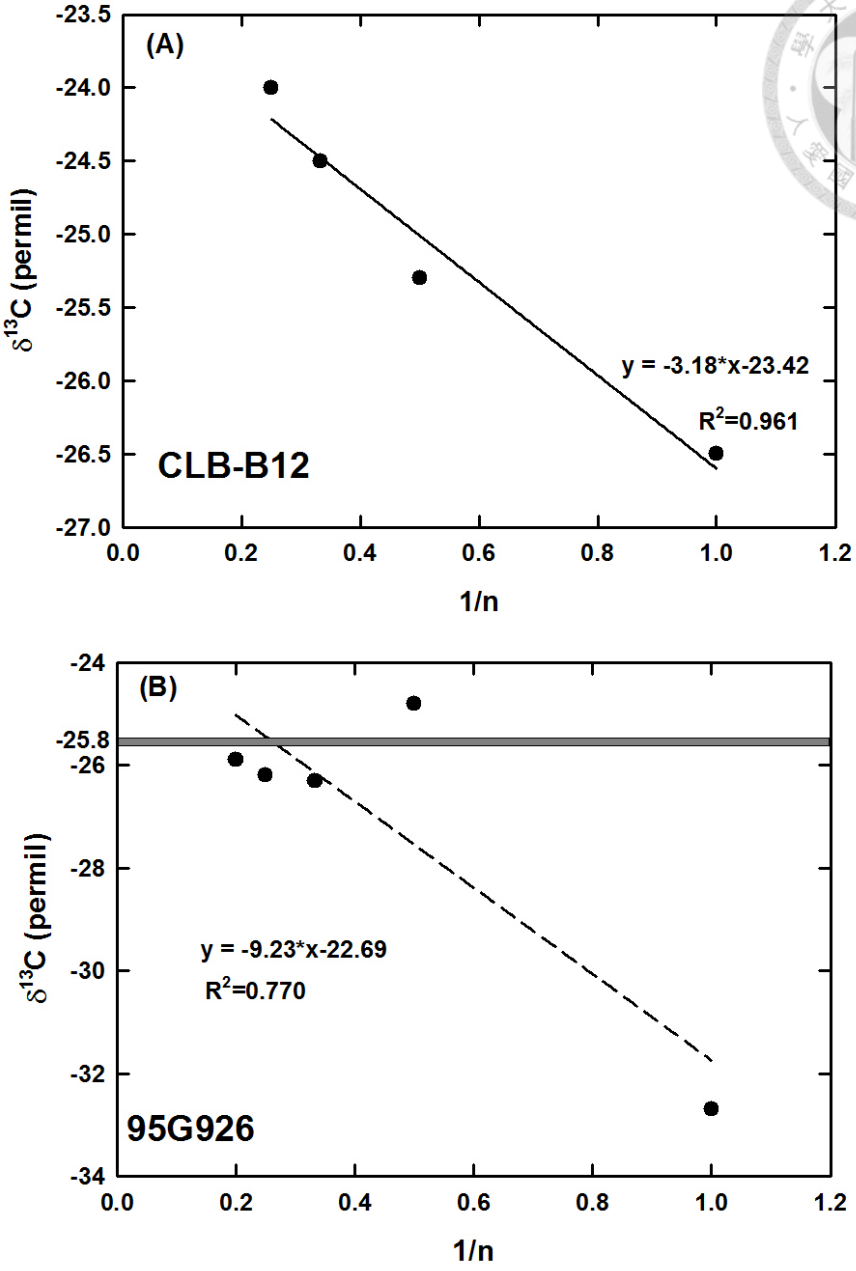

Figure A3.3. Examples of regression lines used for calculation of deep microbial methane production in different cases. At site CLB-B12 (Table 2.1), R^2 is more than 0.9 (A). The $\delta^{13}C$ value of thermogenic methane could be derived from the function of regression line (x=1). At site 95G926 (Table 2.1), R^2 is less than 0.9 (B). Averaged $\delta^{13}C$ values of C_{2+} (gray bar; the $\delta^{13}C$ values of C_{2+} generally clustered within ±1‰) was the $\delta^{13}C$ value of themo-hydrocarbon source (-25.8 ‰).

doi:10.6342/NTU202000506

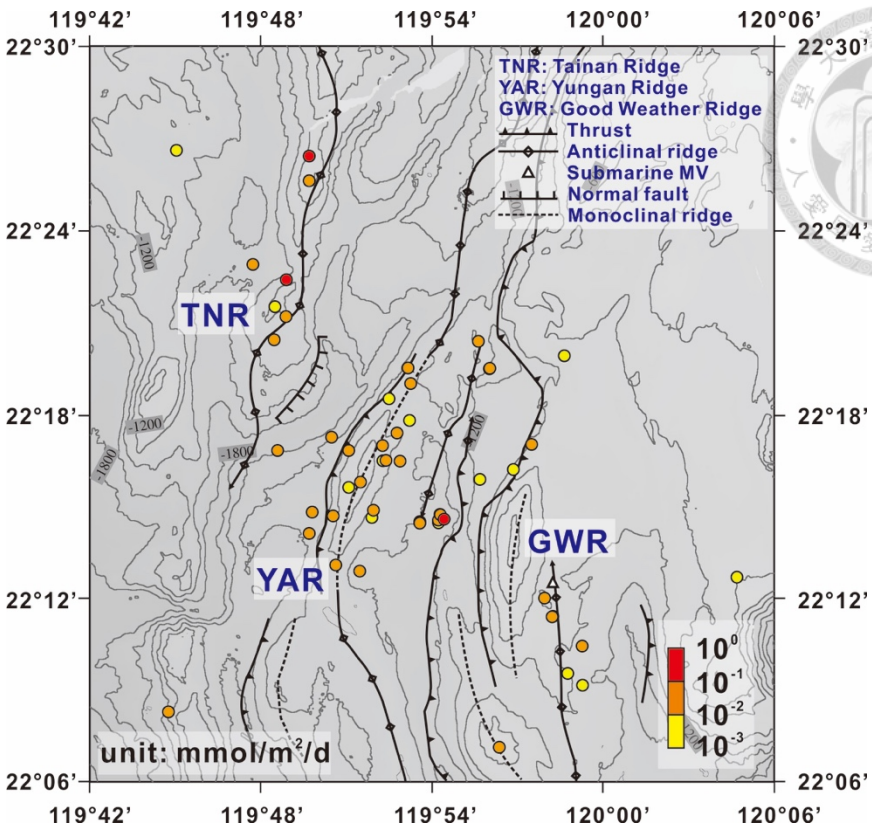

Figure A3.4. An enlarged view of the red square region in Fig. 2.2. The tectonic structures are modified from *Lin et al.* [2013].

doi:10.6342/NTU202000506

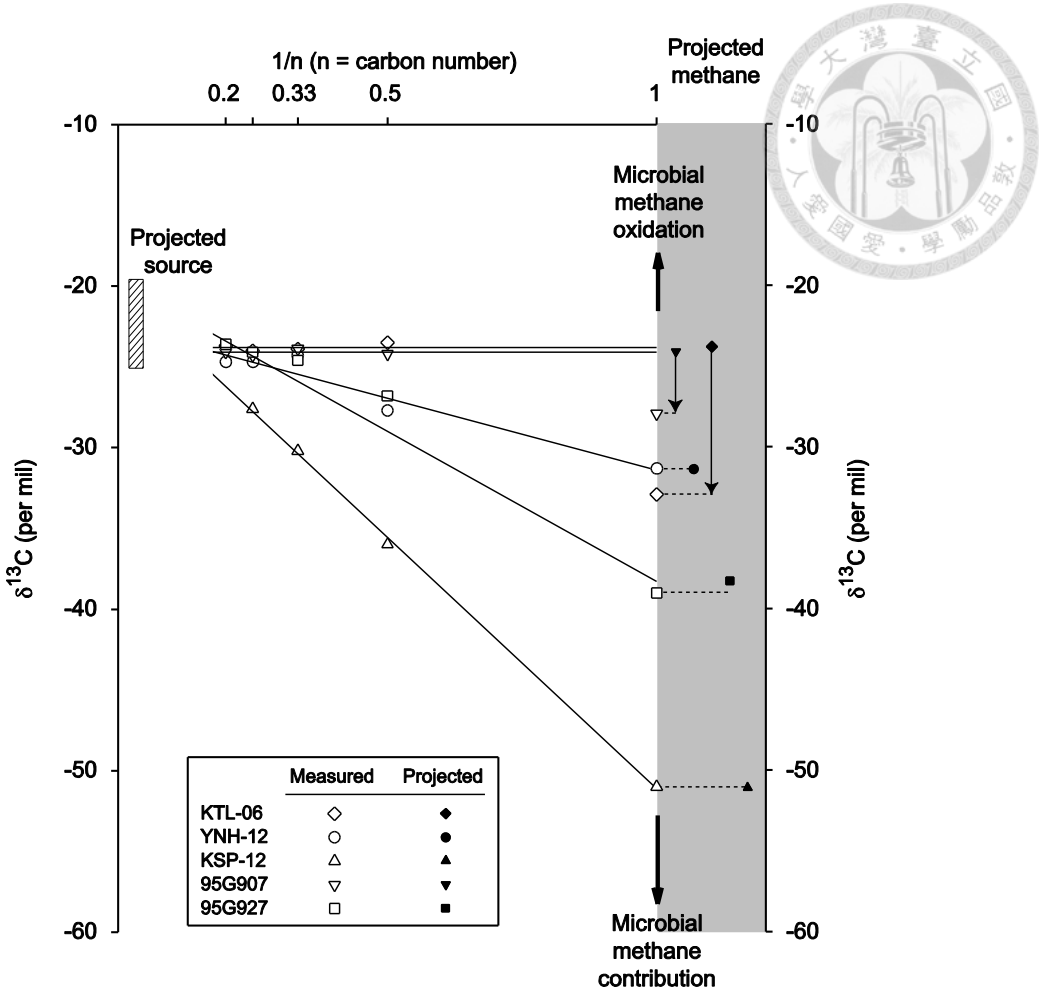

Figure A3.5. Natural gas plot for five representative gas samples collected from mud volcanoes and seeps onshore southwestern Taiwan (15 sets of data from Sun et al. [2008 and 2010] were shown in Table 1). Open symbols represent the measured $\delta^{13}C$ values of hydrocarbons, whereas solid symbols in the right gray panel indicate the $\delta^{13}C$ values of pure thermogenic methane projected (shown in solid lines) from the linear regression of all $\delta^{13}C$ values or averaging $\delta^{13}C$ values of C_{2+} in the corresponding sample. The measured $\delta^{13}C$ values of methane are extended by dashed lines to the right panel for comparisons with the projected values (offsets indicated by the thin arrows). The thick arrows at 1/n =1 indicates the effects of microbial oxidation and methanogenesis on shifting the $\delta^{13}C$ values of methane. The hatched area indicates the projected $\delta^{13}C$ values of hydrocarbon source.

doi:10.6342/NTU202000506

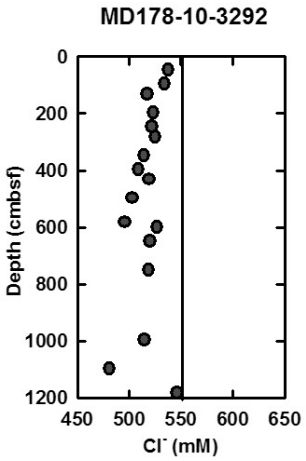

Figure A3.6. Chloride profile for site MD178-10-3292 showed the possible input of low salinity, deep fluid. This site is located at the anticlinical ridge where a submarine mud volcano is situated (Fig. A2.4).

doi:10.6342/NTU202000506

Table A2.1. Activity quotient (Q) and K_{sp} for carbonate precipitation reactions at site A2-2.

		Q			K_{sp} (at 25°C)			Oversaturation		
Depth (m)	Temp (°C)	Dolomite	Mg-calcite	Calcite	Dolomite	Mg-calcite	Calcite	Dolomite	Mg-calcite	Calcite
2.86	16.5	4.03E+07	2.47E+04	1.64E+03	2.85E-04	6.80E-06	9.52E-03	+	+	+
3.16	17.7	1.51E+07	2.25E+04	6.74E+02	2.85E-04	6.80E-06	9.52E-03	+	+	+
3.46	19.1	1.33E+07	1.39E+04	9.62E+02	2.85E-04	6.80E-06	9.52E-03	+	+	+
3.76	20.5	9.19E+06	8.24E+03	1.12E+03	2.85E-04	6.80E-06	9.52E-03	+	+	+
4.06	22.1	8.08E+06	7.44E+03	1.09E+03	2.85E-04	6.80E-06	9.52E-03	+	+	+
4.36	23.8	4.02E+06	5.53E+03	7.26E+02	2.85E-04	6.80E-06	9.52E-03	+	+	+

Note: + represents oversaturation with respect to specific carbonate.

doi:10.6342/NTU202000506

Table A2.2. Porosity extrapolation derived from the IODP 358.

		porosity at depths (m)					
site	r	0 m	500 m	1000 m	3200 m	5700 m	reference
IODP 358, site C0002[a]	0.00043	0.650	0.524	0.423	0.164	0.056	*Tobin et al.* [2019]

Note: calculation follows: a: $\varphi(x) = \varphi_0 \cdot e^{-rx}$

doi:10.6342/NTU202000506

Table A2.3. Parameters comparisons for the Nankai and Taiwan subduction systems.

parameter	Nankai Trough[a]	Taiwan	reference
Taper angles α (slope) and β (subduction angle)	β = 3.4–10.8^o	α = 3^o; β = 6^o	*Suppe* [1981]
Surface heat flow near the trench	90–140 mW/m^2	40–130 mW/m^2	*Chiao* [2015]
Thermal conductivity of incoming sediments	1.0–1.7 W/mK	1.2 W/mK	*Shyu and Hung* [2005]; *Chen et al.* [2012]
Convergence Rate	4.0 cm/yr	6.6–7.6 cm/yr	*Suppe* [1981]
Bulk density of incoming sediment at depth	1.5–2.1 g/cm^3	1.4–2.2 g/cm^3	*Wang et al.* [2000]
Porosity	0.65	0.5	*Wang et al.* [2000]
Smectite abundance in incoming sediments with z	45%	4.5–24.8%	*Wang et al.* [2000]
Mean thickness of the subduction channel	1000 m	1000 m	
Length of the trench for the Kumano Basin and extension of the MVs area	100 km	172km	*Chi et al.* [2003]; *Hwang et al.* [2006]
Smectite temperature stability fields	60–150	60–150	
Smectite initial water content	20%	10–20%	*Bird* [1984]
Distance from deformation front to SMV region	55 km	80 km	*Lin et al.* [2009]
Length of SMV region	35 km	41 km	*Lin et al.* [2009]

Note: a: parameters from Nankai Trough are cited from *Menapace et al.* [2017].

doi:10.6342/NTU202000506

Table A2.4. Parameters used in the numerical model.

			Western center			Southern center			Upper flank	Lower flank
Parameter	Symbol	Unit	A2-2	24[a]	MV12-1[b]	MD4-P1	MD4-P3	24-2	MV12-A	F6-3
Temperature		^oC	10.5							
Diffusion coefficient of chloride	DiCl	$m^2\ yr^{-1}$	0.0448							
Diffusion coefficient of sodium	DiNa	$m^2\ yr^{-1}$	0.0290							
Diffusion coefficient of potassium	DiK	$m^2\ yr^{-1}$	0.0437							
Diffusion coefficient of sulfate	DiSO4	$m^2\ yr^{-1}$	0.0231							
Diffusion coefficient of methane	DiCH4	$m^2\ yr^{-1}$	0.0371							
Length of model column		m	4.4	4.4	4.4	3.7	7.15	3.8	1.1	2.6
Porosity at sediment surface		ϕ_0	0.50	0.50	0.60	0.62	0.62	0.50	0.54	0.42
Porosity at end of column		ϕ_f	0.41	0.41	0.38	0.40	0.42	0.40	0.38	0.38
Empirical coefficient for porosity fitting	γ	m^{-1}	2	2	2	2	2	2	3	1
Cl concentration at upper boundary	ClU	mM	530	550	535	550	552	526	537	540
Cl concentration at lower boundary	ClL	mM	200	310	200	350	120	290	480	530
Na concentration at upper boundary	NaU	mM	465	480	467	466	476	450	470	465
Na concentration at lower boundary	NaL	mM	230	310	230	330	162	292	420	455
K concentration at upper boundary	KU	mM	11	12	11	12	12	10.8	12	11
K concentration at lower boundary	KL	mM	2.5	7.4	2.5	7.3	2.4	5.5	10.7	10
Sulfate concentration at upper boundary	SO4U	mM	27	27	27.3	27.1	27.5	25.7	27.5	26

[a]: Porosities are assumed to be the same as those for A2-2.
[b]: Parameters (core length and lower boundary conditions) are assumed to be the same as those for A2-2.

doi:10.6342/NTU202000506

Table A2.5. Best fitting of all parameters applied to reactive transport modeling.

			Western center			Southern center			Upper flank	Lower flank
Parameter	Symbol	Unit	A2-2	24	MV12-1*	MD4-P1	MD4-P3	24-2	MV12-A	F6-3
Velocity of upward fluid	u_0	m yr^{-1}	0.02	0.03	0.02	0.02	0.05	0.02	0.004	0.00
Depth of bubble irrigation	L_{irr}	m	2.80	1.20	1.30	2.70	2.65	1.50	0.80	2.30
Irrigation coefficient	α_0	yr^{-1}	0.55	0.30	0.20	0.20	0.30	0.25	0.80	0.20
Irrigation coefficient	α_1	m	0.10	0.65	0.10	0.05	0.28	0.15	0.05	0.05
Maximum AOM rate	R_{AOM}^{MAX}	mM yr^{-1}	2	2	2	2	2	2	2	2
Methane concentration at lower boundary	CH4L	mM	96.4	96.4	96.4	96.4	96.4	96.4	7	30

*: Parameters (core length and lower boundary conditions) are assumed to be the same as those for site A2-2.

doi:10.6342/NTU202000506

Table A2.6. Areas of craters and from flank to periphery, and fluid discharge fluxes for individual SMVs off southwestern Taiwan.

SMV name	Crater			Flank to periphery		
	Area (m^2)	Water discharge (kg yr^{-1})		Area (m^2)	Water discharge (kg yr^{-1})	
		Min	Max		Min	Max
MV1	3.53E+03	2.54E+04	6.35E+04	1.76E+06	3.31E+05	5.64E+05
MV2	4.84E+03	3.48E+04	8.71E+04	3.88E+05	1.26E+05	2.46E+05
MV3	2.21E+03	1.59E+04	3.97E+04	3.14E+06	5.02E+05	8.15E+05
MV4	6.07E+04	4.37E+05	1.09E+06	3.24E+06	1.27E+06	2.56E+06
MV5	2.19E+04	1.58E+05	3.94E+05	3.44E+06	8.70E+05	1.60E+06
MV6	2.90E+04	2.09E+05	5.23E+05	2.63E+06	8.19E+05	1.58E+06
MV7	1.39E+03	9.98E+03	2.49E+04	7.84E+05	1.44E+05	2.43E+05
MV8	6.50E+03	4.68E+04	1.17E+05	3.15E+05	1.30E+05	2.63E+05
MV9	3.53E+03	2.54E+04	6.35E+04	8.04E+06	1.22E+06	1.96E+06
MV10	3.53E+03	2.54E+04	6.35E+04	9.08E+06	1.37E+06	2.18E+06
MV11	1.23E+04	8.84E+04	2.21E+05	7.06E+06	1.29E+06	2.18E+06
TY1	1.96E+05	1.41E+06	3.53E+06	9.98E+06	4.00E+06	8.10E+06
MV13	5.94E+04	4.28E+05	1.07E+06	3.15E+06	1.21E+06	2.44E+06
Total		2.92E+06	7.29E+06		1.04E+07	1.74E+07

doi:10.6342/NTU202000506

Table A3.1. Details of tectonic features, location of sites and core lengths. Raw data of methane fluxes across SMTZ, effluxes and biofiltration efficiency values.

location	cruise	site	Longitude	Latitude	porosity for effluxes (%)	porosity at SMTZ(%)	CH_4 efflux (mmol m^{-2} d^{-1})	CH_4 flux (SMTZ, mmol m^{-2} d^{-1})	biofiltration efficiency	core length (cm)	depth of SMTZ (cm)	reference
between Yong-An Ridge and Good weather Ridge	OR1-978	2N	119.90	22.25	0.40	0.40	1.53E-02	1.89E-02	55.22%	185	30	this study; [*Yang*, 2011]
between Yong-An Ridge and Good weather Ridge	OR1-978	2NL	119.90	22.25	0.40	0.40	4.27E-02	1.52E-02	26.30%	273	10	this study
between Yong-An Ridge and Good weather Ridge	MD178-10	3280	119.90	22.24	0.54	0.54		6.02E-02		500	280	*Lin et al.* [2014]
Four way closure Ridge	OR1-1044	C10	119.80	22.05	0.40	0.40	1.86E-05	1.70E-02	99.89%	340	170	*this study*
Four way closure Ridge	OR5-1311	C15	119.81	22.02	0.40		7.58E-05			220		*this study*
Four way closure Ridge	OR5-1311	C17	119.78	22.05	0.40	0.40	9.09E-05	8.00E-02	99.89%	300	235	*this study*
Four way closure Ridge	OR1-758	GH12	119.75	22.14	0.40		2.17E-04			79		*Chuang et al. [2010]*
Four way closure Ridge	OR1-758	GH11	119.77	22.16	0.38		2.78E-04			455		*Chuang et al. [2010]*
Four way closure Ridge	OR5-1311	C18	119.78	22.03		0.40		7.03E-02		490	415	*this study*
Frontal Ridge	OR1-1029	EN4	119.68	21.85	0.44		2.85E-05			287		*this study;*[*Yang*, 2013]
Frontal Ridge	OR1-1029	EN1	119.71	21.79	0.41	0.41	3.02E-05	2.47E-01	99.99%	252	190	*this study;*[*Yang*, 2013]
Frontal Ridge	OR1-1029	EN2	119.71	21.79	0.43	0.40	3.21E-05	1.09E-02	99.71%	224	200	*this study;*[*Yang*, 2013]
Frontal Ridge	OR1-1029	EN3	119.70	21.80	0.44		3.52E-04			252		*this study;*[*Yang*, 2013]
Good weather Ridge	OR1-902B	27	119.87	22.27	0.40	0.40	-1.22E-02	9.44E-03		170	150	*this study*;[*Chen*, 2011; *Yang*, 2009]
Good weather Ridge	OR1-718	N1	119.99	22.11	0.40		4.70E-06			464		*Chuang et al. [2006]*
Good weather Ridge	OR1-902A	9	119.97	22.19	0.47	0.47	3.78E-05	1.56E-02	99.76%	240	80	*this study*;[*Chen*, 2011; *Yang*, 2009]

doi:10.6342/NTU202000506

Table A3.1. (Continued).

location	cruise	site	Longitude	Latitude	porosity for effluxes (%)	porosity at SMTZ(%)	CH_4 efflux (mmol m^{-2} d^{-1})	CH_4 flux (SMTZ, mmol m^{-2} d^{-1})	biofiltration efficiency	core length (cm)	depth of SMTZ (cm)	reference
Good weather Ridge	OR3-1405	8A	119.93	22.12	0.40		3.98E-05			71		*this study*;[*Chen*, 2011; *Yang*, 2009]
Good weather Ridge	OR3-1384	F9	119.97	22.19	0.40		4.25E-05			140		*this study*;[*Chen*, 2010]
Good weather Ridge	OR3-1405	8C	119.94	22.11	0.40		7.03E-05			172		*this study;*[*Chen*, 2011; *Yang*, 2009]
Good weather Ridge	OR3-1405	8B	119.94	22.13	0.40		1.19E-04			42		*this study;*[*Chen*, 2011; *Yang*, 2009]
Good weather Ridge	OR1-978	1N-1	119.94	22.28	0.40		1.33E-04			120		*this study*;[*Chen*, 2011; Yang, 2009]
Good weather Ridge	OR1-902B	5	119.91	22.21	0.40		1.67E-04			170		*this study*;[*Chen*, 2011; Yang, 2009]
Good weather Ridge	OR1-902B	8	119.94	22.12	0.46	0.46	1.97E-04			130		*this study*;[*Chen*, 2011; Yang, 2009]
Good weather Ridge	OR1-902B	N2	119.98	22.09	0.40		1.98E-04			197		*this study*;[*Chen*, 2011; Yang, 2009]
Good weather Ridge	OR1-902A	3	119.94	22.31	0.40	0.40	2.09E-04			296		*this study*;[*Chen*, 2011; Yang, 2009]
Good weather Ridge	OR1-902A	8	119.94	22.12	0.46	0.46	2.86E-04	1.31E-02	97.87%	320	270	*this study*;[*Chen*, 2011; Yang, 2009]
Good weather Ridge	OR1-902B	9	119.97	22.19	0.40	0.40	3.04E-04	6.84E-02	99.56%	137	130	*this study*;[*Chen*, 2011; Yang, 2009]
Good weather Ridge	OR1-902B	T6	119.99	22.11	0.40		3.31E-04			49		*this study*;[*Chen*, 2011; Yang, 2009]
Good weather Ridge	MD147	MD05-2913	119.99	22.15	0.30	0.30	4.42E-04	9.75E-03	95.66%	1260	650	*Chuang et al.* [2013]
Good weather Ridge	OR1-902A	4	119.97	22.20	0.46	0.44	5.13E-04	1.05E-02	95.35%	226	180	*this study;*[*Chen*, 2011; *Yang*, 2009]
Good weather Ridge	OR1-697	G6	119.95	22.25	0.49		5.31E-04			285		*Chuang et al.* [2006]
Good weather Ridge	OR1-732	G1	119.99	22.21	0.40		6.27E-04			137		*Chuang et al.* [2006]

doi:10.6342/NTU202000506

Table A3.1. (continued)

location	cruise	site	Longitude	Latitude	porosity for effluxes (%)	porosity SMTZ(%)	at CH_4 efflux (mmol m^{-2} d^{-1})	CH_4 flux (SMTZ, mmol m^{-2} d^{-1})	biofiltration efficiency	core (cm)	length depth of SMTZ (cm)	reference
Good weather Ridge	OR1-697	GC	119.93	22.24	0.40	0.40	6.70E-04	2.825E-03	80.84%	305	230	*Chuang et al.* [2006]
Good weather Ridge	OR1-718	G4	119.99	22.17	0.40		1.17E-03			108		*Chuang et al.* [2006]
Good weather Ridge	OR1-718	G11	119.96	22.29	0.40		1.20E-03			138		*Chuang et al.* [2006]
Good weather Ridge	OR1-718	G11C	119.95	22.27	0.40		1.24E-03			58		*Chuang et al.* [2006]
Good weather Ridge	OR1-718	N4	119.97	22.20	0.46		1.31E-03			531		*Chuang et al.* [2006]
Good weather Ridge	OR1-697	GA	119.97	22.23	0.40		1.47E-03			355		*Chuang et al.* [2006]
Good weather Ridge	OR1-902B	5	119.91	22.21	0.40		1.67E-04			170		*this study;*[*Chen*, 2011; *Yang*, 2009]
Good weather Ridge	OR1-902B	8	119.94	22.12	0.46	0.46	1.97E-04			130		*this study;*[*Chen*, 2011; *Yang*, 2009]
Good weather Ridge	OR1-697	G15	120.11	22.29	0.62	0.61	1.83E-03	7.28E-03	79.95%	235	100	*Chuang et al.* [2006]
Good weather Ridge	OR1-718	G7	119.94	22.23	0.40		1.87E-03			131		*Chuang et al.* [2006]
Good weather Ridge	OR1-718	G9	119.95	22.27	0.40	0.40	2.72E-03	7.41E-03	73.12%	329	100	*Chuang et al.* [2006]
Good weather Ridge	MD178-10	3292	119.98	22.16	0.50	0.46	3.90E-03	2.71E-03	40.94%	1130	200	*this study;* [*Yang*, 2010]
Good weather Ridge	OR1-697	G10	119.96	22.28	0.48	0.48	4.48E-03	1.27E-02	73.89%	85	60	*Chuang et al.* [2006]
Good weather Ridge	OR1-934	5	119.93	22.32		0.40		2.91E-02		254	120	*this study;* [*Chen*, 2011; *Yang*, 2010]
Good weather Ridge	OR1-1044	C18	119.91	22.24		0.40		2.29E-01		436	370	this study
near deformation front	OR3-1368	22	119.75	22.44	0.40		1.07E-04			169		*this study;* [*Chen*, 2011; *Yang*, 2009]

doi:10.6342/NTU202000506

Table A3.1. (continued)

location	cruise	site	Longitude	Latitude	porosity for effluxes (%)	porosity SMTZ(%)	at CH_4 efflux ($mmol\ m^{-2}\ d^{-1}$)	CH_4 flux (SMTZ, $mmol\ m^{-2}\ d^{-1}$)	biofiltration efficiency	core (cm)	length depth of SMTZ (cm)	reference
Near Frontal Ridge	MD178-10	3265	119.79	21.73	0.60	0.60	8.59E-04	1.56E-02	94.78%	540	480	*this study;* [*Yang*, 2010]
Near Frontal Ridge	OR1-1044	C12	119.79	21.73		0.40		2.78E-01		194	150	this study
Tai-Nan Ridge	OR1-718	N8	119.83	22.44	0.63	0.61	-3.06E-03	2.64E-01		181	90	*Chuang et al.* [2010]
Tai-Nan Ridge	MD147	MD05-2912	119.81	22.36	0.33	0.33	1.40E-03	8.98E-03	86.51%	3050	1000	*Chuang et al.* [2013]
Tai-Nan Ridge	OR3-1384	FN8	119.83	22.43	0.40		1.28E-05			120		*this study;* [*Chen*, 2010]
Tai-Nan Ridge	OR1-765	C	119.81	22.35	0.58	0.58	3.30E-05	3.34E-02	99.90%	445	140	*Chuang et al.* [2010]
Tai-Nan Ridge	OR1-758	GH6	119.81	22.34	0.34	0.67	1.55E-04	4.88E-02	99.68%	410	330	*Chuang et al.* [2010]
Tai-Nan Ridge	OR1-765	A	119.83	22.43	0.61	0.61	1.77E-04	4.16E-02	99.58%	285	80	*Chuang et al.* [2010]
Tai-Nan Ridge	OR1-860	17	119.84	22.45	0.34		2.76E-04			161		*this study;* [*Chen*, 2009; *Yang*, 2008]
Tai-Nan Ridge	OR1-860	15	119.85	22.44	0.40		3.95E-04			210		*this study;* [*Chen*, 2009; *Yang*, 2008]
Tai-Nan Ridge	OR1-860	5	119.83	22.45	0.42		4.47E-04			161		*this study;* [*Chen*, 2009; *Yang*, 2008]
Tai-Nan Ridge	OR1-860	11	119.83	22.39	0.40		4.76E-04			161		*this study;* [*Chen*, 2009; *Yang*, 2008]
Tai-Nan Ridge	OR1-860	1	119.82	22.39	0.45		5.28E-04			390		*Chuang et al.* [2013]
Tai-Nan Ridge	OR1-860	13	119.85	22.40	0.40		6.26E-04			133		*this study;* [*Chen*, 2009; *Yang*, 2008]
Tai-Nan Ridge	OR2-1207	G27	119.85	22.41	0.40		1.06E-03			123		*Chuang et al.* [2006]
Tai-Nan Ridge	OR1-828	GT1	119.82	22.35	0.40	0.40	1.44E-03	2.92E-02	95.29%	500	220	*this study;* [*Chen*, 2009; *Yang*, 2007]

doi:10.6342/NTU202000506

Table A3.1. (continued)

location	cruise	site	Longitude	Latitude	porosity for effluxes (%)	porosity SMTZ(%)	at CH_4 efflux (mmol m^{-2} d^{-1})	CH_4 flux (SMTZ, mmol m^{-2} d^{-1})	biofiltration efficiency	core (cm)	length depth of SMTZ (cm)	reference
Tai-Nan Ridge	OR1-697	G23	119.82	22.37	0.76	0.58	1.70E-03	3.18E-01	99.47%	435	50	*Chuang et al.* [2010]
Tsanyao Ridge	OR5-1309-2	MT7	120.09	21.47		0.55		1.77E-02		760	660	*this study*
Yung-An Ridge	MD178-10	3279	119.87	22.28	0.56	0.58	-1.88E-01	3.78E-02		2430	480	*this study;* [*Yang*, 2010]
Yung-An Ridge	OR1-860	27	119.87	22.27	0.49	0.49	-5.19E-02	5.56E-02		242	80	*this study;* [*Chen*, 2009; *Yang*, 2008]
Yung-An Ridge	OR1-860	24	119.86	22.26	0.38	0.40	-1.44E-03	1.36E-02		150	70	*this study;* [*Chen*, 2009; *Yang*, 2008]
Yung-An Ridge	OR1-718	G22	119.85	22.28	0.64	0.62	-3.12E-04	8.68E-02		458	300	*Chuang et al.* [2010]
Yung-An Ridge	OR1-765	D	119.89	22.30	0.64	0.64	-2.44E-05	7.29E-03		414	210	*Chuang et al.* [2010]
Yung-An Ridge	OR1-718	N11	119.89	22.33	0.40	0.40	-4.98E-06	2.23E-02		431	100	*Chuang et al.* [2006]
Yung-An Ridge	OR1-718	N6	119.89	22.32	0.44	0.64	2.33E-05	2.17E-02	99.89%	431	320	*Chuang et al.* [2010]
Yung-An Ridge	OR3-1405	G22	119.85	22.26	0.40		8.30E-05			106		*this study;*[*Chen*, 2011; *Yang*, 2009]
Yung-An Ridge	OR1-860	22	119.84	22.22	0.44	0.41	9.59E-05	3.46E-02	99.72%	246	160	*this study;* [*Chen*, 2009]
Yung-An Ridge	OR3-1384	F27	119.88	22.27	0.40		1.29E-04			210		*this study;*[*Chen*, 2010]
Yung-An Ridge	OR1-758	GH10	119.84	22.24	0.40	0.71	1.41E-04	5.92E-02	99.76%	315	190	*Chuang et al.* [2010]
Yung-An Ridge	OR1-860	21	119.83	22.24	0.57	0.48	1.87E-04	3.44E-02	99.46%	451	400	*Chuang et al.* [2013]
Yung-An Ridge	OR1-758	GH9	119.86	22.25	0.40		4.59E-04			80		*Chuang et al.* [2010]
Yung-An Ridge	MD178-10	3276	119.87	22.24	0.60	0.60	7.08E-04	8.51E-03	92.32%	2558	170	*this study;* [*Yang*, 2010]

doi:10.6342/NTU202000506

Table A3.1. (continued)

location	cruise	site	Longitude	Latitude	porosity for effluxes (%)	porosity SMTZ(%)	at CH_4 efflux (mmol m^{-2} d^{-1})	CH_4 flux (SMTZ, mmol m^{-2} d^{-1})	biofiltration efficiency	core (cm)	length depth of SMTZ (cm)	reference
Yung-An Ridge	MD178-10	3275	119.83	22.25	0.62	0.64	7.74E-04	1.17E-02	93.82%	3387	400	*this study;* [*Yang*, 2010]
Yung-An Ridge	OR1-697	G21	119.87	22.31	0.66	0.68	8.70E-04	7.29E-02	98.82%	335	250	*Chuang et al.* [2006]
Yung-An Ridge	OR1-697	G19	119.98	22.33	0.49	0.49	1.68E-03	6.97E-03	80.55%	205	100	*Chuang et al.* [2006]
Yung-An Ridge	OR1-860	18	119.84	22.29	0.51	0.44		8.10E-02		401	400	*Chuang et al.* [2013]
Active margin, lower slope	OR1-758	GH19	120.13	21.83	0.42		-2.37E-03			430		*Chuang et al.* [2010]
Active margin, lower slope	OR1-758	GH18	120.12	21.84	0.41		-2.12E-03			463		*Chuang et al.* [2010]
Active margin, lower slope	OR1-758	GH15	119.86	22.10	0.46		-1.98E-03			440		*Chuang et al.* [2010]
Active margin, lower slope	OR1-758	GH20	120.17	22.22	0.31		-1.29E-03			447		*Chuang et al.* [2010]
Active margin, lower slope	OR1-828	GT3	120.11	21.86	0.40		-2.19E-04			140		*this study;*[*Chen*, 2009; *Yang*, 2007]
Active margin, lower slope	OR1-758	GH14	119.85	22.03	0.49		-1.06E-04			423		*Chuang et al.* [2010]
Active margin, lower slope	OR1-758	GH17	119.99	22.07	0.40		-6.39E-05			172		*Chuang et al.* [2010]
Active margin, lower slope	OR1-718	N9	120.01	22.30	0.65		-3.96E-05			304		*Chuang et al.* [2006]
Active margin, lower slope	OR1-758	GH16	119.99	22.11	0.40	0.40	-3.93E-05	6.08E-02		263	200	*Chuang et al.* [2010]
Active margin, lower slope	OR1-834	GT4	120.35	22.08	0.40		1.78E-06			160		*this study;*[*Chen*, 2009; *Yang*, 2007]
Active margin, lower slope	OR1-978	7	119.60	21.99	0.40		9.94E-06			126		*this study;*[*Yang*, 2011]
Active margin, lower slope	OR1-902B	KP7-1	120.01	22.26	0.40		1.26E-05			169		*this study;*[*Chen*, 2011; *Yang*, 2009]
Active margin, lower slope	OR1-1070	C12	120.43	21.35	0.40	0.39	4.20E-05	2.23E-02	99.81%	160	80	*this study;*[*Yang*, 2014]

doi:10.6342/NTU202000506

Table A3.1. (continued)

location	cruise	site	Longitude	Latitude	porosity for effluxes (%)	porosity at SMTZ(%)	CH_4 efflux (mmol m^{-2} d^{-1})	CH_4 flux (SMTZ, mmol m^{-2} d^{-1})	biofiltration efficiency	core length (cm)	depth of SMTZ (cm)	reference
Active margin, lower slope	OR3-1368	5	119.66	22.28	0.40		6.07E-05			169		*this study;*[*Chen*, 2011; *Yang*, 2009]
Active margin, lower slope	OR1-961	21	119.68	22.09	0.40		6.22E-05			264		*this study;*[*Yang*, 2011]
Active margin, lower slope	OR1-902B	G3	120.03	22.14	0.40		6.46E-05			137		*this study;*[*Chen*, 2011; *Yang*, 2009]
Active margin, lower slope	OR1-1029	C11	120.01	21.65	0.39		7.68E-05			218		*this study;*[*Yang*, 2013]
Active margin, lower slope	OR1-828	GT2	119.75	22.06	0.40		8.13E-05			240		*this study;*[*Chen*, 2009; *Yang*, 2007]
Active margin, lower slope	OR1-1029	L3	119.91	21.68	0.39		1.04E-04			120		*this study;*[*Yang*, 2013]
Active margin, lower slope	OR1-758	GH4	119.80	22.28	0.40		1.66E-04			130		*Chuang et al.* [2010]
Active margin, lower slope	OR1-828	GT6	120.46	21.97	0.42		1.70E-04			110		*this study;*[*Chen*, 2009; *Yang*, 2007]
Active margin, lower slope	OR1-828	GT5	120.47	21.93	0.40		2.08E-04			160		*this study;*[*Chen*, 2009; *Yang*, 2007]
Active margin, lower slope	OR1-758	GH2	119.82	22.26	0.40		2.21E-04			383		*Chuang et al.* [2010]
Active margin, lower slope	OR1-902B	HSU1	119.94	22.30	0.40		2.22E-04			169		*this study;*[*Chen*, 2011; *Yang*, 2009]
Active margin, lower slope	OR2-1230	G3	120.03	22.16	0.40		2.37E-04			137		*Chuang et al.* [2006]
Active margin, lower slope	OR1-902B	HSU2	119.93	22.32	0.40	0.40	2.39E-04	2.35E-02	98.99%	169	120	*this study;*[*Chen*, 2011; *Yang*, 2009]
Active margin, lower slope	OR1-1029	L2	120.19	21.54	0.31		2.40E-04			100		*this study;*[*Yang*, 2013]
Active margin, lower slope	OR1-697	G5A	119.99	22.17	0.49	0.61	2.90E-04	6.47E-02	99.55%	285	240	*Chuang et al.* [2010]
Active margin, lower slope	OR1-828	GT8A	119.98	22.19	0.40		3.72E-04			110		*this study;*[*Chen*, 2009; *Yang*, 2007]
Active margin, lower slope	OR1-758	GH13	119.79	22.08	0.43		4.08E-04			423		*Chuang et al.* [2010]

doi:10.6342/NTU202000506

Table A3.1. (continued)

location	cruise	site	Longitude	Latitude	porosity for effluxes (%)	porosity at SMTZ(%)	CH_4 efflux (mmol m^{-2} d^{-1})	CH_4 flux (SMTZ, mmol m^{-2} d^{-1})	biofiltration efficiency	core length (cm)	depth of SMTZ (cm)	reference
Active margin, lower slope	OR1-758	GH1	119.72	22.28	0.40		4.55E-04			170		*Chuang et al.* [2010]
Active margin, lower slope	OR1-1029	C12	120.17	21.74	0.38		4.76E-04			100		*this study;*[*Yang*, 2013]
Active margin, lower slope	OR2-1230	G21	119.88	22.27	0.40		5.01E-04			159		*Chuang et al.* [2006]
Active margin, lower slope	OR1-1070	C17	119.98	21.22	0.35		5.28E-04			147		*this study;*[*Yang*, 2014]
Active margin, lower slope	OR1-758	GH22	120.04	22.37	0.40		5.39E-04			113		*Chuang et al.* [2010]
Active margin, lower slope	OR2-1230	G72	120.02	22.26	0.40		5.52E-04			123		*Chuang et al.* [2006]
Active margin, lower slope	OR2-1230	GA	119.97	22.23	0.40		5.60E-04			152		*Chuang et al.* [2006]
Active margin, lower slope	OR2-1230	G73	120.08	22.15	0.40		5.63E-04			87		*Chuang et al.* [2006]
Active margin, lower slope	OR1-732	G9	120.10	21.82	0.40		5.82E-04			137		*Chuang et al.* [2006]
Active margin, lower slope	OR2-1230	GD	119.91	22.24	0.40		5.88E-04			137		*Chuang et al.* [2006]
Active margin, lower slope	OR2-1230	G86	120.15	21.98	0.40		5.90E-04			87		*Chuang et al.* [2006]
Active margin, lower slope	OR1-732	G10	120.15	21.90	0.40		5.96E-04			137		*Chuang et al.* [2006]
Active margin, lower slope	OR1-732	G3	119.91	22.11	0.40		6.05E-04			137		*Chuang et al.* [2006]
Active margin, lower slope	OR1-732	G5	119.83	22.03	0.40		6.09E-04			202		*Chuang et al.* [2006]
Active margin, lower slope	OR1-697	G3	120.03	22.16	0.36		6.13E-04			385		*Chuang et al.* [2006]
Active margin, lower slope	OR1-732	G8	120.03	21.87	0.40		6.15E-04			137		*Chuang et al.* [2006]
Active margin, lower slope	OR1-732	G7	119.96	21.92	0.40		6.48E-04			116		*Chuang et al.* [2006]
Active margin, lower slope	OR2-1230	GC	119.93	22.26	0.40		6.87E-04			102		*Chuang et al.* [2006]

doi:10.6342/NTU202000506

Table A3.1. (continued)

location	cruise	site	Longitude	Latitude	porosity for effluxes (%)	porosity at SMTZ(%)	CH_4 efflux (mmol m^{-2} d^{-1})	CH_4 flux (SMTZ, mmol m^{-2} d^{-1})	biofiltration efficiency	core length (cm)	depth of SMTZ (cm)	reference
Active margin, lower slope	OR1-732	G4	119.87	22.06	0.40		7.06E-04			102		*Chuang et al.* [2006]
Active margin, lower slope	OR1-758	GH5	119.84	22.30	0.40		7.26E-04			80		*Chuang et al.* [2010]
Active margin, lower slope	OR1-758	GH3	119.81	22.28	0.38	0.66	7.71E-04	3.23E-02	97.67%	380	140	*Chuang et al.* [2010]
Active margin, lower slope	OR1-758	GH7	119.83	22.47	0.30		7.78E-04			236		*Chuang et al.* [2010]
Active margin, lower slope	OR2-1207	G24	119.92	22.45	0.40		8.45E-04			104		*Chuang et al.* [2006]
Active margin, lower slope	OR2-1207	G16	120.04	22.39	0.40		8.61E-04			109		*Chuang et al.* [2006]
Active margin, lower slope	OR2-1207	G17	120.07	22.43	0.40		9.01E-04			102		*Chuang et al.* [2006]
Active margin, lower slope	OR2-1207	G14	119.92	22.30	0.40		9.07E-04			123		*Chuang et al.* [2006]
Active margin, lower slope	OR1-758	GH8	119.86	22.53	0.45		9.39E-04			415		*Chuang et al.* [2010]
Active margin, lower slope	OR2-1207	G18	120.11	22.47	0.40		9.97E-04			122		*Chuang et al.* [2006]
Active margin, lower slope	OR2-1207	G50	119.93	22.63	0.40		1.01E-03			80		*Chuang et al.* [2006]
Active margin, lower slope	OR2-1207	G15	119.97	22.34	0.40		1.01E-03			123		*Chuang et al.* [2006]
Active margin, lower slope	OR2-1207	G21	120.06	22.53	0.40		1.01E-03			102		*Chuang et al.* [2006]
Active margin, lower slope	OR1-697	G2	120.08	22.21	0.14	0.14	1.01E-03	4.07E-03	80.07%	135	100	*Chuang et al.* [2006]
Active margin, lower slope	OR2-1207	G31	119.80	22.57	0.40		1.01E-03			87		*Chuang et al.* [2006]
Active margin, lower slope	OR2-1207	G47	119.93	22.50	0.40		1.03E-03			109		*Chuang et al.* [2006]
Active margin, lower slope	OR1-718	N13	120.01	22.29	0.40		1.07E-03			531		*Chuang et al.* [2006]

doi:10.6342/NTU202000506

Table A3.1. (continued)

location	cruise	site	Longitude	Latitude	porosity for effluxes (%)	porosity at SMTZ(%)	CH_4 efflux (mmol m^{-2} d^{-1})	CH_4 flux (SMTZ, mmol m^{-2} d^{-1})	biofiltration efficiency	core length (cm)	depth of SMTZ (cm)	reference
Active margin, lower slope	OR2-1207	G49	119.93	22.58	0.40		1.21E-03			52		*Chuang et al.* [2006]
Active margin, lower slope	OR2-1207	G23	119.97	22.44	0.40		1.22E-03			109		*Chuang et al.* [2006]
Active margin, lower slope	OR2-1207	G46	119.83	22.60	0.40		1.25E-03			80		*Chuang et al.* [2006]
Active margin, lower slope	OR1-1070	C9	120.16	21.12	0.40	0.36	1.66E-03	5.27E-02	96.95%	161	120	*this study;*[*Yang*, 2014]
Active margin, lower slope	OR1-697	G1	119.88	22.27	0.32		2.09E-03			205		*Chuang et al.* [2006]
Active margin, lower slope	OR1-978	6	119.59	22.03	0.40		2.52E-03			329		*this study;*[*Yang*, 2011]
Active margin, lower slope	OR1-978	4-3	119.94	22.33	0.40		3.06E-03			356		*this study;*[*Yang*, 2011]
Active margin, lower slope	OR1-978	5	119.93	22.34	0.40		3.63E-03			64		*this study;*[*Yang*, 2011]
Active margin, lower slope	MD147	MD05-2914	119.85	22.03	0.40	0.40		6.21E-03		3514	1350	*this study;*[*Yang*, 2011]
96 cold seep	OR1-765	H	120.37	22.18	0.40	0.40	2.79E-03	3.25E-02	92.09%	516	190	*Chuang et al.* [2010]
96 cold seep	OR3-1405	G96V	120.41	22.17	0.40		5.84E-05			160		*this study;*[*Chen*, 2011; *Yang*, 2009]
96 cold seep	OR3-1405	G96MV2	120.39	22.16	0.40		8.62E-05			80		*this study;*[*Chen*, 2011; *Yang*, 2009]
96 cold seep	OR3-1405	G96MV6	120.42	22.17	0.40		1.41E-04			156		*this study;*[*Chen*, 2011; *Yang*, 2009]
96 cold seep	OR3-1368	96D	120.41	22.18	0.40		1.50E-04			170		*this study;*[*Chen*, 2011; *Yang*, 2009]
96 cold seep	OR3-1368	96C	120.41	22.19	0.40		1.55E-04			120		*this study;*[*Chen*, 2011; *Yang*, 2009]
96 cold seep	OR3-1368	96F	120.40	22.17	0.40		1.60E-04			130		*this study;*[*Chen*, 2011; *Yang*, 2009]
96 cold seep	OR3-1368	96E	120.41	22.18	0.40		1.66E-04			160		*this study;*[*Chen*, 2011; *Yang*, 2009]

doi:10.6342/NTU202000506

Table A3.1. (continued)

location	cruise	site	Longitude	Latitude	porosity for effluxes (%)	porosity at SMTZ(%)	CH_4 efflux (mmol m^{-2} d^{-1})	CH_4 flux (SMTZ, mmol m^{-2} d^{-1})	biofiltration efficiency	core length (cm)	depth of SMTZ (cm)	reference
96 cold seep	OR3-1405	G96MV1-G2	120.39	22.16	0.40		2.40E-04			66		*this study;*[*Chen*, 2011; *Yang*, 2009]
96 cold seep	OR1-1107	96-6	120.40	22.18	0.40		1.90E-02			115		*this study;*[*Su*, 2015]
96 cold seep	OR1-1107	96J-3	120.41	22.19	0.40		2.40E-02			100		*this study;*[*Su*, 2015]
96 cold seep	OR2-1230	G96	120.43	22.20	0.40	0.40	4.01E-02	3.26E-02	44.85%	130	20	*Chuang et al.* [2006]
96 cold seep	OR1-1107	96-1	120.41	22.18	0.40		4.27E-01			118		*this study;*[*Su*, 2015]
96 cold seep	OR1-1107	96V2-2	120.41	22.18	0.40	0.40	4.29E-01	1.64E-01	27.69%	180	5	*this study;*[*Su*, 2015]
96 cold seep	OR1-1107	96-3	120.41	22.18	0.40		3.17E+00			100		*this study;*[*Su*, 2015]
above mud diapir	OR1-934	19-3	120.45	21.84	0.40	0.40	4.71E-02	2.16E-02	31.41%	275	10	*this study*;[*Chen*, 2011; *Yang*, 2010]
Fang-Liao Ridge	OR3-1384	FGT39B	120.50	21.99	0.40		1.41E-05			110		*this study*;[*Chen*, 2010]
Fang-Liao Ridge	OR1-934	F2	120.50	21.98	0.40		1.41E-05			320		*this study*;[*Chen*, 2011; *Yang*, 2010]
Fang-Liao Ridge	OR1-934	8	120.50	21.99	0.40		2.92E-05			297		*this study*;[*Chen*, 2011; *Yang*, 2010]
Fang-Liao Ridge	OR1-835	GT39B	120.47	22.00	0.40	0.40	1.21E-04	5.24E-02	99.77%	490	280	*this study*;[*Chen*, 2009; Yang, 2007]
Fang-Liao Ridge	OR1-934	B1-2	120.52	22.08	0.40	0.40	2.75E-04	3.86E-02	99.29%	292	150	*this study*;[*Chen*, 2011; *Yang*, 2010]
Fang-Liao Ridge	OR3-1384	FGT39B-2	120.50	22.00	0.40		2.04E-03			105		*this study*;[*Chen*, 2010]
Fang-Liao Ridge	OR1-934	9F	120.52	22.07	0.40	0.40	3.62E-02	9.87E-03	21.42%	387	180	*this study*;[*Chen*, 2011; *Yang*, 2010]
Kaoping Canyon	OR1-732	G33	120.41	22.46	0.40		5.83E-04			59		*Chuang et al.* [2006]
Kaoping Canyon	OR1-732	G36	120.27	22.37	0.40		8.94E-04			123		*Chuang et al.* [2006]

doi:10.6342/NTU202000506

Table A3.1. (continued)

location	cruise	site	Longitude	Latitude	porosity for effluxes (%)	porosity at SMTZ(%)	CH_4 efflux (mmol m^{-2} d^{-1})	CH_4 flux (SMTZ, mmol m^{-2} d^{-1})	biofiltration efficiency	core length (cm)	depth of SMTZ (cm)	reference
southern TYMV	OR1-934	23	120.56	21.80	0.40	0.40	1.80E-04	1.14E-02	98.44%	313	275	*this study*;[*Chen*, 2011; *Yang*, 2010]
TYMV	OR1-1107	MV13-1	120.41	21.78	0.52		1.30E-02			83		*this study;*[*Su*, 2015]
TYMV	OR1-1107	MV12-C	120.55	21.82	0.40		4.18E-02			111		*this study;*[*Su*, 2015]
TYMV	OR1-1107	MV12-2	120.56	21.83	0.40		7.39E-02			57		*this study;*[*Su*, 2015]
TYMV	OR1-1107	MV12-A	120.55	21.82	0.54	0.35	8.63E-02	1.04E-01	54.65%	112	95	*this study;*[*Su*, 2015]
TYMV	OR1-1107	MV12-E	120.55	21.83	0.50		1.04E-01			95		*this study;*[*Su*, 2015]
Active margin, upper slope	OR1-834	GTS5	120.35	22.02	0.40		-1.32E-03			450		*this study*;[*Chen*, 2009; *Yang*, 2007]
Active margin, upper slope	OR1-834	GT35	120.23	21.91	0.40		-4.80E-04			440		*this study*;[*Chen*, 2009; *Yang*, 2007]
Active margin, upper slope	OR1-834	GT9	120.25	21.80	0.40		-4.36E-04			440		*this study*;[*Chen*, 2009; *Yang*, 2007]
Active margin, upper slope	OR3-1323	5-1new	120.25	22.42	0.40		-2.49E-04			104		*this study*;[*Chen*, 2010]
Active margin, upper slope	OR1-828	GT9	120.28	21.80	0.40		-1.79E-04			110		*this study*;[*Chen*, 2009; *Yang*, 2007]
Active margin, upper slope	OR1-834	GT12	120.50	22.32	0.40		-1.75E-04			510		*this study*;[*Chen*, 2009; *Yang*, 2007]
Active margin, upper slope	OR3-1323	temp2	120.34	22.30	0.40		-3.06E-05			85		*this study*;[*Chen*, 2010]
Active margin, upper slope	OR3-1323	4-1	120.33	22.35	0.40		-3.00E-05			87		*this study*;[*Chen*, 2010]
Active margin, upper slope	OR3-1323	3-3	120.33	22.25	0.40		-1.52E-05			105		*this study*;[*Chen*, 2010]
Active margin, upper slope	OR1-934	S18B	120.34	22.09	0.40		-1.08E-05			140		*this study*;[*Chen*, 2011; *Yang*, 2010]
Active margin, upper slope	OR3-1323	3-4	120.27	22.08	0.40		-7.35E-06			103		*this study*;[*Chen*, 2010]

doi:10.6342/NTU202000506

Table A3.1. (continued)

location	cruise	site	Longitude	Latitude	porosity for effluxes (%)	porosity at SMTZ(%)	CH_4 efflux (mmol m^{-2} d^{-1})	CH_4 flux (SMTZ, mmol m^{-2} d^{-1})	biofiltration efficiency	core length (cm)	depth of SMTZ (cm)	reference
Active margin, upper slope	OR1-834	GTS4	120.40	22.04	0.48		-1.37E-06			450		*this study*;[*Chen*, 2009; *Yang*, 2007]
Active margin, upper slope	OR1-834	GT22	120.47	21.95	0.36		1.04E-05			340		*this study*;[*Chen*, 2009; *Yang*, 2007]
Active margin, upper slope	OR3-1323	GT39B	120.50	21.99	0.40		1.12E-05			70		*this study*;[*Chen*, 2010]
Active margin, upper slope	OR1-834	GTM2B	120.48	22.30	0.40		1.22E-05			490		*this study*;[*Chen*, 2009; *Yang*, 2007]
Active margin, upper slope	OR1-834	GT38	120.37	22.19	0.40		1.23E-05			460		*this study*;[*Chen*, 2009; *Yang*, 2007]
Active margin, upper slope	OR3-1323	1-1	120.55	22.25	0.40		1.23E-05			110		*this study*;[*Chen*, 2010]
Active margin, upper slope	OR3-1323	2-3	120.39	22.13	0.40		1.25E-05			105		*this study*;[*Chen*, 2010]
Active margin, upper slope	OR3-1323	6-2	120.02	22.38	0.40		1.26E-05			120		*this study*;[*Chen*, 2010]
Active margin, upper slope	OR1-1029	ES2	120.54	21.51	0.41		1.89E-05			344		*this study*;[*Yang*, 2013]
Active margin, upper slope	OR3-1323	6-1	120.08	22.50	0.40		1.89E-05			120		*this study*;[*Chen*, 2010]
Active margin, upper slope	OR3-1323	6-4new	119.98	22.32	0.40		1.93E-05			150		*this study*;[*Chen*, 2010]
Active margin, upper slope	OR1-1029	C3	120.49	21.68	0.28		2.30E-05			74		*this study*;[*Yang*, 2013]
Active margin, upper slope	OR1-834	GT29	120.48	22.13	0.40		3.01E-05			290		*this study*;[*Chen*, 2009; *Yang*, 2007]
Active margin, upper slope	OR3-1323	4	120.14	22.51	0.40		3.17E-05			116		*this study*;[*Chen*, 2010]
Active margin, upper slope	OR1-834	GTS3	120.36	22.07	0.40		3.46E-05			410		*this study*;[*Chen*, 2009; *Yang*, 2007]
Active margin, upper slope	OR1-834	GT42	120.21	22.01	0.40		3.52E-05			410		*this study*;[*Chen*, 2009; *Yang*, 2007]
Active margin, upper slope	OR1-1029	C4	120.49	21.61	0.29		3.55E-05			99		*this study*;[*Yang*, 2013]
Active margin, upper slope	OR1-834	GTS1	120.41	22.07	0.49		3.86E-05			460		*this study*;[*Chen*, 2009; *Yang*, 2007]
Active margin, upper slope	OR3-1323	7-5	119.98	22.40	0.40		4.62E-05			120		*this study*;[*Chen*, 2010]
Active margin, upper slope	OR1-1029	C5	120.27	21.63	0.41	0.36	4.76E-05	4.53E-02	99.89%	428	380	*this study*;[*Yang*, 2013]

doi:10.6342/NTU202000506

Table A3.1. (continued)

location	cruise	site	Longitude	Latitude	porosity for effluxes (%)	porosity SMTZ(%)	at CH_4 efflux (mmol m^{-2} d^{-1})	CH_4 flux (SMTZ, mmol m^{-2} d^{-1})	biofiltration efficiency	core (cm)	length depth of SMTZ (cm)	reference
Active margin, upper slope	OR3-1323	8	120.17	22.58	0.40		5.15E-05			102		*this study*;[*Chen*, 2010]
Active margin, upper slope	OR1-1029	C2	120.48	21.73	0.34		5.46E-05			165		*this study*;[*Yang*, 2013]
Active margin, upper slope	OR3-1384	FYB3	120.03	22.54	0.40		5.65E-05			190		*this study*;[*Chen*, 2010]
Active margin, upper slope	OR3-1323	temp8	120.34	22.09	0.40		5.91E-05			70		*this study*;[*Chen*, 2010]
Active margin, upper slope	OR1-828	GT10	120.36	21.83	0.40		6.13E-05			110		*this study*;[*Chen*, 2009; *Yang*, 2007]
Active margin, upper slope	OR3-1384	FYB	120.09	22.57	0.40		6.66E-05			90		*this study*;[*Chen*, 2010]
Active margin, upper slope	OR3-1323	1-2	120.50	22.17	0.40		7.55E-05			120		*this study*;[*Chen*, 2010]
Active margin, upper slope	OR1-834	GT5	120.44	21.93	0.60		9.17E-05			490		*this study*;[*Chen*, 2009; *Yang*, 2007]
Active margin, upper slope	OR1-834	GTS2	120.39	22.05	0.40		1.01E-04			410		*this study*;[*Chen*, 2009; *Yang*, 2007]
Active margin, upper slope	OR3-1323	7-2	120.11	22.60	0.40		1.03E-04			50		*this study*;[*Chen*, 2010]
Active margin, upper slope	OR3-1323	5-2	120.14	22.58	0.40		1.23E-04			100		*this study*;[*Chen*, 2010]
Active margin, upper slope	OR3-1323	9	120.17	22.51	0.40		1.30E-04			80		*this study*;[*Chen*, 2010]
Active margin, upper slope	OR1-1070	C11	120.57	21.43	0.40	0.33	1.30E-04	1.53E-02	99.15%	474	180	*this study*;[*Yang*, 2014]
Active margin, upper slope	OR3-1323	3	120.11	22.51	0.40		1.38E-04			160		*this study*;[*Chen*, 2010]
Active margin, upper slope	OR1-834	GT17	120.44	21.75	0.40		1.46E-04			460		*this study*;[*Chen*, 2009; *Yang*, 2007]
Active margin, upper slope	OR1-934	25	120.53	21.77	0.40		1.49E-04			193		*this study*;[*Chen*, 2011; *Yang*, 2010]
Active margin, upper slope	OR1-1029	C1	120.65	21.81	0.36		1.51E-04			280		*this study*;[*Yang*, 2013]
Active margin, upper slope	OR1-934	S3	120.32	22.14	0.40		2.00E-04			227		*this study*;[*Chen*, 2011; *Yang*, 2010]
Active margin, upper slope	OR1-1070	C14	120.61	21.54	0.28		2.10E-04			103		*this study*;[*Yang*, 2014]
Active margin, upper slope	OR2-1230	G91	120.22	22.42	0.40		2.59E-04			109		*Chuang et al.* [2006]
Active margin, upper slope	OR2-1230	G82	120.21	22.22	0.40		2.99E-04			116		*Chuang et al.* [2006]
Active margin, upper slope	OR2-1230	G70	120.28	21.97	0.40		3.54E-04			173		*Chuang et al.* [2006]

doi:10.6342/NTU202000506

Table A3.1. (continued)

location	cruise	site	Longitude	Latitude	porosity for effluxes (%)	porosity at SMTZ(%)	CH_4 efflux (mmol m^{-2} d^{-1})	CH_4 flux (SMTZ, mmol m^{-2} d^{-1})	biofiltration efficiency	core length (cm)	depth of SMTZ (cm)	reference
Active margin, upper slope	OR2-1230	G95	120.44	22.25	0.40		3.89E-04			102		*Chuang et al.* [2006]
Active margin, upper slope	OR1-828	GT11	120.24	22.22	0.50		4.03E-04			160		*this study*;[*Chen*, 2009; *Yang*, 2007]
Active margin, upper slope	OR1-732	G17	120.19	21.96	0.40		4.66E-04			66		*Chuang et al.* [2006]
Active margin, upper slope	OR2-1230	G89	120.18	22.39	0.40		4.90E-04			116		*Chuang et al.* [2006]
Active margin, upper slope	OR2-1230	G81	120.27	22.27	0.40		5.04E-04			130		*Chuang et al.* [2006]
Active margin, upper slope	OR2-1230	G99	120.34	22.02	0.40		5.42E-04			173		*Chuang et al.* [2006]
Active margin, upper slope	OR2-1230	G107	120.23	22.12	0.40		5.63E-04			80		*Chuang et al.* [2006]
Active margin, upper slope	OR2-1230	G94	120.37	22.17	0.40		5.65E-04			137		*Chuang et al.* [2006]
Active margin, upper slope	OR1-834	GT28	120.48	22.20	0.40		5.65E-04			460		*this study*;[*Chen*, 2009; *Yang*, 2007]
Active margin, upper slope	OR2-1230	G90	120.13	22.35	0.40		5.68E-04			130		*Chuang et al.* [2006]
Active margin, upper slope	OR1-732	G27	120.26	22.21	0.40		5.72E-04			137		*Chuang et al.* [2006]
Active margin, upper slope	OR2-1230	G105	120.15	22.07	0.40		5.78E-04			145		*Chuang et al.* [2006]
Active margin, upper slope	OR2-1230	G85	120.18	22.01	0.40		5.80E-04			150		*Chuang et al.* [2006]
Active margin, upper slope	OR2-1230	G111	120.40	22.25	0.40		5.85E-04			66		*Chuang et al.* [2006]
Active margin, upper slope	OR2-1230	G87	120.32	22.32	0.40		5.88E-04			123		*Chuang et al.* [2006]
Active margin, upper slope	OR2-1230	G103	120.22	21.93	0.40		5.98E-04			173		*Chuang et al.* [2006]
Active margin, upper slope	OR1-834	GT31	120.35	21.93	0.40		6.13E-04			440		*this study*;[*Chen*, 2009; *Yang*, 2007]
Active margin, upper slope	OR2-1230	G69	120.22	22.04	0.40		6.16E-04			173		*Chuang et al.* [2006]
Active margin, upper slope	OR1-732	G31	120.43	22.38	0.40		6.27E-04			116		*Chuang et al.* [2006]
Active margin, upper slope	OR2-1230	G88	120.24	22.25	0.40		6.34E-04			116		*Chuang et al.* [2006]
Active margin, upper slope	OR2-1230	G109	120.31	22.20	0.40		6.35E-04			73		*Chuang et al.* [2006]

doi:10.6342/NTU202000506

Table A3.1. (continued)

location	cruise	site	Longitude	Latitude	porosity for effluxes (%)	porosity at SMTZ(%)	CH_4 efflux (mmol m^{-2} d^{-1})	CH_4 flux (SMTZ, mmol m^{-2} d^{-1})	biofiltration efficiency	core length (cm)	depth of SMTZ (cm)	reference
Active margin, upper slope	OR1-834	GT21	120.43	21.89	0.40		6.49E-04			410		*this study*;[*Chen*, 2009; *Yang*, 2007]
Active margin, upper slope	OR1-732	G26	120.22	22.16	0.40		6.55E-04			150		*Chuang et al.* [2006]
Active margin, upper slope	OR1-834	GT24	120.45	22.02	0.38		6.74E-04			460		*this study*;[*Chen*, 2009; *Yang*, 2007]
Active margin, upper slope	OR3-1384	FHLC-1	120.34	22.30	0.40		6.89E-04			140		*this study*;[*Chen*, 2010]
Active margin, upper slope	OR1-732	G28	120.32	22.26	0.40		6.91E-04			173		*Chuang et al.* [2006]
Active margin, upper slope	OR1-732	G18	120.22	22.01	0.40		6.96E-04			73		*Chuang et al.* [2006]
Active margin, upper slope	OR1-934	S4B	120.32	22.14	0.40		9.82E-04			156		*this study*;[*Chen*, 2011; *Yang*, 2010]
Active margin, upper slope	OR1-1107	C1	120.65	21.81	0.51		1.05E-02			180		*this study*;[*Su*, 2015]
Active margin, upper slope	OR1-1107	A2	120.48	21.73	0.50		1.46E-02			109		*this study*;[*Su*, 2015]
Active margin, upper slope	OR1-828	GT7	120.41	22.18	0.40		2.22E-02			110		*this study*;[*Chen*, 2009; *Yang*, 2007]
Active margin, upper slope	OR1-1107	A1	120.65	21.81	0.64		2.23E-02			265		*this study*;[*Su*, 2015]
Active margin, upper slope	MD178-10	3289	120.35	21.89	0.57	0.54		8.58E-03		1760	850	*this study*;[*Yang*, 2010]
Formosa Ridge	OR1-835	GTF1	119.29	22.12	0.40		1.74E-06			400		*this study*;[*Chen*, 2009; *Yang*, 2007]
Formosa Ridge	OR1-835	GTF3	119.26	22.14	0.40		3.40E-06			445		*this study*;[*Chen*, 2009; *Yang*, 2007]
Formosa Ridge	OR1-835	GTF7	119.24	22.18	0.40		7.55E-06			145		*this study*;[*Chen*, 2009; *Yang*, 2007]
Formosa Ridge	OR3-1384	FGS5-2	119.29	22.12	0.40		2.42E-05			90		*this study*;[*Chen*, 2010]
Formosa Ridge	OR1-835	GTF0	119.29	22.11	0.49		5.54E-05			395		*this study*;[*Chen*, 2009; *Yang*, 2007]
Formosa Ridge	OR1-804	GS5	119.29	22.14	0.40		7.06E-05			445		*Chuang et al.* [2010]
Formosa Ridge	OR3-1384	FGS5-1	119.29	22.12	0.40		4.60E-04			100		*this study*;[*Chen*, 2010]
Formosa Ridge	OR1-792	GS6	119.27	22.17	0.51		1.51E-03			450		*Chuang et al.* [2010]

doi:10.6342/NTU202000506

Table A3.1. (continued)

location	cruise	site	Longitude	Latitude	porosity for effluxes (%)	porosity at SMTZ(%)	CH_4 efflux (mmol m^{-2} d^{-1})	CH_4 flux (SMTZ, mmol m^{-2} d^{-1})	biofiltration efficiency	core length (cm)	depth of SMTZ (cm)	reference
Formosa Ridge	OR1-792	GS5	119.29	22.14	0.40		1.44E-01			42		*Chuang et al.* [2010]
Juilong methane reef		B				0.75		9.72E-04		750	900	*Ye et al.* [2016]
near deformation front	OR3-1368	23	119.72	22.47	0.40		2.33E-05			169		*this study*;[*Chen*, 2011; *Yang*, 2009]
near deformation front	OR3-1368	4	119.63	22.32	0.40		4.69E-05			169		*this study*;[*Chen*, 2011; *Yang*, 2009]
near deformation front	OR3-1368	13	119.66	22.36	0.40		5.65E-05			137		*this study*;[*Chen*, 2011; *Yang*, 2009]
near deformation front	OR3-1368	7	119.64	22.34	0.40		7.28E-05			169		*this study*;[*Chen*, 2011; *Yang*, 2009]
near deformation front	OR3-1368	9	119.58	22.39	0.40		8.71E-05			137		*this study*;[*Chen*, 2011; *Yang*, 2009]
near deformation front	OR3-1368	20	119.69	22.44	0.40		8.97E-05			77		*this study*;[*Chen*, 2011; *Yang*, 2009]
near Formosa Ridge	OR1-765	22G	119.32	22.11	0.40		3.50E-05			130		*Chuang et al.* [2010]
near Formosa Ridge	OR1-765	22p	119.32	22.11	0.40		1.43E-04			427		*Chuang et al.* [2010]
Near Juilong Methane Reef	OR1-835	GTS10	118.75	22.06	0.40		1.80E-06			445		*this study*;[*Chen*, 2009; *Yang*, 2007]
Near Juilong Methane Reef	OR1-835	GTS15	118.67	22.07	0.40		2.74E-06			145		*this study*;[*Chen*, 2009; *Yang*, 2007]
Near Juilong Methane Reef	OR1-835	GTS23	118.69	22.07	0.40		4.72E-06			170		*this study*;[*Chen*, 2009; *Yang*, 2007]
Near Juilong Methane Reef	OR1-835	GT43	118.77	22.00	0.46		5.17E-06			395		*this study*;[*Chen*, 2009; *Yang*, 2007]
Near Juilong Methane Reef	OR1-835	GTS27	118.75	21.98	0.40		9.70E-06			495		*this study*;[*Chen*, 2009; *Yang*, 2007]
Near Juilong Methane Reef	OR1-835	GTS17	118.66	22.01	0.52		1.01E-05			420		*this study*;[*Chen*, 2009; *Yang*, 2007]
Near Juilong Methane Reef	OR1-835	GT44	118.75	22.07	0.40		1.38E-05			470		*this study*;[*Chen*, 2009; *Yang*, 2007]
Near Juilong Methane Reef	OR1-835	GTYC1	118.77	22.13	0.40		3.73E-04			245		*this study*;[*Chen*, 2009; *Yang*, 2007]
Passive margin	OR1-804	36	119.66	22.52	0.40		1.29E-06			62		*Chuang et al.* [2010]
Passive margin	OR1-765	14	119.29	22.29	0.40		4.05E-06			52		*Chuang et al.* [2010]

doi:10.6342/NTU202000506

Table A3.1. (continued)

location	cruise	site	Longitude	Latitude	porosity for effluxes (%)	porosity at SMTZ(%)	CH_4 efflux (mmol m^{-2} d^{-1})	CH_4 flux (SMTZ, mmol m^{-2} d^{-1})	biofiltration efficiency	core length (cm)	depth of SMTZ (cm)	reference
Passive margin	OR1-804	5	119.71	22.59	0.40		4.09E-06			136		*Chuang et al.* [2010]
Passive margin	OR1-765	16	119.33	22.19	0.40		6.73E-06			156		*Chuang et al.* [2010]
Passive margin	OR1-804	4	119.73	22.57	0.40		6.89E-06			128		*Chuang et al.* [2010]
Passive margin	OR1-804	25	119.56	22.52	0.40		9.69E-06			29		*Chuang et al.* [2010]
Passive margin	OR1-804	7	119.67	22.62			9.69E-06			12		*Chuang et al.* [2010]
Passive margin	OR1-765	42	119.10	22.17	0.40		1.02E-05			110		*Chuang et al.* [2010]
Passive margin	OR1-765	5	119.57	22.28	0.40		1.10E-05			222		*Chuang et al.* [2010]
Passive margin	OR1-765	32	119.19	22.15	0.40		1.10E-05			142		*Chuang et al.* [2010]
Passive margin	OR1-765	M2	119.12	22.06	0.40		1.18E-05			475		*Chuang et al.* [2010]
Passive margin	OR1-765	M1	119.14	22.06	0.40		1.27E-05			458		*Chuang et al.* [2010]
Passive margin	OR1-765	8	119.48	22.23	0.40		1.66E-05			142		*Chuang et al.* [2010]
Passive margin	OR1-804	10	119.64	22.60	0.40		1.81E-05			34		*Chuang et al.* [2010]
Passive margin	OR1-765	3	119.51	22.37	0.40		1.82E-05			182		*Chuang et al.* [2010]
Passive margin	OR1-804	3	119.76	22.54	0.40		1.95E-05			26		*Chuang et al.* [2010]
Passive margin	OR1-804	35	119.69	22.50	0.40		2.23E-05			170		*Chuang et al.* [2010]
Passive margin	OR1-765	25	119.18	22.26	0.40		2.24E-05			102		*Chuang et al.* [2010]
Passive margin	OR1-765	6	119.60	22.22	0.40		2.85E-05			142		*Chuang et al.* [2010]
Passive margin	OR1-792	GS3	119.33	22.17	0.51		2.87E-05			359		*Chuang et al.* [2010]
Passive margin	OR1-765	24	119.21	22.22	0.40		2.88E-05			151		*Chuang et al.* [2010]
Passive margin	OR1-804	13	119.69	22.55	0.40		2.93E-05			160		*Chuang et al.* [2010]
Passive margin	OR1-765	4	119.54	22.33	0.40		3.19E-05			14		*Chuang et al.* [2010]
Passive margin	OR1-765	34	119.24	22.04	0.40		3.53E-05			170		*Chuang et al.* [2010]
Passive margin	OR1-804	37	119.64	22.55	0.40		3.91E-05			38		*Chuang et al.* [2010]
Passive margin	OR1-765	18	119.40	22.13	0.40		4.03E-05			155		*Chuang et al.* [2010]
Passive margin	OR1-765	21	119.33	22.04	0.40		4.33E-05			182		*Chuang et al.* [2010]
Passive margin	OR1-804	30	119.60	22.54	0.40		4.47E-05			144		*Chuang et al.* [2010]
Passive margin	OR1-765	30	119.15	22.24	0.40		4.55E-05			147		*Chuang et al.* [2010]
Passive margin	OR1-804	29	119.58	22.56	0.40		4.61E-05			84		*Chuang et al.* [2010]

doi:10.6342/NTU202000506

Table A3.1. (continued)

location	cruise	site	Longitude	Latitude	porosity for effluxes (%)	porosity at SMTZ(%)	CH_4 efflux (mmol m^{-2} d^{-1})	CH_4 flux (SMTZ, mmol m^{-2} d^{-1})	biofiltration efficiency	core length (cm)	depth of SMTZ (cm)	reference
Passive margin	OR3-1368	2	119.55	22.37	0.40		4.94E-05			169		*this study*;[*Chen*, 2011; *Yang*, 2009]
Passive margin	OR1-804	14	119.73	22.52	0.40		5.03E-05			132		*Chuang et al.* [2010]
Passive margin	OR1-765	15	119.30	22.26	0.40		5.44E-05			103		*Chuang et al.* [2010]
Passive margin	OR1-765	31	119.17	22.20	0.40		5.47E-05			97		*Chuang et al.* [2010]
Passive margin	OR1-765	41	119.15	22.10	0.40		5.58E-05			42		*Chuang et al.* [2010]
Passive margin	OR3-1368	1	119.52	22.39	0.40		5.73E-05			137		*this study*;[*Chen*, 2011; *Yang*, 2009]
Passive margin	OR1-765	33	119.19	22.10	0.40		5.81E-05			143		*Chuang et al.* [2010]
Passive margin	OR1-804	31	119.61	22.52	0.40		5.87E-05			122		*Chuang et al.* [2010]
Passive margin	OR3-1368	kp9	119.60	22.41	0.40		6.64E-05			49		*this study*;[*Chen*, 2011; *Yang*, 2009]
Passive margin	OR1-804	23	119.58	22.49	0.40		6.99E-05			149		*Chuang et al.* [2010]
Passive margin	OR1-804	24	119.56	22.50	0.40		7.31E-05			108		*Chuang et al.* [2010]
Passive margin	OR1-792	GS11A	119.24	22.06	0.56		7.82E-05			1075		*Chuang et al.* [2010]
Passive margin	OR1-804	22	119.59	22.47	0.40		8.24E-05			122		*Chuang et al.* [2010]
Passive margin	OR3-1368	3	119.59	22.34	0.40		9.01E-05			137		*this study*;[*Chen*, 2011; *Yang*, 2009]
Passive margin	OR1-804	21	119.61	22.45	0.40		9.37E-05			157		*Chuang et al.* [2010]
Passive margin	OR1-765	2	119.49	22.40	0.40		9.77E-05			162		*Chuang et al.* [2010]
Passive margin	OR1-792	GS11	119.23	22.05	0.56		1.13E-04			443		*Chuang et al.* [2010]
Passive margin	MD178-10	3267	119.67	21.61	0.39		1.49E-04			720		*this study;*[*Yang, 2010*]
Passive margin	OR1-804	11	119.66	22.59	0.40		1.52E-04			106		*Chuang et al.* [2010]
Passive margin	OR1-792	GS2	119.30	22.21	0.48		1.87E-04			386		*Chuang et al.* [2010]
Passive margin	OR3-1368	19	119.64	22.43	0.40		2.19E-04			109		*this study;*[*Chen*, 2011; *Yang, 2009*]
Passive margin	OR1-765	11	119.39	22.35	0.40		2.20E-04			102		*Chuang et al.* [2010]
Passive margin	OR3-1368	11	119.58	22.43	0.40		2.66E-04			197		*this study;*[*Chen*, 2011; *Yang, 2009*]
Passive margin	OR1-792	GS1	119.28	22.25	0.47		3.00E-04			363		*Chuang et al.* [2010]
Passive margin	OR1-765	9	119.43	22.28	0.40		5.37E-04			182		*Chuang et al.* [2010]

doi:10.6342/NTU202000506

Table A3.1. (continued)

location	cruise	site	Longitude	Latitude	porosity for effluxes (%)	porosity at SMTZ(%)	CH_4 efflux (mmol m^{-2} d^{-1})	CH_4 flux (SMTZ, mmol m^{-2} d^{-1})	biofiltration efficiency	core length (cm)	depth of SMTZ (cm)	reference
Passive margin	OR1-792	GS7	119.22	22.25	0.36		8.51E-04			263		*Chuang et al.* [2010]
Passive margin	OR1-765	10	119.41	22.33	0.40		9.12E-04			62		*Chuang et al.* [2010]
Passive margin	OR2-1207	G30	119.68	22.56	0.40		9.21E-04			116		*Chuang et al.* [2006]
Passive margin	OR1-792	GS10A	119.19	22.12	0.47		9.79E-04			386		*Chuang et al.* [2010]
Passive margin	OR1-1118	PR7	119.09	22.04	0.40		1.04E-03			330		this study
Passive margin	OR1-792	GS9A	119.20	22.19	0.40		1.95E-03			430		*Chuang et al.* [2010]
Passive margin	OR1-1118	PR5	119.09	22.02	0.40		2.04E-03			140		this study
Passive margin	OR1-1118	PR4	119.08	22.04	0.40		2.36E-03			330		this study
Passive margin	OR1-1118	PR8	119.09	22.07	0.40		2.78E-02			380		this study
Passive margin	OR1-1118	PR6-2	119.06	22.06	0.40		3.26E-02			380		this study

doi:10.6342/NTU202000506

Table A3.2.1. Raw data of methane, sulfate, and chloride concentrations collected from this and previous studies [*Chen*, 2009; *Chen*, 2010; *Chen*, 2011; *Chuang et al.*, 2006; *Chuang et al.*, 2010; *Chuang et al.*, 2013; *Hu et al.*, 2017; *Yang*, 2007–2014; *Su*, 2015].

cruise	site	depth (cmbsf)	CH_4 (mM)	depth (cmbsf)	SO_4^{2-} (mM)	Cl^- (mM)	cruise	site	depth (cmbsf)	CH_4 (mM)	depth (cmbsf)	SO_4^{2-} (mM)	Cl^- (mM)
MD178-10	3279	0	7.50E-02	46.5	28.6	544	MD178-10	3275	96.5	7.00E-03	131.5	29.1	566
		46.5	2.36E-02	96.5	26.1	538			150	9.65E-03	196.5	26.8	527
		96.5	3.93E-02	131.5	24.2	535			196.5	4.64E-03	246.5	23.9	526
		150	2.11E-02	196.5					246.5	1.06E-02	281.5	20.4	523
		196.5	7.23E-03	246.5	18.4	542			196.5	4.64E-03	246.5	23.9	523
		246.5	1.39E-02	281.5	15.6	536			346.5	9.10E-02	396.5	9.9	522
		300	3.09E-02	346.5	10.8	495			396.5	5.66E-02	431.5	6.9	525
		346.5	1.13E-02	396.5	14.0	535			425.5	8.28E-02	496.5	3.4	524
		396.5	1.05E-01	431.5	7.7	535			450	4.77E-02	546.5	3.1	523
		450	3.82E-02	497.0					496.5	3.73E-01	581.5	3.5	523
		496.5	3.65E-01	546.5	3.6	539			546.5	3.78E-01	646.5	3.4	522
		546.5	1.74E+00	581.5	3.8	535			600	3.45E-01	696.5	2.2	523
		600	1.48E+00	646.5					646.5	3.21E-01	731.5	2.3	527
		646.5	3.97E-01	696.5	3.1	525			696.5	4.56E-01	796.5	0.9	526
		696.5	2.84E-01	731.5	2.4	503			750	2.59E-01	846.5	1.2	526
		750	1.54E+00	796.5	1.4	527			796.5	4.62E-01	881.5	1.4	522
		796.5	1.39E+00	847.0					846.5	4.41E-01	946.5	1.1	522
		846.5	8.75E-01	881.5	1.0	529			900	2.22E-01	996.5	5.6	525
		900	9.11E-01	946.5	0.9	524			946.5	2.99E-01	1031.5	3.4	523
		939	3.83E-01	996.5	1.5	528			996.5	3.12E-01	1096.5	3.4	528
		946.5	1.65E+00	1031.5	1.1	535			1050	1.65E-01	1146.5	4.4	526
		996.5	1.16E+00	1096.5	1.5	507			1096.5	4.77E-01	1246.5	1.8	524
		1050	8.09E-01	1146.5	1.7	512			1146.5	3.09E-01	1296.5	4.1	532
		1096.5	1.35E+00	1181.5	1.3	529			1200	1.56E-01	1331.5	2.4	548
		1146.5	9.14E-01	1246.5	1.1	523			1246.5	1.65E-01	1396.5	3.0	530
		1200	5.39E-01	1296.5	2.1	524			1296.5	3.89E-01	1446.5	2.0	531
		1246.5	7.07E-01	1331.5	1.2	519			1350	2.13E-01	1481.5	0.9	529
		1296.5	1.02E+00	1396.5	1.3	530			1396.5	2.90E-01	1546.5	1.6	530
		1350	4.38E-01	1446.5	1.5	513			1446.5	2.90E-01	1596.5	1.7	534
		1396.5	7.40E-01	1481.5	1.5	506			1500	2.74E-01	1631.5	1.9	533
		1446.5	6.70E-01	1546.5	1.3	523			1546.5	5.79E-01	1696.5	1.6	530
		1500	5.16E-01	1596.5					1596.5	2.25E-01	1746.5	2.8	530
		1546.5	1.32E+00	1631.5	1.0	532			1631.5	3.49E-01	1781.5	2.3	529
		1596.5	1.14E+00	1694.0	1.8	522			1650	3.88E-01	1813.5	2.9	533
		1650	6.39E-01	1746.5	1.8	534			1696.5	3.09E-01	1896.5	1.3	536
		1694	5.40E-01	1781.5					1746.5	3.27E-01	1925.5	2.3	528
		1746.5	1.42E+00	1846.5	1.7	502			1800	1.66E-01	1996.5	1.0	543
		1800	6.10E-01	1896.5	2.0	524			1813.5	4.16E-01	2026.5	4.3	524
		1846.5	1.01E+00	1920.5	1.6	515			1896.5	5.08E-01	2081.5	0.9	525
		1896.5	3.88E-01	1995.0	1.9	498			1925.5	3.92E-01	2146.5	1.7	524
		1920.5	5.13E-01	2046.5	1.3	513			1950	2.78E-01	2196.5	3.6	529
		1950	1.45E-01	2068.5	1.2	528			1996.5	4.33E-01	2231.5	2.5	539
		1995	5.40E-01	2146.5	1.3	525			2026.5	3.89E-01	2296.5	1.3	532
		2046.5	4.14E-01	2196.5	0.9	504			2100	2.58E-01	2346.5	2.3	531
		2100	2.85E-01	2231.5	0.8	496			2146.5	2.48E-01	2381.5	1.7	530
		2196.5	4.06E-01	2296.5	2.1	513			2196.5	4.30E-01	2446.5	0.9	528
		2250	1.49E-01	2326.5	1.9	500			2250	3.65E-01	2496.5	1.4	543
		2296.5	4.17E-01	2381.5	1.2	496			2296.5	1.80E-01	2596.5	1.1	530
		2326.5	4.01E-01	2426.5	2.2	526			2346.5	1.97E-01	2646.5	1.0	530
		2400	1.49E-01						2381.5	3.41E-01	2681.5	1.1	526
		2426.5	4.00E-01						2400	1.55E-01	2736.5	0.5	527
		2446.5	4.32E-01						2446.5	1.91E-01	2788.5	0.9	529
MD178-10	3275	0	1.75E-01	46.5	29.9	547			2496.5	2.43E-01	2831.5	0.3	526
		46.5	1.50E-02	96.5	27.8	521			2550	2.42E-01	2896.5	0.9	527

doi:10.6342/NTU202000506

Table A3.2.1. (continued).

cruise	site	depth (cmbsf)	CH_4 (mM)	depth (cmbsf)	SO_4^{2-} (mM)	Cl^- (mM)	cruise	site	depth (cmbsf)	CH_4 (mM)	depth (cmbsf)	SO_4^{2-} (mM)	Cl^- (mM)
MD178-10	3275	2596.5	4.13E-01	2946.5	0.6	528	MD178-10	3276	1996.5	4.76E-01	2333.5	0.8	510
		2646.5	3.31E-01	2981.5	0.6	536			2046.5	4.06E-01	2381.5	0.8	517
		2700	8.40E-01	3046.5	0.9	533			2071.5	5.69E-01	2450.5	0.9	509
		2800	1.72E-01	3196.5	1.0	545			2100	1.19E-01	2496.5	0.8	526
		2831.5	2.15E-01	3246.5	1.0	539			2141.5	3.63E-01	2531.5	0.6	516
		2896.5	3.53E-01	3281.5	1.6	533			2196.5	7.92E-01			
		2946.5	2.01E-01	3346.5	1.1	535			2223.5	6.90E-01			
		2981.5	2.86E-01						2250	2.49E-01			
		3000	2.01E-01						2333.5	4.81E-01			
		3046.5	3.19E-01						2400	2.35E-01			
		3096.5	3.54E-01						2450.5	1.02E+00			
		3131.5	1.95E-01						2496.5	8.81E-01			
		3150	3.31E-01				MD178-10	3278	0	b.d.l.	0.0	29.5	527
		3196.5	3.57E-01						50	b.d.l.	50.0	28.1	528
		3246.5	3.22E-01						100	b.d.l.	75.0	27.3	534
		3281.5	4.04E-01						150	4.60E-03	100.0	26.8	527
		3300	1.89E-01						200	4.44E-03	125.0	25.8	531
		3346.5	1.87E-01						250	5.07E-03	150.0	26.9	532
MD178-10	3276	0	8.81E-03	46.5	24.2	531			300	4.52E-03	175.0	23.7	519
		41.5	1.44E-02	96.5	17.2	520			350	4.53E-03	200.0	23.9	530
		96.5	1.39E-02	131.5	13.6	527			400	4.51E-03	225.0	22.1	530
		131.5	1.74E-02	196.5	4.4	526			450	4.68E-03	250.0	21.4	533
		150	4.28E-02	246.5	3.7	521			500	4.63E-03	275.0	19.6	531
		196.5	3.35E-01	281.5	2.9	519			550	4.78E-03	300.0	19.6	536
		246.5	4.07E-01	346.5	2.9	515			600	4.82E-03	325.0	17.9	526
		300	6.29E-01	396.5	2.7	523			650	5.76E-03	350.0	18.0	530
		346.5	3.33E-01	431.5	2.2	516			700	5.38E-03	375.0	16.7	532
		396.5	3.71E-01	496.5	1.3	515			750	9.07E-03	400.0	16.8	534
		450	3.63E-01	546.5	1.5	523			800	5.78E-01	425.0	15.3	534
		496.5	3.90E-01	581.5	2.0	513			850	1.56E+00	450.0	14.9	526
		546.5	5.99E-01	646.5	1.5	511					475.0	14.01	534
		581.5	5.28E-01	696.5	1.9	520					500.0	13.87	525
		600	1.06E+00	731.5	1.3	510					525.0	11.66	522
		646.5	5.19E-01	796.5	1.7	507					550.0	11.57	525
		696.5	5.46E-01	846.5	2.6	514					575.0	9.50	531
		731.5	5.92E-01	881.5	1.3	508					600.0	9.34	525
		750	5.27E-01	946.5	1.4	513					625.0	7.65	532
		796.5	5.40E-01	994.5	1.6	511					650.0	7.36	540
		846.5	9.01E-01	1031.5	1.4	515					675.0	5.68	532
		900	4.43E-01	1096.5	1.6	513					700.0	4.74	525
		946.5	3.56E-01	1121.5	2.1	510					725.0	2.78	526
		994.5	6.23E-01	1155.5	1.8	516					750.0	1.84	529
		1050	3.73E-01	1155.5	1.8	511					775.0	0.73	523
		1096.5	4.70E-01	1231.5	1.8	510					800.0	0.97	529
		1121.5	4.11E-01	1286.5	1.9	519					825.0	0.42	531
		1155.5	6.01E-01	1331.5	0.6	513					850.0	1.15	528
		1200	3.31E-01	1396.5	1.5	507					875.0	0.57	547
		1228.5	2.42E-01	1446.5	2.1	510	OR1-860	22	13	1.12E-03	0.0	26.8	564
		1286.5	4.26E-01	1481.5	1.6	513			46	5.22E-03	10.0	27.0	586
		1350	3.05E-01	1546.5	1.7	510			73	1.92E-02	43.0	24.8	603
		1396.5	4.10E-01	1596.5	1.8	512			106	6.74E-02	103.0	16.5	618
		1446.5	7.41E-01	1623.5	1.6	511			133	6.42E-02			
		1500	4.06E-01	1696.5	2.4	526			166	2.41E-01			
		1546.5	2.19E-01	1746.5	1.6	513			193	2.77E-01			
		1596.5	5.53E-01	1861.5	1.3	511			226	1.29E+00			
		1623.5	2.20E-01	1896.5	2.8	510	OR1-860	24	13	8.43E-04			
		1650	2.81E-01	1923.5	1.3	512			46	9.88E-03			
		1696.5	8.45E-01	1996.5	1.2	508			73	5.48E-01			
		1746.5	5.04E-01	2046.5	0.9	508			106	7.83E-01			
		1800	3.59E-01	2072.0	1.0	512			133	7.11E-01			
		1861.5	6.02E-01	2141.5	0.9	507	OR1-860	26	13	b.d.l.	10.0	26.4	575
		1896.5	7.88E-01	2196.5	0.7	515							
		1923.5	5.27E-01	2223.5	0.5	521							
		1950	1.26E-01	2283.5	1.4	512							

doi:10.6342/NTU202000506

Table A3.2.1. (continued).

cruise	site	depth (cmbsf)	CH_4 (mM)	depth (cmbsf)	SO_4^{2-} (mM)	Cl^- (mM)	cruise	site	depth (cmbsf)	CH_4 (mM)	depth (cmbsf)	SO_4^{2-} (mM)	Cl^- (mM)
OR1-860	26	46	b.d.l.	43.0	25.5	590	OR3-1384	F-27	45	1.02E-02	85.0	23.5	555
		73	b.d.l.	70.0	21.5	536			55	5.21E-03	125.0	23.6	568
		106	2.05E-01	103.0	21.3	574			65	1.08E-02	145.0	22.6	561
		133	3.19E-03	130.0	19.0	561			75	1.51E-02	165.0	22.9	579
		166	6.08E-03	163.0	17.2	588			85	1.28E-02	185.0	22.2	564
		193	1.02E-02	190.0	14.9	582			95	1.72E-02	205.0	21.0	563
		226	1.75E-02	223.0	11.9	561			105	1.44E-02			
		253	2.79E-02	250.0	10.2	619			115	1.15E-02			
		286	6.35E-02	283.0	6.9	568			125	1.41E-02			
		313	2.29E-01	310.0	3.6	574			135	1.95E-02			
		346	9.63E-01	343.0	2.1	580			145	1.45E-02			
		373	1.39E+00	370.0	2.6	570			155	1.07E-02			
OR1-860	27	13	1.45E-01	0.0	27.1	570			165	1.37E-02			
		46	1.32E-02	10.0	27.4	579			175	1.07E-02			
		73	3.13E-02	43.0	21.7	586			185	1.27E-02			
		106	1.21E+00	70.0	12.1	571			195	2.21E-02			
		133	1.23E+00	103.0	3.2	591			205	9.40E-03			
		166	9.46E-01	130.0	2.2	585	OR3-1405	G22	11	b.d.l.			
		193	8.72E-01	163.0	1.9	588			27	2.18E-03			
		226	1.25E+00	190.0	1.8	586			43	2.92E-03			
				223.0	2.3	601			59	4.13E-03			
OR1-860	28	13	b.d.l.	0.0	27.1	570			75	5.43E-03			
		46	b.d.l.	10.0	27.9	599			91	8.49E-03			
		73	1.55E-03	43.0	25.5	573	MD178-10	3292	46.5	1.13E-01	46.5	33.7	538
		106	b.d.l.	103.0	22.0	572			96.5	1.47E-02	96.5	27.8	534
		133	b.d.l.	130.0	19.9	570			150	6.64E-02	131.5	24.2	518
		166	3.89E-03	163.0	18.0	582			196.5	1.42E-01	196.5	21.4	523
		193	5.64E-03	190.0	15.2	584			300	6.41E-02	246.5	17.7	522
		226	1.16E-02	223.0	11.6	545			346.5	5.51E-01	281.5	11.0	525
		253	2.61E-02	283.0	5.7	588			396.5	1.80E-01	346.5	9.3	514
		286	3.90E-02	310.0	1.5	562			450	1.99E-01	396.5	7.8	509
		313	9.83E-02	310.0	2.8	567			496.5	4.95E-01	431.5	4.9	520
		346	1.07E+00	403.0	b.d.l.	560			546.5	5.69E-01	496.5	7.4	503
		373	1.81E+00						600	4.48E-01	581.5	4.1	496
		406	1.66E+00						996.5	5.67E-01	600	26.0	527
OR1-860	30	13	b.d.l.						1050	2.76E-01	650	25.7	520
		46	b.d.l.						1096.5	3.60E-01	750	25.7	519
		73	b.d.l.								996.5	25.19	514.90
		106	b.d.l.								1096.5	5.99	481.10
		133	b.d.l.				OR1-1044	C18	53	b.d.l.	0	27.3	543
		166	b.d.l.						93	b.d.l.	53	25.9	545
		193	b.d.l.						133	b.d.l.	93	24.1	545
		226	b.d.l.						173	b.d.l.	133	22.6	541
		253	9.82E-04						213	1.67E-03	173	21.2	548
		286	b.d.l.						253	2.09E-03	213	19.2	550
		313	9.38E-04						293	7.45E-03	253	16.2	541
		346	1.15E-02						333	1.54E-02	293	12.3	538
		373	1.13E-01						373	1.19E-01	333	10.1	555
		406	5.68E-01						413	6.97E-01	373	4.5	547
OR1-902B	27	15	3.94E-03	10.0		569			436	1.49E+01	413	0.7	546
		45	1.68E-02	40.0		569	OR1-902A	9	13	1.06E-03	10	28.2	599
		77	5.78E-03	130.0		578			46	2.93E-03	103	4.0	569
		135	7.92E-02	220.0		592			73	7.49E-03	163	2.2	534
		225	8.86E-01						106	4.83E-01	190	2.3	557
		255	1.10E+00						133	6.35E-01	223	1.4	532
		265	6.97E-01						166	4.62E-01			
OR3-1384	F-27	0	1.45E-04	0.0	27.6	567			193	5.09E-01			
		5	7.36E-04	5.0	24.8	508			226	6.54E-01			
		15	4.90E-04	25.0	25.3	553	OR1-902A	4	13	5.06E-03	10	26.7	575
		25	3.81E-03	45.0	25.0	572			46	6.69E-03	43	26.5	575
		35	6.07E-03	65.0	23.7	549			73	3.39E-03	70	26.7	576

doi:10.6342/NTU202000506

Table A3.2.1. (continued).

cruise	site	depth (cmbsf)	CH_4 (mM)	depth (cmbsf)	SO_4^{2-} (mM)	Cl^- (mM)	cruise	site	depth (cmbsf)	CH_4 (mM)	depth (cmbsf)	SO_4^{2-} (mM)	Cl^- (mM)
OR1-902A	4	106	3.16E-03	103	25.6	581			208.5	8.17E-01			
		133	7.58E-03						241	8.62E-01			
		166	7.55E-02				OR1-978	1N-1	11.5	1.44E-03			
		193	5.16E-01						31.5	8.24E-03			
		226	5.99E-01						51.5	1.21E-02			
OR1-902A	3	13	2.65E-03	10		574			71.5	1.59E-02			
		46	b.d.l.	70		576			91.5	2.01E-02			
		73	b.d.l.	130		582			111.5	2.76E-02			
		106	b.d.l.	190		583			131.5	2.62E-02			
		133	3.18E-03	250		589			151.5	3.15E-02			
		166	b.d.l.						171.5	5.04E-02			
		193	b.d.l.				OR3-1384	F9	0	3.53E-06	15	28.2	580
		226	b.d.l.						5	b.d.l.	35	28.6	605
		253	b.d.l.						15	b.d.l.	55	24.9	519
		286	b.d.l.						25	b.d.l.	95	24.9	537
OR1-902A	8	46	9.66E-03	43	26.9	594			35	1.36E-03	115	25.1	564
		73	9.94E-03	70	26.9	582			45	6.71E-04	135	25.5	587
		106	1.05E-02	130	22.5	588			55	1.33E-03			
		133	1.25E-02	250	8.5	588			65	1.15E-03			
		166	2.22E-02	310	1.8	540			75	1.69E-03			
		193	2.08E-02						85	1.56E-03			
		226	2.99E-02						95	3.36E-03			
		253	3.77E-02						105	4.41E-03			
		286	4.37E-01						115	5.71E-03			
		313	5.98E-01						125	4.73E-03			
OR1-902B	9	12	3.41E-03	24		576			135	6.33E-03			
		27	4.70E-03	68		572	OR3-1405	8A	12	b.d.l.			
		57	0.00E+00	128		568			27	b.d.l.			
		71	6.66E-03						44	1.67E-03			
		117	3.23E-02						60	b.d.l.			
		131	9.07E-01				OR3-1405	8B	12	1.37E-03			
OR1-902B	8	12	2.23E-03	8		582			27	1.37E-03			
		27	1.95E-03	24		573	OR3-1405	8C	12	b.d.l.			
		71	8.22E-03	98		584			27	1.80E-03			
OR1-902B	5	12	1.91E-03	8		574			44	1.81E-03			
		27	1.65E-03	84		605			60	1.56E-03			
		87	2.19E-03	114		587			76	1.63E-03			
		102	2.21E-03	130		588			92	1.55E-03			
		118	2.11E-03						108	2.01E-03			
		133	2.21E-03				OR1-1029	EN1	7.5	1.99E-04	0	27.6	542
OR1-902B	N2	12	2.69E-03	8		575			27.5	3.44E-04	12.5	25.9	539
		27	2.77E-03	68		560			47.5	5.21E-04	32.5	25.4	551
		72	2.01E-03	84		573			67.5	6.90E-04	52.5	24.3	550
		87	2.07E-03						87.5	9.78E-04	72.5	23.3	551
OR1-902B	T6	42	3.70E-03	38		574			107.5	1.08E-03	92.5	22.7	553
		57	3.14E-03	54		580			127.5	1.34E-03	112.5	21.2	535
		102	6.64E-03	98		588			147.5	2.00E-03	132.5	20.3	540
		117	1.34E-02	114		553			167.5	1.49E-03	152.5	16.5	548
OR1-934	5	13.5	b.d.l.						187.5	1.30E-02	172.5	11.3	544
		41	4.86E-03						207.5	2.62E-01	192.5	5.7	539
		63.5	1.24E-02						227.5	1.17E+00	212.5	1.2	548
		91	3.63E-02						252	9.46E+00	232.5	0.4	548
		113.5	1.33E-01				OR1-1029	EN2	7.5	1.95E-04	0	28.6	564
		141	7.05E-01						27.5	3.24E-04	12.5	27.2	554
		163.5	1.47E+00						47.5	5.25E-04	32.5	25.4	555
		191	1.05E+00						67.5	8.76E-04	52.5	23.9	561
		106	3.16E-03	103	25.6	581			87.5	1.10E-03	72.5	21.7	551
		133	7.58E-03						107.5	1.39E-03	92.5	19.6	545
		141	7.05E-01						127.5	1.62E-03	112.5	18.3	557
		163.5	1.47E+00						147.5	2.02E-03	132.5	16.3	548
		191	1.05E+00						167.5	2.65E-03	152.5	14.1	556

doi:10.6342/NTU202000506

Table A3.2.1. (continued).

cruise	site	depth (cmbsf)	CH_4 (mM)	depth (cmbsf)	SO_4^{2-} (mM)	Cl^- (mM)	cruise	site	depth (cmbsf)	CH_4 (mM)	depth (cmbsf)	SO_4^{2-} (mM)	Cl^- (mM)
OR1-1029	EN2	187.5	9.28E-03	172.5	8.7	546	OR5-1311	C17	175	4.92E-03	175	15.7	553
		207.5	2.82E-02	192.5	5.7	561			205	1.59E-02	205	9.3	563
		227.5	3.54E+00	212.5	3.3	555			235	1.74E+00	235	1.6	548
OR1-1029	EN3	7.5	2.09E-03	0	28.8	562			265	1.40E+00	265	0.7	546
		27.5	2.07E-03	12.5	28.5	565			295	7.43E+00	295	0.5	546
		47.5	2.26E-03	32.5	28.2	563	OR5-1311	C18	25	b.d.l.	0	26.5	563
		67.5	3.10E-03	52.5	28.2	561			55	b.d.l.	25	25.4	557
		87.5	3.73E-03	72.5	27.0	552			85	b.d.l.	385	6.4	552
		107.5	1.14E-03	92.5	27.3	557			115	b.d.l.	415	2.5	552
		127.5	9.47E-04	112.5	27.6	561			145	b.d.l.	445	6.1	548
		147.5	1.02E-03	132.5	27.1	554			175	b.d.l.	475	2.9	554
		167.5	1.07E-03	152.5	27.4	561			205	b.d.l.			
		187.5	9.38E-04	172.5	27.3	560			235	b.d.l.			
		207.5	2.11E-03	192.5	26.6	558			265	b.d.l.			
		227.5	1.02E-02	212.5	26.6	558			295	b.d.l.			
		247.5	1.98E-02	232.5	23.6	563			325	b.d.l.			
		252	4.24E-02	249.5	21.1	555			355	b.d.l.			
OR1-1029	EN4	7.5	1.67E-04	0	27.5	544			385	b.d.l.			
		27.5	2.42E-04	12.5	26.2	535			415	b.d.l.			
		47.5	3.19E-04	32.5	25.6	541			445	1.11E-01			
		67.5	5.11E-04	52.5	24.9	544			475	2.04E+00			
		87.5	6.04E-04	72.5	24.0	552	OR1-828	GT1	2.5	3.36E-03			
		107.5	6.38E-04	92.5	23.0	541			52.5	2.65E-04			
		127.5	7.32E-04	112.5	21.9	542			80	3.75E-04			
		147.5	8.59E-04	132.5	20.8	544			102.5	2.57E-04			
		167.5	8.12E-04	152.5	19.2	538			130	2.06E-03			
		187.5	8.58E-04	172.5	17.9	547			152.5	5.20E-04			
		207.5	1.26E-03	192.5	15.6	546			202.5	3.75E-03			
		227.5	9.80E-04	212.5	13.3	548			230	3.83E-01			
		247.5	1.17E-03	232.5	10.1	543			252.5	1.02E+00			
		267.5	1.35E-03	252.5	6.9	558			280	1.72E+00			
		287	2.65E-03	272.5	3.8	548			302.5	1.57E+00			
		187.5	9.28E-03	172.5	8.7	546			352.5	1.27E+00			
		207.5	2.82E-02	192.5	5.7	561			380	1.36E+00			
		227.5	9.80E-04	212.5	13.3	548			402.5	9.75E-01			
		247.5	1.17E-03	232.5	10.1	543			452.5	1.31E+00			
		267.5	1.35E-03	252.5	6.9	558			480	1.91E+00			
		287	2.65E-03	272.5	3.8	548	OR1-860	5	13	5.03E-03			
OR1-1044	C10	13	b.d.l.	0	27.5	544			46	6.20E-03			
		53	9.12E-04	13	27.7	552			73	1.04E-02			
		93	5.12E-03	53	26.8	548			106	9.20E-03			
		133	1.43E-02	93	24.9	556			133	7.23E-03			
		173	1.31E-01	133	16.1	540			166	7.50E-03			
		213	1.14E+00	173	5.1	544	OR1-860	11	13	5.99E-03	13	25.3	555
		253	1.37E+00	213	1.6	551			46	6.28E-03	73	19.7	561
		293	9.63E-01	253	0.9	558			73	7.20E-03	133	11.9	569
		333	1.09E+00	293	0.7	550			106	8.31E-03			
		340	4.56E+00	333	b.d.l.	550			133	8.51E-03			
OR5-1311	C15	25	b.d.l.	0	26.7	540			166	1.18E-02			
		55	3.82E-03	25	27.0	551	OR1-860	13	13	7.57E-03	43	22.5	575
		85	5.53E-03	55	26.4	553			46	7.14E-03	70	20.7	577
		115	8.73E-03	85	25.6	553			73	3.90E-03			
		145	2.03E-02	115	22.0	554			133	6.31E-03			
		175	5.86E-02	145	19.2	567	OR1-860	15	13	4.82E-03			
		205	2.61E-01	175	13.5	555			46	5.06E-03			
				215	7.7	549			73	6.31E-03			
OR5-1311	C17	25	b.d.l.	25	26.7	553			106	4.64E-03			
		55	4.58E-03	55	27.0	556			133	6.39E-03			
		85	4.48E-03	85	26.1	551			166	5.44E-03			
		115	b.d.l.	115	22.9	555			193	7.89E-03			
		145	b.d.l.	145	19.6	558	OR1-860	17	13	b.d.l.			

doi:10.6342/NTU202000506

Table A3.2.1. (continued).

cruise	site	depth (cmbsf)	CH_4 (mM)	depth (cmbsf)	SO_4^{2-} (mM)	Cl^- (mM)	cruise	site	depth (cmbsf)	CH_4 (mM)	depth (cmbsf)	SO_4^{2-} (mM)	Cl^- (mM)
OR1-860	17	46	4.47E-03				MD178-10	3265	250	9.65E-04			
		73	4.51E-03						300	5.06E-04			
		106	b.d.l.						350	8.92E-04			
		133	3.38E-03						400	2.58E-03			
		166	2.86E-02						450	4.14E-02			
OR3-1384	FN8	5	0.00E+00						500	1.81E-04			
		15	0.00E+00				OR1-1029	C12	7.5	3.50E-03	0	28.2	538
		25	4.18E-04						27.5	2.12E-02	12.5	14.9	531
		35	3.16E-04						47.5	2.11E-02	32.5	4.2	543
		45	2.56E-04						67.5	2.07E-02	52.5	3.8	527
		55	0.00E+00						87.5	2.14E-02	72.5	3.5	533
		65	0.00E+00								92.5	3.0	533
		75	5.00E-04				OR1-1029	L2	7.5	2.49E-03	0	28.9	569
		85	8.66E-04						27.5	3.82E-03	32.5	27.1	570
		95	1.04E-03						47.5	2.91E-03	52.5	25.5	561
		105	1.04E-03						67.5	2.25E-03	92.5	24.8	559
		115	1.77E-03						87.5	2.62E-03			
OR1-978	2NL	11.5	5.04E-01				OR1-1029	L3	7.5	7.38E-04	0	28.3	542
		31.5	5.26E-01						27.5	8.43E-04	12.5	28.3	555
		51.5	1.06E+00						47.5	1.04E-03	32.5	28.4	552
		71.5	8.32E-01						67.5	1.17E-03	52.5	27.9	541
		91.5	1.29E+00						87.5	2.32E-03	72.5	27.9	548
		71.5	1.02E+00						107.5	4.10E-03	92.5	27.6	553
		111.5	1.08E+00								112.5	26.0	542
		131.5	5.80E-01				OR1-1029	C11	7.5	5.61E-04	0	27.9	551
		151.5	1.11E+00						27.5	1.07E-03	12.5	27.1	561
		171.5	1.31E+00						47.5	1.09E-03	32.5	23.4	551
		191.5	1.28E+00						67.5	1.03E-03	52.5	22.8	557
		211.5	8.06E-01						87.5	1.17E-03	72.5	21.6	557
		231.5	1.02E+00						107.5	1.20E-03	92.5	20.8	555
		241.5	1.08E+00						127.5	1.30E-03	112.5	19.5	550
		270.5	7.59E-01						147.5	1.03E-03	132.5	17.4	559
OR1-978	2N	11.5	1.74E-01						167.5	9.32E-04	152.5	13.8	554
		31.5	9.57E-02						187.5	1.36E-03	172.5	11.2	560
		51.5	5.28E-01								192.5	8.2	552
		72	7.95E-01				OR1-1044	C12	13	b.d.l.	0	27.6	545
		91.5	7.82E-01						53	b.d.l.	13	26.6	546
		111.5	1.06E+00						93	b.d.l.	53	22.7	544
		131.5	1.09E+00						133	1.54E-02	93	20.0	543
		151.5	1.32E+00						173	1.27E+00	133	8.5	542
		181.5	1.05E+00						194	1.76E+01	173	0.4	543
OR5-1309-2	MT7-P	22.5	b.d.l.	0	27.9	550	OR1-1070	C9	7.5	1.15E-02	0	23.8	529
		72.5	b.d.l.	10	27.1	572			27.5	8.70E-03	12.5	26.1	549
		125.5	7.24E-04	60	24.2	553			47.5	b.d.l.	32.5	24.2	525
		172.5	1.36E-03	110	24.1	555			67.5	b.d.l.	52.5	19.4	518
		225.5	1.57E-03	160	23.7	543			87.5	9.29E-03	72.5	24.0	523
		272.5	1.32E-03	210	22.8	556			107.5	2.32E-02	92.5	19.2	510
		322.5	3.41E-03	260	22.6	569			127.5	2.37E-01	112.5	4.7	497
		372.5	5.49E-03	310	19.1	551			147.5	9.13E-01	132.5	1.7	492
		422.5	2.68E-02	360	17.4	548			161	2.21E+00	152.5	1.9	449
		472.5	1.49E-02	410	16.4	561	OR1-1070	C12	12.5	1.10E-03	0	25.9	531
		522.5	1.72E-02	460	13.5	538			42.5	8.93E-03	22.5	21.6	658
		572.5	1.01E-02	510	11.5	546			72.5	2.51E-02	52.5	10.8	510
		602.5	7.86E-02	560	8.3	542			102.5	7.91E-01	82.5	2.8	617
		672.5	9.63E-01	570	5.1	534			132.5	7.86E-01	112.5	0.5	623
		722.5	6.74E-01	660	0.8	526			160	2.08E+00	142.5	0.3	694
MD178-10	3265	0	3.86E-04				OR1-1070	C17	7.5	4.56E-03	0	25.8	528
		50	b.d.l.						27.5	b.d.l.	12.5	25.0	545
		100	b.d.l.						47.5	4.28E-03	32.5	24.2	554
		150	3.70E-04						67.5	b.d.l.	52.5	22.0	539
		200	6.22E-04						87.5	b.d.l.	72.5	19.7	542
									107.5	b.d.l.	92.5	17.3	531
									127.5	b.d.l.	112.5	17.6	539
									147	b.d.l.	132.5	16.6	526

doi:10.6342/NTU202000506

Table A3.2.1. (continued).

cruise	site	depth (cmbsf)	CH_4 (mM)	depth (cmbsf)	SO_4^{2-} (mM)	Cl^- (mM)	cruise	site	depth (cmbsf)	CH_4 (mM)	depth (cmbsf)	SO_4^{2-} (mM)	Cl^- (mM)
OR1-828	GT2	2.5	1.97E-04				OR1-978	4-3	11.5	3.22E-02			
		30	6.29E-04						31.5	3.50E-02			
		52.5	6.63E-04						51.5	3.57E-02			
		80	1.64E-03						71.5	3.30E-02			
		102.5	9.74E-04						91.5	3.71E-02			
		130	1.54E-03						111.5	3.47E-02			
		152.5	2.24E-03						131.5	3.78E-02			
		180	8.05E-03						151.5	3.54E-02			
		202.5	7.31E-03						171.5	2.40E-04			
		230	1.13E-02						191.5	2.70E-04			
OR1-828	GT3	2.5	2.19E-04						211.5	3.06E-04			
		30	1.52E-03						231.5	3.58E-04			
		52.5	1.52E-03						271.5	2.44E-04			
		80	1.88E-03						266.5	3.16E-04			
		102.5	2.27E-03						291.5	3.09E-04			
		130	2.46E-03						311.5	2.91E-04			
OR1-828	GT8A	2.5	9.20E-04						331.5	3.05E-04			
		30	9.18E-04						351.5	2.91E-04			
		52.5	1.27E-03				OR1-978	5	11.5	3.82E-02			
		80	1.82E-03						31.5	3.62E-02			
		102.5	1.08E-03						51.5	3.76E-02			
OR1-902B	G3	28.5	1.76E-03				OR1-978	6	11.5	2.66E-02			
		42	1.90E-03						31.5	2.83E-02			
		55.5	2.34E-03						51.5	2.75E-02			
		88.5	3.19E-03						71.5	4.12E-04			
		102	2.07E-03						91.5	2.45E-04			
		115.5	2.76E-03						111.5	2.56E-02			
OR1-902B	HSU2	42	9.27E-03	38		565			131.5	2.68E-02			
		87	2.65E-02	84		592			151.5	2.67E-02			
		100	3.13E-02	98		573			171.5	4.82E-04			
		147	1.05E+00	144		565			191.5	3.74E-04			
		162	1.33E+00						211.5	8.94E-04			
OR1-902B	HSU1	12	2.53E-03	8		566			231.5	6.68E-04			
		64	2.14E-03	28		581			251.5	6.64E-04			
		82.5	2.46E-03	60		574			271.5	7.03E-04			
		116	3.40E-03	76		594			291.5	8.78E-04			
		131	2.01E-03	112		572			311.5	1.08E-03			
OR1-902B	KP7-1	57	1.71E-03	54		565			331.5	5.68E-04			
		72	2.72E-03	68		588	MD147	MD05-2914	150	3.36E-04			
		117	2.25E-03	114		570			300	4.32E-04			
		132	3.33E-03	128		563			450	6.95E-04			
OR1-961	21	13	b.d.l.						600	6.73E-02			
		27	1.55E-03						750	9.94E-04			
		43	3.06E-03						900	4.32E-02			
		57	1.98E-03						1050	6.34E-02			
		73	2.35E-03						1200	4.82E-03			
		87	2.08E-03						1350	1.17E-01			
		103	2.27E-03						1500	1.96E-03			
		133	2.95E-03						1650	1.82E+00			
		147	4.09E-03						1800	1.20E+00			
		163	2.45E-03						1950	2.00E-01			
		177	3.28E-03						2100	1.71E+00			
		193	3.81E-03						2550	4.90E-01			
		207	4.89E-03						2700	8.63E-01			
		223	4.22E-03						2850	1.01E+00			
		237	5.99E-03						3000	8.39E-01			
OR1-978	7	11.5	1.07E-04						3150	7.31E-01			
		31.5	3.21E-04						3300	3.05E-01			
		51.5	3.49E-04						3400	9.25E-01			
		71.5	3.62E-02						3450	8.47E-01			
		111.5	3.41E-04						3514	8.33E-01			

doi:10.6342/NTU202000506

Table A3.2.1. (continued).

cruise	site	depth (cmbsf)	CH_4 (mM)	depth (cmbsf)	SO_4^{2-} (mM)	Cl^- (mM)	cruise	site	depth (cmbsf)	CH_4 (mM)	depth (cmbsf)	SO_4^{2-} (mM)	Cl^- (mM)
OR1-828	GT6	2.5	4.07E-04				OR1-934	B1-2	13.5	3.72E-03			
		30	9.87E-04						41	2.19E-03			
		52.5	4.38E-04						63.5	4.60E-03			
		80	3.22E-04						91	5.35E-03			
		102.5	7.76E-04						113.5	1.06E-02			
OR1-835	GT39B	13.5	1.54E-03						141	1.64E-02			
		35.5	1.74E-03						163.5	8.10E-01			
		63.5	1.23E-03						191	6.77E-01			
		85.5	7.79E-03						213.5	6.91E-01			
		113.5	2.56E-02						241	7.09E-01			
		135.5	3.41E-02						263.5	8.55E-01			
		163.5	5.17E-02						289.5	5.75E-01			
		185.5	6.57E-02				OR3-1323	GT39B	5	b.d.l.	5	27.6	563
		213.5	4.26E-02						15	1.56E-04	25	27.1	554
		235.5	2.86E-02						25	b.d.l.	45	30.1	614
		263.5	8.81E-02						35	b.d.l.	105	29.0	596
		285.5	5.97E-01						45	6.68E-04			
		313.5	1.94E+00						55	b.d.l.			
		335.5	1.63E+00				OR3-1384	FGT39B	5	b.d.l.			
		363.5	1.13E+00						15	b.d.l.			
		385.5	1.21E+00						25	3.26E-04			
		413.5	1.32E+00						35	1.66E-04			
		435.5	1.22E+00						45	5.28E-04			
		463.5	1.32E+00						55	b.d.l.			
		485.5	1.55E+00						65	b.d.l.			
OR1-934	F2	13.5	b.d.l.						75	2.86E-04			
		41	5.75E-04						85	4.98E-04			
		63.5	5.01E-04						95	4.91E-04			
		91	1.13E-03						105	b.d.l.			
		113.5	6.90E-04				OR3-1384	FGT39B-2	5	9.35E-03	15	27.3	555
		141	7.81E-04						15	1.59E-02	35	27.4	559
		163.5	4.12E-04						25	2.87E-02	55	27.4	560
		191	6.40E-04						35	8.20E-02	75	27.6	566
		213.5	b.d.l.						45	7.97E-02	95	28.1	575
		241	4.27E-04						55	3.99E-02			
		263.5	3.38E-04						65	3.30E-02			
		291	4.35E-04						75	4.22E-02			
		313.5	6.04E-04						85	2.84E-02			
OR1-934	8	13.5	b.d.l.						95	2.23E-02			
		41	1.14E-03						102.5	2.38E-02			
		63.5	1.36E-03				OR1-1107	MV12-A	1	4.78E-02	0	27.5	538
		91	1.89E-03						11	7.58E-02	5	27.2	534
		113.5	2.27E-03						21	7.72E-02	15	26.8	534
		141	3.18E-03						31	8.59E-02	25	26.5	536
		163.5	2.92E-03						41	6.63E-02	35	26.1	534
		191	2.64E-03						51	7.55E-02	45	25.7	533
		213.5	3.03E-03						61	1.03E-01	55	25.7	548
		241	3.85E-03						71	1.22E-01	65	23.7	534
		263.5	2.97E-03						81	1.40E-01	75	21.2	527
		291	4.12E-03						91	1.11E-01	85	13.1	501
OR1-934	9F	13.5	4.48E-01						101	1.00E+00	95	4.70	503
		41	7.94E-02						111	1.10E+00	105	0.54	487
		63.5	5.76E-02						112	3.48E+00			
		91	3.88E-02				OR1-1107	MV12-1	1	2.21E-01	0	27.3	534
		113.5	4.62E-02						11	5.02E-01	5	25.8	532
		141	6.47E-02						21	9.12E-01	15	24.5	527
		163.5	6.44E-02						31	8.25E-01	25	22.8	521
		191	2.17E-01						41	2.94E-01	35	22.4	525
		313.5	6.47E-01										
		341	1.16E+00										
		363.5	9.99E-01										

doi:10.6342/NTU202000506

Table A3.2.1. (continued).

cruise	site	depth (cmbsf)	CH_4 (mM)	depth (cmbsf)	SO_4^{2-} (mM)	Cl^- (mM)	cruise	site	depth (cmbsf)	CH_4 (mM)	depth (cmbsf)	SO_4^{2-} (mM)	Cl^- (mM)
OR1-1107	MV12-1	51	2.53E-01	45	21.1	518	OR1-1107	96V2-2	21	9.91E-01	15	7.3	540
		61	3.52E-01	55	21.1	511			31	2.22E+00	25	2.8	519
		71	1.28E-01	65	21.2	517			41	2.70E-01	35	5.7	497
		81	2.45E-01	75	19.2	520			51	9.80E-01	45	2.6	584
		91	3.01E-01	85	16.9	516			61	1.17E+00	55	1.0	524
		101	8.64E-01	95	12.1	506			71	1.10E+00	65	0.6	498
		102	2.22E+00						81	1.56E+00	75	0.7	515
OR1-1107	MV12-C	1	3.87E-02	0	27.2	541			91	1.30E+00	85	0.8	539
		11	5.40E-02	15	26.2	535			101	9.19E-01	95	1.2	523
		21	5.00E-02	23	26.6	558			111	1.20E+00	105	0.3	530
		31	5.02E-02	35	24.9	539			121	1.14E+00	115	0.6	658
		41	2.14E-02	45	24.6	540			131	9.92E-01	125	0.4	514
		51	6.18E-02	55	24.4	537			141	1.61E+00	135	0.5	566
		61	4.82E-02	65	24.2	535			151	9.94E-01	145	0.4	521
		71	4.80E-02	75	24.7	544			161	1.39E+00	155	1.5	536
		81	4.80E-02	85	24.8	547			171	1.28E+00	165	1.0	539
		91	7.41E-02	95	24.0	527			181	1.42E+00	175	0.7	518
		101	6.49E-02						183	2.72E+00			
		111	4.42E-02				OR3-1323	temp2	7.5	b.d.l.	7.5	26.7	547
OR1-1107	MV12-E	1	6.57E-02						22.5	1.09E-03	37.5	26.9	572
		51	8.09E-02						37.5	1.82E-03	67.5	24.6	562
		94.5	1.00E-01						52.5	2.92E-03			
OR1-1107	MV12-2	1	6.84E-02						67.5	3.96E-03			
		3	9.11E-02						82.5	6.04E-03			
		5	1.13E-01				OR3-1368	96J	8	3.94E-02	6	22.3	580
OR1-1107	MV12-D	1	1.06E-01						18	1.68E-01	16	19.1	561
		46	8.23E-02						28	1.39E-01	26	10.2	569
OR1-1107	MV13-1	1	7.66E-03						38	9.57E-01	36	5.4	572
		41	3.77E-02						38	1.11E+00	46	3.6	573
OR1-1107	MV12-3	1	1.85E+00						48	4.25E-01	56	4.1	575
		3	1.91E+00						48	5.18E-01	66	3.7	575
		5	1.90E+00						58	1.09E+00	76	5.1	592
OR1-1107	96-4	1	1.01E-02						68	1.09E+00	86	3.8	560
		3	1.45E-02						78	1.26E+00	96	8.4	585
		5	1.78E-02						88	9.07E-01			
OR1-1107	96-5	1	1.04E-02						88	9.10E-01			
		3	1.40E-02						98	6.85E-01			
		5	1.27E-02						98	6.72E-01			
OR1-1107	96-2	1	1.37E-02				OR3-1368	96L	8	5.22E-03	6	27.6	566
		3	1.85E-02						18	4.65E-03	16	27.2	560
		5	1.60E-02						28	6.10E-03	26	28.3	573
OR1-1107	96-v2	1	1.11E-02						38	4.60E-03	36	27.8	571
		3	1.19E-02						48	9.92E-03	46	27.9	598
		5	1.59E-02						58	1.26E-02	56	27.2	581
OR1-1107	96-6	1	1.76E-02						68	1.06E-02	66	26.9	575
		3	1.73E-02						78	1.42E-02	76	26.0	535
		5	1.74E-02						88	8.51E-02	86	26.5	582
OR1-1107	96-1	1	3.95E-01						88	7.48E-02	96	25.0	571
		3	6.63E-01						98	4.86E-02	106	23.3	586
		5	4.36E+00						98	4.22E-02	116	18.9	585
OR1-1107	96-3	1	2.95E+00						108	2.40E-02	126	13.9	580
		3	3.94E+00						118	2.59E-02			
		5	3.79E+00						128	4.14E-02			
OR1-1107	96J-1	1	8.29E-03						138	7.96E-02			
		3	1.06E-02				OR3-1368	96C	8	1.22E-03	6	27.0	571
		5	1.26E-02						18	1.08E-03	26	26.3	580
OR1-1107	96J-3	1	2.23E-02						28	9.24E-04	46	25.7	570
		3	9.34E-02						38	9.85E-04	66	25.2	570
		5	1.45E-02						48	8.57E-04	86	25.1	569
OR1-1107	96V2-2	1	4.03E-01	0	26.0	519			58	8.36E-04	106	24.9	567
		11	1.90E+00	5	5.2	530			68	8.66E-04			

doi:10.6342/NTU202000506

Table A3.2.1. (continued).

cruise	site	depth (cmbsf)	CH_4 (mM)	depth (cmbsf)	SO_4^{2-} (mM)	Cl^- (mM)	cruise	site	depth (cmbsf)	CH_4 (mM)	depth (cmbsf)	SO_4^{2-} (mM)	Cl^- (mM)
OR3-1368	96C	78	9.08E-04						38	1.33E-03	66	26.3	564
		88	7.22E-04						48	1.15E-03	86	26.6	582
		98	9.20E-04						58	1.22E-03	106	26.0	568
		108	1.00E-03						68	1.09E-03	126	26.3	583
		118	8.76E-04						78	1.47E-03	146	26.2	588
OR3-1368	96B	8	1.78E-02	56	26.1	574			88	1.63E-03			
		18	8.26E-02	76	25.7	578			98	1.24E-03			
		28	1.67E-01	96	25.1	575			108	1.09E-03			
		38	4.93E-02	116	24.9	580			118	1.12E-03			
		48	2.88E-03	136	25.0	593			128	1.23E-03			
		58	6.78E-03	156	24.4	583			138	1.13E-03			
		68	2.22E-03						148	1.32E-03			
		78	3.13E-03						158	1.38E-03			
		88	3.49E-03				OR3-1368	G96MV1-G1	12	3.17E-02			
		98	1.72E-03						27	4.20E-03			
		108	1.61E-03						44	b.d.l.			
		118	3.80E-03						60	b.d.l.			
		128	1.93E-03				OR3-1368	G96MV1-G2	12	2.76E-03			
		138	2.14E-03						27	b.d.l.			
		148	1.83E-03						44	2.64E-03			
		158	3.34E-03						60	b.d.l.			
		158	2.15E-03						76	b.d.l.			
		168	1.57E-03				OR3-1368	G96MV2	12	b.d.l.			
OR3-1368	96D	8	1.17E-03	6	26.9	562			27	2.25E-03			
		18	1.68E-03	26	26.2	565			44	1.89E-03			
		28	1.48E-03	46	26.8	592			60	b.d.l.			
		38	2.66E-03	66	0.0	578			76	b.d.l.			
		48	2.02E-03	86	26.5	575	OR3-1368	G96MV6	12	1.67E-03			
		58	1.49E-03	106	26.9	588			27	b.d.l.			
		68	2.07E-03	126	28.0	626			44	b.d.l.			
		78	2.18E-03	146	27.1	603			60	b.d.l.			
		88	2.86E-03	166	25.7	572			76	b.d.l.			
		98	3.59E-03						92	b.d.l.			
		108	3.49E-03						108	b.d.l.			
		118	2.35E-03						124	b.d.l.			
		128	2.91E-03						140	1.61E-03			
		138	2.88E-03						154	b.d.l.			
		148	1.87E-03				MD10-178	3289	0	b.d.l.	47	26.4	531
		158	1.81E-03						46.5	b.d.l.	97	24.7	524
		168	1.52E-03						96.5	5.04E-03	132	24.4	521
OR3-1368	96F	8	1.27E-03	6	28.6	603			150	5.42E-03	197	22.1	526
		18	1.11E-03	26	27.1	577			196.5	5.09E-03	247	21.0	525
		28	1.05E-03	46	26.7	573			246.5	6.77E-03	282	18.7	527
		38	1.14E-03	66	26.0	567			300	b.d.l.	347	18.0	525
		48	1.18E-03	86	25.5	568			346.5	b.d.l.	397	15.3	534
		58	1.42E-03	106	25.2	568			496.5	4.02E-03	432	14.8	527
		68	1.36E-03	126	24.9	568			546.5	2.59E-03	497	15.2	525
		78	2.11E-03						600	2.84E-03	547	11.9	528
		88	1.56E-03						646.5	3.41E-03	582	10.6	526
		98	1.39E-03						796.5	9.65E-03	647	8.5	527
		108	1.24E-03						846.5	7.54E-02	697	6.1	528
		118	1.56E-03						900	2.74E-01	732	4.9	526
		128	1.46E-03						946.5	5.39E-01	797	3.9	528
		78	9.08E-04						996.5	7.36E-01	847	3.0	528
		88	7.22E-04						1050	6.60E-01	882	2.4	528
		98	9.20E-04						1096.5	6.40E-01	947	3.4	524
		108	1.00E-03						1146.5	7.06E-01	1032	2.9	526
		118	8.76E-04						1200	4.63E-01	1097	2.6	529
OR3-1368	96E	8	1.33E-03	6	26.6	549			1246.5	8.14E-01	1147	1.2	529
		18	1.29E-03	26	26.5	560			1296.5	5.04E-01	1182	1.3	527
		28	1.31E-03	46	26.8	571			1350	6.15E-01	1247	1.1	530

doi:10.6342/NTU202000506

Table A3.2.1. (continued).

cruise	site	depth (cmbsf)	CH_4 (mM)	depth (cmbsf)	SO_4^{2-} (mM)	Cl^- (mM)	cruise	site	depth (cmbsf)	CH_4 (mM)	depth (cmbsf)	SO_4^{2-} (mM)	Cl^- (mM)
MD10-178	3289	1396.5	7.52E-01	1297	1.5	527	OR1-1029	C5	367.5	5.48E-02	352.5	3.1	551
		1446.5	5.69E-01	1332	1.0	529			387.5	4.11E-01	372.5	1.9	549
		1500	3.80E-01	1397	1.3	533			407.5	1.85E+00	392.5	1.2	545
		1546.5	3.65E-01	1447	3.1	531			428	2.73E+00	412.5	1.8	558
		1596.5	4.37E-01	1482	1.9	528					432.5	0.5	544
		1650	4.82E-01	1547	2.1	530	OR1-1029	ES2	7.5	1.27E-04	0	28.0	550
		1696.5	1.33E-01	1597	6.6	530			27.5	2.20E-04	12.5	27.6	544
				1632	4.2	529			47.5	2.43E-04	32.5	27.1	547
				1697	2.6	531			67.5	1.81E-04	52.5	27.5	558
				1747	5.4	534			87.5	1.76E-04	72.5	26.9	544
OR1-1029	C1	7.5	1.30E-03	0	27.4	555			107.5	2.10E-04	92.5	27.4	555
		27.5	2.42E-03	12.5	23.5	544			127.5	2.06E-04	112.5	27.3	553
		47.5	3.06E-03	32.5	17.8	541			147.5	2.66E-04	232.5	27.4	556
		67.5	2.08E-03	52.5	16.0	543			167.5	3.18E-04	252.5	26.6	539
		87.5	2.92E-03	72.5	15.8	542							
		107.5	2.41E-03	92.5	14.8	550			207.5	2.78E-04	292.5	27.2	556
		127.5	2.44E-03	112.5	13.3	539			227.5	2.71E-04	312.5	26.9	548
		147.5	2.63E-03	132.5	12.6	541			247.5	2.29E-04	332.5	26.9	556
		167.5	3.29E-03	152.5	11.9	541			267.5	2.66E-04			
		187.5	2.21E-03	172.5	11.6	559			287.5	3.03E-04			
		207.5	2.60E-03	192.5	10.9	557			307.5	3.81E-04			
		227.5	2.56E-03	212.5	10.5	550			327.5	3.14E-04			
		247.5	2.10E-03	232.5	10.1	545	OR1-1070	C11	12.5	b.d.l.	0	26.6	531
		267.5	2.39E-03	252.5	9.4	537			42.5	5.10E-03	22.5	25.4	516
				272.5	9.6	559			72.5	3.54E-02	52.5	25.4	526
OR1-1029	C2	7.5	4.84E-04	0	28.4	556			102.5	6.44E-03	82.5	21.7	523
		27.5	1.28E-03	12.5	28.1	551			132.5	b.d.l.	112.5	17.7	518
		47.5	4.98E-04	32.5	27.5	546			162.5	4.98E-02	142.5	13.0	523
		67.5	5.68E-04	52.5	29.2	543			192.5	2.24E-01	172.5	7.1	520
		87.5	9.31E-04	72.5	29.2	550			222.5	1.19E+00	202.5	3.1	518
		107.5	1.10E-03	92.5	28.1	554			252.5	4.41E-01	232.5	1.8	513
		127.5	8.33E-04	112.5	29.8	555			282.5	4.50E-01	262.5	2.1	512
		147.5	1.27E-03	132.5	27.9	547			312.5	3.49E-01	292.5	1.5	510
				154	27.6	550			342.5	8.63E-01	322.5	1.5	493
OR1-1029	C3	7.5	2.90E-04	0	28.0	549			402.5	7.72E-01	352.5	0.2	508
		27.5	4.16E-04	12.5	27.9	555			432.5	2.70E-01	382	0.2	491
		47.5	5.50E-04	52.5	27.5	545			462.5	9.81E-01	412.5	0.1	489
		67.5	4.09E-04						474	1.03E+00	442.5	0.1	492
OR1-1029	C4	7.5	4.14E-04								470	b.d.l.	485
		27.5	4.90E-04				OR1-1070	C14	12.5	b.d.l.			
		47.5	1.24E-03						42.5	4.33E-03			
		67.5	3.66E-04						72.5	4.21E-03			
		87.5	5.20E-04						102.5	b.d.l.			
OR1-1029	C5	7.5	3.28E-04	0	28.2	554	OR1-1107	A2	1	9.31E-03			
		27.5	4.31E-04	12.5	26.3	556			51	2.92E-02			
		47.5	5.77E-04	32.5	23.7	535			1	8.92E-03			
		67.5	9.30E-04	52.5	22.4	550			51	8.01E-03			
		87.5	1.21E-03	72.5	20.5	542			101	4.99E-03			
		107.5	1.32E-03	92.5	19.2	548			151	9.78E-03			
		127.5	1.35E-03	112.5	17.5	543			201	6.62E-03			
		147.5	1.61E-03	132.5	16.4	546			265	1.17E-02			
		167.5	2.18E-03	152.5	14.6	535	OR1-1107	C1	1	6.53E-03			
		187.5	2.40E-03	172.5	13.5	542			3	2.47E-02			
		207.5	2.99E-03	192.5	12.1	538			5	7.66E-03			
		227.5	2.64E-03	212.5	10.6	523			51	7.78E-03			
		247.5	2.72E-03	232.5	9.9	534			101	3.37E-02			
		267.5	2.87E-03	252.5	8.8	540			151	6.42E-02			
		287.5	3.24E-03	272.5	8.1	549			168.5	5.83E-02			
		307.5	4.86E-03	292.5	6.9	546	OR1-828	GT5	2.5	5.24E-04			
		327.5	6.98E-03	312.5	5.6	552			30	1.02E-03			
		347.5	2.44E-02	332.5	4.3	558			52.5	1.30E-03			

doi:10.6342/NTU202000506

Table A3.2.1. (continued).

cruise	site	depth (cmbsf)	CH_4 (mM)	depth (cmbsf)	SO_4^{2-} (mM)	Cl^- (mM)	cruise	site	depth (cmbsf)	CH_4 (mM)	depth (cmbsf)	SO_4^{2-} (mM)	Cl^- (mM)
OR1-828	GT5	80	1.77E-03				OR1-834	GT9	102.5	4.92E-04			
		102.5	2.58E-03						130	5.74E-04			
		130	2.30E-03						152.5	3.07E-04			
		152.5	3.86E-03						180	4.71E-04			
OR1-828	GT7	2.5	5.11E-02						202.5	5.53E-04			
		30	b.d.l.						230	5.74E-04			
		52.5	1.01E-02						252.5	5.02E-04			
		80	1.19E-02						280	7.38E-04			
		102.5	3.01E-02						302.5	1.02E-03			
OR1-828	GT9	2.5	7.04E-04						330	9.53E-04			
		30	1.41E-03						352.5	1.13E-03			
		52.5	1.91E-03						380	1.02E-03			
		102.5	2.48E-03						402.5	1.02E-03			
OR1-828	GT10	2.5	2.11E-04						430	8.30E-04			
		52.5	4.39E-04				OR1-834	GT12	2.5	1.33E-04			
		80	4.48E-04						30	6.15E-04			
		102.5	3.71E-04						52.5	1.50E-03			
OR1-828	GT11	2.5	6.61E-04						102.5	6.97E-04			
		30	7.20E-04						130	6.05E-04			
		52.5	b.d.l.						152.5	5.12E-04			
		80	1.23E-03						180	2.15E-04			
		102.5	2.23E-03						202.5	2.87E-04			
		130	2.15E-03						230	1.33E-04			
		152.5	3.08E-03						252.5	9.22E-05			
OR1-834	GT4	30	1.84E-04						280	4.71E-04			
		52.5	3.38E-04						302.5	3.07E-04			
		80	4.20E-04						330	9.84E-04			
		102.5	6.76E-04						352.5	1.35E-03			
		130	4.00E-04						380	1.14E-03			
		152.5	3.59E-04						402.5	8.61E-04			
OR1-834	GT5	2.5	2.56E-04						430	1.01E-03			
		30	2.46E-04						452.5	3.07E-04			
		52.5	5.02E-04						480	1.43E-03			
		80	7.38E-04						502.5	9.53E-04			
		102.5	6.76E-04				OR1-834	GT17	2.5	3.38E-04			
		130	7.17E-04						30	4.82E-04			
		152.5	8.50E-04						52.5	5.02E-04			
		180	1.23E-03						80	6.56E-04			
		202.5	7.07E-04						102.5	6.05E-04			
		230	7.89E-04						130	2.77E-04			
		252.5	1.23E-03						152.5	4.00E-04			
		280	7.17E-04						180	6.35E-04			
		302.5	1.43E-03						202.5	4.41E-04			
		330	6.76E-04						230	8.71E-04			
		352.5	1.02E-03						252.5	2.97E-04			
		380	6.35E-04						280	9.73E-04			
		402.5	7.99E-04						302.5	5.94E-04			
		430	1.00E-03						330	3.48E-04			
		452.5	1.02E-03						352.5	3.28E-04			
		480	6.35E-04						380	9.63E-04			
		80	1.77E-03						402.5	7.38E-04			
		102.5	2.58E-03						430	1.13E-03			
		130	2.30E-03						452.5	9.22E-04			
		152.5	3.86E-03				OR1-834	GT21	2.5	1.54E-03			
OR1-828	GT7	2.5	5.11E-02						30	2.66E-03			
		30	b.d.l.						52.5	2.15E-03			
		52.5	1.01E-02						80	2.05E-03			
OR1-834	GT9	2.5	1.13E-04						102.5	2.15E-03			
		30	2.56E-04						130	1.74E-03			
		52.5	3.89E-04						152.5	1.54E-03			
		80	4.92E-04						180	2.25E-03			

doi:10.6342/NTU202000506

Table A3.2.1. (continued).

cruise	site	depth (cmbsf)	CH_4 (mM)	depth (cmbsf)	SO_4^{2-} (mM)	Cl^- (mM)	cruise	site	depth (cmbsf)	CH_4 (mM)	depth (cmbsf)	SO_4^{2-} (mM)	Cl^- (mM)
OR1-834	GT21	202.5	2.05E-03				OR1-834	GT31	152.5	2.46E-03			
		230	2.46E-03						180	2.15E-03			
		252.5	2.87E-03						202.5	2.15E-03			
		280	3.07E-03						230	2.05E-03			
		302.5	3.69E-03						252.5	1.95E-03			
		402.5	1.64E-03						280	1.95E-03			
OR1-834	GT22	30	3.92E-04						302.5	1.95E-03			
		52.5	1.15E-04						330	1.54E-03			
		80	6.56E-04						352.5	1.54E-03			
		102.5	2.15E-04						380	1.64E-03			
		130	2.25E-04						402.5	1.64E-03			
		152.5	5.12E-05						430	1.54E-03			
		180	1.64E-04				OR1-834	GT35	2.5	3.59E-04			
		202.5	b.d.l.						30	2.05E-04			
		230	3.18E-04						62.5	3.18E-04			
		252.5	2.25E-04						90	2.97E-04			
		280	3.28E-04						112.5	2.97E-04			
		302.5	2.36E-04						150	3.38E-04			
		330	3.89E-04						172.5	4.20E-04			
OR1-834	GT24	2.5	1.71E-03						200	1.95E-03			
		30	2.25E-03						222.5	1.95E-03			
		52.5	2.15E-03						260	2.15E-03			
		80	1.95E-03						282.5	2.05E-03			
		102.5	1.95E-03						310	2.15E-03			
		130	1.74E-03						332.5	2.05E-03			
		152.5	1.84E-03						370	1.95E-03			
		180	2.15E-03						392.5	2.15E-03			
		202.5	2.36E-03						425	1.54E-03			
		230	1.02E-03				OR1-834	GT38	2.5	6.15E-05			
		252.5	1.23E-03						30	9.22E-05			
		280	8.61E-04						52.5	9.22E-05			
		302.5	9.84E-04						80	1.33E-04			
		330	7.38E-04						102.5	1.64E-04			
		352.5	5.53E-04						130	8.20E-05			
		380	6.35E-04						152.5	1.23E-04			
		402.5	5.84E-04						180	1.43E-04			
		430	5.64E-04						202.5	b.d.l.			
		452.5	7.58E-04						230	1.54E-04			
OR1-834	GT28	2.5	1.33E-03						252.5	b.d.l.			
		30	1.74E-03						280	4.61E-04			
		52.5	1.23E-03						302.5	1.74E-04			
		80	5.33E-04						330	1.43E-04			
		102.5	6.86E-04						352.5	1.84E-04			
		130	8.30E-04						380	1.54E-04			
		152.5	6.05E-04						402.5	1.84E-04			
		180	9.02E-04						430	3.79E-04			
		202.5	8.71E-04						452.5	8.50E-04			
		230	7.68E-04				OR1-834	GT42	2.5	9.22E-05			
		252.5	7.48E-04						30	2.77E-04			
		280	5.64E-04						52.5	5.02E-04			
		302.5	6.86E-04						80	8.61E-04			
		330	4.82E-04						102.5	7.38E-04			
		352.5	7.68E-04						130	1.23E-03			
		380	4.82E-04						152.5	1.23E-03			
		402.5	5.23E-04						180	1.33E-03			
		430	4.71E-04						202.5	1.95E-03			
		452.5	5.74E-04						230	1.54E-03			
OR1-834	GT31	2.5	2.87E-03						252.5	1.95E-03			
		52.5	2.10E-02						280	2.56E-03			
		80	5.64E-03						302.5	2.25E-03			
		102.5	4.30E-03						330	2.36E-03			

doi:10.6342/NTU202000506

Table A3.2.1 (continued).

cruise	site	depth (cmbsf)	CH_4 (mM)	depth (cmbsf)	SO_4^{2-} (mM)	Cl^- (mM)	cruise	site	depth (cmbsf)	CH_4 (mM)	depth (cmbsf)	SO_4^{2-} (mM)	Cl^- (mM)
OR1-834	GT42	352.5	2.66E-03				OR1-834	GTS3	102.5	5.33E-04			
		380	2.66E-03						130	6.35E-04			
		402.5	3.07E-03						152.5	6.35E-04			
OR1-834	GTM2B	2.5	5.64E-04						180	6.56E-04			
		30	1.33E-03						202.5	5.23E-04			
		52.5	1.33E-03						230	6.56E-04			
		80	1.33E-03						252.5	6.86E-04			
		102.5	1.84E-03						280	9.32E-04			
		130	1.33E-03						302.5	9.43E-04			
		152.5	1.54E-03						330	8.09E-04			
		180	1.64E-03						380	1.13E-03			
		202.5	1.54E-03						402.5	1.23E-03			
		230	1.33E-03				OR1-834	GTS4	2.5	6.81E-05			
		252.5	8.71E-04						40	5.10E-05			
		280	1.00E-03						62.5	8.74E-04			
		302.5	8.40E-04						90	3.59E-04			
		330	6.66E-04						112.5	4.20E-04			
		352.5	1.02E-03						150	3.79E-04			
		380	3.79E-04						172.5	1.43E-04			
		402.5	2.87E-04						200	4.30E-04			
		430	3.38E-04						222.5	1.84E-04			
		452.5	3.79E-04						260	4.51E-04			
		480	2.97E-04						282.5	6.05E-04			
OR1-834	GTS1	2.5	3.83E-04						310	5.43E-04			
		30	8.32E-04						332.5	5.74E-04			
		52.5	1.16E-03						370	5.84E-04			
		80	1.33E-03						392.5	6.25E-04			
		102.5	1.74E-03						420	6.66E-04			
		130	1.95E-03						442.5	6.05E-04			
		152.5	1.64E-03				OR1-834	GTS5	2.5	1.16E-04			
		180	1.74E-03						30	2.04E-04			
		202.5	2.15E-03						52.5	2.87E-04			
		230	2.56E-03						80	5.12E-04			
		252.5	2.15E-03						102.5	8.09E-04			
		280	1.84E-03						130	5.33E-04			
		302.5	2.36E-03						152.5	6.86E-04			
		330	1.84E-03						180	4.61E-04			
		352.5	1.74E-03						202.5	6.45E-04			
		380	1.54E-03						230	5.33E-04			
		402.5	1.54E-03						252.5	3.38E-04			
		430	1.13E-03						280	7.17E-04			
		452.5	1.23E-03						302.5	7.68E-04			
OR1-834	GTS2	2.5	2.77E-04						330	1.43E-03			
		30	6.66E-04						352.5	9.22E-04			
		52.5	5.53E-04						380	8.30E-04			
		80	1.33E-03						402.5	8.71E-04			
		102.5	1.64E-03						430	5.33E-04			
		130	1.33E-03				OR1-834	GT29	2.5	1.02E-04			
		152.5	2.05E-03						30	2.46E-04			
		202.5	1.64E-03						52.5	1.74E-04			
		230	2.66E-03						80	1.23E-04			
		252.5	2.87E-03						102.5	1.43E-04			
		280	2.46E-03						130	1.54E-04			
		302.5	1.23E-03						152.5	1.95E-04			
		330	2.05E-03						180	1.33E-04			
		380	1.43E-03						202.5	2.15E-04			
		402.5	1.64E-03						230	6.76E-04			
OR1-834	GTS3	2.5	2.15E-04						252.5	6.86E-04			
		30	2.36E-04						280	2.77E-04			
		52.5	4.30E-04				OR1-934	19-3	13.5	5.82E-01			
		80	4.51E-04						41	1.12E+00			

doi:10.6342/NTU202000506

Table A3.2.1. (continued).

cruise	site	depth (cmbsf)	CH_4 (mM)	depth (cmbsf)	SO_4^{2-} (mM)	Cl^- (mM)	cruise	site	depth (cmbsf)	CH_4 (mM)	depth (cmbsf)	SO_4^{2-} (mM)	Cl^- (mM)
OR1-934	19-3	63.5	9.32E-01				OR3-1323	1-2	55	3.85E-04	85	22.2	574
		91	1.00E+00						65	7.37E-04	105	21.1	558
		113.5	1.13E+00						75	1.05E-03			
		141	9.05E-01						85	8.98E-04			
		163.5	1.50E+00						95	1.46E-03			
		191	1.45E+00						105	2.00E-03			
		213.5	1.38E+00						110	1.21E-03			
		241	1.78E+00				OR3-1323	2-3	7.5	2.12E-04	0	27.5	563
		263.5	1.32E+00						22.5	5.52E-04	7.5	27.5	565
OR1-934	25	13.5	1.90E-03						37.5	b.d.l.	37.5	27.5	570
		41	1.17E-03						52.5	b.d.l.	67.5	25.9	534
		63.5	8.80E-04						67.5	8.62E-04			
		91	8.77E-04						82.5	b.d.l.			
		113.5	1.16E-03						97.5	b.d.l.			
		141	b.d.l.				OR3-1323	3	7.5	1.02E-03	0	27.5	565
		163.5	b.d.l.						22.5	5.86E-04	7.5	27.0	562
OR1-934	23	13.5	2.29E-03						37.5	b.d.l.	37.5	26.3	557
		41	4.86E-03						52.5	b.d.l.	97.5	26.4	575
		63.5	4.31E-03						67.5	b.d.l.	127.5	26.3	580
		91	6.97E-03						82.5	b.d.l.	157.5	25.5	564
		113.5	1.86E-02						97.5	b.d.l.			
		141	6.39E-02						112.5	b.d.l.			
		163.5	5.33E-02						127.5	b.d.l.			
		191	2.95E-02						142.5	b.d.l.			
		213.5	2.42E-02						157.5	5.13E-04			
		241	4.81E-02				OR3-1323	3-3	7.5	b.d.l.	0	27.1	556
		263.5	7.28E-02						22.5	b.d.l.	7.5	26.4	551
		291	3.58E-01						37.5	5.79E-04	52.5	26.3	576
OR1-934	S3	13.5	2.51E-03						52.5	b.d.l.	67.5	24.7	552
		41	6.61E-03						67.5	5.16E-04	97.5	24.2	557
		63.5	7.80E-03						82.5	b.d.l.			
		91	8.17E-03				OR3-1323	3-4	7.5	b.d.l.	0	26.9	549
		113.5	1.30E-02						22.5	b.d.l.	7.5	27.2	556
		141	1.92E-02						37.5	3.70E-04	37.5	27.8	573
		163.5	1.66E-02						52.5	b.d.l.	67.5	27.6	566
		191	2.11E-02						67.5	1.83E-03	97.5	26.6	542
		213.5	2.04E-02						82.5	b.d.l.			
OR1-934	S4B	13.5	1.22E-02						97.5	b.d.l.			
		41	2.37E-02				OR3-1323	4-1	5	b.d.l.	5	27.4	564
		63.5	1.92E-02						15	b.d.l.	25	27.6	565
		91	1.95E-02						25	b.d.l.	45	27.1	560
		113.5	2.07E-02						35	b.d.l.	65	27.0	567
		141	2.08E-02						45	4.86E-04	85	26.1	559
		163.5	1.78E-02						55	2.27E-04			
OR1-934	S19	13.5	2.30E-02						65	5.17E-04			
		41	3.80E-03						75	9.45E-04			
OR3-1323	1-1	5	5.92E-04	5	26.8	569			85	1.27E-03			
		15	1.02E-03	25	23.4	572	OR3-1323	4	5	b.d.l.	5	26.5	549
		25	1.59E-03	45	22.5	570			15	5.01E-04	25	26.6	561
		35	2.30E-03	65	21.7	563			25	7.18E-04	45	25.6	543
		45	2.28E-03	85	21.3	566			35	b.d.l.	65	26.0	558
		55	2.64E-03	105	20.1	560			45	1.83E-04	85	21.2	444
		65	2.45E-03						55	6.71E-04			
		75	3.11E-03						65	5.96E-03			
		85	7.22E-04						75	5.50E-03			
		95	2.97E-03						85	1.26E-03			
		105	2.48E-03						95	b.d.l.			
OR3-1323	1-2	5	3.79E-04	5	26.9	555			105	4.54E-04			
		15	3.79E-04	25	25.4	552	OR3-1323	5-1new	5	b.d.l.	5	27.8	574
		35	5.62E-04	45	23.9	560			15	2.89E-04	25	27.2	570
		45	8.58E-04	65	23.3	577			25	b.d.l.	45	26.6	559

doi:10.6342/NTU202000506

Table A3.2.1. (continued).

cruise	site	depth (cmbsf)	CH_4 (mM)	depth (cmbsf)	SO_4^{2-} (mM)	Cl^- (mM)	cruise	site	depth (cmbsf)	CH_4 (mM)	depth (cmbsf)	SO_4^{2-} (mM)	Cl^- (mM)
OR3-1323	5-1new	35	6.09E-04	65	27.0	573	OR3-1323	8	15	7.73E-04			
		45	b.d.l.	85	26.0	556			25	4.09E-04			
		55	9.60E-04						35	3.54E-04			
		65	7.72E-04						45	8.47E-04			
		75	4.22E-04						55	5.13E-04			
		85	8.13E-04						65	5.62E-04			
OR3-1323	5-2	5	6.28E-04	5	27.0	561			75	3.90E-04			
		15	9.02E-04	25	25.9	560			85	5.22E-04			
		25	7.31E-04	45	25.6	565	OR3-1323	9	0	b.d.l.	5	26.9	552
		35	7.42E-04	65	24.6	557			10	1.87E-03	15	26.7	553
		45	1.08E-03	85	25.7	594			20	6.37E-03	35	25.8	555
		55	1.36E-03						30	6.28E-03	55	25.4	560
		65	1.55E-03						40	2.07E-03	75	25.4	563
		75	3.03E-04						50	b.d.l.			
		85	1.10E-03						60	3.76E-04			
		95	1.85E-03						70	7.12E-04			
OR3-1323	6-1	7.5	b.d.l.				OR3-1384	FYB	5	3.08E-04	5	27.5	563
		22.5	4.55E-04						15	6.74E-04	25	27.6	564
		37.5	5.27E-04						25	b.d.l.	45	27.3	562
		52.5	4.10E-04						35	3.15E-04			
		67.5	8.16E-04						45	7.72E-04			
		82.5	3.45E-04						55	b.d.l.			
		97.5	6.68E-04						65	b.d.l.			
		112.5	9.26E-04						75	b.d.l.			
OR3-1323	6-2	7.5	b.d.l.						85	b.d.l.			
		22.5	b.d.l.				OR3-1384	FYB3	5	b.d.l.	0	27.6	564
		37.5	4.98E-04						15	7.77E-04	5	28.1	551
		52.5	b.d.l.						25	2.84E-04	25	28.9	572
		67.5	b.d.l.						35	2.85E-04	45	27.8	551
		82.5	7.22E-04						45	1.24E-03	65	27.6	588
		97.5	b.d.l.						55	b.d.l.	85	27.7	572
		112.5	b.d.l.						65	b.d.l.	105	27.2	569
		127.5	9.12E-04						75	b.d.l.	125	26.5	565
OR3-1323	6-4new	7.5	b.d.l.	0	27.1	555			85	b.d.l.	145	26.1	575
		22.5	b.d.l.	7.5	27.5	564			95	2.14E-04	165	24.2	560
		37.5	b.d.l.	37.5	27.0	574			105	b.d.l.	185	23.7	562
		52.5	9.58E-04	67.5	28.7	629			115	b.d.l.			
		67.5	1.04E-03	97.5	26.2	571			125	b.d.l.			
		82.5	1.13E-03	127.5	25.8	576			135	b.d.l.			
		97.5	6.91E-04						145	b.d.l.			
		112.5	8.42E-04						155	b.d.l.			
		127.5	7.07E-04						165	b.d.l.			
		142.5	4.77E-04						175	4.40E-04			
OR3-1323	7-2	5	5.36E-04						185	6.39E-04			
		15	b.d.l.				OR3-1384	FHLC-1	0	4.38E-06	0	27.2	555
		25	b.d.l.						5	3.16E-03	5	27.3	566
		35	4.04E-04						15	7.55E-04	25	27.3	572
		45	b.d.l.						25	7.05E-04	45	26.7	560
OR3-1323	7-5	5	b.d.l.	5	27.7	571			35	6.70E-04	65	26.3	555
		15	6.66E-04	25	27.2	559			45	7.31E-04	85	25.9	551
		25	1.07E-03	45	26.7	557			55	b.d.l.	105	26.1	559
		35	8.25E-04	65	28.0	641			65	b.d.l.	125	26.0	559
		45	2.33E-03	85	26.0	574			75	b.d.l.			
		55	2.66E-03	105	25.7	567			85	8.42E-04			
		65	3.45E-03						95	1.41E-03			
		75	2.58E-03						105	5.84E-04			
		85	4.10E-03						115	b.d.l.			
		95	3.48E-03						125	b.d.l.			
		105	2.33E-03						135	7.49E-04			
		115	1.09E-03				OR3-1323	temp8	7.5	4.72E-04			
OR3-1323	8	5	b.d.l.						22.5	b.d.l.			

doi:10.6342/NTU202000506

Table A3.2.1. (continued).

cruise	site	depth (cmbsf)	CH_4 (mM)	depth (cmbsf)	SO_4^{2-} (mM)	Cl^- (mM)	cruise	site	depth (cmbsf)	CH_4 (mM)	depth (cmbsf)	SO_4^{2-} (mM)	Cl^- (mM)
OR3-1323	temp8	37.5	5.07E-04				OR1-835	GT43	163.5	2.77E-04			
		52.5	3.51E-04						185.5	2.36E-03			
		67.5	1.52E-03						213.5	3.48E-04			
MD10-178	3267	46.5	6.57E-03	47	27.6	537			235.5	3.48E-04			
		127.5	6.33E-03	97	24.5	525			263.5	3.07E-04			
		196.5	6.37E-03	128	23.6	526			285.5	4.82E-04			
		246.5	6.27E-03	197	22.9	524			313.5	4.41E-04			
		277.5	5.30E-03	247	20.5	532			335.5	3.89E-04			
		346.5	6.41E-03	278	19.2	523			363.5	4.41E-04			
		396.5	6.22E-03	347	16.9	531			385.5	6.76E-04			
		427.5	4.35E-03	397	15.1	525	OR1-835	GT44	13.5	1.73E-04			
		496.5	4.11E-03	428	14.6	522			35.5	2.96E-04			
		546.5	b.d.l.	497	12.5	527			63.5	b.d.l.			
		577.5	6.31E-03	547	9.6	522			85.5	1.02E-04			
		646.5	7.51E-02	578	8.5	525			113.5	1.14E-04			
		696.5	1.05E-01	647	3.3	530			135.5	8.22E-05			
				697	2.0	528			163.5	8.75E-05			
OR1-1118	PR4	1	2.19E-03						185.5	b.d.l.			
		11	1.79E-03						213.5	b.d.l.			
		71	2.58E-03						235.5	b.d.l.			
		131	2.60E-03						263.5	2.34E-04			
		191	2.84E-03						285.5	2.11E-04			
		251	2.74E-03						313.5	1.19E-04			
		311	4.52E-02						335.5	b.d.l.			
		430	1.92E-03						363.5	b.d.l.			
OR1-1118	PR5	1	1.90E-03						385.5	b.d.l.			
		11	2.27E-03						413.5	b.d.l.			
		71	1.73E-03						435.5	b.d.l.			
		131	1.47E-03						463.5	b.d.l.			
		184	1.66E-03				OR1-835	GTYC1	13.5	4.61E-03			
OR1-1118	PR6-2	1	3.02E-02						35.5	1.64E-04			
		11	1.92E-03						63.5	1.54E-04			
		71	1.90E-03						135.5	b.d.l.			
		131	1.47E-03						163.5	1.84E-04			
		191	2.01E-02						185.5	2.36E-04			
		251	1.91E-02						213.5	2.56E-04			
		311	2.10E-02						235.5	1.95E-04			
		371	2.34E-02				OR1-835	GTS10	13.5	b.d.l.			
		430	2.44E-02						35.5	6.15E-05			
OR1-1118	PR7	1	9.67E-04						63.5	8.20E-05			
		11	1.93E-03						85.5	9.22E-05			
		71	3.17E-03						113.5	b.d.l.			
		131	7.64E-03						135.5	1.02E-04			
		191	9.84E-03						163.5	1.13E-04			
		251	6.00E-03						185.5	1.43E-04			
		311	1.13E-02						213.5	1.13E-04			
		365	3.44E-01						235.5	1.02E-04			
OR1-1118	PR8	1	2.58E-02						263.5	1.23E-04			
		11	3.05E-02						285.5	1.43E-04			
		71	2.66E-02						313.5	4.10E-05			
		131	4.07E-02						335.5	b.d.l.			
		191	6.75E-02						363.5	b.d.l.			
		251	1.08E-01						385.5	1.23E-04			
		311	1.31E-01						413.5	1.13E-04			
		371	1.67E-01						435.5	9.22E-05			
		426	2.49E-01				OR1-835	GTS23	13.5	6.15E-05			
OR1-835	GT43	13.5	5.38E-05						35.5	4.41E-04			
		35.5	1.08E-04						63.5	1.84E-04			
		63.5	1.61E-04						113.5	2.66E-04			
		113.5	4.61E-04						135.5	4.30E-04			
		135.5	2.36E-04						163.5	2.66E-04			

doi:10.6342/NTU202000506

Table A3.2.1. (continued).

cruise	site	depth (cmbsf)	CH_4 (mM)	depth (cmbsf)	SO_4^{2-} (mM)	Cl^- (mM)	cruise	site	depth (cmbsf)	CH_4 (mM)	depth (cmbsf)	SO_4^{2-} (mM)	Cl^- (mM)
OR1-835	GTS15	35.5	9.22E-05				OR3-1368	13	106	3.45E-03			
		63.5	9.22E-05						133.5	1.44E-03			
		85.5	b.d.l.				OR3-1368	11	13.5	3.38E-03			
		113.5	9.22E-05						46	b.d.l.			
		135.5	7.17E-05						73.5	5.38E-03			
		163.5	1.13E-04						106	1.14E-03			
		185.5	1.54E-04						133.5	1.18E-03			
		213.5	1.43E-04						166	9.40E-04			
		235.5	6.15E-05						193.5	1.09E-03			
		263.5	7.17E-05				OR3-1368	kp9	13.5	8.92E-04			
OR1-835	GTS17	13.5	8.20E-05						46	3.61E-03			
		35.5	b.d.l.				OR3-1368	9	13.5	1.14E-03			
		63.5	b.d.l.						46	1.23E-03			
		85.5	9.22E-05						73.5	1.69E-03			
		113.5	8.20E-05						106	1.96E-03			
		135.5	6.15E-05						133.5	1.60E-03			
		163.5	b.d.l.				OR3-1368	7	13.5	9.64E-04			
		185.5	7.17E-05						46	1.11E-03			
		213.5	1.13E-04						73.5	1.03E-03			
		235.5	1.02E-04						106	1.18E-03			
		263.5	b.d.l.						133.5	1.52E-03			
		285.5	3.07E-04						166	1.84E-03			
		335.5	1.74E-04				OR3-1368	4	13.5	6.45E-04			
		363.5	2.87E-04						46	7.76E-04			
		413.5	b.d.l.						73.5	7.98E-04			
OR1-835	GTS27	13.5	1.23E-04						106	1.18E-03			
		35.5	9.22E-05						133.5	1.79E-03			
		63.5	1.02E-04						166	1.41E-03			
		85.5	b.d.l.				OR3-1368	3	13.5	1.18E-03			
		113.5	9.22E-05						46	9.74E-04			
		135.5	1.13E-04						73.5	1.06E-03			
		163.5	1.95E-04						106	1.29E-03			
		185.5	4.20E-04						133.5	1.06E-03			
		213.5	1.33E-04				OR3-1368	2	13.5	6.75E-04			
		235.5	1.43E-04						46	1.11E-03			
		263.5	1.33E-04						73.5	1.29E-03			
		285.5	1.84E-04						106	1.83E-03			
		313.5	1.64E-04						133.5	2.15E-03			
		335.5	1.84E-04						166	1.39E-03			
		363.5	1.54E-04				OR3-1368	1	13.5	7.90E-04			
		385.5	1.43E-04						46	1.10E-03			
		413.5	1.33E-04						73.5	1.27E-03			
		435.5	1.43E-04						106	1.78E-03			
		463.5	1.43E-04						133.5	1.24E-03			
		485.5	2.15E-04				OR1-804	7	8	9.99E-02			
OR3-1368	23	13.5	b.d.l.						33	9.99E-02			
		46	7.63E-04				OR1-835	GTF0	13.5	5.64E-04			
		73.5	2.51E-03						35.5	b.d.l.			
		106	9.55E-04						63.5	b.d.l.			
		133.5	2.37E-03						85.5	1.33E-03			
		166.5	b.d.l.						113.5	b.d.l.			
OR3-1368	20	13.5	b.d.l.						135.5	b.d.l.			
		46	2.71E-03						163.5	b.d.l.			
		73.5	3.85E-03						185.5	b.d.l.			
OR3-1368	19	13.5	2.80E-03						385.5	6.25E-04			
		46	2.94E-03				OR1-835	GTF1	13.5	1.13E-04			
		73.5	3.07E-03						35.5	5.12E-05			
		106	b.d.l.						63.5	1.13E-04			
OR3-1368	13	13.5	0.00E+00						85.5	1.02E-04			
		46	1.70E-03						113.5	1.02E-04			
		73.5	2.02E-03						135.5	1.13E-04			

doi:10.6342/NTU202000506

Table A3.2.1. (continued).

cruise	site	depth (cmbsf)	CH_4 (mM)	depth (cmbsf)	SO_4^{2-} (mM)	Cl^- (mM)
OR1-835	GTF1	163.5	2.97E-04			
		185.5	1.43E-04			
		213.5	2.15E-04			
		263.5	1.64E-04			
		285.5	1.95E-04			
		313.5	1.95E-04			
		335.5	1.64E-04			
		385.5	2.05E-04			
OR1-835	GTF7	13.5	1.84E-04			
		35.5	1.64E-04			
		63.5	1.33E-04			
		85.5	1.23E-04			
		113.5	1.54E-04			
		135.5	1.23E-04			
OR1-835	GTF3	13.5	b.d.l.			
		35.5	1.33E-04			
		63.5	2.97E-04			
		113.5	1.74E-04			
		135.5	2.15E-04			
		163.5	b.d.l.			
		185.5	4.30E-04			
		213.5	1.64E-04			
		235.5	3.07E-04			
		263.5	3.28E-04			
		285.5	3.07E-04			
		313.5	2.97E-04			
		335.5	b.d.l.			
		363.5	1.64E-04			
		385.5	b.d.l.			
		413.5	2.36E-04			
		435.5	1.95E-04			
OR3-1384	FGS5-1	5	2.12E-03	0	27.5	563
		35	1.83E-02	5	27.3	562
		55	3.66E-02	25	24.6	565
		75	4.38E-02	45	20.9	560
		95	5.47E-02	65	18.5	572
				85	15.5	573
OR3-1384	FGS5-2	0	3.66E-06	0	27.3	557
		5	0.00E+00	5	28.0	575
		15	0.00E+00	25	27.3	561
		25	0.00E+00	45	27.1	563
		35	7.78E-04	65	26.7	563
		45	7.08E-04	85	25.3	576
		55	2.30E-03			
		65	3.44E-03			
		75	2.52E-03			
		85	8.35E-03			

doi:10.6342/NTU202000506

Table A3.2.1. (continued).

cruise	site	CH_4 in BW (mM)	assummed CH_4 in BW (mM)	CH_4 in core top (mM)	reference
OR2-1207	G14		3.04E-04	3.60E-02	*Chuang et al.* [2006]
OR2-1207	G15	3.20E-05		4.15E-02	*Chuang et al.* [2006]
OR2-1207	G16	3.68E-05		3.55E-02	*Chuang et al.* [2006]
OR2-1207	G17		3.20E-05	3.71E-02	*Chuang et al.* [2006]
OR2-1207	G18	6.61E-05		4.11E-02	*Chuang et al.* [2006]
OR2-1207	G21		6.61E-05	4.16E-02	*Chuang et al.* [2006]
OR2-1207	G23		3.20E-05	5.02E-02	*Chuang et al.* [2006]
OR2-1207	G24	6.03E-05		3.48E-02	*Chuang et al.* [2006]
OR2-1207	G27	6.25E-05		4.36E-02	*Chuang et al.* [2006]
OR2-1207	G30	3.82E-05		3.79E-02	*Chuang et al.* [2006]
OR2-1207	G31		6.87E-05	4.18E-02	*Chuang et al.* [2006]
OR2-1207	G46		6.87E-05	5.16E-02	*Chuang et al.* [2006]
OR2-1207	G47	2.74E-05		4.25E-02	*Chuang et al.* [2006]
OR2-1207	G49		6.87E-05	4.98E-02	*Chuang et al.* [2006]
OR2-1207	G50	4.98E-05		4.14E-02	*Chuang et al.* [2006]
OR2-1230	A	1.65E-03		2.47E-02	*Chuang et al.* [2006]
OR2-1230	D	4.09E-04		2.46E-02	*Chuang et al.* [2006]
OR2-1230	G103	1.84E-04		2.48E-02	*Chuang et al.* [2006]
OR2-1230	G105	8.24E-05		2.39E-02	*Chuang et al.* [2006]
OR2-1230	G107	6.22E-04		2.38E-02	*Chuang et al.* [2006]
OR2-1230	G109	3.96E-05		2.50E-02	*Chuang et al.* [2006]
OR2-1230	G111		3.07E-03	2.72E-02	*Chuang et al.* [2006]
OR2-1230	G21	4.50E-03		2.51E-02	*Chuang et al.* [2006]
OR2-1230	G3	1.77E-03		2.27E-02	*Chuang et al.* [2006]
OR2-1230	G69	2.52E-03		2.79E-02	*Chuang et al.* [2006]
OR2-1230	G70	1.46E-03		3.22E-02	*Chuang et al.* [2006]
OR2-1230	G72		1.06E-03	2.38E-02	*Chuang et al.* [2006]
OR2-1230	G73	9.21E-04		2.41E-02	*Chuang et al.* [2006]
OR2-1230	G81	3.45E-03		2.42E-02	*Chuang et al.* [2006]
OR2-1230	G82	5.44E-03		1.77E-02	*Chuang et al.* [2006]
OR2-1230	G85	1.13E-05		2.39E-02	*Chuang et al.* [2006]
OR2-1230	G86	2.22E-04		2.45E-02	*Chuang et al.* [2006]
OR2-1230	G87	1.72E-03		2.59E-02	*Chuang et al.* [2006]
OR2-1230	G88		3.45E-03	2.95E-02	*Chuang et al.* [2006]
OR2-1230	G89	4.86E-03		2.50E-02	*Chuang et al.* [2006]
OR2-1230	G90	8.31E-06		2.34E-02	*Chuang et al.* [2006]
OR2-1230	G91	3.70E-03		1.43E-02	*Chuang et al.* [2006]
OR2-1230	G94	9.28E-04		2.42E-02	*Chuang et al.* [2006]
OR2-1230	G95	3.07E-03		1.91E-02	*Chuang et al.* [2006]
OR2-1230	G96	3.97E-03		1.67E+00	*Chuang et al.* [2006]
OR2-1230	G99	1.56E-03		2.39E-02	*Chuang et al.* [2006]
OR2-1230	GC		4.15E-04	2.87E-02	*Chuang et al.* [2006]
OR1-697	G23	1.66E-02		2.79E-02	*Chuang et al.* [2006]
OR1-697	G5A	1.77E-05		1.39E-02	*Chuang et al.* [2006]
OR1-718	G22	6.57E-03		2.28E-03	*Chuang et al.* [2006]
OR1-718	N6	2.04E-04		8.57E-04	*Chuang et al.* [2006]
OR1-718	N8	5.12E-02		7.67E-03	*Chuang et al.* [2006]
OR1-758	GH1		9.94E-06	1.06E-03	*Chuang et al.* [2006]
OR1-758	GH10		1.33E-04	4.58E-04	*Chuang et al.* [2006]
OR1-758	GH11		9.94E-06	7.06E-04	*Chuang et al.* [2006]
OR1-758	GH12		9.94E-06	5.09E-04	*Chuang et al.* [2006]
OR1-758	GH13		9.94E-06	8.28E-04	*Chuang et al.* [2006]
OR1-758	GH14		4.58E-04	2.89E-04	*Chuang et al.* [2006]
OR1-758	GH15		3.82E-03	2.13E-04	*Chuang et al.* [2006]
OR1-758	GH16		5.18E-04	4.27E-04	*Chuang et al.* [2006]
OR1-758	GH17		5.18E-04	3.71E-04	*Chuang et al.* [2006]
OR1-758	GH18		5.35E-03	6.63E-04	*Chuang et al.* [2006]
OR1-758	GH19		5.35E-03	3.88E-04	*Chuang et al.* [2006]
OR1-758	GH2		1.33E-04	6.41E-04	*Chuang et al.* [2006]
OR1-758	GH20		5.44E-03	9.92E-04	*Chuang et al.* [2006]
OR1-758	GH22		3.20E-05	1.27E-03	*Chuang et al.* [2010]
OR1-758	GH3		1.27E-03	3.22E-03	*Chuang et al.* [2010]
OR1-758	GH4		8.17E-05	4.62E-04	*Chuang et al.* [2010]

doi:10.6342/NTU202000506

Table A3.2.1. (continued).

cruise	site	CH_4 in BW (mM)	assummed CH_4 in BW (mM)	CH_4 in core top (mM)	reference
OR1-758	GH5		1.86E-04	1.85E-03	*Chuang et al.* [2010]
OR1-758	GH6		4.31E-05	5.17E-04	*Chuang et al.* [2010]
OR1-758	GH7		6.87E-05	2.91E-03	*Chuang et al.* [2010]
OR1-758	GH8		6.87E-05	1.81E-03	*Chuang et al.* [2010]
OR1-758	GH9		1.33E-04	1.19E-03	*Chuang et al.* [2010]
OR1-765	2		9.13E-05	8.06E-04	*Chuang et al.* [2010]
OR1-765	3		9.13E-05	2.24E-04	*Chuang et al.* [2010]
OR1-765	4		9.13E-05	3.25E-04	*Chuang et al.* [2010]
OR1-765	5		9.13E-05	1.72E-04	*Chuang et al.* [2010]
OR1-765	6		9.13E-05	3.00E-04	*Chuang et al.* [2010]
OR1-765	8	1.65E-06		3.67E-04	*Chuang et al.* [2010]
OR1-765	9		9.13E-05	4.03E-03	*Chuang et al.* [2010]
OR1-765	10		9.13E-05	6.77E-03	*Chuang et al.* [2010]
OR1-765	11		9.13E-05	1.70E-03	*Chuang et al.* [2010]
OR1-765	14	2.13E-06		3.18E-05	*Chuang et al.* [2010]
OR1-765	15	2.27E-06		4.01E-04	*Chuang et al.* [2010]
OR1-765	16	7.05E-06		5.64E-05	*Chuang et al.* [2010]
OR1-765	18	1.29E-05		1.98E-04	*Chuang et al.* [2010]
OR1-765	21	4.44E-06		3.22E-04	*Chuang et al.* [2010]
OR1-765	24	1.27E-06		2.12E-04	*Chuang et al.* [2010]
OR1-765	25	3.10E-06		1.67E-04	*Chuang et al.* [2010]
OR1-765	30	2.06E-06		3.35E-04	*Chuang et al.* [2010]
OR1-765	31	1.88E-06		4.03E-04	*Chuang et al.* [2010]
OR1-765	32		9.13E-05	1.72E-04	*Chuang et al.* [2010]
OR1-765	33	4.58E-06		4.30E-04	*Chuang et al.* [2010]
OR1-765	34	5.67E-06		2.64E-04	*Chuang et al.* [2010]
OR1-765	41		9.13E-05	5.00E-04	*Chuang et al.* [2010]
OR1-765	42	4.10E-06		7.89E-05	*Chuang et al.* [2010]
OR1-765	a	3.24E-04		1.26E-03	*Chuang et al.* [2010]
OR1-765	c	4.31E-05		1.00E-03	*Chuang et al.* [2010]
OR1-765	D		2.04E-04	8.77E-05	*Chuang et al.* [2010]
OR1-765	H		1.29E-05	3.20E-02	*Chuang et al.* [2010]
OR1-765	M1	1.86E-06		1.48E-04	*Chuang et al.* [2010]
OR1-765	M2	3.15E-06		4.08E-04	*Chuang et al.* [2010]
OR1-792	GS1	3.05E-05		5.47E-04	*Chuang et al.* [2010]
OR1-792	GS10A	7.00E-05		1.77E-03	*Chuang et al.* [2010]
OR1-792	GS11	1.49E-05		1.57E-04	*Chuang et al.* [2010]
OR1-792	GS11A	1.69E-05		1.14E-04	*Chuang et al.* [2010]
OR1-792	GS2		7.05E-06	3.20E-04	*Chuang et al.* [2010]
OR1-792	GS3	1.96E-05		6.31E-05	*Chuang et al.* [2010]
OR1-792	GS5		2.62E-05	3.98E-01	*Chuang et al.* [2010]
OR1-792	GS6	1.97E-05		2.25E-03	*Chuang et al.* [2010]
OR1-792	GS7	3.34E-05		2.40E-03	*Chuang et al.* [2010]
OR1-792	GS9A	1.70E-05		3.99E-03	*Chuang et al.* [2010]
OR1-804	3	4.66E-07		1.43E-04	*Chuang et al.* [2010]
OR1-804	4		8.28E-05	1.33E-04	*Chuang et al.* [2010]
OR1-804	5		8.28E-05	1.13E-04	*Chuang et al.* [2010]
OR1-804	10		8.28E-05	2.15E-04	*Chuang et al.* [2010]
OR1-804	11		8.28E-05	5.02E-04	*Chuang et al.* [2010]
OR1-804	13		8.28E-05	2.97E-04	*Chuang et al.* [2010]
OR1-804	14		8.28E-05	4.51E-04	*Chuang et al.* [2010]
OR1-804	21	3.92E-07		6.86E-04	*Chuang et al.* [2010]
OR1-804	22		8.28E-05	6.86E-04	*Chuang et al.* [2010]
OR1-804	23		8.28E-05	5.94E-04	*Chuang et al.* [2010]
OR1-804	24		8.28E-05	3.69E-03	*Chuang et al.* [2010]
OR1-804	25		8.28E-05	1.54E-04	*Chuang et al.* [2010]
OR1-804	29		8.28E-05	4.20E-04	*Chuang et al.* [2010]
OR1-804	30		8.28E-05	4.10E-04	*Chuang et al.* [2010]
OR1-804	31		8.28E-05	5.12E-04	*Chuang et al.* [2010]
OR1-804	35		8.28E-05	2.46E-04	*Chuang et al.* [2010]
OR1-804	36		8.28E-05	9.22E-05	*Chuang et al.* [2010]
OR1-804	37		8.28E-05	3.69E-04	*Chuang et al.* [2010]
OR1-804	GS5		2.62E-05	5.43E-04	*Chuang et al.* [2010]

doi:10.6342/NTU202000506

Table A3.2.1. (continued).

cruise	site	CH_4 in BW (mM)	assummed CH_4 in BW (mM)	CH_4 in core top (mM)	reference
OR1-1118	PR8	4.46E-06		2.58E-02	this study
OR1-697	G1	2.35E-05		6.94E-02	this study; [*Chuang et al*., 2006]
OR1-697	G10	1.30E-05		7.31E-02	this study; [*Chuang et al*., 2006]
OR1-697	G15	1.30E-05		1.88E-02	this study; [*Chuang et al*., 2006]
OR1-697	G17	1.02E-04		4.29E-01	this study; [*Chuang et al*., 2006]
OR1-697	G19	3.25E-05		2.67E-02	this study; [*Chuang et al*., 2006]
OR1-697	G2		3.12E-04	1.13E-01	this study; [*Chuang et al*., 2006]
OR1-697	G21	5.11E-05		2.35E-02	this study; [*Chuang et al*., 2006]
OR1-697	G3		3.12E-04	5.00E-02	this study; [*Chuang et al*., 2006]
OR1-697	G6	1.23E-05		2.56E-02	this study; [*Chuang et al*., 2006]
OR1-697	GA		3.16E-04	3.38E-02	this study; [*Chuang et al*., 2006]
OR1-697	GC		6.57E-03	5.25E-02	this study; [*Chuang et al*., 2006]
OR1-718	G11	3.04E-04		3.93E-02	this study; [*Chuang et al*., 2006]
OR1-718	G11C	6.86E-05		4.02E-02	this study; [*Chuang et al*., 2006]
OR1-718	G4	3.12E-04		3.84E-02	this study; [*Chuang et al*., 2006]
OR1-718	G7		4.15E-04	6.10E-02	this study; [*Chuang et al*., 2006]
OR1-718	G9	4.15E-04		8.88E-02	this study; [*Chuang et al*., 2006]
OR1-718	N1	5.18E-04		6.70E-04	this study; [*Chuang et al*., 2006]
OR1-718	N11	8.80E-04		7.18E-04	this study; [*Chuang et al*., 2006]
OR1-718	N13		1.06E-03	3.58E-02	this study; [*Chuang et al*., 2006]
OR1-718	N4	3.16E-04		3.35E-02	this study; [*Chuang et al*., 2006]
OR1-718	N9	1.06E-03		5.48E-04	this study; [*Chuang et al*., 2006]
OR1-732	G1	4.48E-04		2.62E-02	this study; [*Chuang et al*., 2006]
OR1-732	G10	1.11E-03		2.56E-02	this study; [*Chuang et al*., 2006]
OR1-732	G17	4.49E-03		2.37E-02	this study; [*Chuang et al*., 2006]
OR1-732	G18	1.79E-03		3.04E-02	this study; [*Chuang et al*., 2006]
OR1-732	G26	1.17E-05		2.69E-02	this study; [*Chuang et al*., 2006]
OR1-732	G27	3.73E-03		2.73E-02	this study; [*Chuang et al*., 2006]
OR1-732	G28	1.10E-03		2.95E-02	this study; [*Chuang et al*., 2006]
OR1-732	G3	3.82E-03		2.87E-02	this study; [*Chuang et al*., 2006]
OR1-732	G31	3.49E-04		2.61E-02	this study; [*Chuang et al*., 2006]
OR1-732	G33	7.30E-04		2.47E-02	this study; [*Chuang et al*., 2006]
OR1-732	G36	1.18E-05		3.68E-02	this study; [*Chuang et al*., 2006]
OR1-732	G4	4.58E-04		2.95E-02	this study; [*Chuang et al*., 2006]
OR1-732	G5	6.80E-03		3.19E-02	this study; [*Chuang et al*., 2006]
OR1-732	G7	7.23E-04		2.74E-02	this study; [*Chuang et al*., 2006]
OR1-732	G8	5.20E-04		2.58E-02	this study; [*Chuang et al*., 2006]
OR1-732	G9	5.35E-03		2.93E-02	this study; [*Chuang et al*., 2006]
OR1-732	G96	4.47E-02		1.31E-01	this study; [*Chuang et al*., 2006]
OR1-828	GT1		4.31E-05	3.36E-03	this study; [*Chen*, 2009;*Yang*, 2007]
OR1-828	GT10		7.03E-05	2.11E-04	this study; [*Chen*, 2009;*Yang*, 2007]
OR1-828	GT11		3.96E-05	6.61E-04	this study; [*Chen*, 2009;*Yang*, 2007]
OR1-828	GT2		9.94E-06	1.97E-04	this study; [*Chen*, 2009;*Yang*, 2007]
OR1-828	GT3		7.23E-04	2.19E-04	this study; [*Chen*, 2009;*Yang*, 2007]
OR1-828	GT5		4.56E-05	5.24E-04	this study; [*Chen*, 2009;*Yang*, 2007]
OR1-828	GT6		4.56E-05	4.07E-04	this study; [*Chen*, 2009;*Yang*, 2007]
OR1-828	GT7		3.32E-05	5.11E-02	this study; [*Chen*, 2009;*Yang*, 2007]
OR1-828	GT8A		6.65E-05	9.20E-04	this study; [*Chen*, 2009;*Yang*, 2007]
OR1-828	GT9		1.11E-03	7.04E-04	this study; [*Chen*, 2009;*Yang*, 2007]
OR1-834	GT12		5.36E-04	1.00E-04	this study; [*Chen*, 2009;*Yang*, 2007]
OR1-834	GT17		3.07E-06	3.00E-04	this study; [*Chen*, 2009;*Yang*, 2007]
OR1-834	GT21		4.56E-05	1.50E-03	this study; [*Chen*, 2009;*Yang*, 2007]
OR1-834	GT22		4.56E-05	4.00E-04	this study; [*Chen*, 2009;*Yang*, 2007]
OR1-834	GT24		4.56E-05	1.70E-03	this study; [*Chen*, 2009;*Yang*, 2007]
OR1-834	GT28		3.32E-05	1.30E-03	this study; [*Chen*, 2009;*Yang*, 2007]
OR1-834	GT31		1.46E-03	2.90E-03	this study; [*Chen*, 2009;*Yang*, 2007]
OR1-834	GT35		1.46E-03	4.00E-04	this study; [*Chen*, 2009;*Yang*, 2007]
OR1-834	GT38		3.32E-05	1.00E-04	this study; [*Chen*, 2009;*Yang*, 2007]
OR1-834	GT4		1.36E-04	2.00E-04	this study; [*Chen*, 2009;*Yang*, 2007]
OR1-834	GT42		1.13E-05	1.00E-04	this study; [*Chen*, 2009;*Yang*, 2007]
OR1-834	GT5		4.56E-05	3.00E-04	this study; [*Chen*, 2009;*Yang*, 2007]
OR1-834	GT9		1.11E-03	1.00E-04	this study; [*Chen*, 2009;*Yang*, 2007]
OR1-834	GTM29		3.32E-05	1.00E-04	this study; [*Chen*, 2009;*Yang*, 2007]

doi:10.6342/NTU202000506

Table A3.2.1. (continued).

cruise	site	CH_4 in BW (mM)	assummed CH_4 in BW (mM)	CH_4 in core top (mM)	reference
OR1-834	GTM2B	5.36E-04		6.00E-04	this study; [*Chen*, 2009;*Yang*, 2007]
OR1-834	GTS1	3.21E-04		4.00E-04	this study; [*Chen*, 2009;*Yang*, 2007]
OR1-834	GTS2	4.56E-05		3.00E-04	this study; [*Chen*, 2009;*Yang*, 2007]
OR1-834	GTS3	1.36E-04		2.00E-04	this study; [*Chen*, 2009;*Yang*, 2007]
OR1-834	GTS4		7.03E-05	1.00E-04	this study; [*Chen*, 2009;*Yang*, 2007]
OR1-834	GTS5		1.56E-03	1.00E-04	this study; [*Chen*, 2009;*Yang*, 2007]
OR1-835	GT39B		4.56E-05	1.50E-03	this study; [*Chen*, 2009;*Yang*, 2007]
OR1-835	GT43		3.15E-06	1.00E-04	this study; [*Chen*, 2009;*Yang*, 2007]
OR1-835	GT44		3.15E-06	2.00E-04	this study; [*Chen*, 2009;*Yang*, 2007]
OR1-835	GTF0		9.13E-05	6.00E-04	this study; [*Chen*, 2009;*Yang*, 2007]
OR1-835	GTF1		9.13E-05	1.00E-04	this study; [*Chen*, 2009;*Yang*, 2007]
OR1-835	GTF3	9.13E-05		1.00E-04	this study; [*Chen*, 2009;*Yang*, 2007]
OR1-835	GTF7		9.13E-05	2.00E-04	this study; [*Chen*, 2009;*Yang*, 2007]
OR1-835	GTS10		3.15E-06	1.00E-04	this study; [*Chen*, 2009;*Yang*, 2007]
OR1-835	GTS15		3.15E-06	1.00E-04	this study; [*Chen*, 2009;*Yang*, 2007]
OR1-835	GTS17		3.15E-06	1.00E-04	this study; [*Chen*, 2009;*Yang*, 2007]
OR1-835	GTS23		3.15E-06	1.00E-04	this study; [*Chen*, 2009;*Yang*, 2007]
OR1-835	GTS27		3.15E-06	1.00E-04	this study; [*Chen*, 2009;*Yang*, 2007]
OR1-835	GTYC1		3.15E-06	4.60E-03	this study; [*Chen*, 2009;*Yang*, 2007]
OR1-860	5	6.87E-05		5.00E-03	this study; [*Chen*, 2009;*Yang*, 2008]
OR1-860	11		3.24E-04	6.00E-03	this study; [*Chen*, 2009;*Yang*, 2008]
OR1-860	13	1.25E-04		7.60E-03	this study; [*Chen*, 2009;*Yang*, 2008]
OR1-860	15	1.25E-04		4.80E-03	this study; [*Chen*, 2009;*Yang*, 2008]
OR1-860	17	1.35E-04		4.50E-03	this study; [*Chen*, 2009;*Yang*, 2008]
OR1-860	22	1.33E-04		1.10E-03	this study; [*Chen*, 2009;*Yang*, 2008]
OR1-860	24	1.94E-02		8.00E-04	this study; [*Chen*, 2009;*Yang*, 2008]
OR1-860	27	5.78E-01		1.45E-01	this study; [*Chen*, 2009;*Yang*, 2008]
OR1-902A	3	6.67E-05		2.65E-03	this study; [*Chen*, 2011;*Yang*, 2009]
OR1-902A	4	8.43E-05		5.06E-03	this study; [*Chen*, 2011;*Yang*, 2009]
OR1-902A	8	6.69E-05		9.66E-03	this study; [*Chen*, 2011;*Yang*, 2009]
OR1-902A	9	7.12E-04		1.06E-03	this study; [*Chen*, 2011;*Yang*, 2009]
OR1-902B	5	6.69E-05		1.91E-03	this study; [*Chen*, 2011;*Yang*, 2009]
OR1-902B	8	6.77E-05		2.23E-03	this study; [*Chen*, 2011;*Yang*, 2009]
OR1-902B	9	6.65E-05		3.41E-03	this study; [*Chen*, 2011;*Yang*, 2009]
OR1-902B	27	1.71E-01		3.94E-03	this study; [*Chen*, 2011;*Yang*, 2009]
OR1-902B	G3		6.65E-05	1.75E-03	this study; [*Chen*, 2011;*Yang*, 2009]
OR1-902B	HSU1		1.02E-04	2.53E-03	this study; [*Chen*, 2011;*Yang*, 2009]
OR1-902B	HSU2	1.09E-04		9.27E-03	this study; [*Chen*, 2011;*Yang*, 2009]
OR1-902B	KP7-1		1.06E-03	1.71E-03	this study; [*Chen*, 2011;*Yang*, 2009]
OR1-902B	N2		5.18E-04	2.69E-03	this study; [*Chen*, 2011;*Yang*, 2009]
OR1-902B	T6	6.77E-05		3.70E-03	this study; [*Chen*, 2011;*Yang*, 2009]
OR1-934	8		4.56E-05	1.14E-03	this study; [*Yang*, 2010]
OR1-934	23		7.03E-05	2.29E-03	this study; [*Yang*, 2010]
OR1-934	25		7.03E-05	1.90E-03	this study; [*Yang*, 2010]
OR1-934	42813		7.03E-05	5.82E-01	this study; [*Yang*, 2010]
OR1-934	9F		3.21E-04	4.48E-01	this study; [*Yang*, 2010]
OR1-934	B1-2		3.21E-04	3.72E-03	this study; [*Yang*, 2010]
OR1-934	F2		4.56E-05	5.75E-04	this study; [*Yang*, 2010]
OR1-934	S18B		9.28E-04	5.21E-04	this study; [*Yang*, 2010]
OR1-934	S19		9.28E-04	2.30E-02	this study; [*Yang*, 2010]
OR1-934	S3		3.96E-05	2.51E-03	this study; [*Yang*, 2010]
OR1-934	S4B		3.96E-05	1.22E-02	this study; [*Yang*, 2010]
OR1-961	21C		9.94E-06	1.55E-03	this study; [*Yang*, 2011]
OR1-978	5		2.92E-06	3.82E-02	this study; [*Yang*, 2011]
OR1-978	6	9.94E-06		2.66E-02	this study; [*Yang*, 2011]
OR1-978	7	2.91E-06		1.07E-04	this study; [*Yang*, 2011]
OR1-978	1N-1	3.75E-05		1.44E-03	this study; [*Yang*, 2011]
OR1-978	2N	1.27E-02		1.74E-01	this study; [*Yang*, 2011]
OR1-978	2NL	5.46E-02		5.04E-01	this study; [*Yang*, 2011]
OR1-978	4-3	2.92E-06		3.22E-02	this study; [*Yang*, 2011]
OR3-1323	1-1		5.36E-04	5.92E-04	this study; [*Chen*, 2010]
OR3-1323	1-2		3.32E-05	3.79E-04	this study; [*Chen*, 2010]
OR3-1323	2-3		1.26E-04	2.12E-04	this study; [*Chen*, 2010]

doi:10.6342/NTU202000506

Table A3.2.1. (continued).

cruise	site	CH_4 in BW (mM)	assummed CH_4 in BW (mM)	CH_4 in core top (mM)	reference
OR3-1323	3-1		6.61E-05	1.02E-03	this study; [*Chen*, 2010]
OR3-1323	3-3		1.10E-03	5.79E-04	this study; [*Chen*, 2010]
OR3-1323	3-4		6.22E-04	3.70E-04	this study; [*Chen*, 2010]
OR3-1323	4		6.61E-05	5.01E-04	this study; [*Chen*, 2010]
OR3-1323	4-1		1.72E-03	4.86E-04	this study; [*Chen*, 2010]
OR3-1323	5-1new		3.70E-03	2.89E-04	this study; [*Chen*, 2010]
OR3-1323	5-2		6.61E-05	6.28E-04	this study; [*Chen*, 2010]
OR3-1323	6-1		6.61E-05	4.55E-04	this study; [*Chen*, 2010]
OR3-1323	6-3		6.61E-05	4.98E-04	this study; [*Chen*, 2010]
OR3-1323	6-4new		3.20E-05	9.58E-04	this study; [*Chen*, 2010]
OR3-1323	7-2		6.61E-05	5.36E-04	this study; [*Chen*, 2010]
OR3-1323	7-5		3.20E-05	6.66E-04	this study; [*Chen*, 2010]
OR3-1323	8-1		6.61E-05	7.73E-04	this study; [*Chen*, 2010]
OR3-1323	9		8.62E-05	1.87E-03	this study; [*Chen*, 2010]
OR3-1323	GT39B		3.13E-06	1.56E-04	this study; [*Chen*, 2010]
OR3-1323	temp2		1.72E-03	1.09E-03	this study; [*Chen*, 2010]
OR3-1323	temp8		6.61E-05	4.72E-04	this study; [*Chen*, 2010]
OR3-1368	1	8.28E-05		7.90E-04	this study; [*Chen*, 2011; *Yang*, 2009]
OR3-1368	11	9.53E-05		3.38E-03	this study; [*Chen*, 2011; *Yang*, 2009]
OR3-1368	13	4.57E-05		2.27E-03	this study; [*Chen*, 2011; *Yang*, 2009]
OR3-1368	19		9.53E-05	2.80E-03	this study; [*Chen*, 2011; *Yang*, 2009]
OR3-1368	2		6.53E-05	6.75E-04	this study; [*Chen*, 2011; *Yang*, 2009]
OR3-1368	20	8.65E-05		3.61E-03	this study; [*Chen*, 2011; *Yang*, 2009]
OR3-1368	22	9.86E-04		2.30E-03	this study; [*Chen*, 2011; *Yang*, 2009]
OR3-1368	23	9.99E-05		1.02E-03	this study; [*Chen*, 2011; *Yang*, 2009]
OR3-1368	3		6.53E-05	1.18E-03	this study; [*Chen*, 2011; *Yang*, 2009]
OR3-1368	4	6.53E-05		6.45E-04	this study; [*Chen*, 2011; *Yang*, 2009]
OR3-1368	5		6.53E-05	8.15E-04	this study; [*Chen*, 2011; *Yang*, 2009]
OR3-1368	7		6.53E-05	9.64E-04	this study; [*Chen*, 2011; *Yang*, 2009]
OR3-1368	9		6.53E-05	1.14E-03	this study; [*Chen*, 2011; *Yang*, 2009]
OR3-1368	96B	2.70E-04		1.78E-02	this study; [*Chen*, 2011; *Yang*, 2009]
OR3-1368	96C	8.62E-05		1.22E-03	this study; [*Chen*, 2011; *Yang*, 2009]
OR3-1368	96D	6.78E-05		1.17E-03	this study; [*Chen*, 2011; *Yang*, 2009]
OR3-1368	96E	1.11E-04		1.33E-03	this study; [*Chen*, 2011; *Yang*, 2009]
OR3-1368	96F	9.77E-05		1.27E-03	this study; [*Chen*, 2011; *Yang*, 2009]
OR3-1368	96J		1.26E-04	3.94E-02	this study; [*Chen*, 2011; *Yang*, 2009]
OR3-1368	96L		1.26E-04	5.22E-03	this study; [*Chen*, 2011; *Yang*, 2009]
OR3-1368	kp9	7.17E-05		8.92E-04	this study; [*Chen*, 2011; *Yang*, 2009]
OR3-1384	F-27	1.45E-04		7.36E-04	this study; [*Chen*, 2010]
OR3-1384	F-9	3.53E-06		1.36E-03	this study; [*Chen*, 2010]
OR3-1384	FGS5-1	9.46E-06		2.12E-03	this study; [*Chen*, 2010]
OR3-1384	FGS5-2	3.66E-06		7.78E-04	this study; [*Chen*, 2010]
OR3-1384	FN8		1.25E-04	4.18E-04	this study; [*Chen*, 2010]
OR3-1384	FYB	2.31E-06		3.08E-04	this study; [*Chen*, 2010]
OR3-1384	FYB3		2.31E-06	7.77E-04	this study; [*Chen*, 2010]
OR3-1384	GT39B-1	3.13E-06		3.26E-04	this study; [*Chen*, 2010]
OR3-1384	GT39B-2	1.18E-05		9.35E-03	this study; [*Chen*, 2010]
OR3-1384	HLC-1	4.38E-06		3.16E-03	this study; [*Chen*, 2010]
OR3-1405	8A		6.77E-05	1.67E-03	this study; [*Chen*, 2011; *Yang*, 2009]
OR3-1405	8B		6.77E-05	1.37E-03	this study; [*Chen*, 2011; *Yang*, 2009]
OR3-1405	8C		6.77E-05	1.80E-03	this study; [*Chen*, 2011; *Yang*, 2009]
OR3-1405	G22		1.33E-04	2.18E-03	this study; [*Chen*, 2011; *Yang*, 2009]
OR3-1405	G96MV1-G1		1.26E-04	3.17E-02	this study; [*Chen*, 2011; *Yang*, 2009]
OR3-1405	G96MV1-G2		1.26E-04	2.76E-03	this study; [*Chen*, 2011; *Yang*, 2009]
OR3-1405	G96MV2		1.26E-04	2.25E-03	this study; [*Chen*, 2011; *Yang*, 2009]
OR3-1405	G96MV6		1.26E-04	1.67E-03	this study; [*Chen*, 2011; *Yang*, 2009]
OR3-1405	G96V		1.26E-04	1.57E-03	this study; [*Chen*, 2011; *Yang*, 2009]
OR5-1311	C15		9.94E-06	3.82E-03	this study
OR5-1311	C17		9.94E-06	4.58E-03	this study

doi:10.6342/NTU202000506

Table A3.2.2. Raw data of carbon isotope values and weight percentage of total organic carbon [*Yang*, 2012].

Crusie	site	depth (cmbsf)	δ^{13}C-TOC (VPDB, permil)	TOC (wt%)
OR1-1029	EN1	1	-22.70	0.65
		21	-22.62	0.68
		41	-22.72	0.67
		61	-23.00	0.62
		81	-22.82	0.61
		101	-22.87	0.63
		121	-22.89	0.63
		141	-22.92	0.61
		161	-22.69	0.66
		181	-22.60	0.71
		201	-22.59	0.71
		221	-22.40	0.83
		241	-22.44	0.88
OR1-1029	C5	1	-23.96	0.67
		21	-23.21	0.62
		41	-23.48	0.61
		61	-23.19	0.64
		81	-23.63	0.64
		101	-23.48	0.59
		121	-23.27	0.62
		141	-23.32	0.60
		161	-23.29	0.60
		181	-23.32	0.59
		201	-23.46	0.58
		221	-23.00	0.57
		241	-23.19	0.60
		261	-23.01	0.59
		281	-23.05	0.60
		301	-23.11	0.58
		321	-22.84	0.64
		341	-22.82	0.63
		361	-23.03	0.61
		381	-22.92	0.60
		401	-23.35	0.59
		421	-23.52	0.62
OR1-1070	C11	2.5	-23.20	0.49
		32.5	-22.54	0.34
		62.5	-21.88	0.27
		92.5	-22.06	0.36
		122.5	-21.89	0.38
		152.5	-21.95	0.34

doi:10.6342/NTU202000506

Table A3.2.2. (continued)

Crusie	site	depth (cmbsf)	δ^{13}C-TOC (VPDB, permil)	TOC (wt%)
OR1-1070	C11	182.5	-22.73	0.31
		212.5	-23.56	0.36
		242.5	-23.96	0.33
		272.5	-23.81	0.29
		302.5	-23.46	0.38
		332.5	-23.53	0.24
		362.5	-23.22	0.39
		392.5	–23.14	0.37
		422.5	–23.69	0.37
		452.5	–23.65	0.41
OR1-1070	C9	2.5	–23.85	0.58
		22.5	–23.28	0.51
		42.5	–23.18	0.53
		62.5	–23.02	0.58
		82.5	–23.23	0.62
		102.5	–23.59	0.57
		122.5	–23.43	0.69
		142.5	–28.05	0.67
OR1-1070	C12	2.5	–23.47	0.50
		32.5	–23.25	0.61
		62.5	–23.39	0.72
		92.5	–24.86	0.83
		122.5	–24.11	0.83
		152.5	–22.92	0.74

doi:10.6342/NTU202000506

Table A3.3. Reaction rates within the SMTZ based on the box model and corresponding diffusive fluxes.

	Site										
rates / fluxes	C9	C12	MT7	C17	C10	C11	EN1	C5	3289	3279	3280
AOM	22.6	12.6	7.05	4.92	5.43	8.71	24.2	4.32	0.76	12.6	8.55
CR	8.40	4.48	2.78	1.95	1.74	3.13	7.40	0.78	0.20	5.05	2.7
CP	6.71	19.17	2.29	5.34	4.23	5.97	9.64	2.67	1.45	6.07	7.88
ME	2.60	5.74	1.61	2.45	3.53	2.25	0.95	0.36	1.10	0.79	2.51
OSR	5.20	11.5	3.22	4.89	7.06	4.50	1.90	0.72	2.20	1.58	5.02
CH_4 diffusive flux	5.27	2.23	1.77	8.00	1.70	1.53	24.7	4.53	0.86	3.78	6.02
CH_4 diffusive flux / AOM	0.23	0.18	0.25	1.62	0.31	0.18	1.02	1.05	1.12	0.30	0.70
AOM/OSR	4.4	1.1	2.2	1.0	0.8	1.9	12.7	6.0	0.3	8.0	1.7
sulfate consumed by AOM (%)	81.3	52.4	68.6	50.2	43.5	66.0	92.7	85.7	25.7	88.8	63.0
Efflux	1.66	0.04		0.10	0.02	0.13	0.03	0.05			
(ME+CR)/AOM	0.5	0.8	0.6	0.9	1.0	0.6	0.3	0.3	1.7	0.5	0.6
Flux from deep source	11.6	2.4	2.7	0.5	0.2	3.3	15.9	3.2		6.7	3.4

Note: Unit: $\times 10^{-2}$ mmol m^{-2} d^{-1}

doi:10.6342/NTU202000506

Table A3.4. Parameters used for estimation of thermogenic methane production.

Terms	Max	Min	Reference
Sediment mass ($R_{acc\text{-}M}$)			
Sediment thickness in trench (H_{tr}; km)	4.49	1.24	*Chen et al.* [2017]; *Liao et al.* [2016]; *Yeh and Hsu* [2004]
Length of trench (L_{tr}; km; 71% of the length of trench considered from 21 to 24.5 ^{o}N)	284	284	*Chi et al.* [2003]; *Huang et al.* [2006]
Subduction rate (R_{sd}; km Ma^{-1})	76	66	*Suppe* [1981]; *Lundberg et al.* [1997]
Bulk sediment density (ρ_{bulk}; kg km^{-3})	1.8E12	1.6E12	*Wang et al.* [2000]
Percentage of matured sediments for methane production (*m*; with propotion of non-cycling hydrocarbon)	42%	42%	*von Huene and Scholl* [1991]; *Hunt* [1995]
hydrocarbon potential (*PP*; g HC / kg rock)	0.5	0.15	*Wang et al.* [2000]
Total methane generate (Tg Ma^{-1})	36,630	1,340	
Percentage of investigated area	60%	60%	
Total methane production (Tg Ma^{-1})	21,979	1,406	

doi:10.6342/NTU202000506

Table A3.5. Parameters used for estimation of thermogenic methane production.

Site	depth (cmbsf)	CH_4 (mM)	C_2H_6 (μM)	C_3H_8 (μM)	C_1/C_{2+}	$\delta^{13}C$-CH_4 ‰ (VPDB)	$\delta^{2}H$-CH_4 ‰ (VSMOW)
Passive margin							
MD10-3264[a]	2046.5	0.66	0.71		935	-90.5[c]	
Active margin, lower slope							
OR5-1309-2-MT7-P	788	2.76				-73.2	
OR1-1029-C5	428	2.73	1.04	0.03	2567	-95.9	
OR1-1029-EN1	252	9.46	0.35	0.60	9943	-88.4	
OR1-1029-EN2	228	3.54	0.64	0.07	4996	-98.6	
OR1-1044-C10	333	1.09	2.51		433	-73.2	
OR1-1070-C11	474	1.03				-68.1	
OR1-828-GT1	480.5	1.91	0.05		38115	-83.8	
OR1-860-26	373	1.39				-94.2	-178.1
OR1-860-27	226	0.94				-72.8	-182.2
OR1-860-28	406	1.66				-90.6	-186.9
OR1-978-2N	181.5	1.05				-81.4[b]	
OR1-978-2NL	270.5	0.76				-74.0[b]	
MD178-10-3265	500	0.38	0.18		2143	-103.0[b]	
MD178-10-3266[a]	2146.5	0.60				-78.1[b]	
MD178-10-3274[a]	2346.5	0.44				-74.4[b]	
MD178-10-3275	3281.5	0.40				-70.2[b]	
MD178-10-3276	2450.5	1.02				-72.7[b]	
MD178-10-3277[a]	2496.5	1.30	1.61		823	-68.8[b]	
MD178-10-3279	2296.5	0.42	3.34		125	-70.2	-205.0
MD178-10-3280	475	0.89	3.02		294	-85.0[b]	
MD178-10-3288[a]	2146.5	0.60				-70.8[b]	
MD178-10-3292	1096.5	0.36	4.64		78	-72.1	-225.0
Active margin, upper slope							
OR5-1309-2-MD4-P3	700	1.58	39.76	4.02	36	-38.2	
OR1-1107-96V2	185	1.81	2.4	0.1	731	-37.5	
OR1-1107-MV12-1	102	1.48	7.9	1.4	158	-45.4	
OR1-1107-MV12-3	6	1.26	94.1	38.6	9.2	-35.6	
OR1-1107-MV12-A	112	2.31	5.8	0.8	349	-62.5	
OR1-835-GT39B	463.5	1.32	0.34		3893	-45.3	-169.9
MD178-10-3289	1650	0.48	5.28		91	-81.0	-221.3

[a] Methane concentrations are cited from *Hu et al.* [2017].
[b] Carbon isotopic compositions of methane were measured by a MCIA.

doi:10.6342/NTU202000506

Table A3.6. Global rates of AOM and OSR at SMTZ, effluxes and biological filtration efficiency.

Location	site	CH4 efflux (mmol $m^{-2}d^{-1}$)	CH4 flux at SMTZ (mmol $m^{-2}d^{-1}$)	AOM (mmol $m^{-2}d^{-1}$)	OSR (mmol $m^{-2}d^{-1}$)	ME (mmol $m^{-2}d^{-1}$)	POC (wt %)	Biofiltration efficiency of AOM (%)*	reference
Hydrate Ridge	SO-148/1 19-2	0.6	13.3	13.3				95.68	*Treude et al.* [2003]
	SO-148/1 14	4	15.4	15.4				79.38	*Treude et al.* [2003]
	SO143/55-2		25.342	25.342	1.452	0.142	1.3-1.6		*Luff and Wallmann* [2003]
Gulf of Mexico	MD02-2571			20.1-67.0					*Ussler and Paull* [2008]
	BIGO 4	0.6	16.5	15.1				96.49	*Sommer et al.* [2006]
	BIGO 5	0.001	3.6					99.99	*Sommer et al.* [2006]
Costa Rica, Mound 12	BC1	12.05	28.27	16.11				70.11	*Linke et al.* [2005]
Dvurechenskii MV (Black sea)	MIC-3	11.1	58.3	47.2				84.01	*Wallmann et al.* [2006a]
	MIC-4	10.3	38.3	28				78.81	*Wallmann et al.* [2006a]
	MIC-5	3.4	21.6	18.2				86.4	*Wallmann et al.* [2006a]
Blake Ridge	ODP 997		0.029	0.029	0.008	0.001	0.5-2		*Wallmann et al.* [2006b]
Derugin Basin (Sakhalin Island)	SO178 3-4 KAL		0.001	0.001	0.017	0.002	0.5-0.8		*Wallmann et al.* [2006b]
	LV28 2-4 SL		0.001	0.001	0.052	0.007	0.5-1.5		*Wallmann et al.* [2006b]
	SO178 10-6 SL		0.044	0.044	0.087	0.111	0.75-1.75		*Wallmann et al.* [2006b]
	SO178 13-6 KL		0.215	0.215	0.334	0.073	1.1-2		*Wallmann et al.* [2006b]
	SO178 29-2 KL		0.162	0.162	0.211	0.036	1.4-1.7		*Wallmann et al.* [2006b]
	LV28 20-2 SL		0.124	0.124	0.285	0.03	1.1-1.8		*Wallmann et al.* [2006b]
advection-dominated system		0.1	19.4	19.4				99.49	*Dale et al.* [2008b]

* Biofiltration efficiency of AOM (%) was calculated as the difference of methane fluxes at SMTZ and effluxes divided by methane flux at SMTZ for each site.

doi:10.6342/NTU202000506

Table A3.6. (continued)

Location	site	CH4 efflux (mmol $m^{-2}d^{-1}$)	CH4 flux at SMTZ (mmol $m^{-2}d^{-1}$)	AOM (mmol $m^{-2}d^{-1}$)	OSR (mmol $m^{-2}d^{-1}$)	ME (mmol $m^{-2}d^{-1}$)	POC (wt %)	Biofiltration efficiency of AOM (%)*	reference
Denmark, Skagerrak	station 13		0.091	0.091					*Dale et al.* [2008a]
	station 10		0.25	0.25					*Dale et al.* [2008a]
Opouawe Bank (New Zealand)		12	18.2					60.26	*Dale et al.* [2010]
Ulleung Basin	UBGH2-1_1		0.124	0.124	0.021	0.144	0.5-4		*Hong et al.* [2013b]; *Kim et al.* [2007]
	UBGH2-2_1		0.145	0.145	0.041	0.188	0.5-4		*Hong et al.* [2013b]; *Kim et al.* [2007]
	UBGH2-5		0.127	0.127	0.041	0.164	0.5-4		*Hong et al.* [2013b]; *Kim et al.* [2007]
	UBGH2-6		0.152	0.152	0.064	0.193	0.5-4		*Hong et al.* [2013b]; *Kim et al.* [2007]
	UBGH2-10		0.124	0.124	0.148	0.049	0.5-4		*Hong et al.* [2013b]; *Kim et al.* [2007]
Vestnesa Ridge (Svalbard)	HH13-197		0.298	0.298	0.045				*Hong et al.* [2016]
	HH13-199		0.002	0.002	0.068				*Hong et al.* [2016]
	HH13-200		0.923	0.923	0.016				*Hong et al.* [2016]
	HH-13-203		0.803	0.803	0.012				*Hong et al.* [2016]
Offshore SW Taiwan (YAR)	OR1-860-18	0.004	0.101	0.101	0.129	0.041	0.4-0.7	96.1	*Chuang et al.* [2013]
	OR1-860-21	0.002	0.096	0.096	0.101	0.036	0.4-0.7	98.04	*Chuang et al.* [2013]
	MD05-2911	0.007	0.195	0.195	0.088	0.03	0.5-0.6	96.34	*Chuang et al.* [2013]
	MD10-178-3279		0.038	0.126	0.016	0.008			this study; [*Yang*, 2010]
	MD10-178-3280		0.06	0.129	0.041	0.025	0.5-0.6		this study; *Lin et al.* [2014]
Offshore SW Taiwan (TNR)	OR1-860-1	0.002	0.068	0.068	0.012	0.016	0.2-0.5	96.53	*Chuang et al.* [2013]

* Biofiltration efficiency of AOM (%) was calculated as the difference of methane fluxes at SMTZ and effluxes divided by methane flux at SMTZ for each site.

doi:10.6342/NTU202000506

Table A3.6. (continued)

Location	site	CH4 efflux (mmol $m^{-2}d^{-1}$)	CH4 flux at SMTZ (mmol $m^{-2}d^{-1}$)	AOM (mmol $m^{-2}d^{-1}$)	OSR (mmol $m^{-2}d^{-1}$)	ME (mmol $m^{-2}d^{-1}$)	POC (wt %)	Biofiltration efficiency of AOM (%)*	reference
Offshore SW Taiwan (TNR)	OR1-860-2	0.001	0.06	0.06	0.012	0.015	0.2-0.5	97.78	*Chuang et al.* [2013]
	MD05-2912	0.002	0.068	0.068	0.015	0.009	0.3-0.7	97.66	*Chuang et al.* [2013]
Offshore SW Taiwan (GWR)	MD05-2913	0.002	0.093	0.093	0.026	0.024	0.3-0.4	97.98	*Chuang et al.* [2013]
Offshore SW Taiwan (FTR)	OR1-1029-EN1	0.00003	0.247	0.234	0.003	0.01	0.6-0.9	99.99	this study; [*Yang*, 2013]
Offshore SW Taiwan (FWCR)	OR1-1044-C10	0.00002	0.017	0.054	0.071	0.035		99.89	this study
	OR5-1311-C17	0.0001	0.08	0.075	0.038	0.024		99.89	this study
Offshore SW Taiwan (TYR)	OR5-1309-2-MT7		0.018	0.07	0.032	0.016			this study
Offshore SW Taiwan (lower slope)	OR1-1029-C5	0.00005	0.045	0.043	0.007	0.004	0.5-0.7	99.89	this study; [*Yang*, 2013]
	OR1-1070-C9	0.00166	0.053	0.226	0.052	0.026	0.5-0.7	96.95	this study; [*Yang*, 2014]
	OR1-1070-C11	0.00013	0.015	0.087	0.045	0.022	0.2-0.5	99.15	this study; [*Yang*, 2014]
	OR1-1070-C12	0.00004	0.022	0.126	0.115	0.057	0.5-0.8	99.81	this study; [*Yang*, 2014]
Offshore SW Taiwan (upper slope)	MD178-10-3289		0.009	0.013	0.021	0.011			this study; [*Yang*, 2010]

* Biofiltration efficiency of AOM (%) was calculated as the difference of methane fluxes at SMTZ and effluxes divided by methane flux at SMTZ for each site.

doi:10.6342/NTU202000506

References in appendix

Berner, R. A. *Early Diagenesis—A Theoretical Approach*, Princeton University Press, Princeton, N. J. (1980).

Bird, P. Hydration-phase diagrams and friction of montmorillonite under laboratory and geologic conditions, with implications for shale compaction, slope stability, and strength of fault gouge. *Tectonophysics*, **107**(3–4), 235–260; 10.1016/0040-1951(84)90253-1 (1984).

Boudreau, B. P. Diagenetic models and their implementation, vol. 505, 132 pp. Springer, Berlin (1997).

Boudreau, B. P. The diffusive tortuosity of fine-grained unlithified sediments. *Geochim. Cosmochim. Acta*, **60**(16), 3139–3142; 10.1016/0016-7037(96)00158-5 (1996).

Burdige, D. J., Komada, T., Magen, C., & Chanton, J. P. Carbon cycling in Santa Barbara Basin sediments: A modeling study. *J. Mar. Res.*, **74**(3), 133–159; 10.1357/002224016819594818 (2016).

Chen, H. C. Halogen Profiles of Pore Waters from Gas Hydrate Potential Area Offshore of SW Taiwan. Master thesis, Department of Geosciences, National Taiwan University (in Chinese with English abstract); 10.6342/NTU.2010.02645 (2010).

Chen, H. W. Geochemistry and Origin of Pore Water Compositions of Cored Sediments in Offshore Southwestern Taiwan. Master thesis, Department of Geosciences, National Taiwan University (in Chinese with English abstract); 10.6342/NTU.2011.00960 (2011).

Chen L. W. *et al.* Deriving regional vertical fluid migration rates offshore southwestern Taiwan using bottom-simulating reflectors. *Mar. Geophys. Res.*, **33**(4), 379–388; 10.1007/s11001-012-9162-4 (2012).

Chen, M. P. Geotechnical properties of sediments off the coast of Hsinchu-northwest Taiwan related to sedimentary environment. *Acta Oceanogr. Taiwan.*, 12, 28–53 (1981).

Chen, N. C. The carbon isotopes of DIC and methane gas from gas hydrate potential area offshore SW Taiwan. Master thesis, Department of Geosciences, National Taiwan University (in Chinese with English abstract); 10.6342/NTU.2009.02789 (2009).

doi:10.6342/NTU202000506

Chen, N. C. *et al.* Production, consumption, and migration of methane in accretionary prism of southwestern Taiwan. *Geochem. Geophys. Geosyst.*, **18**(8), 2970–2989; 10.1002/2017GC006798 (2017).

Chen, S. C. *et al.* Distribution and characters of the mud diapirs and mud volcanoes off southwest Taiwan. *J. Asian Earth Sci.*, **92**, 201–214; 10.1016/j.jseaes.2013.10.009 (2014).

Chi, W. C. *et al.* Tectonic wedging along the rear of the offshore Taiwan accretionary prism. *Tectonophysics*, **374**(3), 199–217; 10.1016/j.tecto.2003.08.004 (2003).

Chiao, L.-Y. Investigation of heat flow in gas hydrate potential area (4/4). *Report of Central Geological Survey*, 104-11-D, 82 pp. (2015)

Chuang, P. C. *et al.* Extremely High Methane Concentration in Bottom Water and Cored Sediments from Offshore Southwestern Taiwan. *Terr. Atmos. Oceanic Sci.*, **17**(4), 903–920 (2006).

Chuang, P. C. *et al.* Estimation of Methane Flux Offshore SW Taiwan and the Influence of Tectonics on Gas Hydrate Accumulation. *Geofluids*, **10**, 497–510, doi:10.1111/j.1468-8123.2010.00313.x (2010).

Chuang, P. C. *et al.* Relating sulfate and methane dynamics to geology: the accretionary prism offshore SW Taiwan. *Geochem. Geophys. Geosyst.*, **14**(7), 2523–2545; 10.1002/ggge.20168 (2013).

Freundt, A. *et al.* Volatile (H_2O, CO_2, Cl, S) budget of the Central American subduction zone. *International Journal of Earth Sciences*, **103**(7), 2101–2127; 10.1007/s00531-014-1001-1 (2014).

Haeckel, M., Boudreau, B. P., & Wallmann, K. Bubble-induced porewater mixing: A 3-D model for deep porewater irrigation. *Geochim. Cosmochim. Acta*, **71**(21), 5135–5154, doi: 10.1016/j.gca.2007.08.011 (2007).

Hong, W. L. *et al.* Seepage from an arctic shallow marine gas hydrate reservoir is insensitive to momentary ocean warming. *Nat. commun.*, **8**, 15745; 10.1038/ncomms15745 (2017).

Hu, D. *et al.* Deep sea records of the continental weathering and erosion response to East Asian monsoon intensification since 14 ka in the South China Sea. *Chem. Geol.*, **326**, 1–18 (2012).

Huang, C. Y., Yuan, P. B., & Tsao, S. J. Temporal and spatial records of active arc continent collision in Taiwan: A synthesis. *Geol. Soc. Am. Bull.*, **118**, 274–288; 10.1130/B25527.1 (2006).

Jarrard, R. D. Subduction fluxes of water, carbon dioxide, chlorine, and potassium.

doi:10.6342/NTU202000506

Geochem. Geophys. Geosyst., **4**(5); 10.1029/2002GC000392 (2003).

Lin C. C. *et al.* Tectonic features of the incipient arc-continent collision zone of Taiwan: Implications for seismicity. *Tectonophysics*, **476** (1-2), 28–42; 10.1016/j.tecto.2008.11.004 (2009).

Liu, Z. *et al.* Clay mineral assemblages in the northern South China Sea: implications for East Asian monsoon evolution over the past 2 million years. *Mar. Geol.*, **201**(1), 133–146; 10.1016/S0025-3227(03)00213-5 (2003).

Lundberg, N., Reed, D. L., Liu, C. S., & Lieske Jr, J. Forearc-basin closure and arc accretion in the submarine suture zone south of Taiwan. *Tectonophysics*, **274**(1–3), 5–23; 10.1016/S0040-1951(96)00295-8 (1997).

Manov, G. G. *et al.* Values of the constants in the Debye—Hückel equation for activity coefficients. *J. Am. Chem. Soc.*, **65**(9), 1765–1767 (1943).

Menapace, W., Völker, D., Kaul, N., Tryon, M. D., & Kopf, A. J. The role of mud volcanism and deep-seated dewatering processes in the Nankai Trough accretionary prism and Kumano Basin, Japan. *Geochem. Geophys. Geosyst.*, **18**(7), 2486–2509; 10.1002/2016GC006763 (2017).

Nauhaus, K., Boetius, A., Krüger, M., & Widdel, F. In vitro demonstration of anaerobic oxidation of methane coupled to sulphate reduction in sediment from a marine gas hydrate area. *Environ. Microbial.*, **4**(5), 296–305, doi:10.1046/j.1462-2920.2002.00299.x (2002).

Middelburg, J. J. A simple rate model for organic matter decomposition in marine sediments. *Geochim. Cosmochim. Acta*, **53**(7), 1577–1581; 10.1016/0016-7037(89)90239-1 (1989).

Miyazaki, S. I. & Heki, K. Crustal velocity field of southwest Japan- Subduction and arc-arc collision, *J. Geophys. Res. Solid Earth*, **106**(B3), 4305–4326; 10.1029/2000JB900312 (2001).

Seno, T., Stein, S., & Gripp, A. E. A model for the motion of the Philippine Sea plate consistent with NUVEL- and geological data. *J. Geophys. Res. Solid Earth*, **98**(B10), 17941–17948; 10.1029/93JB00782 (1993).

Shyu, C. T. & Hung, C. Determination of Seafloor Temperatures Using Data from High-Resolution Marine He at Probes. *Terrestrial, Atmospheric and Oceanic Sciences*, **16**(1),137–153; 10.3319/TAO.2005.16.1.137(Oc) (2005).

Su, C. C. Investigation of Gas Hydrate Resource Potential: Seismic, Heat Flow and Geochemical Studies (4/4) – gas composition of bottom water and sediments

doi:10.6342/NTU202000506

offshore southwest Taiwan. *Report of Central Geological Survey* **2015**, 104-11-F, 106 pp (in Chinese with English abstract) (2015).

Su, C. C., Hsu, S. T., Hsu, H. H., Lin, J. Y., & Dong, J. J. Sedimentological characteristics and seafloor failure offshore SW Taiwan. *Terr. Atmos. Ocean. Sci.*, **29**(1); 10.3319/TAO.2017.06.21.01 (2018).

Suppe, J. Mechanics of mountain building and metamorphism in Taiwan. *Memoir of the Geological Society of China*, **4**(6), 67–89 (1981).

Tishchenko, P., Hensen, C., Wallmann, K., & Wong, C. S. Calculation of the stability and solubility of methane hydrate in seawater. *Chem. Geol.*, **219**(1–4), 37–52; 10.1016/j.chemgeo.2005.02.008 (2005).

Tobin, H. *et al.* NanTroSEIZE Plate Boundary Deep Riser 4: Nankai Seismogenic/Slow Slip Megathrust. *International Ocean Discovery Program Expedition 358 Preliminary Report*; 10.14379/iodp.pr.358.2019 (2019).

Vanneste, H. *et al.* Spatial variation in fluid flow and geochemical fluxes across the sediment–seawater interface at the Carlos Ribeiro mud volcano (Gulf of Cadiz). *Geochim. Cosmochim. Acta*, **75**(4), 1124–1144; 10.1016/j.gca.2010.11.017 (2011).

Vavilin, V. A. Estimating changes of isotopic fractionation based on chemical kinetics and microbial dynamics during anaerobic methane oxidation: apparent zero-and first-order kinetics at high and low initial methane concentrations. *Antonie van Leeuwenhoek*, **103**(2), 375–383; 10.1007/s10482-012-9818 (2013).

von Huene, R. & D. W. Scholl Observations at convergent margins concerning sediment subduction, subduction erosion, and the growth of continental crust. *Rev. Geophys.*, **29**(3), 279–316; 10.1029/91RG00969 (1991).

Wallmann, K. et al. Kinetics of organic matter degradation, microbial methane generation, and gas hydrate formation in anoxic marine sediments. *Geochim. Cosmochim. Acta*, **70**(15), 3905–3927; 10.1016/j.gca.2006.06.003 (2006).

Wan, S., Li, A., Clift, P. D., & Stuut, J. B. W. Development of the East Asian monsoon: mineralogical and sedimentologic records in the northern South China Sea since 20 Ma. *Palaeogeogr., Palaeoclimatol., Palaeoecol.*, **254**(3–4), 561–582; 10.1016/j.palaeo.2007.07.009 (2007).

Wang, P. *et al.* Exploring the Asian monsoon through drilling in the South China Sea. In *Proceedings of the Ocean Drilling Program: Initial Report* (Vol. 184, pp. 1-77); 10.2973/odp.proc.ir.184.2000 (2000).

Wegener, G. & Boetius, A. An experimental study on short-term changes in the

doi:10.6342/NTU202000506

anaerobic oxidation of methane in response to varying methane and sulfate fluxes. *Biogeosciences*, **6**, 867–876; 10.5194/bg-6-867-2009 (2009).

Wu, J. X. New data processing algorithm for marine heat flow and thermal modeling for Tsan-Yao mud volcano offshore SW Taiwan. Master thesis, Institute of Oceanography College of Science, National Taiwan University (in Chinese with English abstract); 10.6342/NTU201602190 (2016).

Xie, Y. *et al*. Sediment compaction and pore pressure prediction in deepwater basin of the South China Sea: Estimation from ODP and IODP drilling well data. *Journal of Ocean University of China*, **17**(1), 25–34; 10.1007/s11802-018-3449-2 (2018)

Yang, T. F. Gas Hydrate Resource Potential Area: Geological Surveys and Geochemical Investigation (4/4) – gas composition of bottom water and sediments offshore southwest Taiwan. *Report of Central Geological Survey* **2007**, 96-27-F, 71 pp (in Chinese with English abstract) (2007).

Yang, T. F. Investigation and Assessment of Gas Hydrate Resource Potential: Geochemical Studies (1/4) – gas composition of bottom water and sediments offshore southwest Taiwan. *Report of Central Geological Survey* **2011**, 97-29-A, 64 pp (in Chinese with English abstract) (2008).

Yang, T. F. Investigation and Assessment of Gas Hydrate Resource Potential: Geochemical Studies (2/4) – gas composition of bottom water and sediments offshore southwest Taiwan. *Report of Central Geological Survey* **2011**, 98-27-A, 62 pp (in Chinese with English abstract) (2009).

Yang, T. F. Investigation and Assessment of Gas Hydrate Resource Potential: Geochemical Studies (3/4) – gas composition of bottom water and sediments offshore southwest Taiwan. *Report of Central Geological Survey* **2011**, 99-26-A, 56 pp (in Chinese with English abstract) (2010).

Yang, T. F. Investigation and Assessment of Gas Hydrate Resource Potential: Geochemical Studies (4/4) – gas composition of bottom water and sediments offshore southwest Taiwan. *Report of Central Geological Survey* **2012**, 100-25-A, 99 pp (in Chinese with English abstract) (2011).

Yang, T. F. Investigation of Gas Hydrate Resource Potential: Seismic, Heat Flow and Geochemical Studies (1/4) – gas composition of bottom water and sediments offshore southwest Taiwan. *Report of Central Geological Survey* **2012**, 101-22-F, 108 pp (in Chinese with English abstract) (2012).

doi:10.6342/NTU202000506

Yang, T. F. Investigation of Gas Hydrate Resource Potential: Seismic, Heat Flow and Geochemical Studies (2/4) – gas composition of bottom water and sediments offshore southwest Taiwan. *Report of Central Geological Survey* **2013**, 102-19-F, 113 pp (in Chinese with English abstract) (2013).

Yang, T. F. Investigation of Gas Hydrate Resource Potential: Seismic, Heat Flow and Geochemical Studies (3/4) – gas composition of bottom water and sediments offshore southwest Taiwan. *Report of Central Geological Survey* **2014**, 103-16-F, 105 pp (in Chinese with English abstract) (2014).

doi:10.6342/NTU202000506